

Investigation of the impact of EHV underground power cables on the resonant and transient grid behavior

Citation for published version (APA):

Barakou, F. (2018). *Investigation of the impact of EHV underground power cables on the resonant and transient grid behavior*. [Phd Thesis 1 (Research TU/e / Graduation TU/e), Electrical Engineering]. Technische Universiteit Eindhoven.

Document status and date:

Published: 04/12/2018

Document Version:

Publisher's PDF, also known as Version of Record (includes final page, issue and volume numbers)

Please check the document version of this publication:

- A submitted manuscript is the version of the article upon submission and before peer-review. There can be important differences between the submitted version and the official published version of record. People interested in the research are advised to contact the author for the final version of the publication, or visit the DOI to the publisher's website.
- The final author version and the galley proof are versions of the publication after peer review.
- The final published version features the final layout of the paper including the volume, issue and page numbers.

[Link to publication](#)

General rights

Copyright and moral rights for the publications made accessible in the public portal are retained by the authors and/or other copyright owners and it is a condition of accessing publications that users recognise and abide by the legal requirements associated with these rights.

- Users may download and print one copy of any publication from the public portal for the purpose of private study or research.
- You may not further distribute the material or use it for any profit-making activity or commercial gain
- You may freely distribute the URL identifying the publication in the public portal.

If the publication is distributed under the terms of Article 25fa of the Dutch Copyright Act, indicated by the "Taverne" license above, please follow below link for the End User Agreement:

www.tue.nl/taverne

Take down policy

If you believe that this document breaches copyright please contact us at:

openaccess@tue.nl

providing details and we will investigate your claim.

Investigation of the Impact of EHV Underground Power Cables on the Resonant and Transient Grid Behavior

PROEFSCHRIFT

ter verkrijging van de graad van doctor aan de Technische Universiteit
Eindhoven, op gezag van de rector magnificus prof.dr.ir. F.P.T. Baaijens, voor
een commissie aangewezen door het College voor Promoties, in het openbaar te
verdedigen op dinsdag 4 december 2018 om 13:30 uur

door

Fani Barakou

geboren te Athene, Griekenland

Dit proefschrift is goedgekeurd door de promotoren en de samenstelling van de promotiecommissie is als volgt:

Voorzitter:	prof. dr. ir. T. Koonen	
Promotor:	prof. dr. ir. E.F. Steennis	
2 nd Promotor:	prof. dr. ir. J.J. Smit	
Copromotor:	prof. dr. P.A.A.F. Wouters	
Leden:	prof. dr. ir. M.H.J. Bollen	Luleå University of Technology
	prof. N. Hatziargyriou PhD	National Technical University of Athens
	prof. dr. ir. P.C.J.M. van der Wielen	
adviseur	dr. S. Mousavi-Gargari	TenneT TSO BV

Het onderzoek of ontwerp dat in dit proefschrift wordt beschreven is uitgevoerd in overeenstemming met de TU/e Gedragscode Wetenschapsbeoefening.

Στους αγαπημένους μου γονείς...

This research is financed by TenneT TSO B.V. in Arnhem, The Netherlands.

Printed by Ipskamp drukkers, Enschede, The Netherlands

A catalogue record is available from the Eindhoven University of Technology Library.

ISBN: 978-90-386-4648-0

Copyright © 2018 by F. Barakou

Summary

Investigation of the Impact of EHV Underground Power Cables on the Resonant and Transient Grid Behavior

In the past, overhead lines were the dominant means for transmitting electrical energy at HV and EHV levels. However, weather-related incidents, technical changes, strong competition in the cable sector, increased urbanization as well as other political and environmental aspects are leading to an increasing utilization of EHV underground power cables. Recently, the Dutch 380 kV transmission network is being extended with two new connections, namely Randstad south-ring and Randstad north-ring, to reinforce its transmission capacity where underground power cables are integrated in the connection. Since the Dutch TSO is keen to expand its expertise concerning the integration of underground power cables in the transmission network at this voltage level a research program, called Randstad380, was initiated to investigate possible consequences of underground power cables in the 380 kV network. In the present dissertation the focus is on the Randstad south-ring connection where measurements are being performed in order to obtain information concerning the 380 kV power cable resonant and transient behavior.

The first step for investigating the system's resonant and transient behavior is the modeling of its components and more specifically of transmission lines (i.e. overhead lines and underground power cables) in order to predict the risks of such phenomena for power system operation allowing for taking countermeasures. For modeling the Randstad south-ring cable the Frequency Dependent Phase Model (FDPM) was used since it strives to represent the full frequency dependency of a transmission line and is considered the most accurate and stable model employed in commercially available PSCAD/EMTDC. However, for the fully detailed south-ring cable model stability problems due to large passivity violations were encountered when transforming from frequency to time domain. Two cable models were developed, referred to as "detailed" and "simplified", and compared in frequency domain using frequency scans. The simplified model was used to perform a sensitivity analysis on aspects that can affect the accuracy of the simulation results for resonance and slow-front transients in order to identify

which of them are important and need to be accurately modeled. These aspects are related to uncertainties in the cable design parameters or in the cable laying configuration. They can also be related to simplifications that need to be made due to software limitations or for reduction of the simulation time.

In order to overcome the stability problem of the FDPM a numerical method for approximately determining the time-domain solution of the transmission line equations, known as Finite Difference Time Domain (FDTD) method has been formulated and incorporated into PSCAD/EMTDC. For the formulation of the FDTD model the fitted quantities in frequency domain are the series impedance, $Z(\omega)$, and the shunt admittance, $Y(\omega)$, which are much smoother functions in respect to frequency compared with the propagation function used by the FDPM. In FDTD the partial differential equations (Telegrapher's equations) are discretized and directly solved in time domain using an explicit central difference scheme where the voltages and currents are interleaved spatially and temporally. The FDTD model is compared with the well established FDPM in respect with simulation accuracy, model stability and computational time. Furthermore, the FDTD approach is used to model in detail the south-ring cable connection in order to verify the effect of the simplifications made using the FDPM in time domain, for different network configurations and transient phenomena. From the comparison it was observed that the model simplifications which needed to be made in the south-ring cable connection do not affect the resonance and the slow-front transient behavior of the 380 kV network when incorporated. The same applies for the very fast wave reflections.

To predict the impact of cables on transient behavior, an extensive part of the network needs to be modeled as seen from the cable. However, there is a lack of guidelines on the level of detail and depth of the network that needs to be modeled both at the same voltage level as well as at lower voltage levels. There are reasons to limit the extension of the simulated network since it can be time consuming to gather all the information, especially in the case of the lower voltage (distribution) network. Furthermore, when systematically studying the effect of parameters on circuit response, the evaluation time can be significantly reduced. The phenomena of interest in this dissertation are slow front transients mainly caused by line switching and resonance phenomena. For slow front transients the interest is mainly the correct representation of the maximum overvoltage while for resonance phenomena the interest is mainly the accurate representation of the frequency and magnitude of the resonance peaks. For the modeling extent at the same voltage level an iterative process is employed to determine the amount of connections that should be modeled among with their model detail and it turns out that different phenomena require different modeling approaches. For the lower voltage network a sensitivity analysis is performed to investigate the effect of downstream network components. Moreover, different types of simplified downstream network models are compared with the fully detailed one both in time

domain (maximum overvoltage during energization) and in frequency domain in order to identify the most suitable one.

The next step is to verify that the behavior of the network components is accurately depicted in their mathematical representation which can be achieved by means of comparing simulation results with measurements. For measuring transient voltages conventional measurement equipment, such as RC dividers, can be used although, such measurement equipment can face problems due to disturbing signals, especially at transition points. The need for a more robust measuring system leads to the utilization of a rather unconventional method with sensors based on open air capacitances sensing the electric fields from the line having a wide frequency bandwidth and excellent electromagnetic compatibility performance. However, since the sensors are open air capacitors, they also intercept field lines from the other phases and measurement decoupling is necessary. Results from measurements, using the Differentiating/Integrating technique, at a 380 kV mixed overhead line underground power cable connection obtained at a transition point and at a substation are presented and compared with PSCAD/EMTDC simulations. The measurement system gives accurate results for low and high frequency transients, while the effect of uncertainties in the decoupling is investigated and turns out to be minor. For switching transients the simulation model was validated in terms of measured and simulated voltage waveforms resulting in similar maximum overvoltage and frequency content.

Finally, the validated model is used to perform resonance and slow-front transient studies. A series resonance between the leakage transformer inductance and HV cable capacitance can be excited by a voltage disturbance at the EHV side of the transformer. A parametric study is performed to depict the effect of the load model, the value of leakage inductance and HV cable length on the intensity of the resonance where the Dutch EHV transmission network is used as a case study. It is concluded that the type of load model greatly affects the harmonic impedance of the system leading to different resonance behavior and the secondary circuit consisting of the transformer, the HV cable and the load considerably affects the frequency of the harmonic content produced during EHV cable energization. Furthermore, statistical studies for energization and restrike of the south-ring cable connection are shown and the distribution of the maximum overvoltage for various configurations as well as for cable additions close and further away of Randstad south-ring is presented. The same approach is used for fault and fault clearing studies. It is shown that differences in the configuration of the connection of interest affect the maximum overvoltages especially during restrike. However, in the majority of the cases the switching impulse withstand voltage is not exceeded.

Contents

Summary	v
1 Introduction	1
1.1 Background	1
1.2 Project Status	4
1.3 Research Goals	5
1.4 Research Approach	6
1.5 Dissertation Outline	7
2 Transmission Line Modeling	9
2.1 Transmission Line formulation	10
2.2 Frequency-Independent models	13
2.2.1 Pi model	13
2.2.2 Bergeron model	14
2.3 Frequency-Dependent models	16
2.3.1 Frequency-Dependent Phase Model	16
2.3.2 Frequency-Dependent Mode Model	19
3 Underground Power Cable Modeling	21
3.1 Frequency Dependent Phase Model	22
3.1.1 Southring cable model	22
3.1.2 Detailed versus simplified model in frequency domain . . .	23
3.1.3 Sensitivity analysis	25
3.1.4 Limitation of FDPM in time domain	31
3.2 Finite Difference Time Domain Model	31

3.2.1	Model formulation	31
3.2.2	Model discretization	33
3.2.3	Model implementation	36
3.3	FDPM versus FDTD Model	38
3.3.1	Simulation accuracy	38
3.3.2	Model stability	41
3.3.3	Computational time	43
3.4	Model comparison for Randstad south-ring	45
3.4.1	Stand-alone cable and south-ring connection	46
3.4.2	South-ring and Full Dutch 380 kV network	49
3.5	Conclusion	52
4	Network Modeling Detail	53
4.1	Network extent at the same voltage level	54
4.1.1	Approach	55
4.1.2	Reference Model	58
4.1.3	Accurate representation of transient overvoltage	63
4.1.4	Accurate representation of harmonic behaviour	66
4.2	Network extent across voltage levels	68
4.2.1	Downstream network benchmark	69
4.2.2	Sensitivity analysis	71
4.2.3	Simplified downstream network model formulations	75
4.2.4	Downstream network model comparison	78
4.3	Conclusion	82
5	Simulation Model Validation with Measurements	85
5.1	Differentiating/Integrating measurement	86
5.1.1	Measurement principle	87
5.1.2	Measuring system set-up	90
5.1.3	Measuring system placement	93
5.2	Measurement analysis	94
5.2.1	Measurement decoupling	95
5.2.2	Measurement sensitivity	99
5.3	Simulation model validation	102
5.3.1	Low-frequency transients	103

5.3.2	High-frequency transients	106
5.4	Conclusion	111
6	Resonance and Slow-front Overvoltage Study	113
6.1	Series resonance study	114
6.1.1	Introduction	114
6.1.2	Derivation of analytical expressions	115
6.1.3	Sensitivity analysis	116
6.1.4	Parametric Analysis	121
6.1.5	Study on Dutch 380 kV grid	122
6.2	Slow-front Transients	124
6.2.1	Energization statistical overvoltage	127
6.2.2	Re-strike statistical overvoltage	131
6.2.3	Fault and fault-clearing statistical overvoltage	135
6.3	Conclusion	137
7	Conclusions and Recommendations	141
7.1	Conclusions	141
7.2	Dissertation Contribution	144
7.3	Recommendations for future work	145
A	PSCAD Model Implementation	147
A.1	Cable data	148
A.2	OHL data	152
A.3	Implementation in EMTP software	153
B	Downstream model	155
B.1	Statistical analysis	155
C	Measurement Decoupling	161
C.1	Electrostatic simulations	161
C.2	Uncertainty definition	164
C.3	Accuracy of D/I measurement system	165

C.3.1	Error propagation	166
C.3.2	Reconstructed transient waveforms	167
C.4	Energization measurements	169
D	Transient studies	179
D.1	Series resonance	179
D.1.1	ABCD matrix components	179
D.1.2	Network parameters	180
D.2	Statistics for slow front transients	181
D.2.1	Energization transient overvoltages	181
D.2.2	Re-strike transients	184
	Bibliography	197
	List of Publications	199
	Acknowledgments	203
	Curriculum Vitae	207

1

Introduction

1.1 Background

The worldwide demand for electricity is steadily increasing and this subsequently leads to a continuous need for developing and extending the electrical transmission networks [1]. Network expansion is also a consequence of the large-scale integration of renewable energy, especially connections to offshore wind farms, in power systems [2]. The majority of Extra-High Voltage (EHV) electricity networks is based on overhead lines (OHL) and any upgrade is traditionally realized by means of them. However, the installation of new OHLs faces many challenges due to societal and environmental reasons and rules regarding transmission become more complicated due to the expansion of cities and further additions of land reserves. Moreover, in some countries, including the Netherlands, the governments have passed laws to limit the construction of new OHLs. More specifically, the Dutch government demands any new 150 kV connection to be built using UGCs (completely excluding OHLs). For 380 kV a maximum value of kilometers for OHLs is set and any new connection should be either underground or if a new OHL need to be built another OHL part need to be placed underground in order for the amount of OHL kilometers to remain below the maximum [3].

One solution is the installation of EHV AC underground cables (UGC). UGCs can

overcome the limitations of OHL connections in specific situations like densely populated and natural beauty areas. The public is also less reluctant to UGCs since they have no visual and audible impact. Although this development is quite encouraging from a societal perspective, new challenges might arise, mainly from a technical perspective. This is, on the one hand, due to the limited experience with UGCs at EHV transmission level, which corresponds to a maximum of 380 kV in the Netherlands, and on the other hand due to the different electrical characteristics of UGCs compared to OHLs [4, 5]. The series inductance of a cable can be up to five times smaller and the shunt capacitance can be up to thirty times larger than the corresponding values of an equivalent OHL [6]. Therefore, several system operational aspects need to be investigated beforehand in order to ensure that the system operation will not be jeopardized by connection of UGCs in EHV grids [7–10]. More specifically, the steady-state of the system needs to be studied to allocate compensation for the increased reactive power produced by UGCs [11, 12]. Moreover, transient operation of the system needs to be investigated for insulation-coordination purposes as well as for establishing the harmonic behavior of the transmission network [13–15]. Another aspect is related to the reliability of the power system since the failure rate of UGCs is reduced compared to OHLs but the repair time in case of a failure is much larger [16].

Presently, the Dutch 380 kV transmission network, depicted in Fig. 1.1, is being extended with two new connections to reinforce its transmission capacity, referred to as the Randstad380 project, where UGCs are integrated in the connection.

- The Randstad south-ring [17], extends from substations Weteringen (WTR) to Bleiswijk (BWK), as illustrated in Fig. 1.2, and is in operation since May 2013. It is a double-circuit mixed OHL-UGC connection. The connection begins with an OHL segment from WTR to the cable first transition point (OSP14). Then the line continues as UGC containing three major sections, each with crossbonding. Each phase of the OHL part is connected to two parallel UGCs in order to match the transport capacity of the OHL, which results in twelve parallel UGCs. From the second transition point (OSP32) there is an OHL to substation BWK.
- The Randstad north-ring [18], which is under construction and will be realized in 2019, extends from substations Bleiswijk to Beverwijk (BVW) and its configuration together with the lengths of each OHL and UGC parts is depicted in Fig. 1.3. As for the south-ring case, all OHL parts are double-circuited and two parallel UGCs are connected to each OHL phase.

In the present Dutch transmission grid the UGC double circuit integration is limited to 20 km (Randstad south-ring and north-ring). However, there



Figure 1.1: Dutch transmission network including connections and substations; red is the 380 kV, green is the 220 kV, blue is the 150 kV and black is the 110 kV network.

is an imperative need to increase the amount of UGCs both onshore and offshore (windfarms close to Borssele, Maasvlakte and Beverwijk). Since the Dutch TSO is keen to expand its expertise concerning the integration of UGCs in the transmission network at this voltage level a research program, called Randstad380, was initiated to investigate possible consequences of UGCs in the

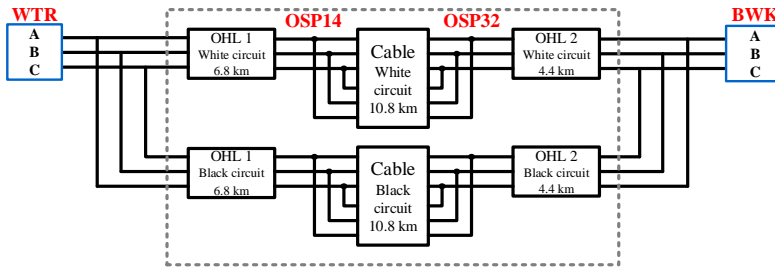


Figure 1.2: *Mixed OHL-UGC part of Randstad south-ring.*

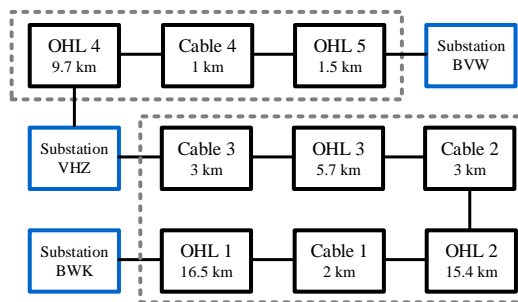


Figure 1.3: *Mixed OHL-UGC part of Randstad north-ring.*

380 kV network. The four main research areas defined in the project include the steady state analysis, the low frequency (slow-front) transient and resonant analysis [19], the fast (fast-front) transient analysis [20] and the reliability analysis [21] of the transmission system. In the present dissertation the focus is on the Randstad south-ring connection where measurements are being performed in order to obtain information concerning the 380 kV power cable transient behavior.

1.2 Project Status

At the start of the research project the four main research areas were divided in work-packages. More specifically, from the resonant and slow-front transient analysis presented in [19] a model of the south-ring cable connection as well as for the general 380 kV Dutch grid was derived. For the cable, initially a simplified model was developed in PSCAD/EMTDC [22] mainly due to limitations in the simulation software. For the modeling of the cable a frequency domain description was implemented in Matlab. It allowed to model the WTR-BWK connection in

large detail but it was not possible to incorporate this model in the complete transmission network model developed in PSCAD/EMTDC.

In order to validate the existing transient simulation models and evaluate the effect of simplifications in the cable model a third party measuring system was installed in Randstad south-ring capable of measuring voltage and current waveforms upon a transient event. The system was installed at substations WTR and BWK and at both OHL-UGC transition points, OSP14 and OSP32. It was specifically designed to contribute to the present knowledge on mixed OHL-UGC connections.

Although the research topics were highly motivated by the development of the Randstad connections, the aim is to extend knowledge to be prepared for future EHV projects involving UGCs. The present thesis is a continuation focusing on model accuracy, measurement validation and on study of specific network configurations also beyond the scope of Randstad380 connections.

1.3 Research Goals

The research goals defined for this PhD project are listed below:

- Implement a methodology to reliably measure voltage waveforms during transient events and more specifically during cable energization. The Randstad south-ring cable connection should be used as test case. Results from both the transition points and the adjacent substations are aimed for.
- Validate the existing simulation models of the Dutch 380 kV network with the aforementioned measurements of transient voltages.
- Identify the causes of deviations between the results of the simulation model and the transient measurements and apply the appropriate corrections to the models.
- Develop an approach to determine the appropriate network extent at the same voltage level (380 kV) for accurate transient response at the connection of interest. Identify the effect of network extension at lower voltage levels (220 kV, 150 kV, 110 kV) on the transient response at the connection of interest.
- Analyze the effect increasing cable integration in the EHV network transient behavior and more specifically in the event of resonance and slow front transient events.

Completion of these goals should allow addressing the following aspects regarding cable integration in general: First, a methodology to reliably measure transient phenomena; Second, the importance of specific parameters of the cable modeling itself as well as the transmission network as a whole in order to accurately study resonant and transient phenomena; Third, the general trend in slow-front overvoltages with the addition of more UGCs in the network.

1.4 Research Approach

To realize the goals the research is divided into three parts; measurements, modeling and transient studies:

- Measurements; Results from energization transients captured by voltage and current sensors already installed at the transition points and substations of the connection (e.g. from Resistive/Capacitive (RC) dividers, voltage and current transformers etc. [23]) were initially studied. However, the measurements especially at the transition points were unreliable and could not be used for model validation. In order to have a robust measurement system capable of accurately measuring at all locations, a new system was designed and constructed as part of the research project based on a Differentiating/Integrating principle [24], where a set of capacitive sensors is applied to measure the various voltages at a certain location.
- Modeling; The simulation model of the Dutch EHV transmission network was developed in PSCAD/EMTDC software. Improvements were made for the generator and HVDC filter models. Moreover, the modeling depth for the same voltage level as well as for lower voltage levels was investigated. The main simplification made in the previous research model was regarding the UGC modeling. Since the configuration of the cable installed in Randstad south-ring is complicated with many small segments of different layout, the well established frequency dependent model of the fully detailed cable connection in PSCAD/EMTDC software was unstable. In order to overcome this problem, a new cable model using the Finite-Difference Time Domain (FDTD) approach [25], was developed and the outcome was compared with the one from the previous simplified cable model.
- Transient studies; The transmission network simulation model, which was validated by the measurements performed in the first part, was used to perform resonance and slow-front transient studies where the effect of additional cable with various configurations was tested. More specifically, series resonance phenomena caused by cable energization were investigated

together with statistical overvoltage studies caused by cable energization, re-strike, fault and fault-clearing [26].

1.5 Dissertation Outline

The thesis is organized in seven chapters, where Chapters 3 and 4 are related to the second part of the research approach, Chapter 5 addresses the first part and Chapter 6 relates to the third part of the approach. More specifically:

Chapter 2 describes the mathematical formulation of transmission lines for use in transient studies. The various transmission line models and their properties (both frequency-independent and frequency dependent) are briefly described

Chapter 3 shows the frequency domain comparison between the detailed and simplified cable model of the Randstad south-ring connection using the Frequency Dependent Phase Model of the PSCAD/EMTDC software. Moreover, a sensitivity analysis to identify the parameters that mostly affect the harmonic impedance of the connection is presented. In addition, the formulation of a new cable model, with improved stability in time domain, is described. This model is then compared with the well-established Frequency Dependent Phase Model in terms of model accuracy, stability and computational time.

Chapter 4 studies the effect of the network extent at the same voltage level and across voltage levels. For the same voltage level two models are derived; one that can accurately represent the maximum transient overvoltage and one that can accurately represent the harmonic behavior at the connection of interest. For lower voltage levels, a sensitivity analysis with the effect of various components on the harmonic impedance is presented. Furthermore, the use of a simplified downstream network is compared with a fully detailed one and an accurate enough equivalent model is proposed.

Chapter 5 focuses on the transient measurements performed at the Randstad south-ring connection. First the Differentiating/Integrating measurement principle is described. Then the set-up used for the measurement in the Dutch system as well as the sensor placement are shown. Finally, the results from cable energization obtained from the aforementioned measurement system which includes both low frequency and high frequency phenomena (responses) are explained and compared with simulations.

Chapter 6 shows the results of transient studies using the validated simulation model. The causes of series resonance are explained and a parametric study is presented to depict the effect of key parameters in the intensity of the resonance, where the Dutch EHV transmission network is used as a case study. Furthermore,

statistical studies for line energization and restrike are shown and the distribution of the maximum overvoltage for various cable configurations is presented. The same applies for fault and fault clearing studies.

Chapter 7 summarizes the main conclusions and gives recommendations for future work.

2

Transmission Line Modeling

Modeling of transmission lines (TL) started at the end of the 19th century and is still ongoing until the present day [27]. Acquiring accurate models for TLs is a prerequisite to be able to simulate the operation of a power system under all possible conditions (steady state, transient etc.). However, the electrical parameters (series impedance and shunt admittance) of both aerial transmission lines and underground power cables present a non-linearity with respect to frequency. This non-linearity mainly originates from the frequency dependency of conductors due to skin effect as well as the earth return path.

Since the behavior of TLs is frequency dependent, it is more straightforward to calculate the parameters and electrical characteristics of the TLs and solve the equations in frequency domain. Even though, such method is adequate for a certain type of studies (steady state, harmonics etc.), transient analysis require the solution of the TL equations to be represented in time domain. The techniques required for this convolution are complex, and are one of the primary attributes that differentiate the various transmission system modeling methods available today.

Generally, there are two types of representation for transmission systems. The first is the frequency independent representation where the series resistance and inductance are calculated for a single frequency. The second and more accurate representation is the frequency dependent modeling where the skin

effect of the conductors and earth return is taken into account and the resistance and inductance values change with frequency. Another division of the models is related to the use of either lumped representation using lumped passive elements or distributed parameter representation which operates on the principle of traveling waves. These aspects will be briefly addressed for a two-conductor TL formulation.

2.1 Transmission Line formulation

The transmission line segment, as shown in Fig. 2.1 represents an infinitesimal section of the line. The voltages and currents along the conductor in frequency domain (telegrapher's equations) are related in the following form [28]:

$$\frac{dV(x, \omega)}{dx} = -Z(\omega) \cdot I(x, \omega) \quad (2.1)$$

$$\frac{dI(x, \omega)}{dx} = -Y(\omega) \cdot V(x, \omega) \quad (2.2)$$

where Z is the per meter series impedance and Y the per meter shunt admittance of the transmission line.

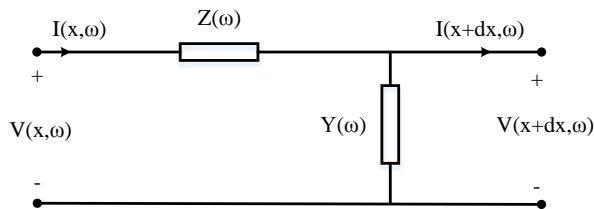


Figure 2.1: *Equivalent circuit of a differential length dx , single conductor line.*

Due to the skin effect of conductors and return path (e.g. soil) the series impedance $Z(\omega)$ is frequency dependent. The shunt admittance which accounts for the capacitance between the transmission line, also present frequency dependency $Y(\omega)$, mainly due to the dielectric losses [29]. Detailed formulation of the series impedance and shunt admittance of both OHLs and UGCs can be found in [30–42].

The series impedance and shunt admittance can be written as:

$$Z(\omega) = R(\omega) + j\omega L(\omega) \quad (2.3)$$

$$Y(\omega) = G + j\omega C \quad (2.4)$$

where R represents the resistance and L the inductance of the conductor which are frequency dependent, while G is the conductance and C the capacitance of the insulation which are considered as frequency independent, which choice will be explained below.

The capacitance is independent of the frequency since for both overhead lines and single core cables the permittivity value of the insulator is assumed to be constant [29, 43] which is an accurate approximation for air and for many synthetic insulation materials, like XLPE. The same does not apply for some cases of pipe type cables where the frequency dependency of the permittivity may be significant. The conductance also presents a frequency dependency due to the loss angle but because of its small value the effect of conductance on electromagnetic transient simulations is insignificant in practical cases. Hence it is reasonable to assume a constant conductance [29, 44, 45].

By solving (2.1) and (2.2) the obtained voltages and currents are (for convenience the dependency with angular frequency in Z , Y , V and I will not be explicitly indicated):

$$V(x) = e^{-\sqrt{ZY}x} V_f + e^{\sqrt{ZY}x} V_b \quad (2.5)$$

$$I(x) = \sqrt{\frac{Y}{Z}} e^{-\sqrt{ZY}x} V_f - \sqrt{\frac{Y}{Z}} e^{\sqrt{ZY}x} V_b \quad (2.6)$$

V_f and V_b are the forward and backward voltage waves which can be obtained by applying boundary conditions at the sending end and receiving end of the TL, see Fig. 2.2.

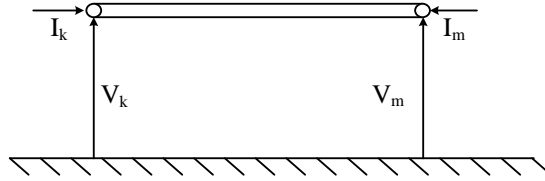


Figure 2.2: Transmission line sending and receiving end voltages and currents.

For the voltage and current at the sending end of the line $x = 0$ is substituted in (2.5) and (2.6) and they become:

$$V_k = V_f + V_b \quad (2.7)$$

$$I_k = \sqrt{\frac{Y}{Z}} V_f - \sqrt{\frac{Y}{Z}} V_b \quad (2.8)$$

Substituting $x = l$ the voltage and current at the receiving end are calculated as:

$$V_m = e^{-\sqrt{ZY}l}V_f + e^{\sqrt{ZY}l}V_b \quad (2.9)$$

$$I_m = -\sqrt{\frac{Y}{Z}}e^{-\sqrt{ZY}l}V_f + \sqrt{\frac{Y}{Z}}e^{\sqrt{ZY}l}V_b \quad (2.10)$$

Eliminating variables V_f and V_b from (2.7)-(2.10) the equations of the sending and receiving end currents become:

$$I_k = Y_c \cdot V_k - H_c \cdot (Y_c \cdot V_m + I_m) \quad (2.11)$$

$$I_m = Y_c \cdot V_m - H_c \cdot (Y_c \cdot V_k + I_k) \quad (2.12)$$

where

$$Y_c(\omega) = \sqrt{\frac{Y(\omega)}{Z(\omega)}} \quad (2.13)$$

is the characteristic admittance and

$$H_c(\omega) = e^{-\sqrt{Y(\omega)Z(\omega)}l} \quad (2.14)$$

is the propagation function of the TL.

The aforementioned analysis used to associate the sending and receiving end voltages and currents of the TL was performed in frequency domain. However, generally the time domain response is of interest. When constant lumped parameters are used for the representation of the TL, the solution of the differential equations is straightforward. For distributed parameter models the representation in time domain is done using the Method of Characteristics [46].

To demonstrate the Method of Characteristics, a loss-less line, $R = G = 0$, with constant inductance and capacitance calculated at a specific frequency (either at steady state or at the dominant frequency produced during a transient event) is considered and the partial differential equations become:

$$\frac{\partial v(x, t)}{\partial x} = -L \cdot \frac{\partial i(x, t)}{\partial t} \quad (2.15)$$

$$\frac{\partial i(x, t)}{\partial x} = -C \cdot \frac{\partial v(x, t)}{\partial t} \quad (2.16)$$

Their general solution is given by [38]:

$$v(x, t) + Z_0 \cdot i(x, t) = 2Z_0 \cdot f_1(x - \nu t) \quad (2.17)$$

$$v(x, t) - Z_0 \cdot i(x, t) = -2Z_0 \cdot f_2(x + \nu t) \quad (2.18)$$

where $Z_0 = \sqrt{\frac{L}{C}}$ is the characteristic impedance of the loss-less line and ν is the phase velocity.

As shown in [46] (2.17) and (2.18) can be rewritten in two-port format as:

$$i_k(t) = \frac{1}{Z_0} \cdot v_k(t) + i_{hist,k}(t - \tau) \quad (2.19)$$

$$i_m(t) = \frac{1}{Z_0} \cdot v_m(t) + i_{hist,m}(t - \tau) \quad (2.20)$$

where τ is the travel time over the TL.

The Norton equivalent circuit of (2.19) and (2.20) is illustrated in Fig. 2.3 and is the one used for EMT-type programs to represent overhead lines and underground cables.

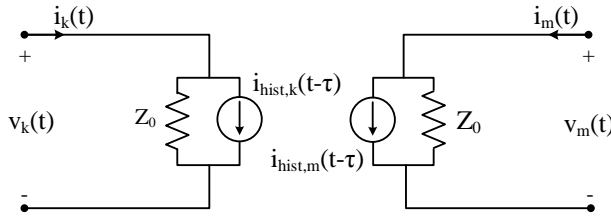


Figure 2.3: Norton equivalent circuit of distributed parameter transmission line.

2.2 Frequency-Independent models

The main characteristic of the frequency independent models is that the series impedance and shunt admittance of the TL are calculated at a specific frequency and it is assumed that their calculated values remain constant over the complete frequency range for transforming the equations in time domain.

2.2.1 Pi model

The nominal Pi-section model is one of the simplest models to be used for representing a TL. It is recommended to be used only for short TLs (e.g. when the length of the line is more than four times smaller than the wavelength at steady state), where the propagation delays are negligible. The circuit representation of the Pi model is shown in Fig. 2.4 where the total shunt admittance is halved

and placed at the sending and receiving end of the TL and the series impedance is placed between the two ends and both of them are represented using lumped passive components.

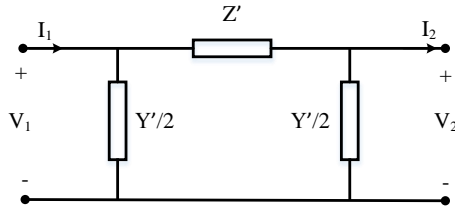


Figure 2.4: *Single-Phase pi-section equivalent circuit.*

The accuracy of the Pi-section equivalent circuits will decrease as the line becomes longer. This is mainly due to the fact that a pi-section does not account for the uniform distribution of line parameters. To incorporate the distributed nature of the parameters the so called "exact" pi-model is used where the expressions of Z and Y become [36]:

$$Z' = Zl \left(\frac{\sinh [(ZY)^{1/2}l]}{(ZY)^{1/2}l} \right) \quad (2.21)$$

$$\frac{Y'}{2} = \frac{Yl}{2} \left(\frac{\tanh \left[\frac{(ZY)^{1/2}l}{2} \right]}{\frac{(ZY)^{1/2}l}{2}} \right) \quad (2.22)$$

where l is the length of the transmission line and Z and Y are the per unit length values of the series impedance and shunt admittance respectively.

This model is mostly used for frequency domain analysis or frequency scan validation of TLs since it is very accurate for a single frequency and when numerical calculations of the impedances are used.

2.2.2 Bergeron model

The Bergeron model is a distributed parameter model based of traveling wave theory and does not use lumped parameters. For this model the characteristic impedance of an ideal loss-less line, Z_0 , is calculated at a specified frequency. It approximates losses by adding series lumped resistance elements into the loss-less, distributed parameter branch. The loss-less line is broken into two segments, each with a quarter of the total TL resistance at each end as shown in Fig. 2.5 [46, 47].

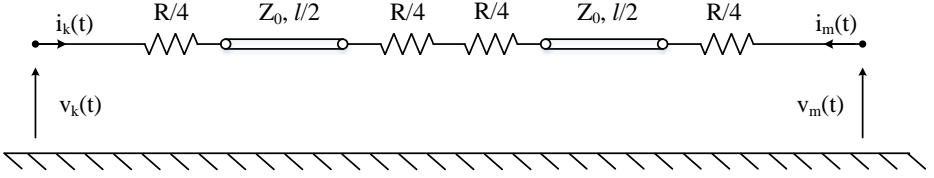


Figure 2.5: *Bergeron model equivalent circuit.*

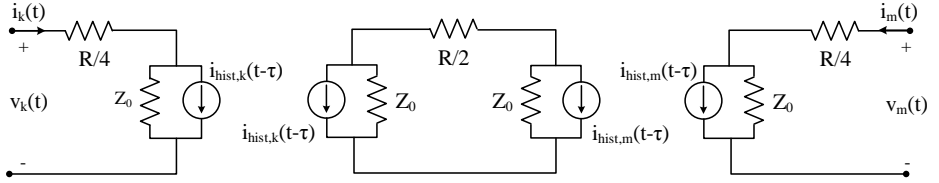


Figure 2.6: *Norton equivalent circuit of Bergeron model.*

The Norton equivalent circuit representation of the Bergeron model is shown in Fig. 2.6. Cascading the two half-line sections and eliminating the mid-point variables, since only the terminals are of interest, the Norton current injections in the TL terminals are given as [38, 48]:

$$i_{hist,k}(t-\tau) = \frac{1+H}{2} \cdot \left\{ -\frac{1}{Z} \cdot v_m(t-\tau) - i_m(t-\tau) \right\} + \quad (2.23)$$

$$+ \frac{1-H}{2} \cdot \left\{ -\frac{1}{Z} \cdot v_k(t-\tau) - i_k(t-\tau) \right\}$$

$$i_{hist,m}(t-\tau) = \frac{1+H}{2} \cdot \left\{ -\frac{1}{Z} \cdot v_k(t-\tau) - i_k(t-\tau) \right\} + \quad (2.24)$$

$$+ \frac{1-H}{2} \cdot \left\{ -\frac{1}{Z} \cdot v_m(t-\tau) - i_m(t-\tau) \right\}$$

where

$$Z = Z_0 + \frac{R}{4} \quad (2.25)$$

$$H = \frac{Z_0 - \frac{R}{4}}{Z_0 + \frac{R}{4}} \quad (2.26)$$

Although the Bergeron model can indeed be used for transients simulation in the time domain (which includes all frequencies), only results at the specified

steady-state frequency are meaningful. As such, the Bergeron model is sufficiently accurate for general fundamental frequency impedance studies, such as relay testing or matching load-flow results.

2.3 Frequency-Dependent models

The Frequency-Dependent (FD) models are using distributed parameters for all electrical characteristics (resistance, inductance and capacitance) which are also calculated in multiple frequencies instead of having a constant value in the complete frequency range [49]. The two FD models widely used in commercial EMT software are the Frequency Dependent Mode model (FDMM), which is accurate when modeling balanced systems and the Frequency Dependent Phase model (FDPM), which accurately represents unbalanced and balanced systems. Because of its required completeness, the FDPM is the one used for the simulation of OHLs and UGCs in this dissertation.

2.3.1 Frequency-Dependent Phase Model

In recent years the increasing integration of long UGCs with unbalanced configurations and varying modal time delays as well as the addition of hybrid AC and DC lines stressed the need for a TL model that could accurately represent them [50–59]. In 1999 a Universal Line Model was introduced [60] providing a general and accurate frequency dependent model for all underground cables and overhead line geometries.

As explained in Section 2.1 the sending and receiving end currents are used to form an equivalent circuit for the representation of a distributed parameter transmission line (see Fig. 2.3). In order to take into account the frequency dependency of the TL electrical parameters the currents are first derived in frequency domain and expressed with the use of the characteristic impedance Y_c , and the propagation function H_c . However, in electromagnetic transient calculations a time domain representation of (2.11) and (2.12) is needed. When transforming the two equations in time domain the multiplications become convolutions and the currents are expressed as follows [29]:

$$i_k(t) = y_c(t) * v_k(t) - h_c(t) * (y_c(t) * v_m(t) + i_m(t)) \quad (2.27)$$

$$i_m(t) = y_c(t) * v_m(t) - h_c(t) * (y_c(t) * v_k(t) + i_k(t)) \quad (2.28)$$

Straightforward numerical integration of the convolutions is not computationally efficient in contrast to recursive convolution. The real-time convolution requires

saving the associated voltage values of all time steps previous to the one currently calculated. On the other hand, with recursive techniques the value of the convolution can be expressed as a sum of four multiplications including voltage values of the current and previous time step and the previous value of the convolution. The use of recursive convolution becomes feasible if the characteristic admittance and propagation function are expressed in the time domain as a summation of exponentials. A convenient approach to this end is to approximate these two functions in the frequency domain with a pole residue form using a curve fitting technique.

More specifically, the characteristic admittance is a relatively smooth function which can be readily fitted in the frequency domain taking the following form:

$$Y_c(s) = \sum_{i=1}^n \frac{c_i}{s - a_i} + d \quad (2.29)$$

The unknown coefficients (c_i , a_i and d) can be efficiently evaluated using a robust curve fitting technique based on linear least squares called Vector Fitting [61–64]. The time domain form becomes:

$$y_c(t) = \sum_{i=1}^n c_i e^{a_i t} + d \cdot \delta(t) \quad (2.30)$$

and the two convolutions $y_c(t) * v_k(t)$ and $y_c(t) * v_m(t)$ in (2.27) and (2.28) can be computed.

It is not possible to use the same procedure to fit the propagation function, H_c , since the exponential term $e^{-\sqrt{Y(\omega)Z(\omega)l}}$ prohibits direct curve fitting using low order rational functions. The fitting of H_c is more difficult because its elements are composed of modal components which in general have different time delays [65]. This time delay which characterizes the propagation function in the time domain translates into a phase shift in the frequency domain. Using modal decomposition each mode is characterized by a time delay, τ_k which can be separated with a procedure called "unwinding" and the propagation function can be expressed as:

$$H_c(\omega) = \sum_{k=1}^N H_{uw}(\omega) e^{-j\omega\tau_k} \quad (2.31)$$

where N is the number of modes contained in the system.

The remaining function H_{uw} can be more accurately described as the summation of a number of rational functions and is expressed as:

$$H_{uw} = \sum_{i=1}^{M_k} \frac{c_i}{s - a_i} \quad (2.32)$$

where M_k is the number of poles for mode k .

So the final form of the propagation function is:

$$H_c(\omega) = \sum_{k=1}^N \left[\sum_{i=1}^{M_k} \frac{c_i}{s - a_i} \right] e^{-j\omega\tau_k} \quad (2.33)$$

and using the form in (2.33) the recursive technique can also be applied in the remaining convolutions in (2.27) and (2.28).

The formulas for the sending and receiving end currents (2.27) and (2.28) can be expressed as a summation of present and past values as:

$$i_k(t) = y_{eq}v_k(t) + i_{hist,k}(t) \quad (2.34)$$

$$i_m(t) = y_{eq}v_m(t) + i_{hist,m}(t) \quad (2.35)$$

where y_{eq} is the equivalent conductance obtained after the evaluation of the convolutions in (2.27) and (2.28). Thus, the FDPM of a TL can be represented in time domain using the Method of Characteristics and the equivalent circuit of Fig. 2.3.

Model passivity

The stability of a transmission line model can be ensured by verifying a property called passivity. The physical meaning of passivity, with regards to electrical circuits, is that passive networks always absorb real power and thus the total energy delivered to the network is positive [66, 67]. Transmission lines are passive as a matter of physical reality. However, one of the major problems of the TL models based on the method of characteristics is that the curve-fitted resultant model of the (passive) transmission line cannot be guaranteed to be always passive. Depending on its terminating connections, a non-passive transmission line model may lead to incorrect, unstable simulations [29]. In transient studies the frequency range of interest is between 50 Hz and several kHz, thus an accurate fitting of the characteristic admittance and the propagation function from 1 Hz to 1 MHz would seem adequate. However, poor fitting for frequencies lower than 1 Hz can lead to large passivity violations.

The passivity can be guaranteed by verifying that the eigenvalues of the transfer admittance's Hermitian matrix are positive for the frequency range of interest. Algorithms to enforce passivity on the time domain transmission line FD models have been developed and presented in [29, 68], however when very large passivity violations are encountered the passivity enforcement cannot solve the stability problems as they are based on linearization methods.

DC correction

When dealing with HVDC lines and cables, it is very important to accurately reproduce the response at DC, as this is the nominal operational point of the line. It can be shown that fitting the TL electrical characteristics at extremely low frequencies requires high order fitting and sometimes leads to inaccurate results. There exist two functional forms to implement DC correction. In the first approach, the admittance and propagation function are reformulated so that the DC response is factored out as an additive constant, which can then be directly selected. In the other approach, the transfer function is first fitted over the entire frequency range, which typically results in some fitting error at DC. A low frequency first order pole is then added to the resultant fitted function in order to realize the exact response at DC, without significantly affecting the remainder of the frequency response [38, 69].

2.3.2 Frequency-Dependent Mode Model

The Frequency-Dependent (Mode) model is based on the traveling wave approach with frequency dependent modes and a constant transformation matrix [70]. The modal transformation matrix is derived at one frequency and it is assumed that its frequency dependency is not significant. That is the case only for geometrically balanced transmission systems, such as ideally transposed circuits and does not hold for untransposed OHLs and cables. However, the use of constant transformation matrix does not imply that this model presents measurable errors when simulating transients since the accuracy is highly dependent on the frequencies contained in the transient [28]. The Frequency Dependent Mode model utilizes methods quite different from the Frequency Dependent Phase model since it relies on a rational function approximation of the attenuation function $\Gamma(s)$ and the characteristic impedance $Z_c(s)$ instead of the propagation function and characteristic admittance.

3

Underground Power Cable Modeling

Modeling of transmission lines goes back to the early days of communication along electric wires. In particular, the telegraph has given its name to a set of differential equations describing the propagation of voltage and current signals along these wires. The Telegrapher's equations also hold for transmission in electric power systems and the theory is employed amongst others to analyze transient signal properties. The prediction of transient phenomena and their risks for power system operation allows for taking preventive countermeasures.

The recent shift in transmission systems, from predominantly employing OHLs, towards the integration of UGCs, stresses the need for accurate cable models. The electrical properties of UGCs differ significantly from those of OHLs and mathematical modeling of UGCs demonstrates new challenges compared to OHLs mainly due to the stronger frequency dependence of their transformation matrices [8] [71].

Research in cable modeling has resulted in a range of solution strategies incorporating accurate frequency dependent models of the components. However, numerical implementation of these models encounters problems (mainly instability) in complex cases. Complexity in the context of this thesis relates to many parallel, electromagnetically interacting, cables consisting of short segment lengths. This chapter points out limitations and merits of alternative methodologies applied to both a benchmark cable system as well as the Randstad

south-ring connection.

3.1 Frequency Dependent Phase Model

For modeling the Randstad south-ring cable the FDPM was used since it strives to represent the full frequency dependency of a transmission system and the resistance, inductance and capacitance of the line are represented using distributed parameters. Moreover, it is regarded as one of the most accurate and stable models for transmission line or cable representation and is the basis of the modeling method employed in PSCAD. For the two OHL parts of the south-ring connection the same model was used. Despite all merits, limitations were encountered in modeling the cable part which could be omitted by introducing simplifications. These limitations and their effects on model accuracy are discussed together with a cable parameter sensitivity study.

3.1.1 Southring cable model

A thorough description of the layout and electrical characteristics of the south-ring cable and OHLs is provided in Appendix A. The south-ring cable connection consists of 12 mutually coupled single-phase cables which are divided into 28 different cable segments with varying length and trench type. The 28 different cable segments are grouped into 12 minor sections. Three successive minor sections form one major section of approximately 2.7 km length (see Fig. 3.1). Within one major section, the minor sections are connected via cross-bonding joints, while the major sections are connected via a straight through joint [72, 73]. The models used for the joints are shown in Fig. 3.2.

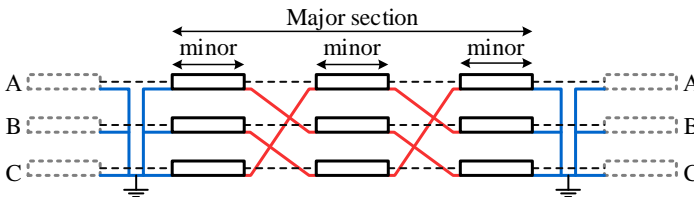


Figure 3.1: *Cable minor and major section configuration.*

This is the actual cable configuration and the model is referred to as "detailed". In the "detailed" model all 28 segments with their different lengths and trench types are incorporated in the model. However, the time to construct and to simulate such a complicated model is excessive. In order to obtain accurate results the

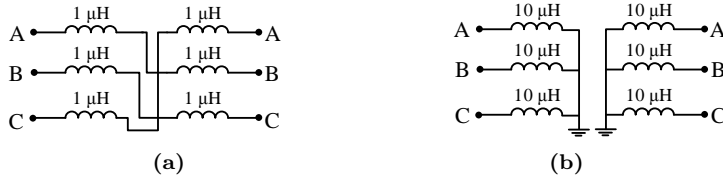


Figure 3.2: *South-ring cable sheath (earth path) bonding where (a) is the cross-bonding joint and (b) the straight through joint model.*

simulation time step should be at least ten times less than the time a traveling wave needs to travel the shortest cable segment [38, 74]. Since the smallest segment is 100 m the simulation time step should be $0.05 \mu s$. Moreover, such small cable length in a complicated cable configuration (12 mutually coupled cables) can cause stability problems due to large passivity violations. The instability arises from the poor curve fitting of the propagation function which is an essential technique in order to solve the time domain convolutions in a recursive manner. Such instability problems can be solved by changing the curve-fitting parameters employed in the FDPM. However, this trial and error procedure is not practical and might not work for large cable systems (as in the case of the south-ring cable connection). Thus, a simplified model of the south-ring cable connection is introduced where:

- All minor sections consist of only one segment (12 segments in total) with the same length (0.9 km).
- For each segment the same trench type was chosen (open trench with typical cable depth of 1.4 m, see Appendix A.1).

However, simplifications introduce inaccuracies that are further investigated.

3.1.2 Detailed versus simplified model in frequency domain

In order to examine whether the aforementioned simplifications in the cable model produce inaccuracies when studying slow front transients a comparison of the detailed and simplified cable model is made in frequency domain [9, 19, 75–77]. The comparison is performed to study the effect of simplification for three configurations: the stand-alone cable only, the mixed OHL-UGC south-ring configuration and the full Dutch 380 kV grid (for the model used to simulate the Dutch 380 kV transmission network, see Chapter 4). For the latter two cases

the harmonic impedances are calculated from WTR side with both circuits in service (referred to as "black" and "white" in Fig. 1.2)

The calculation of the harmonic impedance is performed using the frequency scan component of PSCAD/EMTDC with a fixed step of 2 Hz and the frequencies of interest are up to 10 kHz. The lower frequency resonances are the most severe since they are weakly damped and sustained for longer time [7, 78, 79]. The comparison results between the detailed and simplified model in the frequency domain is shown in Fig. 3.3.

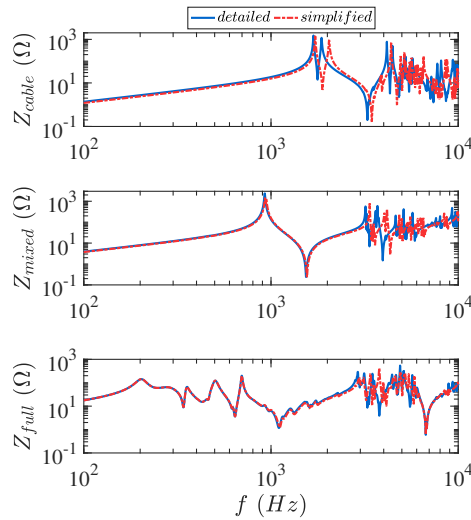


Figure 3.3: Harmonic impedance comparison between detailed and simplified cable model for the stand-alone southring cable configuration (top), the stand-alone mixed OHL-UGC configuration (middle) and the full Dutch 380 kV grid (bottom).

As observed in Fig. 3.3 (top) the implemented simplifications in the cable model affect significantly the harmonic impedance of the stand-alone south-ring cable configuration even from the first resonance points, at around 2 kHz, where a shift to higher frequencies is observed in the simplified case. For frequencies higher than 5 kHz the harmonic impedance of the detailed model is completely different from the simplified model.

For the mixed OHL-UGC configuration (Fig. 3.3 middle) the first two resonant peaks are similar for the two models with only a slight shift to higher frequencies for the simplified model. The main resonances are caused by the inductance of the OHL, which is much larger and dominates the one of the UGC, and the cable capacitance. Thus, the effect of simplifications in the cable model is less

dominant.

Finally, for the complete Dutch 380 kV grid (Fig. 3.3 bottom) the main resonances up to 3 kHz are accurately represented and differences are present for higher frequencies. It is obvious that the low frequency resonances, mainly caused by other components interacting with the south-ring connection, are not affected by the cable model simplifications.

3.1.3 Sensitivity analysis

When modeling a cable system for slow front transient studies there are many aspects that can affect the accuracy of the simulation results. These aspects are related to uncertainties in the cable design parameters (provided by the manufacturer) or in the cable laying configuration. They can also be related to simplifications that need to be made due to software limitations or for reduction of the simulation time. The effect of various parameters on cable design and layout is studied, using frequency scans, in order to identify which of them are important and need to be accurately modeled.

For the sensitivity study the simplified cable model is used since the interest is mostly in the behavior of the resonance frequencies and not on their actual values. In order to reduce the computational time an additional simplification is made to the model, namely the two cable circuits are decoupled from each other. As demonstrated in Fig. 3.4 the harmonic impedances of the two models are similar, because the distance between the two circuits in the trench type used for the simplified cable model (O1, see Appendix A.1) is relatively large.

Cable designing parameters

The actual cable design is implemented by defining equivalent layers as shown in Appendix A. The thicknesses of each of the four equivalent cable layers (see Fig. A.1b) are calculated either from datasheets or from cable sample measurements. However, the nominal thickness of the various layers as stated by manufacturers can differ from the actual (design) thickness of the layers. Therefore, the information on geometrical data from the manufacturer can be inaccurate from the viewpoint of cable parameter calculations [80, 81]. Variations of $\pm 20\%$ (which is more than the standard margins for thickness deviation) in all four layer thicknesses are investigated and the results are shown in Fig. 3.5.

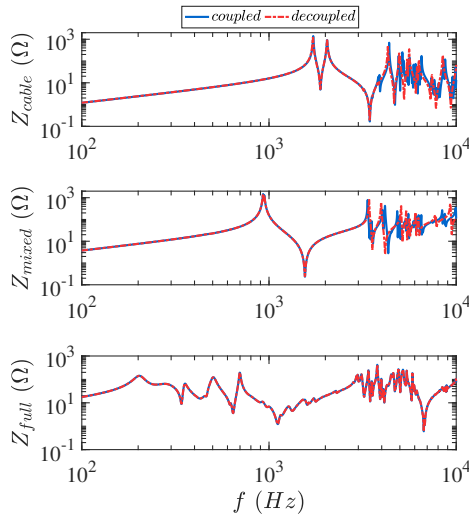


Figure 3.4: Harmonic impedance comparison between coupled and decoupled simplified cable model for the stand-alone southring cable configuration (top), the stand-alone mixed OHL-UGC configuration (middle) and the full Dutch 380 kV grid (bottom).

Conductor radius

The harmonic impedance comparison for deviations in the conductor radius is presented in Fig. 3.5a. As the conductor radius increases the resonance frequencies decrease since the cable capacitance increases. However, this variation also decreases the inductance of the cable and the overall frequency shift is small. This shift is more dominant for the mixed OHL-UGC configuration because the inductance of OHL parts dominates the total inductance and a decrease in the UGC inductance has less impact on the total impedance. The effect on the full Dutch grid is minor up to 1 kHz. There is a slight shift on the main series resonance which is the one caused by the south-ring connection and for higher frequencies the effect is visible.

Insulation thickness

The harmonic impedance comparison for deviations in the insulation thickness is presented in Fig. 3.5b. As the insulation thickness decreases the resonance peaks shift to lower frequencies since the cable capacitance increases. This behavior is evident for both the stand-alone cable and the mixed OHL-UGC configuration. Also in this case the effect on the full Dutch grid is minor up to 1 kHz, but for higher frequencies there is a significant effect.

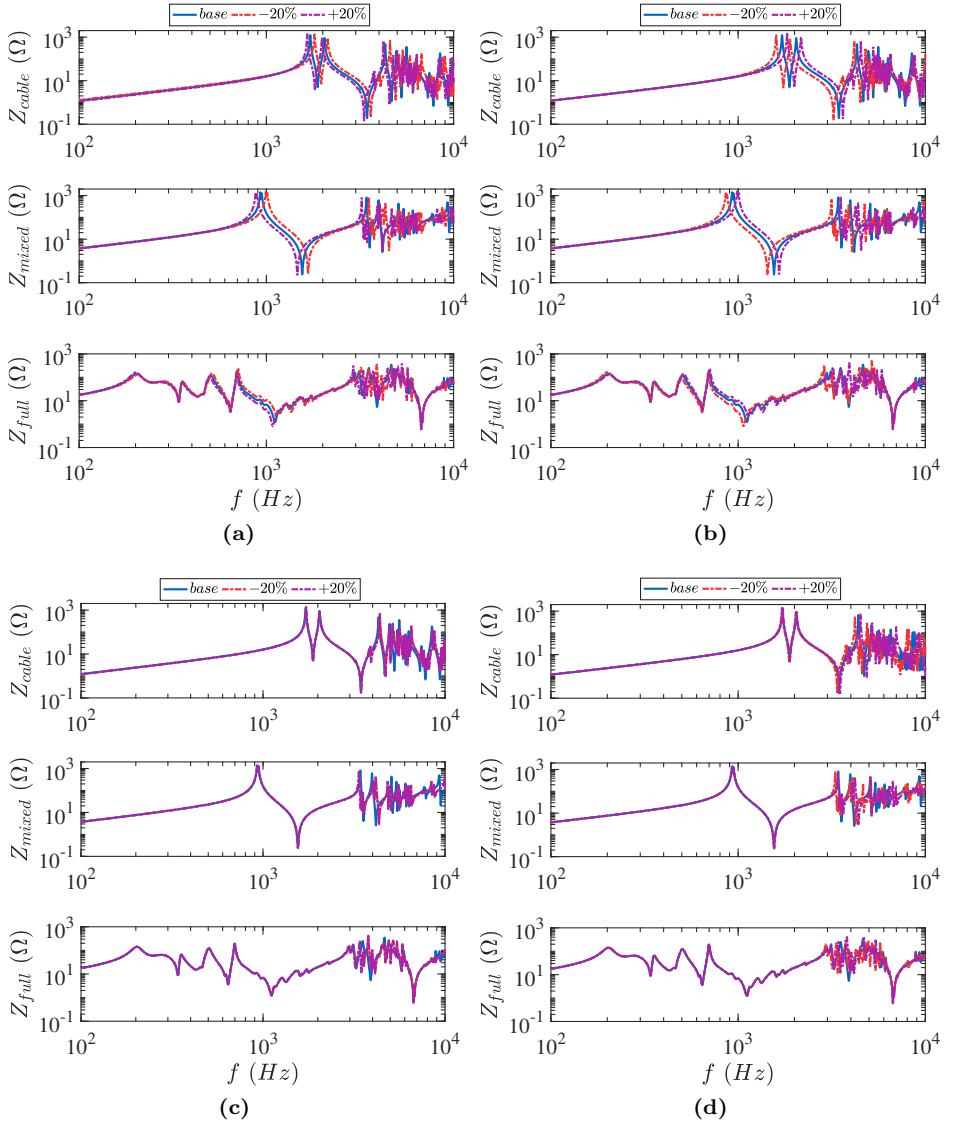


Figure 3.5: Harmonic impedance for deviations of $\pm 20\%$ in (a) conductor radius, (b) insulation thickness (c) metallic screen thickness and (d) outer sheath thickness.

Metallic screen and outer sheath thickness

Changes in the thickness of the metallic screen and outer sheath (see Fig. 3.5c and 3.5d) have no effect for frequencies lower than 3 kHz in all three configurations. The effect in higher frequencies is more dominant for deviations in the outer sheath where a thickness decrease results in shifting the resonances to lower frequencies.

Number of turns in the metallic screen

As can be seen in Fig. 3.6 an increase in the number of turns of the helically wounded earth screen results in a decrease in the resonance frequencies for the stand-alone cable configuration. The equivalent permeability of the insulation increases and subsequently the total cable inductance increases. This effect is minor in the mixed OHL-UGC configuration and the full Dutch grid since the total inductance is dominated by the OHLs.

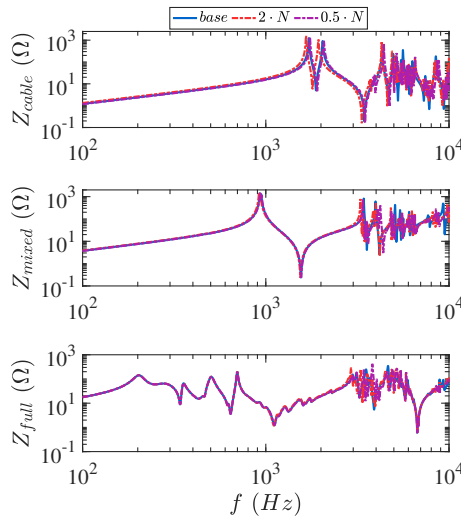


Figure 3.6: Harmonic impedance for different turns per meter: 1.4 turns/m (base).

Cable laying and bonding

Cable installation and layout refer to where and how individual cables are positioned with respect to one another, for example open trench or horizontal directional drilling configurations (Appendix A.1). In the planning stage of a cable connection the exact layout is unknown. Therefore, it is important to study

how different choices of the cable layout can affect the harmonic impedance. The bonding configuration as well as the number of major sections used can greatly influence the frequency response of a cable connection.

Trench type

The harmonic impedance comparison for four cable trenches (base O1, O3, H1 and H2, see Fig. A.2) is illustrated in Fig. 3.7a. It is evident that variations in the cable layout greatly affect both the frequency and the magnitude of the harmonic impedance resonance peaks. More specifically, there is a shift of the resonance peaks to higher frequencies when the distance between individual cables decreases (H2) while the opposite occurs when the distance increases.

Type of bonding

Three types of bonding configurations (base with cross-bonding and 4 major sections, ideal cross-bonding, both-ends bonding) are compared and the results are presented in Fig. 3.7b. The ideal cross-bonding refers to the theoretical case with infinite amount of major sections which results in a perfect transposition of the cable screens. The shunt admittance matrix is equal for cross-bonding and both-ends bonding as the distance between the conductor and the screen is unchanged, but the series impedance matrix presents some differences [74]. The harmonic impedance is affected by the cable bonding type and the resonance points have higher magnitudes and lower frequencies for the cross-bonded cable than for the both-ends bonded cable.

Bonding inductances

Different inductances at the cross-bonding and straight-through joints result in insignificant changes in the harmonic impedance and can even be neglected when the frequencies of interest are limited to several kilohertz, see Fig. 3.7c.

Number of major sections

The harmonic impedance comparison for different numbers of major sections is demonstrated in Fig. 3.7d. The frequency, the magnitude and the number of the resonant peaks are affected for different numbers of major sections. This is more evident when only one major section is used, where deviations are observed even for the first parallel resonance. The cable with three major sections exhibits similar frequency and magnitude characteristics for the first parallel and series resonance and it starts to deviate afterwards. The effect of this change is less significant when studying the mixed OHL-UGC configuration or the full Dutch 380 kV grid but the effect is visible even for 1 kHz in the case of a single major section.

The sensitivity study shows that, from the cable design parameters the conductor radius and insulation thickness significantly affect the harmonic impedance since

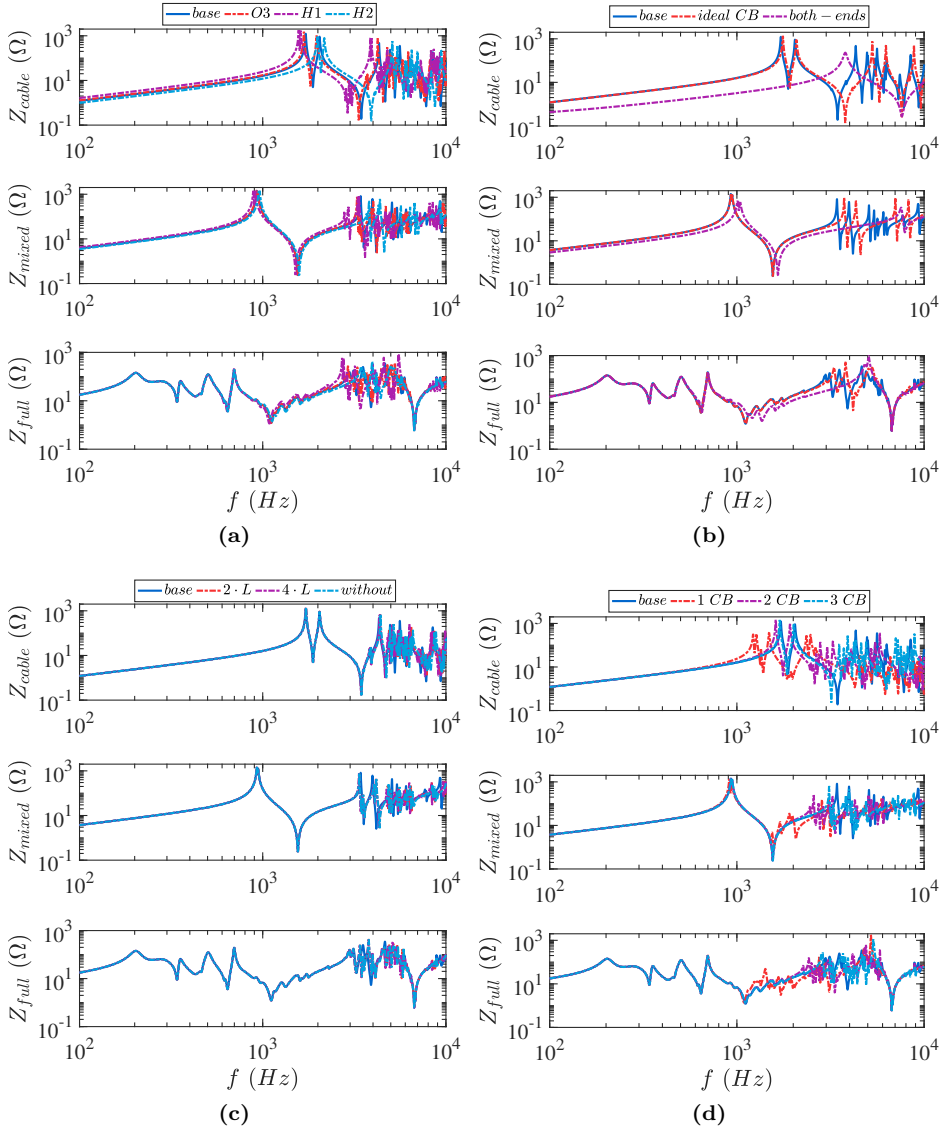


Figure 3.7: Harmonic impedance for differences in (a) cable trench type, (b) bonding type, (c) cross-bonding inductance value and (d) number of simulated major sections.

they modify the inductance and capacitance of the cable. Design parameters

related to cable laying and bonding tend to have more impact than the cable designing parameters. More specifically, it can be concluded that the bonding and trench type and the number of simulated major sections are necessary to be correctly modeled since they can cause significant impedance deviations even in the lower frequency range.

3.1.4 Limitation of FDPM in time domain

Besides the comparison of the two cable models (detailed and simplified) in frequency domain, it is important to investigate the effect of the impedance variation in time domain, especially for slow and fast front transients. However, acquisition of the time domain response of the detailed south-ring cable model was not possible since the solution of the FDPM in PSCAD/EMTDC became unstable. Due to these limitations, a frequency domain description of the south-ring cable model was developed in Matlab from previous research [72], where the transformation to time domain was performed using the Inverse Fourier Transform. However, it was not possible to incorporate this model in the complete transmission network model developed in PSCAD/EMTDC.

The instability in the Frequency Dependent Phase Model is caused by passivity violations due to poor fitting of the propagation function in low frequencies, meaning that the curved-fitted resultant model of the passive cable line cannot be guaranteed to be always passive [29]. Algorithms to enforce passivity on the time-domain transmission line or cable model have been developed and presented in [29, 68, 82–84], however when large passivity violations are encountered the passivity enforcement cannot solve the stability problems as they are based on linearization methods.

3.2 Finite Difference Time Domain Model

In order to improve stability a numerical method for approximately determining the time-domain solution of the transmission line equations, known as Finite Difference Time Domain (FDTD) method, is implemented [85].

3.2.1 Model formulation

For the formulation of the FDTD model the fitted quantities in frequency domain are the series impedance, $Z(\omega)$, and the shunt admittance, $Y(\omega)$, which are much smoother functions in respect to frequency compared with the propagation

function, H_c . In the FDTD method the partial differential equations are directly solved in time domain [25, 27, 86]. The Telegrapher's equations can be formulated in terms of convolutions:

$$\frac{\partial i(x, t)}{\partial x} + y(t) * v(x, t) = 0 \quad (3.1)$$

$$\frac{\partial v(x, t)}{\partial x} + z(t) * i(x, t) = 0 \quad (3.2)$$

In this model the dielectric losses are considered independent of the frequency and the shunt admittance, $Y(s)$, in frequency domain is given by:

$$Y(s) = G + sC \quad (3.3)$$

where $s = j\omega$.

Substituting (3.3) in (3.1):

$$\frac{\partial i(x, t)}{\partial x} + Gv(x, t) + C \frac{\partial v(x, t)}{\partial t} = 0 \quad (3.4)$$

The series impedance, $Z(s)$, is highly frequency dependent due to both the earth return path and the conductor losses. Straightforward numerical integration of the convolution is not computationally efficient so a recursive convolution technique will be employed. This can be achieved if the series impedance is expressed in time domain as a summation of exponentials, meaning that in frequency domain $Z(s)$ needs to be approximated using a pole residue form.

$$\begin{aligned} Z(s) &= \sum_{i=1}^M \frac{c_i}{s - \alpha_i} + sL + R \\ &= \Theta(s) + sL + R \end{aligned} \quad (3.5)$$

The convolution transforms in frequency domain into a multiplication and in order to enhance the accuracy of evaluating the convolution integral the following modification is introduced [86]:

$$\Theta(s) \cdot I(x, s) = \frac{\Theta(s)}{s} \cdot sI(x, s) \quad (3.6)$$

Substituting (3.5) and (3.6) in (3.2):

$$\frac{\partial v(x, t)}{\partial x} + Ri(x, t) + L \frac{\partial i(x, t)}{\partial t} + \int_0^t \Theta(\tau) d\tau * \frac{\partial i(x, t)}{\partial t} = 0 \quad (3.7)$$

where $\Theta(t) = \sum_{i=1}^M c_i \cdot e^{\alpha_i t}$. The integral in (3.7) becomes:

$$\int_0^t \Theta(\tau) d\tau = \sum_{i=1}^M \frac{c_i}{\alpha_i} \cdot e^{\alpha_i t} - \sum_{i=1}^M \frac{c_i}{\alpha_i}$$

The following quantities are defined:

$$\Phi(t) = \sum_{i=1}^M \frac{c_i}{\alpha_i} \cdot e^{\alpha_i t} \quad (3.8)$$

$$\Gamma = \sum_{i=1}^M \frac{c_i}{\alpha_i} \quad (3.9)$$

Substituting (3.8) and (3.9) in (3.7) results in:

$$\frac{\partial v(x, t)}{\partial x} + (R - \Gamma) \cdot i(x, t) + L \frac{\partial i(x, t)}{\partial t} + \Phi(t) * \frac{\partial i(x, t)}{\partial t} = 0 \quad (3.10)$$

3.2.2 Model discretization

In order to solve (3.4) and (3.10), the transmission line is discretized into spatial segments of length Δx and the time is also discretized considering a time step of Δt , as shown in Fig. 3.8. Furthermore, in order to ensure the stability of the model an explicit central difference scheme is used where the voltages and currents are interleaved spatially and temporally resulting in a "leapfrog" scheme [25, 87]. Thus, voltage and adjacent current points are separated by $\Delta x/2$ in space and $\Delta t/2$ in time (see Fig. 3.9).

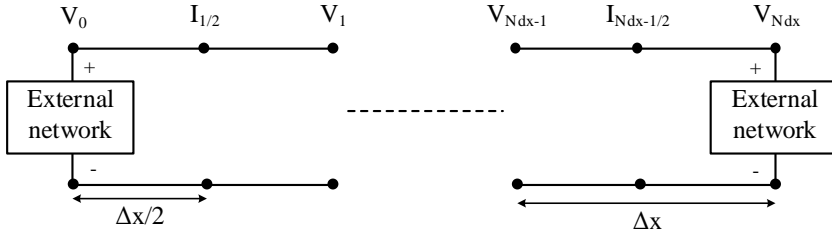


Figure 3.8: Discretization of the line into N_{dx} segments of length Δx for the FDTD analysis with spatial interleaf between voltages and currents.

The model is discretized into $k\Delta x$ points in space and $n\Delta t$ points in time.

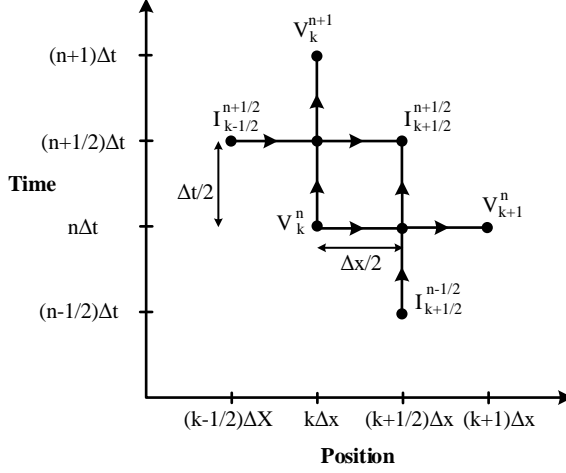


Figure 3.9: Interlacing the current and voltage solutions in space and time for the FDTD analysis.

Then, the partial differentials in (3.4) and (3.10) can be approximated using central differences and the equations take the form:

$$\frac{I_{k+1/2}^{n+1/2} - I_{k-1/2}^{n+1/2}}{\Delta x} + C \frac{V_k^{n+1} - V_k^n}{\Delta t} + G \frac{V_k^{n+1} + V_k^n}{2} = 0 \quad (3.11)$$

$$\begin{aligned} \frac{V_{k+1}^n - V_k^n}{\Delta x} + L \frac{I_{k+1/2}^{n+1/2} - I_{k+1/2}^{n-1/2}}{\Delta t} + \\ + (R - \Gamma) \frac{I_{k+1/2}^{n+1/2} + I_{k+1/2}^{n-1/2}}{2} + \Phi(t) * \frac{\partial i(x, t)}{\partial t} = 0 \end{aligned} \quad (3.12)$$

In order to calculate the value of the current for the next time-step the discretized form of the convolution is calculated as:

$$\begin{aligned} \Phi(t) * \frac{\partial i(x, t)}{\partial t} &= \int_0^{n\Delta t} \Phi(\tau) \overbrace{\frac{\partial}{\partial((n+1/2)\Delta t - \tau)} I_{k+1/2}((n+1/2)\Delta t - \tau)}^{DI_{k+1/2}((n+1/2)\Delta t - \tau)} d\tau \\ &= \int_0^{n\Delta t} \sum_{i=1}^M \frac{c_i}{\alpha_i} \cdot e^{\alpha_i \tau} \cdot DI_{k+1/2}((n+1/2)\Delta t - \tau) d\tau \end{aligned}$$

$$\begin{aligned}\Phi(t) * \frac{\partial i(x, t)}{\partial t} &= \sum_{m=1}^n \int_{(m-1)\Delta t}^{m\Delta t} \sum_{i=1}^M \frac{c_i}{\alpha_i} \cdot e^{\alpha_i \tau} \cdot DI_{k+1/2}((n+1/2)\Delta t - \tau) d\tau \\ &= \sum_{m=1}^n \sum_{i=1}^M \frac{c_i}{\alpha_i} \int_{(m-1)\Delta t}^{m\Delta t} e^{\alpha_i \tau} \cdot DI_{k+1/2}((n+1/2)\Delta t - \tau) d\tau\end{aligned}$$

It is assumed that between time steps $(m-1)\Delta t$ and $m\Delta t$ the equation of the current is given by linear interpolation:

$$\begin{aligned}DI_{k+1/2}((n+1/2)\Delta t - \tau) &= \frac{I_{k+1/2}^{n-m+1/2} - I_{k+1/2}^{n-m-1/2}}{\Delta t} + \\ &\quad + (-I_{k+1/2}^{n-m+3/2} + 2I_{k+1/2}^{n-m+1/2} - I_{k+1/2}^{n-m-1/2}) \cdot \frac{(\tau - m\Delta t)}{\Delta t^2}\end{aligned}$$

Defining the following quantities:

$$\begin{aligned}B_m &= I_{k+1/2}^{n-m+1/2} - I_{k+1/2}^{n-m-1/2} \\ A_m &= -I_{k+1/2}^{n-m+3/2} + 2I_{k+1/2}^{n-m+1/2} - I_{k+1/2}^{n-m-1/2} \\ x_i^m &= \int_{(m-1)\Delta t}^{m\Delta t} \frac{e^{\alpha_i \tau}}{\Delta t} d\tau = \frac{1}{\Delta t} \frac{e^{\alpha_i(m-1)\Delta t}}{\alpha_i} [e^{\alpha_i \Delta t} - 1] = e^{\alpha_i \Delta t} x_i^{m-1} \\ \xi_i^m &= \int_{(m-1)\Delta t}^{m\Delta t} \frac{e^{\alpha_i \tau}}{\Delta t^2} (\tau - m\Delta t) d\tau = \frac{1}{\Delta t^2} \frac{e^{\alpha_i(m-1)\Delta t}}{\alpha_i} \left[\Delta t - \frac{e^{\alpha_i \Delta t}}{\alpha_i} + \frac{1}{\alpha_i} \right] = e^{\alpha_i \Delta t} \xi_i^{m-1}\end{aligned}$$

The convolution is evaluated as:

$$\begin{aligned}\Phi(t) * \frac{\partial i(x, t)}{\partial t} &= \sum_{i=1}^M \frac{c_i}{\alpha_i} \sum_{m=1}^n [B_m x_i^m + A_m \xi_i^m] \\ &= \sum_{i=1}^M \frac{c_i}{\alpha_i} [B_1 x_i^1 + A_1 \xi_i^1 + \Psi_i^n]\end{aligned}\tag{3.13}$$

where Ψ_i^n has a recursive form:

$$\Psi_i^n = \left(2I_{k+1/2}^{n-3/2} - I_{k+1/2}^{n-5/2} - I_{k+1/2}^{n-1/2} \right) \xi_i^2 + \left(I_{k+1/2}^{n-3/2} - I_{k+1/2}^{n-5/2} \right) x_i^2 + e^{\alpha_i \Delta t} \Psi_i^{n-1}\tag{3.14}$$

Substituting (3.14) in (3.13):

$$\Phi(t) * \frac{\partial i(x, t)}{\partial t} = B_1 x + A_1 \xi + \Psi^n\tag{3.15}$$

where:

$$\begin{aligned}
 x &= \sum_{i=1}^M \frac{C_i}{\alpha_i} x_i^1 \\
 \xi &= \sum_{i=1}^M \frac{C_i}{\alpha_i} \xi_i^1 \\
 \Psi_n &= \sum_{i=1}^M \frac{C_i}{\alpha_i} \Psi_i^n
 \end{aligned}$$

Substituting (3.15) in (3.12) the current values are calculated as:

$$I_{k+1/2}^{n+1/2} = Z_2^{-1} \left[Z_1 I_{k+1/2}^{n-1/2} + \Delta x (x + \xi) I_{k+1/2}^{n-3/2} - (V_{k+1}^n - V_k^n) - \Delta x \Psi^n \right] \quad (3.16)$$

where:

$$\begin{aligned}
 Z_1 &= \Delta x \left(\frac{L}{\Delta t} - \frac{R}{2} + \frac{\Gamma}{2} - x - 2\xi \right) \\
 Z_2 &= \Delta x \left(\frac{L}{\Delta t} + \frac{R}{2} - \frac{\Gamma}{2} - \xi \right)
 \end{aligned}$$

The value of the voltage for the next time-step is calculated from (3.11) as:

$$V_k^{n+1} = \left[\frac{C}{\Delta t} + \frac{G}{2} \right]^{-1} \left(\frac{C}{\Delta t} - \frac{G}{2} \right) V_k^n - \left[\frac{C}{\Delta t} + \frac{G}{2} \right]^{-1} \left(\frac{I_{k+1/2}^{n+1/2} - I_{k-1/2}^{n+1/2}}{\Delta x} \right) \quad (3.17)$$

3.2.3 Model implementation

The calculation process for the voltages and currents along the line is as follows:

- The solution starts with a relaxed line having zero voltage and current values at all the spatial segments ($k = 1, \dots, Ndx$) for the first time step, $I^{1/2} = V^1 = 0$.
- For $n = 1$ (3.16) is solved and the current for the next time step is calculated. During the substitution currents prior to $I^{1/2}$ are considered zero.

- Then for $n = 1$ (3.17) is solved (substituting the current calculated in the previous step) and the voltage for the next time step is obtained.

The aforementioned process continues until the end of the simulation time. However, in this iterative process the update equations of the FDTD method cannot be applied to the terminal voltages (sending and receiving end of the transmission line shown in Fig. 3.10). That is because these two points relate

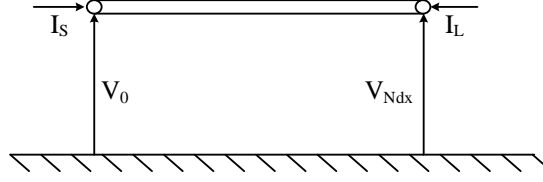


Figure 3.10: Transmission line sending and receiving end voltages and currents.

voltages and currents at the same point in time and space. For implementation of the FDTD model in EMTP it is important to calculate the currents at the sending ($k = 0$) and receiving end ($k = Ndx$) of the line. This is realized using (3.11), replacing Δx with $\Delta x/2$ and the sending end current is calculated as:

$$\frac{1}{\Delta x/2} \left(I_{1/2}^{n+1/2} - \frac{I_S^{n+1} + I_S^n}{2} \right) + C \frac{V_0^{n+1} - V_0^n}{\Delta t} + G \frac{V_0^{n+1} + V_0^n}{2} = 0 \Rightarrow$$

$$I_S^{n+1} = G_{eq} V_0^{n+1} + I_{SH} \quad (3.18)$$

and for the receiving end:

$$\frac{1}{\Delta x/2} \left(-\frac{I_L^{n+1} + I_L^n}{2} - I_{Ndx-1/2}^{n+1/2} \right) + C \frac{V_{Ndx}^{n+1} - V_{Ndx}^n}{\Delta t} + G \frac{V_{Ndx}^{n+1} + V_{Ndx}^n}{2} = 0 \Rightarrow$$

$$I_L^{n+1} = G_{eq} V_{Ndx}^{n+1} + I_{LH} \quad (3.19)$$

where I_{SH} and I_{LH} are history current sources and G_{eq} is the equivalent conductance matrix defined as:

$$G_{eq} = \Delta x \left(\frac{C}{\Delta t} + \frac{G}{2} \right)$$

$$I_{SH} = 2I_{1/2}^{n+1/2} - I_S^n + \Delta x \left(\frac{G}{2} - \frac{C}{\Delta t} \right) V_0^n$$

$$I_{LH} = -2I_{Ndx-1/2}^{n+1/2} - I_L^n + \Delta x \left(\frac{G}{2} - \frac{C}{\Delta t} \right) V_{Ndx}^n$$

A drawback of this method compared to traditional phase domain models is that the division of the transmission line into spatial segments requires the currents and voltages to be calculated for every segment in order to acquire the values of the sending end and receiving end.

Furthermore, the choice of the space step, Δx , and time step, Δt for the FDTD model is of high importance and the following conditions should be met:

- The space step should be chosen sufficiently small such that each Δx section is electrically small at the significant spectral components (with wavelength λ_{spec}) of the voltage excitation. Thus, the relation of the space step is given by [27]:

$$\Delta x = \frac{\lambda_{spec}}{10} \quad (3.20)$$

- The time step must be smaller than the propagation time over each space step. Thus, the relation of the time step is given by [27]:

$$\Delta t = \frac{\Delta x}{v_{wave}} \quad (3.21)$$

The time step calculated from the above formula is known as the "ideal" time step.

Consequently, for different frequency ranges of interest the time step and space step can differ and should be calculated accordingly. The implementation of the FDTD method as toolbox within PSCAD software is described in Appendix A.3.

3.3 FDPM versus FDTD Model

In order to assess the performance of the FDTD model, it is compared with the well established FDPM implementation in PSCAD. Three aspects for model evaluation are selected: simulation accuracy, model stability and computational time.

3.3.1 Simulation accuracy

For simulation accuracy assessment a three cable system is modeled, where each cable has a core and a sheath (six-conductor system) and the cables are laid in flat formation, as shown in Fig. 3.11. For the base case the length of the cable is

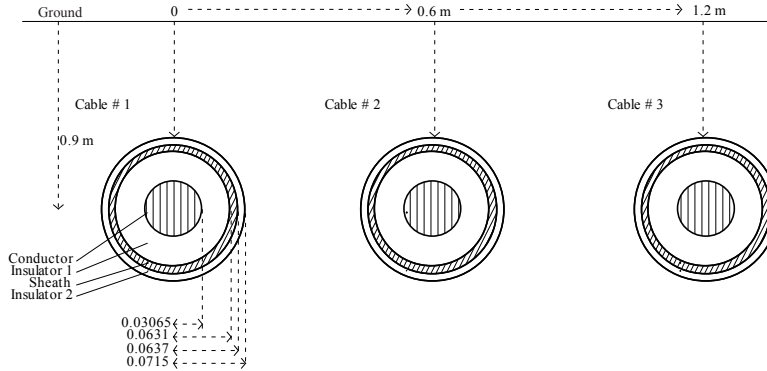


Figure 3.11: Cable parameters and layout (radii in m).

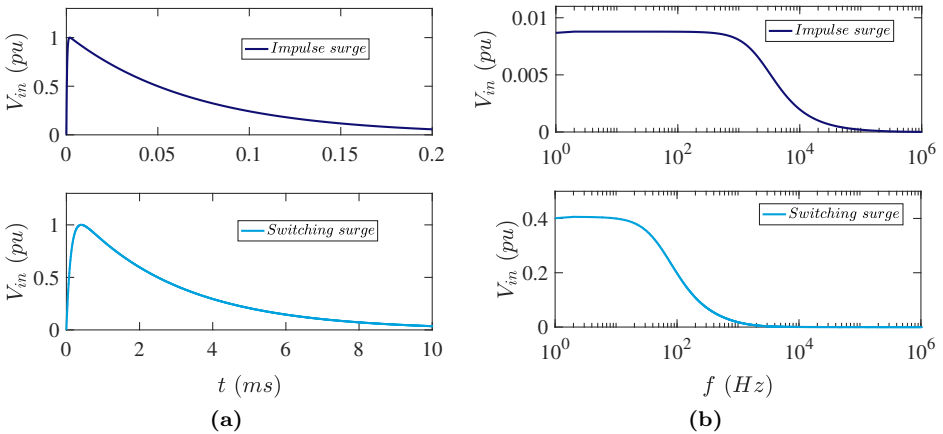


Figure 3.12: (a) Time domain response and (b) frequency spectrum of an impulse surge $1.2/50 \mu\text{s}$ (top) and a switching surge $250/2500 \mu\text{s}$ (bottom).

assumed to be 20 km and the sheaths are grounded at both ends with a grounding resistance of 0.01Ω .

The two models are compared using excitations with different frequency ranges, an impulse surge ($1.2/50 \mu\text{s}$) and a switching surge ($250/2500 \mu\text{s}$). The time domain responses and the frequency spectrums, obtained from Fast Fourier Transform (FFT), of the two excitations are shown in Fig. 3.12a and Fig. 3.12b respectively. For the impulse surge, spectral components including a safe margin up to 1 MHz should be considered while for the switching surge the frequency range extends to 10 kHz. Thus, the appropriate space step and time step of the

FDTD model for the two cases are $0.1 \mu\text{s}$ for the impulse surge and $10 \mu\text{s}$ for the switching surge.

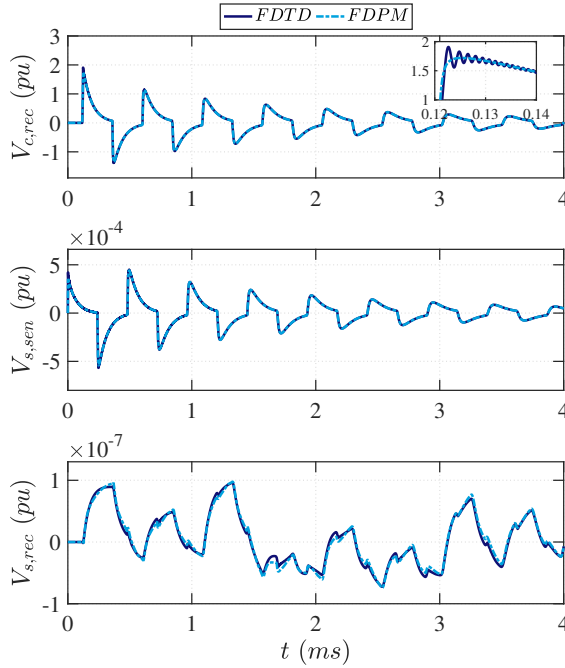


Figure 3.13: Voltage waveforms for impulse surge excitation at the receiving end of the core (top), the sending end of the sheath (middle) and at the receiving end of the sheath (bottom).

The waveform comparison of the receiving end core voltage and both sending and receiving end sheath voltages of the cable for the impulse surge is shown in Fig. 3.13. The responses of the two models are similar except of some ringing observed for the FDTD model during the fast voltage transition. The ringing is not present in the results of the model comparison for the switching surge (see Fig. 3.14) and the two models produce almost identical responses. The maximum voltage error for the receiving end core voltage is 11.0% for the impulse surge and 3.8% for the switching surge.

The choice of the FDTD model time step is crucial for its accuracy and computational time. In order to evaluate how a change in the time step affect the resulting waveforms a sensitivity analysis is performed for both impulse and switching excitation. Fig. 3.15a shows the comparison of the waveforms at the receiving-end of the cable core for impulse surge excitation for three

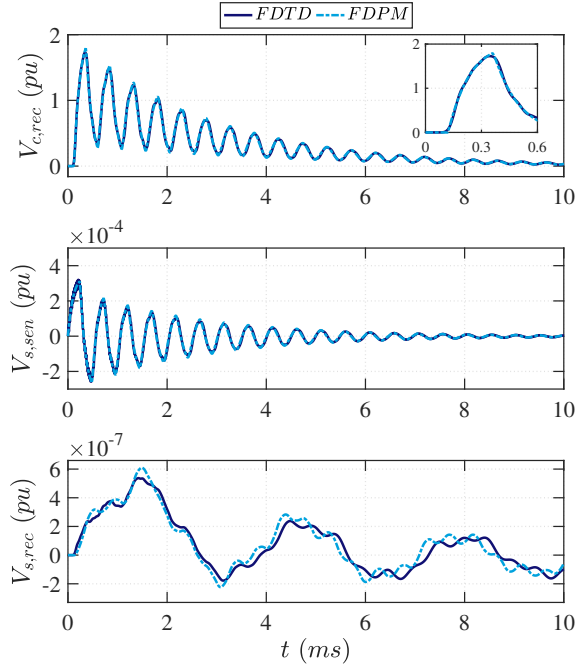


Figure 3.14: Voltage waveforms for switching surge excitation at the receiving end of the core (top), the sending end of the sheath (middle) and at the receiving end of the sheath (bottom).

time step choices. As the time step increases, higher ringing is observed during the voltage transitions which damps out more slowly. For the switching surge (see Fig. 3.15b), even though no ringing is observed, there is a deviation in the maximum overvoltage and for a time step of $50 \mu\text{s}$ there is a slight shift in the frequency of the oscillations.

3.3.2 Model stability

The passivity of an electrical system is an important aspect in determining its stability. The physical meaning of passivity in electrical circuits is that passive networks always absorb active power and thus the total energy delivered to them is positive [29, 66, 67]. In order to guarantee the passivity of a multi-conductor system model, its transfer admittance must be positive real for all frequencies.

The transfer admittance \tilde{Y} relates the sending-end and receiving-end voltages to the currents:

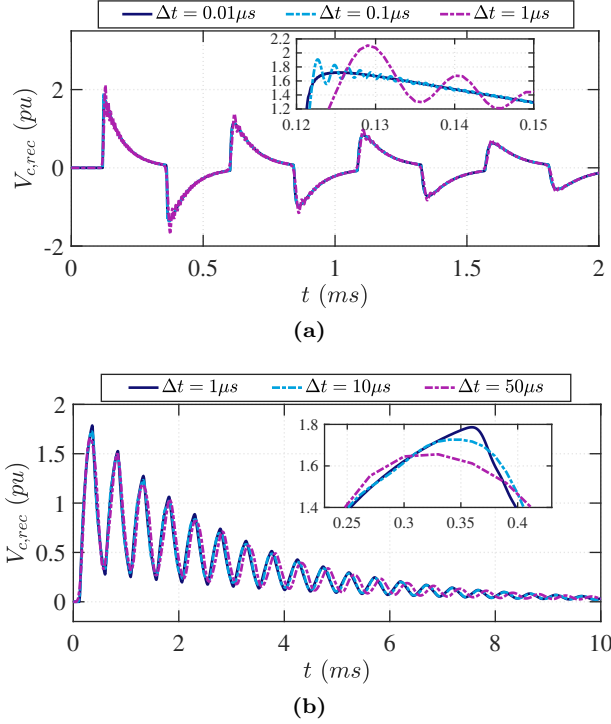


Figure 3.15: Voltage waveform comparison at the receiving end of the core for different time steps with (a) impulse surge and (b) switching surge excitation.

$$\begin{bmatrix} I_s \\ I_r \end{bmatrix} = \tilde{Y} \begin{bmatrix} V_s \\ V_r \end{bmatrix} \quad (3.22)$$

and can be expressed as [29]:

$$\tilde{Y} = \begin{bmatrix} (I - H_c^2)^{-1}(I + H_c^2)Y_c & (I - H_c^2)^{-1}(-2H_c)Y_c \\ (I - H_c^2)^{-1}(-2H_c)Y_c & (I - H_c^2)^{-1}(I + H_c^2)Y_c \end{bmatrix} \quad (3.23)$$

where Y_c is the characteristic admittance and H_c is the propagation function of the transmission line.

The necessary and sufficient conditions for the transfer admittance matrix \tilde{Y} to be positive real (and hence, for the transmission line model to be passive) are [88]:

- $\tilde{Y}(s)$ is analytic, $\forall s : Re(s) > 0$

- $\tilde{Y}(s) = \tilde{Y}(s)^*$
- $Y^H(s) = \frac{1}{2} \left[\tilde{Y}(s) + (\tilde{Y}(s)^*)^T \right]$ (Hermitian matrix) is positive definite.

Since vector fitting is used, the complex poles and residues always appear in conjugate pairs and the first two conditions are automatically fulfilled. In order for the third condition to be satisfied the eigenvalues of the Hermitian matrix need to be positive for all frequencies.

For the FDPM, using the fitted characteristic admittance, Y_c^f , and propagation function, H_c^f , the FDPM transfer admittance \tilde{Y}^f and the Hermitian matrix Y^{H^f} are calculated. For the FDTD model the fitting is performed at the series impedance, Z^f , so the characteristic admittance and propagation function are calculated as:

$$Y_c^{f,FDTD} = \sqrt{\frac{Y}{Z^f}} \quad (3.24)$$

$$H_c^{f,FDTD} = e^{-\sqrt{Y Z^f} l} \quad (3.25)$$

where l is the length of the transmission line.

Using (3.24) and (3.25) the FDTD transfer admittance $\tilde{Y}^{f,FDTD}$ and the Hermitian matrix $Y^{H^{f,FDTD}}$ are calculated. In order to compare the two models in terms of stability their passivity is tested by calculating the eigenvalues of the Hermitian matrices Y^{H^f} and $Y^{H^{f,FDTD}}$ for a cable segment used in the south-ring cable configuration. The length of the segment is 0.7 km and it consists of 12 mutually coupled cables layed in flat formation (O1).

As can be seen from Fig. 3.16, the FDTD model (Fig. 3.16b) displays better passivity condition since there are only small negative eigenvalues, in contrast with the FDPM (Fig. 3.16a) where large negative eigenvalues are observed. The probability of having unstable simulation with very small passivity violations is low as the passivity of the entire network is further improved due to the additional resistors in the electrical network.

In order to see how the passivity violation translates into the time domain, the voltage waveforms of the 0.7 km cable segment for an impulse surge excitation are shown in Fig. 3.17. It is obvious that the FDTD model presents improved stability from the FDPM with comparable accuracy.

3.3.3 Computational time

With regard to the computational time, the FDPM is much more efficient and the required computational time for the example in Section 3.3.1 is approximately

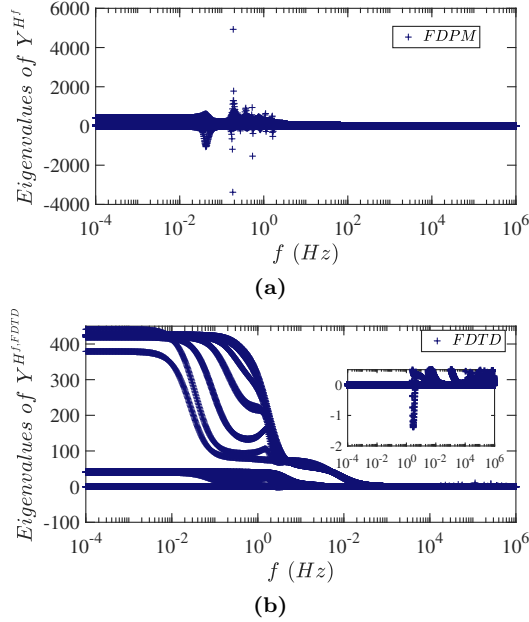


Figure 3.16: Eigenvalues of the Hermitian matrix for (a) the FDPM and (b) the FDTD model.

six times smaller than for the FDTD when the time step according to (3.21) is used. Fig. 3.18 illustrates the change in the computational time and the maximum voltage error for a variety of time steps when having impulse surge (see Fig. 3.18a) and switching surge excitation (see Fig. 3.18b) for the cable configuration described in Section 3.3.1. The maximum voltage error of the FDTD model for each time step is calculated with respect to the maximum value of the FDPM using the optimal time step, see Section 3.3.1.

$$\Delta V_{max} = \frac{V_{FDTD,max} - V_{optFDPM,max}}{V_{optFDPM,max}} * 100\% \quad (3.26)$$

Smaller time steps produce lower errors but need more computational time. However, it is observed that for both excitations the decrease of the time step after some value produces significant increase in the computational time while the gain in the maximum voltage error does not significantly decrease. Finally, comparing the errors for the two excitations it can be concluded that the model accuracy is more sensitive for excitations with steeper front.

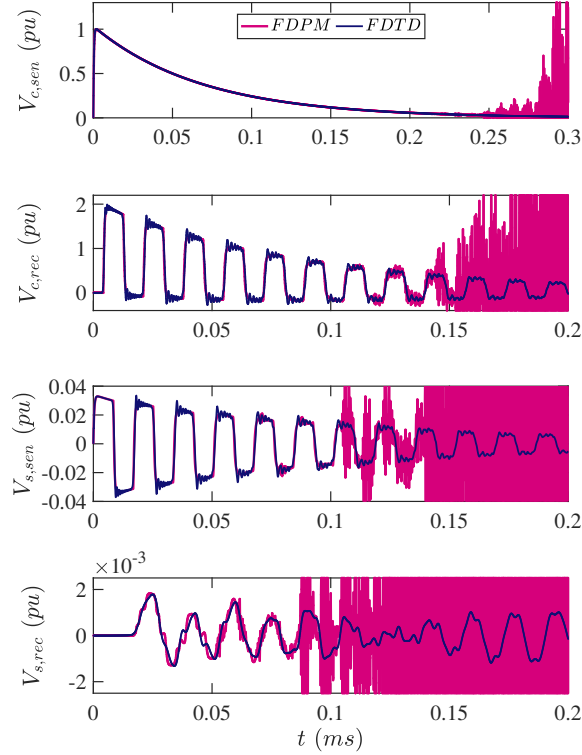


Figure 3.17: Voltage waveforms for switching surge excitation at the sending end of the core (top), the receiving end of the core (second to top), the sending end of the sheath (third to top) and at the receiving end of the sheath (bottom).

3.4 Model comparison for Randstad south-ring

Stability problems were encountered when the south-ring cable configuration was modeled in full detail using FDPM. For that reason a simplified configuration was defined in Section 3.1.1. The comparison between the simplified and the detailed model in frequency domain was shown in Fig. 3.3. In order to verify the effect of simplification in time domain the detailed south-ring configuration is modeled using the FDTD model and compared with the simplified FDPM for different network configurations and transient phenomena.

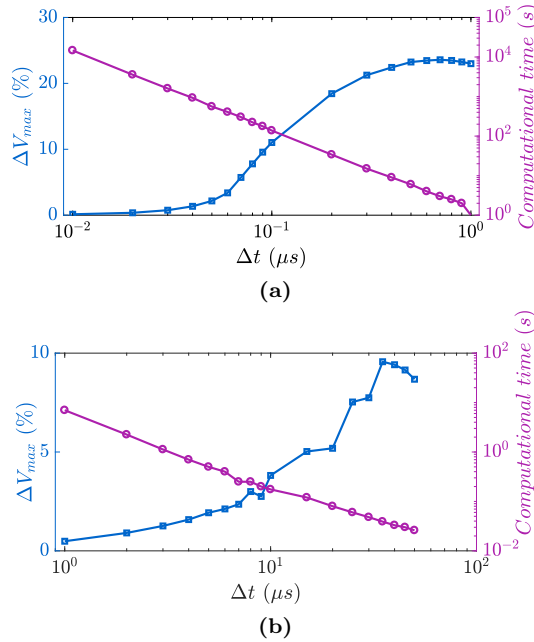


Figure 3.18: Change in maximum voltage error and computational time for different time steps for (a) impulse surge and (b) switching surge excitation.

3.4.1 Stand-alone cable and south-ring connection

The first configuration used to compare the simplified FDPM with the detailed FDTD model is the stand-alone south-ring cable and the comparison is performed both for impulse and switching surge excitation (see Fig. 3.12a). The results are shown in Fig. 3.19 in time (Fig. 3.19a) and frequency (Fig. 3.19b) domain using Fast Fourier Transform (FFT). For both cases the voltage waveforms are similar at the first moments of the surge but later deviations emerge. In terms of the maximum overvoltage, the deviation between the two models is relatively small with 9.8% for the impulse surge and 1.2% for the switching surge. Moreover, it is observed that for both excitations, there is a deviation of 125 Hz in the main frequency of the oscillations and the damping is higher in the simplified case.

For the second configuration the stand-alone mixed OHL-UGC south-ring configuration was used with the same excitations. As demonstrated in Fig. 3.20 the voltage waveforms are almost identical, having the same maximum overvoltage and the deviation of the energization harmonic frequency is only 10 Hz.

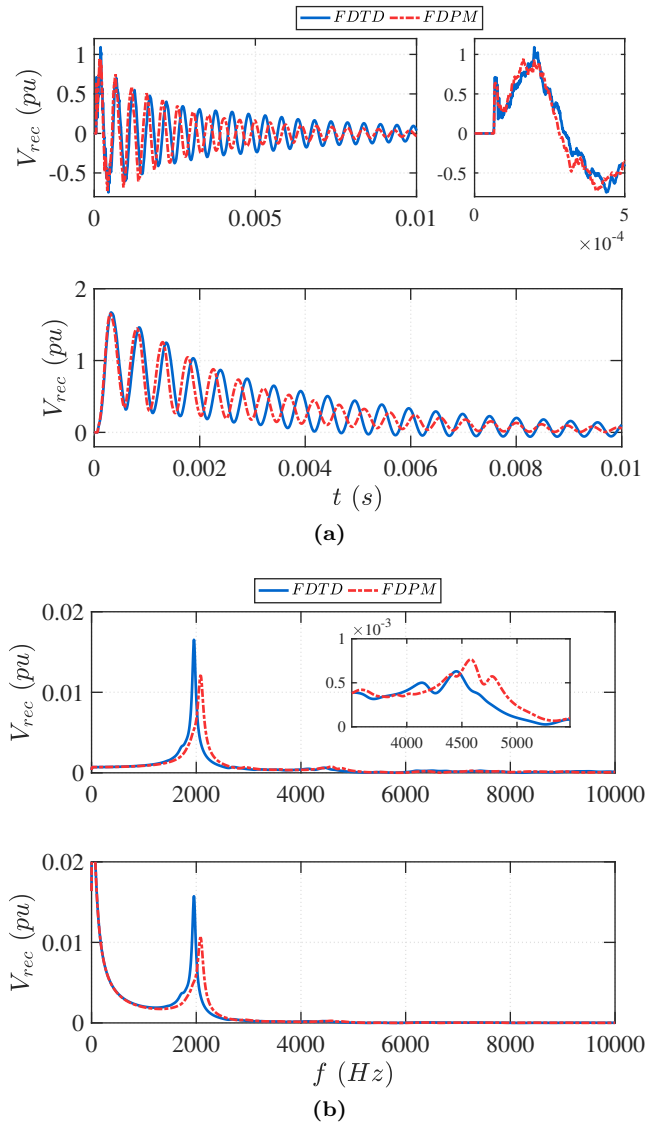


Figure 3.19: Voltage waveform comparison for stand-alone cable configuration at the receiving end of the cable between the detailed FDTD model and the simplified FDPM in (a) time domain and (b) frequency domain for impulse surge (top) and switching surge (bottom) excitation.

Thus, it can be concluded that considerable deviations between the two models

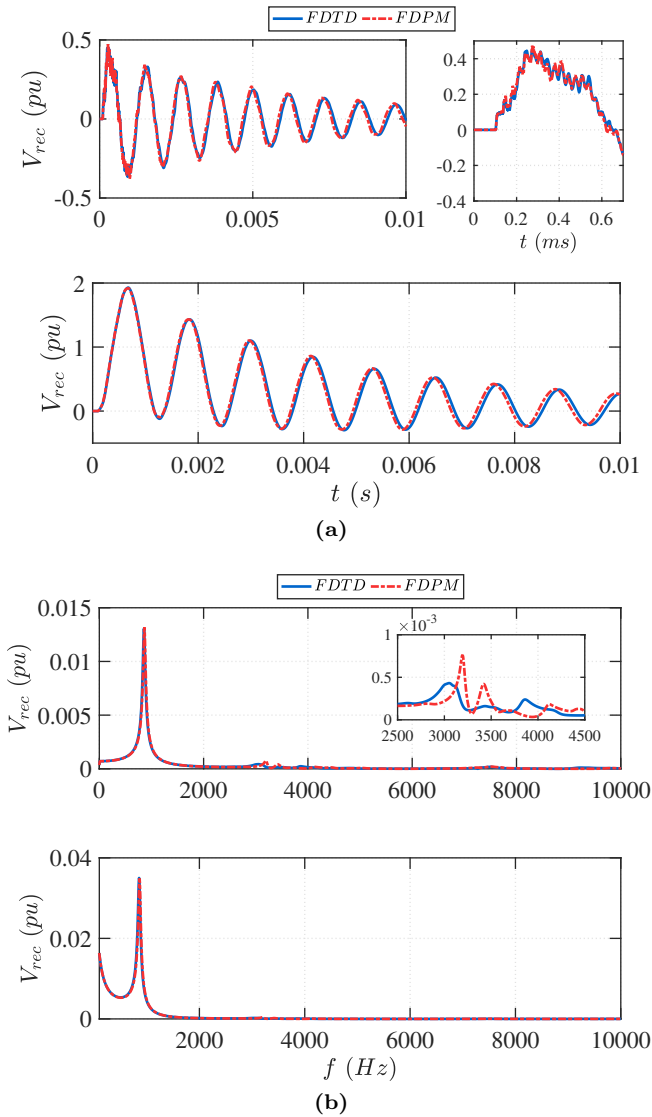


Figure 3.20: Voltage waveform comparison for stand-alone mixed OHL-UGC south-ring configuration at the receiving end of the cable between the detailed FDTD model and the simplified FDPM in (a) time domain and (b) frequency domain for impulse surge (top) and switching surge (bottom) excitation.

are present both in overvoltage magnitude and dominant energization frequencies

when the cable connection is studied as stand-alone. When the two OHL parts are incorporated in the connection the differences are minimized both in time and frequency domain since the inductance of the OHL dominates over the contribution from the cable.

3.4.2 South-ring and Full Dutch 380 kV network

In addition to the stand-alone cable and stand-alone mixed OHL-UGC-OHL connection two other configurations were tested: the south-ring connection with equivalent source impedances at substations WTR and BWK and the whole Dutch 380 kV grid for a specific network snapshot.

The two models in both configurations are compared for two types of switching actions:

- S1: Switching of the black circuit from substation WTR while the white circuit is out of service.
- S2: Switching of the black circuit from substation WTR while the white circuit is in service.

Fig. 3.21a and Fig. 3.21b show the voltage waveforms of the equivalent source impedance configuration at substation WTR (top) and substation BWK (bottom) for switching S1 and S2 respectively. For S1 the two models produce identical results at both substations. For S2 the resulting voltage waveform in WTR is similar for both models and from the zoomed-in part it is evident that even the first moments after energization the voltage wave reflections are identical. The BWK voltage waveforms are also similar and only slight deviations are observed later in time where some higher frequency oscillations present different damping between the two models.

The voltage waveform comparison between the detailed FDTD cable model and the simplified FDPM incorporated in the full Dutch 380 kV grid for switching S1 and S2 are demonstrated in Fig. 3.22a and Fig. 3.22b at substation WTR (top) and substation BWK (bottom). For both switching actions the low-frequency transients are similarly represented in the two models. There is a slight difference in the higher frequency transient oscillations, which are present the first moments after the energizations, but this have almost no effect in the maximum overvoltage magnitude, with a deviation of 1.2% in WTR and 1.1% in BWK.

It can be concluded that the model simplifications which needed to be made in the south-ring cable connection do not affect the resonance and the slow-front transient behavior when the 380 kV network is incorporated. The same applies

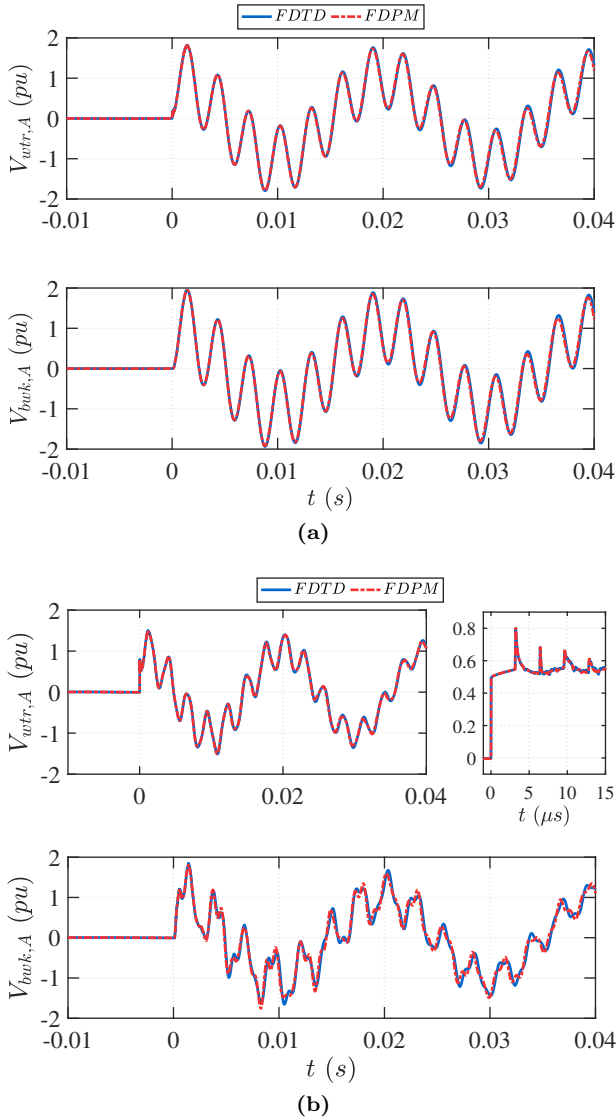


Figure 3.21: Voltage waveform comparison for south-ring configuration with source impedances between the detailed FDTD model and the simplified FDPM in for switching action (a) S1 and (b) S2 at substation WTR (top) and BWK (bottom).

for the very fast wave reflections though there are some slight deviations in the

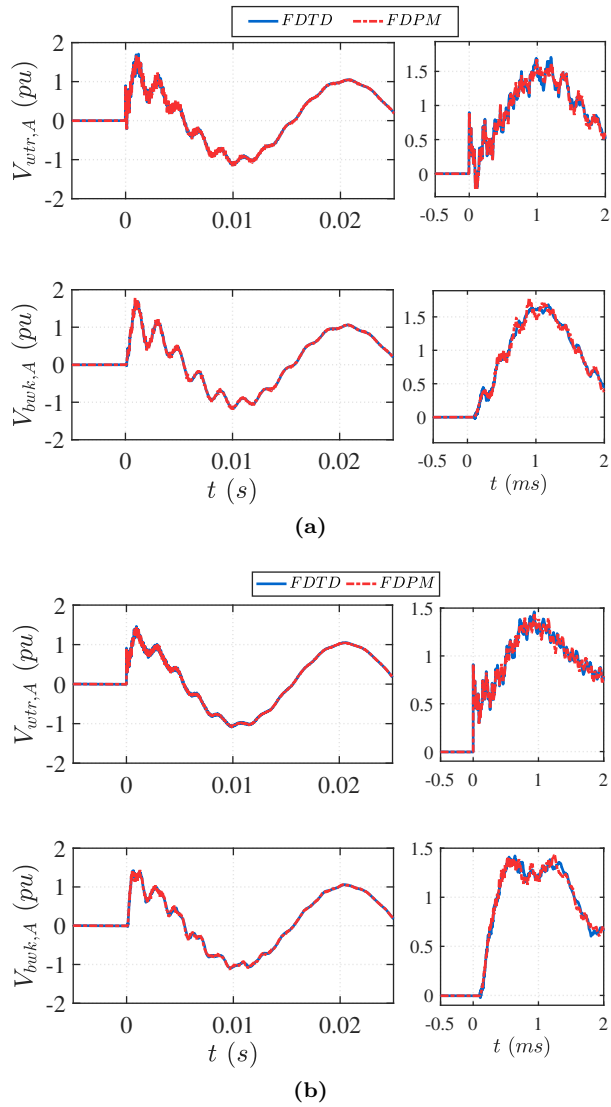


Figure 3.22: Voltage waveform comparison for full Dutch 380 kV grid between the detailed FDTD model and the simplified FDPM in for switching action (a) S1 and (b) S2 at substation WTR (top) and BWK (bottom).

high frequency transients at the beginning of the transient event. However, these deviations do not affect the resulting maximum overvoltage magnitude.

3.5 Conclusion

From the analysis presented in this chapter, it is evident that under certain circumstances the well established FDPM is unstable and its instability cannot be overcome by DC correction or other passivity enforcement algorithms. Such instability is mostly present when the system consists of a large number of mutually coupled cables having relatively short lengths.

A good alternative for simulating such complex cable configurations is the use of the FDTD model. The FDTD model presents improved stability while the accuracy is comparable with the FDPM. However, the increased computational time needed for the FDTD model makes its use less appealing and limited to extreme cases. More specifically, the FDTD model could be used when small cable segments cannot be merged and incorporated as a larger segment. Furthermore, such cable model is more suitable for modeling a system with large amount of mutually coupled cables when the separation of the system to decoupled subsystems results in inaccuracies. Finally, the FDTD model can be used as a benchmark to test simplified FDPM configuration, as in the case of the south-ring connection, to reassure that simplifications do not result in inaccurate results.

4

Network Modeling Detail

There is a lack of guidelines on the level of detail and depth of the network that needs to be modeled for correctly representing its transient behavior. This is the case for networks at the same voltage level as well as at connected lower voltage levels. Moreover, the extent of the model depends on the type of phenomena to be simulated. For lightning surges, it is usually sufficient to concentrate on the section where the lightning is expected to strike, since the level of overvoltage attenuates fast along the network. The affected section requires appropriate modeling for e.g. pylon impedance, cross-bonding method, busbars and substation equipment to adequately simulate fast transients. For power frequency related phenomena the whole grid has to be taken into account, but design details responsible for high frequency surge reflection and transmission may be ignored. The slow-front transients studied in this thesis, and in particular the impact of UGCs, extends beyond the UGC connection itself, but connections will have diminishing effect as they are further away.

There are reasons to limit the extension of the simulated network. It can be time consuming to gather all the information, in particular when information is required on short term, e.g. changing the grid configuration upon a fault. Furthermore, when systematically studying the effect of parameters on circuit response, lowering the level of detail reduces the evaluation time significantly.

4.1 Network extent at the same voltage level

References [89–92] propose a general concept dividing the whole network into three areas: the study area (with detailed line models), the external area (with simpler line models), and the remainder network (considered not important for the study of transients), see Fig. 4.1.

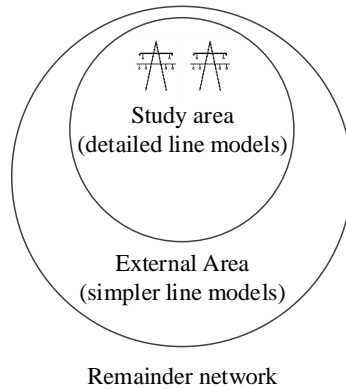


Figure 4.1: *A network subdivided in three areas: study area, external area, and remainder of the network.*

This approach is adopted also here, where the WTR to BWK connection is the focal point of the study area and maximum detail is employed for this section. Connections to other countries and to grids at lower voltage level (220 kV, 150 kV) are always considered as part of the remainder network and need proper equivalent circuits based on the corresponding short-circuit power or the powerflow. The borders between these regions, comprising the external area in Fig. 4.1, are adapted using an iterative process in which the complexity is gradually varied until simulation results remain unaltered. The complete Dutch 380 kV network is demonstrated in Fig. 4.2 with the two substations of interest indicated with blue color and the foreign connections indicated with red arrows.

This research focuses on phenomena containing frequencies up to 10 kHz, often referred to as slow front transients mainly caused by line switching [76] as well as resonance phenomena, where the most important events are observed in frequencies below 2 kHz. The indicators of interest for those two phenomena differ. For slow front transients the interest is mainly the maximum overvoltage, in order to ensure that it is below the Switching Impulse Withstand Voltage (SIWV) for insulation co-ordination purposes. For resonance phenomena the interest is mainly the accurate representation of the frequency and magnitude of the resonance peaks.

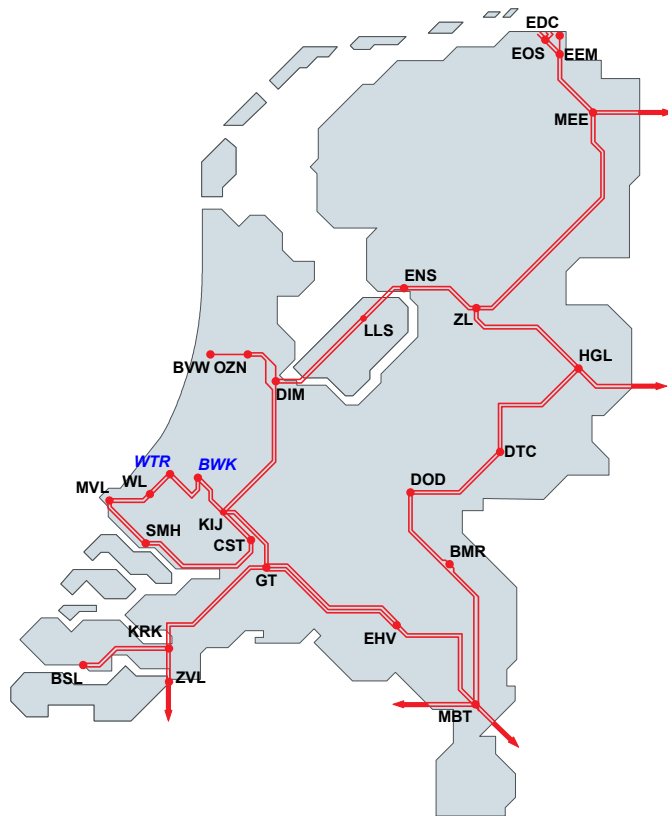


Figure 4.2: *Substations in Dutch 380 kV transmission system with a cable connection located between Wateringen (WTR) and Bleiswijk (BWK)*

4.1.1 Approach

The best way to evaluate the effect of complexity reduction is a comparison with the real network. To this end a reference model is constructed in which high level of detail is incorporated. Next, simplifications are introduced and the resulting method is referred to as the "top-down" method. The whole 380 kV transmission network in the Netherlands, serves as the reference model and includes the following details:

- transmission routes with their length, phase order and transpositions.

- pylons with geometrical information of conductor spacing, ground wires and earth resistance.
- conductors with information about their resistance, diameter and sub-conductors spacing.

The reference model is simplified in successive steps. The effect of simplifications is then compared with the reference model to analyze the reduction of accuracy. For the inverse approach, referred to as the "bottom-up" method the iterative process starts with accurately modeling the connection of interest and gradually increasing the level of detail. For this method it is assumed that a suitable reference model may not be available which is often the case when studying transient phenomena of a large network [93].

Most elaborate both in terms of importing all data and in computational effort is the work related to the modeling of the transmission lines. Various transmission line models are available. The advantage of applying less accurate models is not only related to the computational burden when simulating the complete grid in full detail, but also to the effort needed to gather and process all required data. The most common models are listed below in descending order in terms of accuracy [38]:

- Frequency-dependent Phase model, (FD)
This model strives to represent the full frequency dependency of a transmission system and the resistance, inductance and capacitance of the line are represented using distributed parameters. It is regarded as one of the most accurate and stable models for transmission line or cable representation. However, it requires the geometric and material properties of the line, pylon or cable trench, and earth resistivity.
- Bergeron model, (B)
The Bergeron model uses distributed line inductances and capacitances, but with lumped resistance representing the total line loss. Its electrical parameters are calculated at a specific frequency, which can be tuned and consequently the response of the model is accurate around this frequency.
- Nominal π -Model, (Pi)
The nominal π -model is a lumped representation of the line in terms of resistance, inductance and capacitance. Its electrical parameters are calculated at a specific frequency (usually steady state) and consequently the response of the model is accurate around this frequency.
- Infinite busbar connection, (IBB)
The connection is considered as an ideal busbar. No resistance, inductance,

and capacitance are taken into account. This model ensures that the related substations are modeled.

- Short-circuit Equivalent, (Sc)

The simplest representation of a transmission line is by removing it completely from the network, including the connected substations, and replacing it by an equivalent network consisting of a voltage source in series with a sequence impedance. The parameters of these components can be obtained from the short circuit current and the voltage before the fault at that point.

The requirements for the model comparison depend on the objectives of the study. For the slow front transient study the maximal overvoltage is usually of concern and the standard switching surge, as described in [94], is chosen as input and is applied at the busbar in WTR substation (see Fig. 4.2) on phase A. The same methodology can be used for fast front transients if the applied voltage disturbance is replaced by a lightning impulse surge and the reference model is constructed according to the modeling guidelines for fast front transients [95]. Fig. 4.3a shows the standard IEC switching surge [94] applied at substation WTR and Fig. 4.3b depicts the time domain voltage response at BWK. For the resonance study the quantities of interest are the frequency and magnitude of the resonance peaks which are evaluated using frequency scans at both WTR and BWK substations.

The comparison between the simplified model ("smp") and reference model ("ref") is performed using the following indicators:

1. Change of the maximum voltage of the time domain response in percentage (for slow front transient study):

$$\Delta U_{out,max} = \frac{|U_{out,max,smp} - U_{out,max,ref}|}{U_{out,max,ref}} 100\% \quad (4.1)$$

2. Frequency shift of the main resonance peaks (resonance study):

$$\Delta f_{res} = f_{res,ref} - f_{res,smp} \quad (4.2)$$

3. Change in harmonic impedance magnitude of the main resonance peaks in percentage (resonance study):

$$\Delta |Z_{f_{res}}| = \frac{|Z_{f_{res},ref}| - |Z_{f_{res},smp}|}{|Z_{f_{res},ref}|} 100\% \quad (4.3)$$

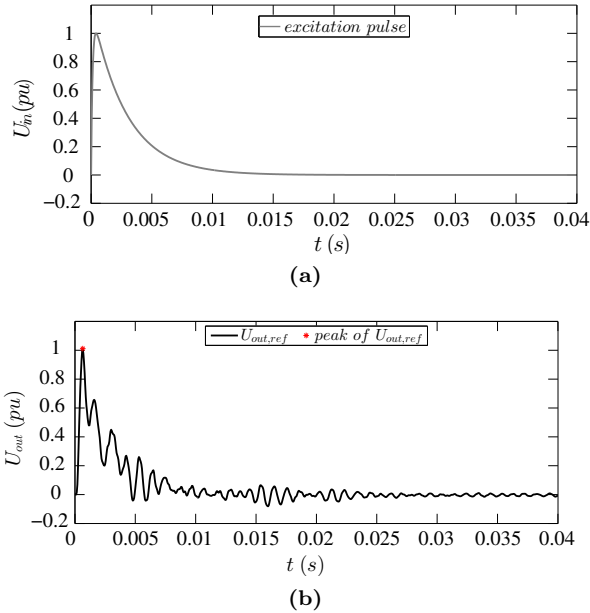


Figure 4.3: Example of (a) a standard switching surge applied in WTR and (b) the voltage of the reference model at substation BWK.

For iteratively judging successive steps when increasing the model detail, basically the same indicators can be employed. The comparison will then be between the current configuration and a previous simulated one with less detail at some point in the connection.

4.1.2 Reference Model

The network model (transmission routes) is based on the 2016 network capacity and quality plan published by the Dutch TSO [96]. Since the concerned frequency range is up to 10 kHz, the reference model is constructed according to slow front surges [75, 76] using the FD model for all transmission lines.

Model of underground power cable circuit

The UGC connection between WTR and BWK is modeled as described in Chapter 3.1.1, i.e. using the simplifications of one segment with the same length (0.9 km) and the same trench type when modeling a minor section. The use

of such simplifications in the cable model will hardly affect the end result when this cable is incorporated in the mixed OHL-UGC south-ring connection and when embedded in the complete Dutch 380 kV grid. This is supported by Fig. 3.20, Fig. 3.21 and Fig. 3.22 where the predicted maximum overvoltage and the harmonic content of both models are almost identical.

Model of overhead line circuit

The overhead lines of the whole Dutch 380 kV grid are modeled using the FD model where material properties, number of bundled conductors, compensating wires and pylon characteristics were inserted. However, a large scale network, as the Dutch 380 kV grid, has thousands of pylons with different configurations (different pylon types or same type with different pylon heights) and transpositions at specific locations (see Fig. 4.4). Obtaining and implementing all relevant data is time consuming so the relevance for model accuracy is investigated. The influence of differences in heights for the same type of pylon and the distance of the transposition to the bus bar are checked for a stand-alone transmission line configuration.

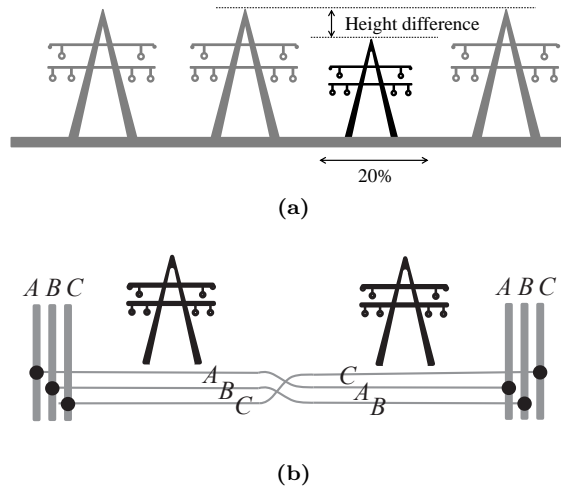


Figure 4.4: Investigation of (a) different pylon height (b) transmission line transposition [19].

Pylon height

Pylons have different heights due to geometric conditions and the number of different pylons is situational, depending on specific network configuration. To

illustrate the effect caused by different pylon heights, a standalone 10 km route is investigated. It is assumed that 20% of the total number of pylons deviate in height with respect to a standard height of 43 m, and they are located in the middle of the route, as shown in Fig. 4.4a. The deviation in height for all 20% is taken -9 m, -6 m, -3 m, 0 m, $+3$ m, $+6$ m, $+9$ m, respectively.

Table 4.1: *Effects when a height difference for 20% of the pylons is ignored, where $f_{1,res}$ is the frequency of the first resonance peak.*

	ΔU_{max} (%)	$\Delta f_{1,res}$ (Hz)
20% pylons +9 m, ignored	0.31	<10
20% pylons +6 m, ignored	0.23	<10
20% pylons +3 m, ignored	0.13	<10
100% standard pylon	0	<10
20% pylons -3 m, ignored	0.23	<10
20% pylons -6 m, ignored	0.50	<10
20% pylons -9 m, ignored	0.87	<10

From the results summarized in Table 4.1 there is not a noticeable effect in the frequency shift and a small effect on the output voltage. A decrease in pylon height has a stronger effect than an increase in pylon height, because of the larger relative change in line to ground capacitance with the same absolute height variation. Only extreme changes in height have a significant effect. Therefore, in the reference model, only the standard pylon is used for each transmission route.

Transposition

Overhead lines are regularly transposed. For the simulated 10 km line the effect of different distances of the transposition to the bus bar is evaluated. The deviations from ignoring the transposition are shown in Table 4.2. It is observed from Table 4.2 that ignoring the transposition has a small effect when the transposition is near to the busbar, but a large effect when the transposition is further away. The unbalance because of incomplete transposition clearly scales on the distance that this unbalance occurs. Therefore, the transpositions need to be modeled.

Model of transformers and shunt reactors

The type of transformer at the substations is a three-phase, three winding three-limb transformer with three categories of nominal voltages; 380/150/50 kV, 380/220/50 kV and 380/110/50 kV. For all three types the leakage inductances and copper losses of the three windings were considered. The magnetizing inductance and iron losses together with the nonlinear relationship between its windings flux linkage and current, which is represented as a piece-wise linear curve were taken into account as well [19]. Moreover, for only the first transformer

Table 4.2: *Effect of ignoring a transposition at a specified distance percentage away from the busbar.*

effect of ignoring a transposition at	ΔU_{max} (%)	$\Delta f_{1,A}$ (Hz)
0% from bus bar	0	<10
0.5% from bus bar	0.03	<10
1.0% from bus bar	0.04	-50
1.5% from bus bar	0.08	-50
2.5% from bus bar	0.15	-50
5.0% from bus bar	0.32	-50
10.0% from bus bar	0.55	-50
15.0% from bus bar	0.66	-50
25.0% from bus bar	0.73	-100
50.0% from bus bar	0.76	-150

type three kinds of capacitive couplings, as winding cross-over capacitance, interwinding capacitance and winding-earth capacitance, were considered [97]. For the two other transformer types no capacitive couplings were considered since they are located far away from the connection of interest (WTR-BWK). Shunt reactors are connected to the tertiary winding of the three winding transformers. The ones located in substations WTR and BWK are modeled in detail with their inductances, resistances and capacitances computed for each of the 11 layers of each winding [97]. The remote shunt reactors were modeled with their total inductance.

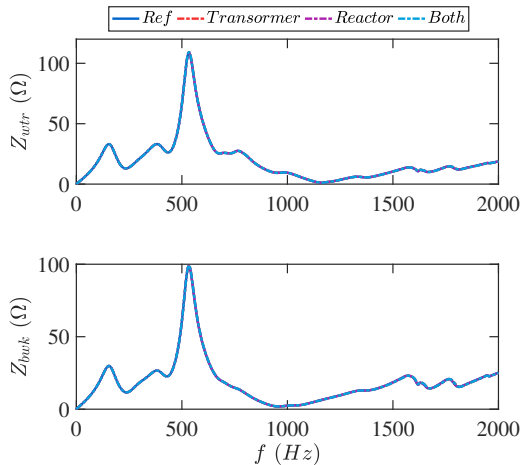
For the type of transformer and shunt reactor used in this model dedicated measurements to obtain the main parasitic capacitances were also performed and thus included in the model. However, generally the parasitic capacitances for this kind of equipment are unknown and a sensitivity analysis is performed to check the effect of ignoring them. In Table 4.3 the deviation of the maximum overvoltage as well as the frequency shift of the first resonance peak are shown for substation Bleiswijk since this is the closest substation to the source of disturbance and thus the one that is expected to be more affected. It is also observed from the harmonic impedance of both substations WTR and BWK (see Fig 4.5) that ignoring the parasitic capacitances of both the transformers and the shunt reactors produce identical impedances for frequencies up to 2 kHz.

Model of generators, loads and foreign connections

For the simulation of the reference model assumptions have to be made regarding the state of the network. This includes mostly the value of loads and the amount of operating generators.

Table 4.3: *Effect of ignoring parasitic capacitances of transformers and shunt reactors.*

effect of ignoring parasitic capacitances of	ΔU_{max} (%)	$\Delta f_{1,A}$ (Hz)
Shunt reactors	0.003	0
Transformers	0.021	0
Both	0.021	0

**Figure 4.5:** *Comparison of the harmonic impedance at substation WTR and BWK when ignoring the parasitic capacitances at the transformer model, reactor model and at both of them.*

- Each synchronous generator is modeled as an ideal source at 20 kV in series with its subtransient reactance and then connected to a step-up transformer.
- The loads, placed directly on the secondary side of the transformers, are modeled with the fixed-load component of PSCAD/EMTDC. The input data of the component is the active and reactive power consumed by the load and an automatic conversion of these values as a constant resistance in parallel with constant inductance or capacitance is performed. The active and reactive power at the secondary side of the transformers were obtained from power flow calculations using the PowerFactory [98] model of the whole transmission network of TenneT.
- Each international connection is modeled as an ideal source with an impedance in series, based on the short-circuit current at the corresponding

busbar.

4.1.3 Accurate representation of transient overvoltage

The main objective of this section is directed to accurately representing the overvoltages occurring upon a local switching surge (at WTR substation) for a chosen modeling depth. This means that the overvoltages in the south-ring are considered with special attention for the closest substations and more specifically for:

- Case1: The voltages observed at the six substations nearby BWK which make up the full Randstad380 southring
- Case 2: The voltages observed at the two closest substations to WTR (being BWK and WL)

A switching surge is applied at substation WTR in one of the two parallel circuits with the other circuit in service. For both methods, "top-down" and "bottom-up", it is considered sufficient if the maximum overvoltage of the resulting model at an aimed substation deviates less than a specific percentage chosen as 1% from the maximum overvoltage of the same busbar in the "reference" and the "current" model respectively. The deviation of 1% is a rather arbitrary value and predictions of overvoltages usually differ more from actual occurring values. However, the target here is to compare prediction results, and their deviations should be clearly less than the deviations with reality.

The distance of each connection to the source of disturbance is mentioned in Table 4.4. The distances refer to the shortest path. Connections starting from the same substation and have the same distance need to be considered (for the "bottom-up" method) or eliminated (for the "top-down" method) simultaneously.

Comparison of "top-down" and "bottom-up" method

For the "top-down" approach the simplification is a step-by-step process starting with the farthest line from the source of disturbance. At each step the line model is reduced to the lowest level. If such change in the line model causes the network model not to fulfill the aforementioned criteria, a more detailed line model is adopted. The procedure is repeated for the lines closer and closer to the source of disturbance, until no more simplification can be made. The resulting model is the most simplified one which still provides acceptable accuracy. For the "bottom-up" approach the step-by-step process starts by modeling only the

connection of interest (WTR - BWK) using the FD model while the rest of the EHV grid is modeled with an equivalent network. When a new connection is added the line models mentioned in Section 4.1.1 are tested and if no significant difference between two models is observed the less complex one is chosen. The process stops when, by adding a new connection, the comparison indicators are lower than the chosen limit. For this method it is assumed that no reference model is available which is often the case in transient studies. The results of both methods for the cases where the interest either concerns the complete south-ring or the closest substations are presented in Table 4.4, where the first columns indicate the transmission line with distance to the switching surge and the other columns indicate the minimum level needed to model.

Comparing the "top-down" and the "bottom-up" methods the results are quite close. Table 4.4 shows that for the defined criteria the highest level of detail is needed for the lines comprising the Randstad380 south-ring. More specifically, for the "top-down" approach if the interest focuses on the two nearby substations only for a few connections outside the south-ring a Bergeron or a Pi model is needed, for the others the lines can be substituted by short-circuit equivalents. Obviously, when the over-voltage predictions of all substations within the south-ring should be reproduced within 1%, connections extending from this ring need more accurate modeling. For the "bottom-up" approach when the interest focuses on the two closest substations only for two connections a simpler model is found when compared with the "top-down" method (Bergeron instead of FD). When the interest extends to over-voltages in the complete south-ring a few gradual differences occur. In particular, the requirement for the connections 11 and 12 starting from substation DIM needs FD modeling here, whereas other connections can be modeled less accurately. However, the overall picture is similar.

The time domain response resulting from the "top-down" method of substation BWK for case 2 is shown in Fig. 4.6. The time domain response resulting from the "bottom-up" method of substation BWK for case 2 is shown in Fig. 4.7. The first moments of the switching surge responses, where the maximum overvoltage occurs, are almost identical for both simplified models and the reference model. Deviations start to become visible after the first 2 ms mainly related on the transient oscillation damping. Moreover, a slight frequency shift of the main harmonic components produced from the switching surge is also visible from the time domain response. However, both deviations related to the frequency components do not affect the maximum overvoltage.

Table 4.5 and Table 4.6 show the values of the maximum overvoltage deviation between the resulting model and the reference model, for the two study cases and the two methods. It should be noted that for the derivation of the simplified model resulted from the "bottom-up" no reference model was used. The slight change in line models of the connections in Case 1 leads to differences of the

Table 4.4: Results for the two methods, for two case: maximum deviation of 1% in complete Randstad south-ring and 1% deviation in the nearest substations. (* connections which are part of south-ring)

Lines	Distance from switching surge (km)	"Top-down" method		"Bottom-up" method	
		Case 1	Case 2	Case 1	Case 2
		Line model type		Line model type	
25: MEE-EEM	290.8	Sc equivalent		Sc equivalent	
24: DTC-DOD	268.2				
23: DTC-HGL	243.3				
22: BMR-DOD	226.5				
21: ZL-MEE	183.0				
20: ZL-HGL	183.0				
19: MBT-BMR	168.6				
18: ENS-ZL	151.0				
17: LLS-ENS	130.0				
16: MBT-EHV	119.9				
15: KRK-BSL	111.7				
14: KRK-ZVL	111.7				
13: BVW-OZN	94.7				
12: DIM-LLS	79.5	B		FD	
11: DIM-OZN	79.5	B		FD	
10: GT-EHV	56.0	Pi	Pi	B	Pi
9: GT-KRK	56.0	Pi	Pi	B	Pi
8: CST-SMH*	52.5	FD	FD	B	B
7: KIJ-DIM	40.6	FD	B	FD	B
6: KIJ-GT	40.6	FD	B	FD	B
5: KIJ-CST*	40.6	FD	B	FD	B
4: MVL-SMH*	26.5	FD	FD	B	B
3: BWK-KIJ*	22.0	FD	FD	FD	FD
2: WL-MVL*	6.8	FD	FD	FD	FD
1: WTR-WL*	0.0	FD	FD	FD	FD

overvoltage deviation between the two methods but the 1% criteria is met. For case 2 a value slightly in excess of 1% is noted at BWK substation which means that even though the current model deviate less than 1% with the previous model it can deviate more than 1% from the reference model.

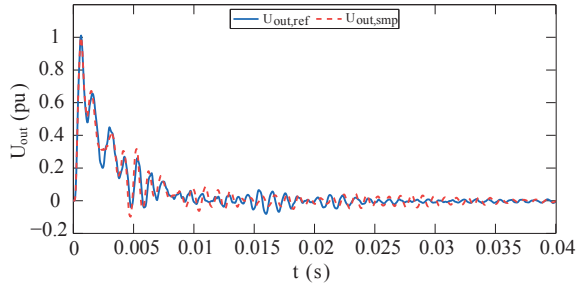


Figure 4.6: Comparison of output voltage and at the busbar in Bleiswijk between "top-down" model of case 1 and the reference model.

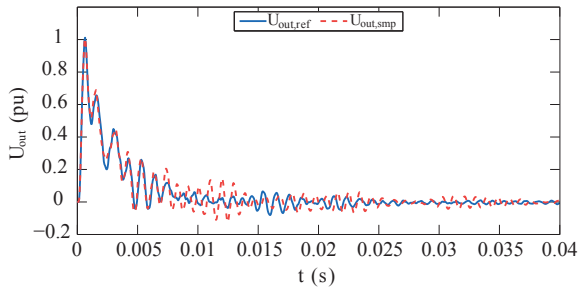


Figure 4.7: Comparison of output voltage and at the busbar in Bleiswijk between "bottom-up" model of case 1 and the reference model.

Table 4.5: "Top-down" overvoltage comparison for two cases: (1) complete Randstad380 Southring and (2) two nearest substations.

		"Top-down" Method					
		BWK	WL	KIJ	MVL	CST	SMH
ΔU_{max} %	Case 1	0.95	0.01	0.37	0.21	0.88	0.82
	Case 2	0.91	0.02	-			

Table 4.6: "Top-down" overvoltage comparison for two cases: (1) complete Randstad380 Southring and (2) two nearest substations.

		"Bottom-up" Method					
		BWK	WL	KIJ	MVL	CST	SMH
ΔU_{max} %	Case 1	0.37	0.02	0.44	0.71	0.05	0.16
	Case 2	1.15	0.02	-			

4.1.4 Accurate representation of harmonic behaviour

The main objective of this section is to investigate the necessary modeling depth for accurate representation of the network harmonic behavior at the substations

adjacent to the UGC connection in Randstad south-ring. For this study the "top-down" method is employed where the comparison indicators are the frequency shift of the resonances (up to 2 kHz) and the harmonic impedance magnitude deviation at the first parallel and series resonance peaks.

Effect of HVDC filters

Before starting with the iterative process the effect of HVDC filter modeling is separately investigated [99]. Two large HVDC converter stations exist in the Dutch EHV grid, namely BritNet which is a DC connection between United Kingdom and Netherlands and NorNed which is a DC connection between Norway and Netherlands. BritNed filters are situated at Maasvlakte (MVL) substation which is relatively close to the connection of interest, while NorNed filters are situated at substation Eemshaven (EDC) which is far away from the south-ring cable connection (see Fig. 4.2).

For the reference model, the HVDC filters (mostly C-type filters) of both connections were explicitly modeled using lumped RLC components. In order to investigate the effect of ignoring an explicit modeling of the filters, the HVDC side was modeled as an RC load based of the powerflow at the point of connection. The effect of such simplification on the network harmonic impedance at substations WTR and BWK is demonstrated in Fig. 4.8. It can be seen that the use of a simplified powerflow model in BritNed causes major changes in the network harmonic impedance of both substations. More specifically, there is a frequency shift of approximately 100 Hz of the main parallel resonance peak. The simplification applied in NorNed had almost no effect on the impedance of the network. Thus, it is evident that explicit modeling of HVDC filters is necessary when a converter station is situated nearby the connection of interest while for faraway filters a simplified model based on the powerflow is adequate.

"Top-down" method for accurate harmonic behavior

For the investigation of the modeling depth needed in order to accurately represent the harmonic behavior of the network the "top-down" approach is utilized. The comparison indicators for this study are the frequency shift of the main resonances up to 2 kHz and the impedance magnitude deviation of the two parallel resonance peaks. The magnitude deviation of the main series resonance peak close to 1 kHz is not considered since it approaches zero and the relative deviations will always be large and it would be a false indicator of inaccuracy. It is considered sufficient if the impedance magnitude deviation of the resulting model at both substations WTR and BWK deviates less than a

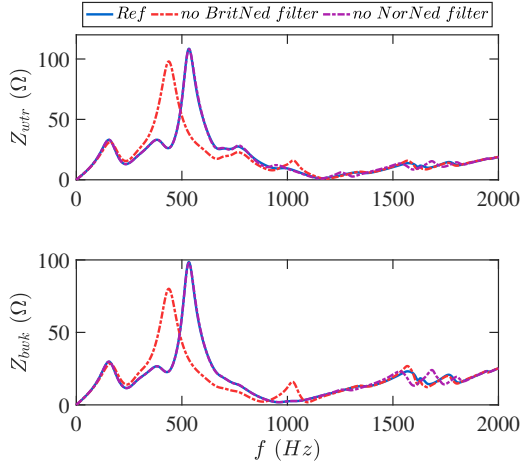


Figure 4.8: Comparison of harmonic impedance at substations WTR and BWK for simplified HVDC filter models of BritNed and NorNed.

specific percentage chosen as 5% from the magnitude of the same substation in the "reference" model and the deviation of the frequency shift at the same locations is less than 3% (meaning that for low order harmonics the absolute frequency difference is around half harmonic order) compared with the reference.

The number of connections that need to be modeled as well as the type of modeling for each connection are shown in Table 4.7. Even though the two results are not directly comparable, it is observed that the number of connections which can be omitted and replaced with a short-circuit equivalent is less than the ones resulting from the method when the maximum overvoltage was of interest (see Table 4.4). The harmonic impedance magnitude and phase comparison between the resulting simplified model and the reference model can be seen in Fig. 4.9 for BWK and WTR substations.

4.2 Network extent across voltage levels

The modeling extent of the HV and EHV network at the same voltage level, when large UGCs are integrated in the grid, has been investigated in the previous section and also in existing literature [92, 93]. The literature on the extent and model type of the downstream network and its effect on the harmonic impedance is less extensive. In [100] it is stated that for the assessment of the harmonic impedance in EHV networks an accurate model for at least the complete primary network is needed. It is also recommended to consider the loads on the secondary

Table 4.7: Results for the "top-down" method for maximum impedance magnitude deviation of 5% and frequency shift deviation of 3% in substations WTR and BWK.

Lines	Line model type	Lines	Line model type
25: MEE-EEM	Sc Equivalent	12: DIM-LLS	FD
24: DTC-DOD	Sc Equivalent	11: DIM-OZN	B
23: DTC-HGL	Sc Equivalent	10: GT-EHV	B
22: BMR-DOD	Sc Equivalent	9: GT-KRK	B
21: ZL-MEE	Sc Equivalent	8: CST-SMH	B
20: ZL-HGL	Sc Equivalent	7: KIJ-DIM	FD
19: MBT-BMR	Pi	6: KIJ-GT	FD
18: ENS-ZL	Sc Equivalent	5: KIJ-CST	FD
17: LLS-ENS	Sc Equivalent	4: MVL-SMH	B
16: MBT-EHV	Pi	3: BWK-KIJ	FD
15: KRK-BSL	Pi	2: WL-MVL	B
14: KRK-ZVL	Pi	1: WTR-WL	FD
13: BVW-OZN	Pi		

transmission network in order to decide whether they should be modeled in detail or only as an equivalent network. If the loads are placed directly on the secondary side of the transformer their effect on damping can be overestimated by simplified modeling of the downstream network. However, no further guidelines or proper equivalent models are proposed. In [101] it was concluded that the load model is important and the harmonic impedance changes if equivalent circuits directly connected at the secondary side of the transmission transformer are used. In [101] only the downstream network was modeled to illustrate how each component influences the harmonic impedance of the network seen from the HV side of the transformer.

4.2.1 Downstream network benchmark

The downstream network is defined as the complete network from 150 kV down to the LV customers and it consists of the 150 kV, 50 kV, 10 kV and 400 V links and the adjacent transformers. The size of such a network is enormous with high complexity. Moreover, the lower voltage network has many operators, which makes it virtually impossible to gather all the information needed. The current downstream benchmark model, developed for this study, is based on known parts of the Dutch grid where from the 10 kV feeders and down an aggregated model was used.

In the base case the transmission lines and cables at 150 kV were modeled using

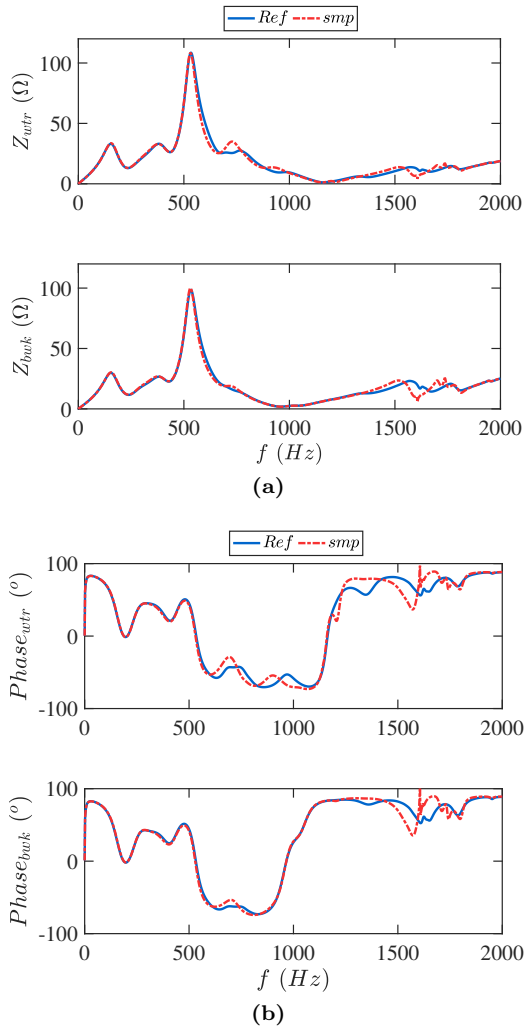


Figure 4.9: Harmonic impedance (a) magnitude and (b) phase comparison between the resulting simplified model and the reference model for WTR and BWK substations.

FD phase models where for the cables also their sheath bonding (cross-bonded) was taken into account. For the cables at lower voltage levels nominal Pi models were utilized. The transformers were modeled with their leakage and magnetizing inductance, copper and iron losses as in [101]. Moreover, capacitor banks are connected to some of the 10 kV substations and are modeled as ideal capacitors.

The loads were modeled as parallel RLC circuits where the values of R and L are obtained from the apparent power and power factor and C is related to the household electronic equipment. According to [102] for a domestic customer (without PV) this capacitance is between 0.6 and 6 μF . For this study an average value of 3 μF was used. The example downstream network, as well as the amount of components used in this study are shown in Fig. 4.10.

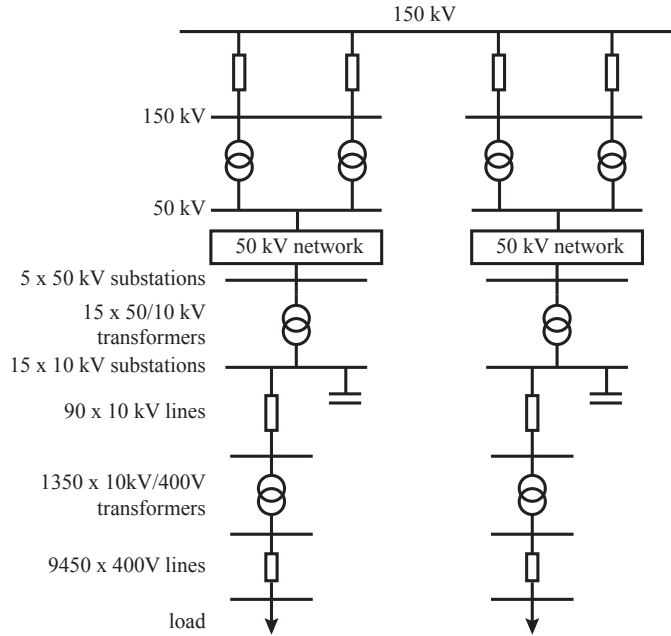


Figure 4.10: *Downstream network benchmark model.*

4.2.2 Sensitivity analysis

In this section, a sensitivity analysis is performed for some of the downstream network components to evaluate their effect on switching transients and to identify which component has the most dominant impact and needs to be most accurately modeled.

Type of 150 kV transmission lines

The benchmark downstream network consists of four 150 kV transmission links and is connected to substation WTR while in all other 380 kV substations no

loads are connected. In general the 150 kV network can consist of both OHLs and UGCs. The effect of the downstream network type is investigated using the following cases:

- **No load:** No downstream network is connected
- **OHL:** Four overhead transmission lines.
- **Cable:** Four underground transmission cables.
- **Mixed:** Two overhead lines and two underground cables.

Two different network configurations were considered:

1. The white circuit is energized from WTR side while the black circuit is out of service.
2. The white circuit is energized from WTR side while the black circuit is in service.

The results are evaluated in frequency domain, using frequency scans for both configurations. In Fig. 4.11 it can be observed that there is a difference in both the magnitude and the frequency of the first parallel resonance. This difference is higher when the black circuit is out of service. For higher frequencies no significant differences are observed. For the case where the black circuit is out of service a switching action is performed at $t = 0.085$ s (when phase A is at its maximum) and the voltage waveforms of phase A at substation WTR and the open end of the connection at BWK are shown in Fig. 4.12. The oscillation frequency and damping as well as the maximum overvoltage differ significantly, as illustrated in Table 4.8. Waveforms are compared both at the sending and at the receiving end of the white circuit when the black circuit is in service. The results for the voltage waveforms are similar as the ones shown in Fig. 4.12, but the difference in the overvoltage magnitude is smaller (see Table 4.8).

Table 4.8: *Overvoltage magnitude for different 150 kV network types with black circuit out of service and in service.*

	Black out of service		Black in service	
	V_{wtr} (pu)	V_{bwk} (pu)	V_{wtr} (pu)	V_{bwk} (pu)
No Load	1.86	1.81	1.42	1.33
OHL	1.79	1.69	1.39	1.29
Cable	1.65	1.46	1.46	1.25
Mixed	1.62	1.41	1.45	1.24

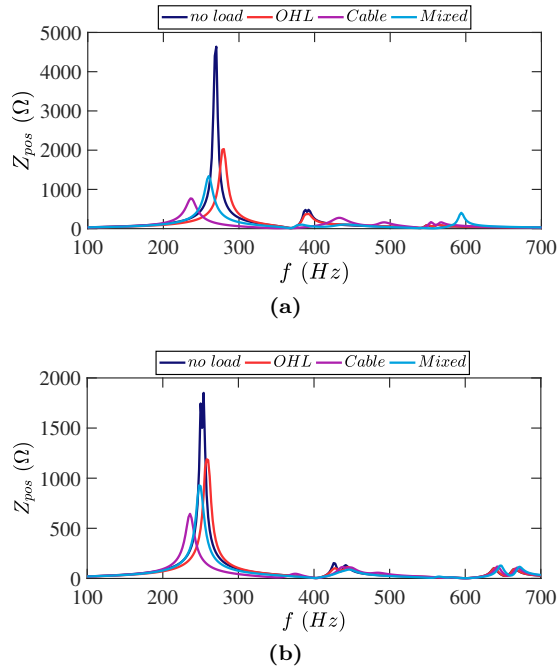


Figure 4.11: Harmonic impedance comparison at Wateringen for different 150 kV network types when (a) the black circuit is out of service and (b) the black circuit is in service.

The sensitivity analysis is further evaluated for the mixed 150 kV case with black circuit out of service since it is more sensitive to changes in the downstream network. This situation also gives the highest overvoltage and therefore is the one of most interest for insulation coordination.

Model detail of 150 kV network

For the 150 kV links FD models were used with the cables sheath cross-bonded every 1.4 km. Modeling of the cross-bondings (C-B) requires the use of small cable segments (1.4 km) which in EMTP software translates into small time steps and long simulation time. Simplifications on the type of line modeling are evaluated and three simplified models are compared:

- FD model using both-ends bonding.
- Bergeron (B) model using both-ends bonding.

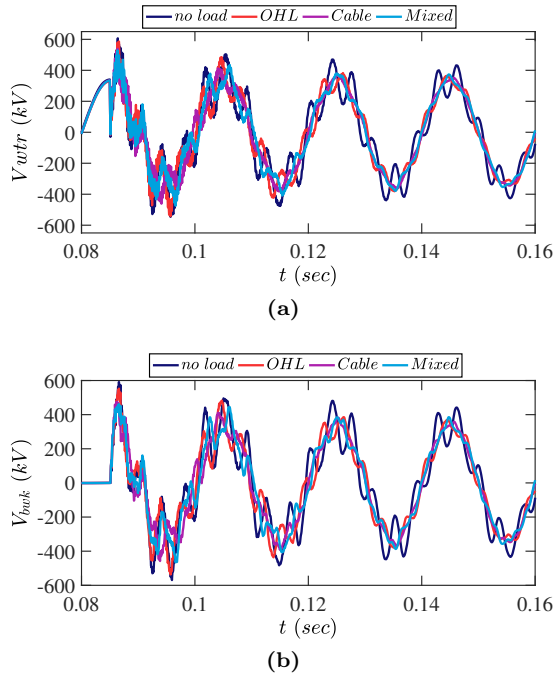


Figure 4.12: Voltage response during energization for different 150 kV network types at (a) substation Weteringen and (b) at receiving open end of the white circuit in Bleiswijk

- Single Pi model for each line.

Fig. 4.13 demonstrates the harmonic impedances of the simplified models compared to the base case and Table 4.9 the maximum overvoltages. It can be concluded that the use of a single Pi model for 150 kV links instead of a fully detailed FD model has no significant effect on both the harmonic content and the maximum overvoltage of a switching action.

End-customer load model

A sensitivity analysis in the resistive and capacitive part of the end-customer load is performed to see whether changes in the LV load affect the EHV response. From the frequency scans (Fig. 4.14) it is observed that these changes result only in a change in the impedance magnitude, but the frequency of the parallel resonance is hardly affected. Moreover, from Table 4.10 it is clear that changes in the LV load have insignificant effect on the maximum overvoltage.

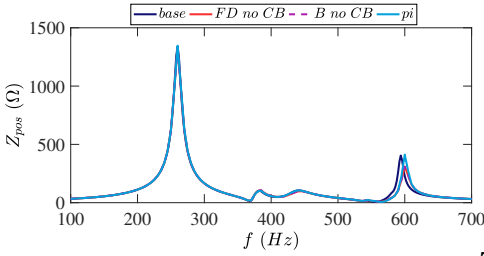


Figure 4.13: Harmonic impedance comparison at Waterningen for different 150 kV model simplifications.

	V_{wtr} (pu)	V_{bwk} (pu)
Base	1.62	1.41
FD no C-B	1.61	1.40
B no C-B	1.63	1.40
Pi	1.62	1.42

Table 4.9: Overvoltage magnitude for different 150 kV line models with black circuit out of service; where C-B refers to cable cross-bonding.

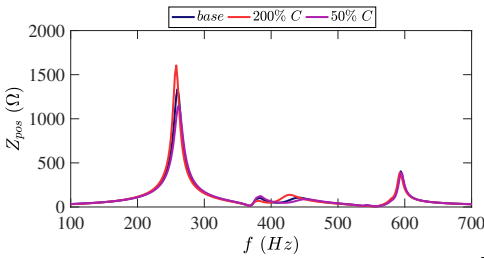
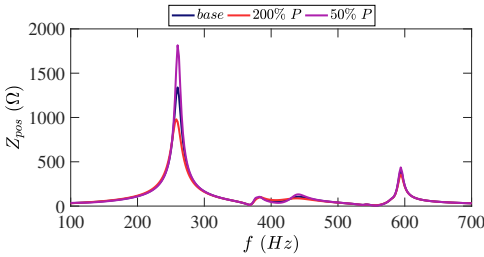


Figure 4.14: Harmonic impedance comparison at Waterningen when the load active power demand (top) and the load capacitance (bottom) change.

	V_{wtr} (pu)	V_{bwk} (pu)
Base	1.41	1.62
200% P	1.40	1.60
50% P	1.42	1.63
200% C	1.42	1.63
50% C	1.41	1.61

Table 4.10: Overvoltage magnitude for different load model values with black circuit out of service; where P is the end user power consumption and C is the household capacitance.

4.2.3 Simplified downstream network model formulations

In order to investigate the effect of simplifications in the formulation of the downstream network model a more complete network than the one used in the sensitivity analysis is utilized. To this end a part of the 150 kV Dutch grid, close to the WTR-BWK connection, is modeled including overhead lines and

cables as well as transformers from HV to MV. At the secondary side of these transformers parallel RL loads are connected with values based on the powerflow. This model is referred to as the detailed model. For this study the Zuid-Holland (see Fig. 4.15a) and Noord-Holland (see Fig. 4.15b) part of the 150 kV network were modeled. In Fig. 4.15 the 150 kV lines and substations are indicated with blue color while for the 380 kV substations red color is used. The Zuid-Holland part includes the 150 kV network that is connected to the 380 kV substations of Randstad south-ring, where the mixed UGC-OHL connection of interest is situated. The Noord-Holland part of the 150 kV network extends from nearby BWK to the northern part including substations BVW, OZN and DIM.

Two types of simplified models were developed which were directly connected to the secondary side of the transmission transformer (380/150 kV) and are presented in Fig. 4.16. The model shown in Fig. 4.16a (*simp 1*) is the simplest one and is based on the loadflow results of the fully detailed case. The values of R and C or L (depending on whether the powerflow is capacitive or inductive) are calculated by (4.4) and (4.5).

$$R_p = \frac{V^2}{P} \quad (4.4)$$

$$X_p = \frac{V^2}{Q} \quad (4.5)$$

The derivation of the RLC values for the model in Fig. 4.16b (*simp 2*) is performed in four steps:

- First, a powerflow calculation of the fully detailed model is run to determine the active and reactive power at the 150 kV side, P_1 and Q_1 .
- For the second step all the HV/MV transformers and loads are ignored and a powerflow analysis is performed, containing only the transmission lines at the 150 kV level. The resulting reactive power, Q_2 , in each substation mainly represents the equivalent capacitance of the lines and C_{eq} is calculated using (4.5).
- Then, from the fully detailed model all the active power demand of the load is ignored and a powerflow calculation is run again. The calculated reactive power, Q_3 , is subtracted from Q_2 and the resulting reactive power, Q_4 , is the contribution coming from the transformer and load inductance.
- Finally, the values of $R_{s,eq}$ and $L_{s,eq}$ are calculated using (4.6) and (4.7).

$$R_{s,eq} = P_1 \frac{V^2}{P_1^2 + Q_4^2} \quad (4.6)$$

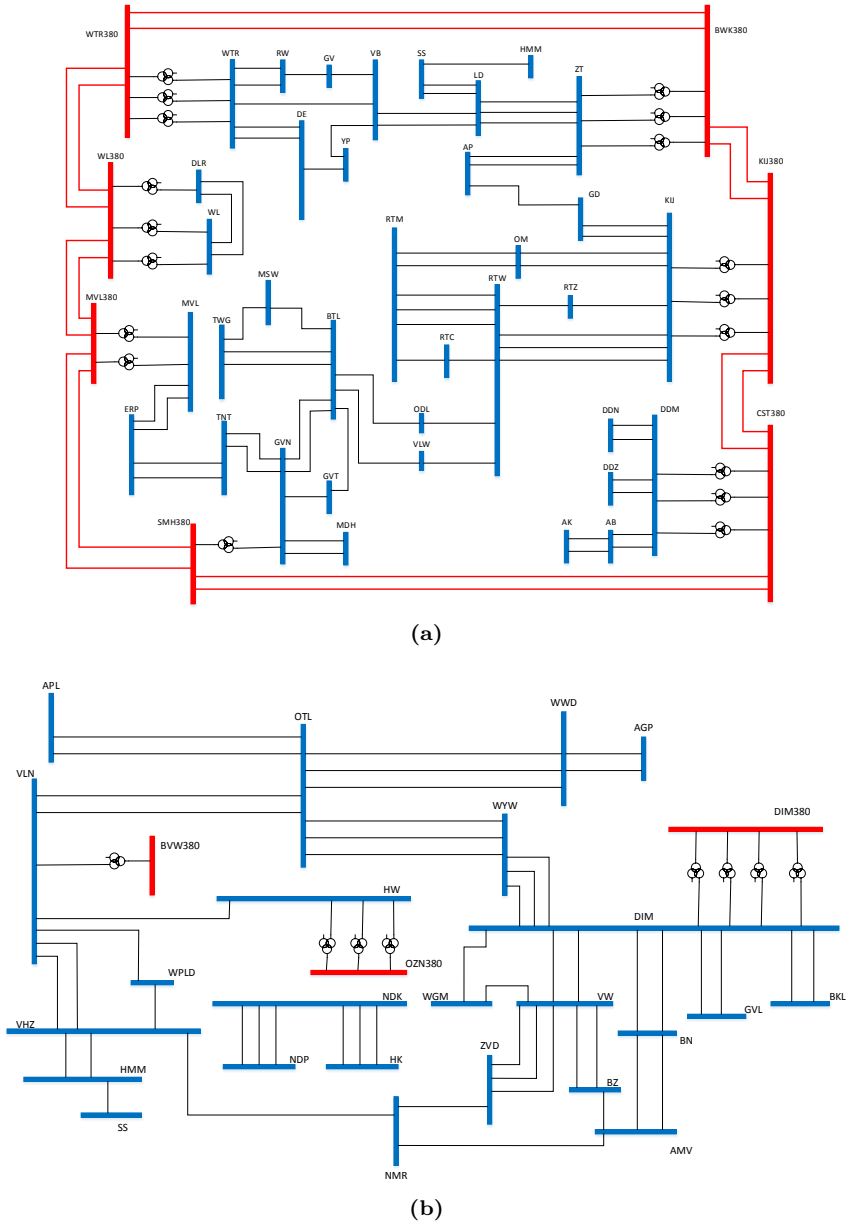


Figure 4.15: Single-line drawing of (a) the Zuid-Holland and (b) the Noord-Holland part of the 150 kV network.

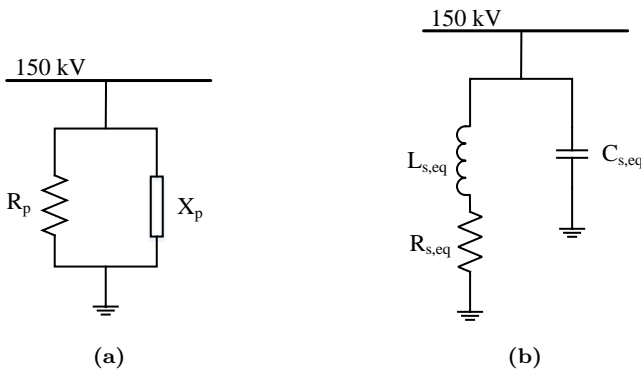


Figure 4.16: Simplified models for the downstream network where in (a) *smpt 1* the elements values are calculated from the powerflow at the 150 kV side of the transmission transformer while in (b) *smpt 2* the aggregated transformer inductance and cable capacitance of the downstream network are separately considered.

$$\omega L_{s,eq} = Q_4 \frac{V^2}{P_1^2 + Q_4^2} \quad (4.7)$$

4.2.4 Downstream network model comparison

The three downstream network models (the reference and the two equivalent models of Fig. 4.16) are compared both in frequency and time domain at the 380 kV side to investigate the effect of simplifications at lower voltage networks.

Frequency domain comparison

The frequency domain comparison is performed using frequency scans for the harmonic impedance at substations WTR and BWK for frequencies up to 2 kHz. The comparison is shown in Fig. 4.17. It is evident that the use of a simplified model for the downstream network results in deviations in the harmonic impedance mainly in the low frequency range. The use of simplified models produce more damping and a slight frequency shift at the first resonance peak at about 150 Hz. The frequency of the first parallel resonance of *smpt 1* is increased by 8 Hz and for *smpt 2* is decreased by 16 Hz, while the resonance peak magnitude of *smpt 2* is closer to the reference model. Furthermore, the second parallel resonance at 600 Hz is represented in all three models but for both

smp 1 and *smp 2* the magnitude is higher. The harmonic impedance of *smp 2* contains an additional resonance peak at about 680 Hz which corresponds to the resonance circuit formed between the equivalent load inductance and capacitance. For frequencies higher than 800 Hz (up to 2 kHz) the impedances of all three models are almost identical.

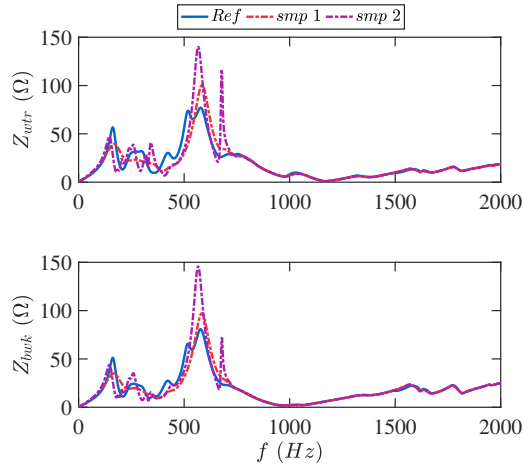


Figure 4.17: Harmonic impedance comparison at WTR (top) and BWK (bottom) for different downstream network model simplifications

Time domain comparison

In order to identify the effect of the difference in harmonic impedance between the three different models in time domain and more specifically in the maximum overvoltage magnitude a statistical overvoltage study is employed [103]. The switching overvoltages are statistical in nature and their values highly depend on the following two parameters [104, 105]:

1. The point-on-(voltage)wave (POW) when the circuit breaker (CB) receives the closing command.
2. The CB's pole span. In a three-phase system, the three-phase contacts of a circuit breaker usually close asynchronously, even if they receive the closing command simultaneously.

In general it is assumed that the POW when the CB receives the closing command may occur at any point of the power frequency cycle with equal likelihood (i.e. it

is uniformly distributed). The closing time of each individual pole after receiving the command is randomly selected according to a probability distribution, which in this case is the normal (Gaussian) distribution. If the closing is described by a normal distribution, two steps are necessary: first a uniform random number is generated to obtain the closing command point; second, a new random generation according to a normal distribution is performed to obtain the closing time of each individual pole [103].

The values of the two uncertainties in timing considered for this study are:

- mean switching timing: 20 timings uniformly distributed over one power cycle;
- closing timing difference between phases: 20 timings normally (Gaussian) distributed around each mean switching timing with a standard deviation of $\sigma = 0.33$ ms.

For this statistical energization study, four types of switching actions were performed:

- S1: Energization of the black circuit from WTR side while the white circuit is out of service.
- S2: Energization of the black circuit from WTR side while the white circuit is in service.
- S3: Energization of the black circuit from BWK side while the white circuit is out of service.
- S4: Energization of the black circuit from BWK side while the white circuit is in service.

For all switching actions the simulated overvoltages were calculated at four locations: WTR, OSP14, OSP32 and BWK. For each switching action the maximum overvoltages among the four measured locations were observed at the far open end, i.e. when the energization was performed from WTR side the maximum overvoltage was observed in BWK while, when the energization was performed from BWK side the maximum overvoltage was observed in WTR. In this section the results of the worst cases for each switching action are shown. For S1 and S2 overvoltage results at BWK are shown while for S3 and S4 overvoltage results at WTR are presented. The results of the four locations for all switching actions are included in Appendix B.

The maximum overvoltage histograms at BWK for S1 and S2 are shown in Fig. 4.18. For S1 (Fig. 4.18a and Fig. 4.18b) the overvoltage histogram of *smp 1*

is shifted to lower values compared with the reference model while the opposite is observed for *smp 2*. On the other hand, for S2 (Fig. 4.18c and Fig. 4.18d) both the highest and the lowest maximum overvoltages are similar between the three models.

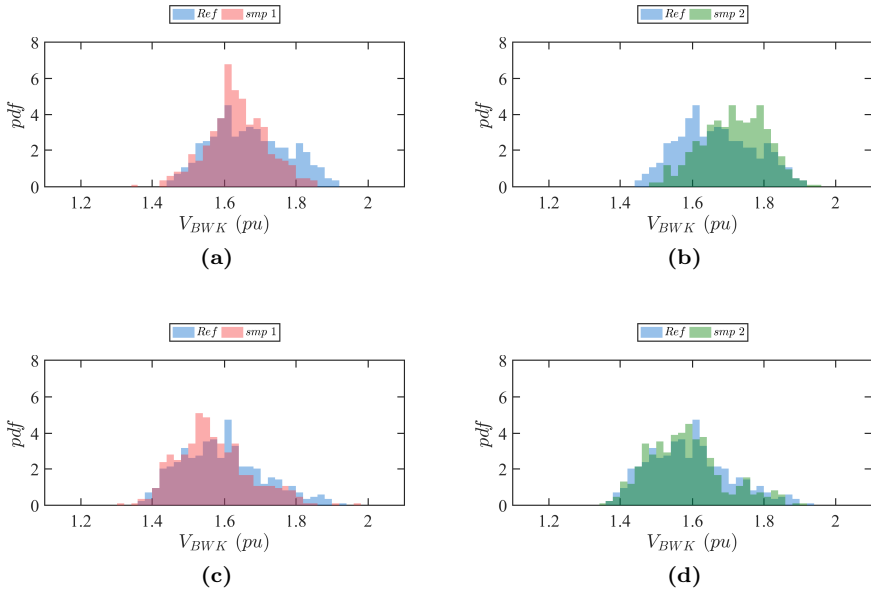


Figure 4.18: Histogram plot comparison of the maximum switching overvoltage at substation BWK between the reference (a) *smp 1* and (b) *smp 2* model for S1 and (c) *smp 1* and (d) *smp 2* model for S2.

The maximum overvoltage histograms at WTR for S3 and S4 are shown in Fig. 4.19. For both types of switching actions the maximum overvoltage of the reference model has slightly shifted to higher values.

Normal distributions are fitted to the resulting overvoltages and the results are presented in Fig. 4.20. For S2, S3 and S4 the reference model demonstrates the highest mean value and standard deviation meaning that it extends to higher overvoltage values compared with the two simplified models. However, the deviations in the mean values and standard deviations between the models do not exceed 3% which is less than the standard deviation of each distribution. Different behavior is observed for S1 where larger deviations between the models are present, especially in the standard deviation where the maximum overvoltages of the reference model span to larger interval.

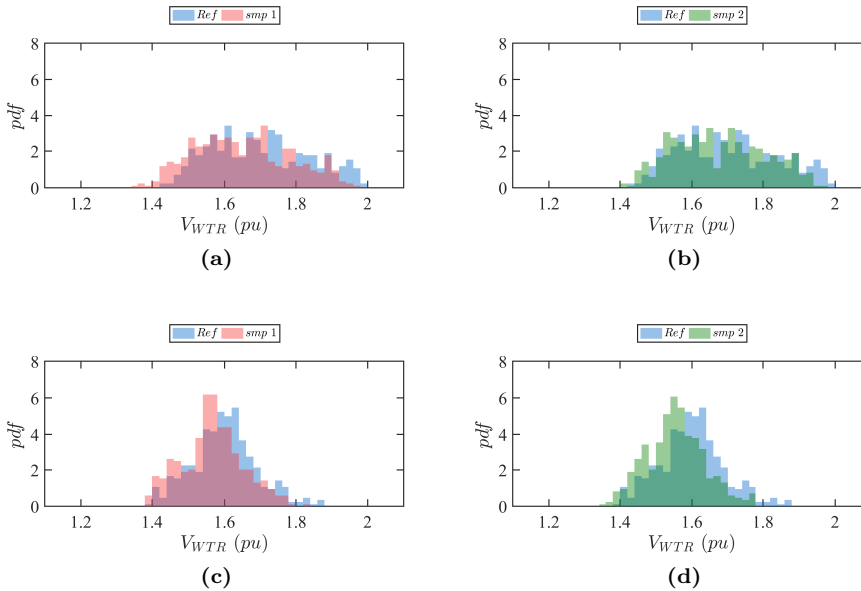


Figure 4.19: Histogram plot comparison of the maximum switching overvoltage at substation WTR between the reference (a) smp 1 and (b) smp 2 model for S3 and (c) smp 1 and (d) smp 2 model for S4.

4.3 Conclusion

For accurate representation of the maximum overvoltage two methods were used to determine necessary modeling depth for adequately predicting a switching surge response in a large-scale network: the "top-down" and the "bottom-up" method. Both methods indicated that it is necessary to include in the model all the lines which are connected to substations, up to about 80 km away in this study from the source of disturbance. It is also important to note that even if the model of the whole network (reference model) is not available the resulting models according to the "bottom-up" approach provide similar required simulation depth with the case where the reference model is available ("top-down" approach). However, even though the current model deviates within the predefined 1% with the previous model a few cases were observed where the deviation exceeded 1% from the reference model. This inaccuracy must be related to differences in the choice of line model type for a few sections, since both approaches agree upon which connections can be replaced by a short-circuit equivalent. This observation suggests that one can define a reduced size reference network, up to a distance of

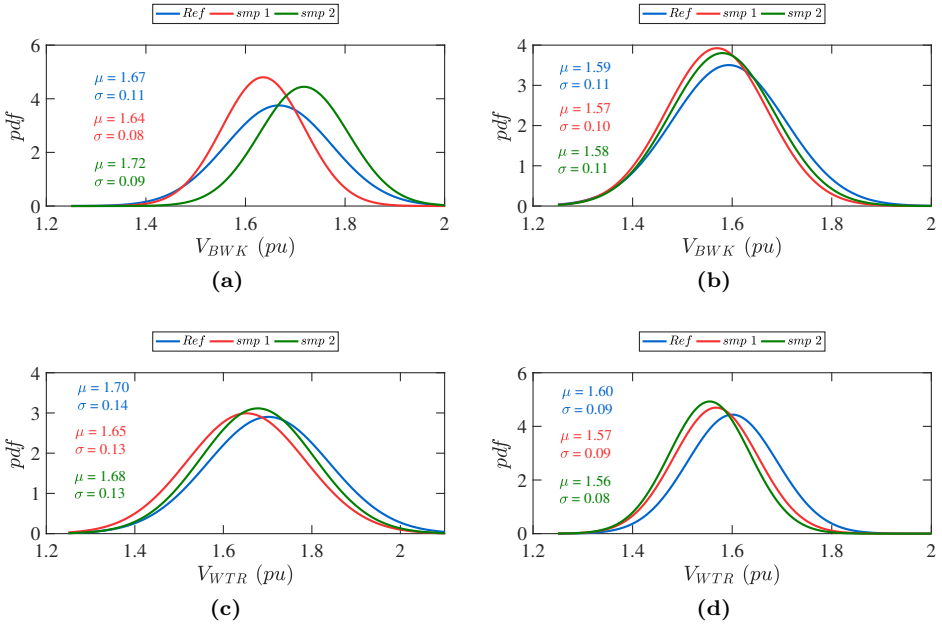


Figure 4.20: Fitted normal distributions comparison of the maximum switching overvoltage (a) at BWK for S_1 , (b) at BWK for S_2 , (c) at WTR for S_3 and (d) at WTR for S_4 .

at least 80 km, where all connections are represented by FD models. It can serve as a local reference to study further simplification and its effect on overvoltage prediction.

For the accurate representation of the EHV network harmonic behavior, for frequencies up to 2 kHz, the effect of explicitly modeling HVDC filters was examined. It was concluded that HVDC filters located nearby the connection of interest greatly affect the frequency and magnitude of the resonance peaks in the low frequency range (below 1 kHz) and thus, accurate modeling is required. On the other hand, HVDC converter stations having a large electrical distance from the point of interest can be modeled as a parallel PQ load based on the powerflow without loss of accuracy in the calculated harmonic impedance. Using the "top-down" approach and defining appropriate comparison indicators a simplified network model was formed where the number of connections which should be included is larger than the ones resulted from the maximum overvoltage study.

From the sensitivity analysis regarding the downstream network, it can be concluded that the type of the 150 kV links has a more significant effect on the

switching transient response than the type and value of the end customer load. The 150 kV lines affect both the damping and the frequency of the energization as well as the maximum overvoltage produced during the first moments of the switching action. On the other hand, the end customer load model affects only the damping of the oscillations and only slightly affects the maximum overvoltage. Furthermore, the model detail of the 150 kV connections has almost no effect in both the harmonic impedance and the maximum overvoltage. Thus, the lower voltage lines can be modeled with a single Pi model without loss in accuracy. The effect of model simplifications was evaluated both in time and frequency domain. From the frequency domain it is evident that both simplified models produce more damping at the first resonance peak but the dominant frequency is close to the detailed model. From the time domain results it can be concluded that both simplified models present good agreement with the reference model for several types of switching actions and locations.

5

Simulation Model Validation with Measurements

It is of utmost importance to develop accurate simulation models since they are the tool for conducting grid development and system operation studies. However, mathematical models of network components include simplifications compared to the physical reality. Thus, it is necessary to verify that the behavior of the network component is accurately depicted in the mathematical representation. This can be achieved by means of comparing simulation results with measurements.

For measuring transient voltages (e.g. during line energization) conventional measurement equipment, such as RC dividers, can be used having an accuracy over the complete measurement chain of typically 5%. However, such measurement equipment can face problems due to disturbing signals, especially at transition points (from OHL to UGC), due to the impedance change which causes high associated currents. The need for a more robust measuring system was raised and a system with open air capacitive sensors using a Differentiating/Integrating principle was utilized instead. The accuracy limits of this alternative measuring system should preferably be at least close to the ones aimed for by conventional measurement equipment, despite the fact that the open-air capacitance values are unknown in advance.

5.1 Differentiating/Integrating measurement

Electromagnetic transients (e.g. from switching, lightning etc.) contain a wide spectrum of frequency components. More specifically, during circuit energizing high overvoltages can arise at the sending and receiving end of the circuit as well as at the transition points between OHL and UGC due to multiple reflections of the voltage wave. Their magnitudes and frequency content need to be measured to make sure that no limit is exceeded and to validate that simulation models correctly predict overvoltage magnitudes.

The installation of high-frequency measurement equipment, such as RC dividers, is costly, leaves a relatively big footprint, should be planned ahead and reliable operation can be easily jeopardised due to electromagnetic compatibility (EMC) issues. Moreover, when continuous online monitoring is not needed, after the simulation model validation there might be no need for having such dedicated measurement equipment installed. In order to conduct three-phase transient measurements at transmission lines already in operation non-intrusive sensors, which can be installed during operation, would be an appealing option.

A not commonly applied method for measuring high-voltage is the open air capacitive sensor measuring system. This system consists of three capacitive pick-up electrodes, used to measure the phase to ground voltage. More specifically, such a measuring system is based on the Differentiating/Integrating (D/I) principle since it probes the time derivative of the phase voltages which can be restored either by numerical integration or by an analog integrator as part of the measuring system. The system is simple, has no special HV components and has a large bandwidth and good EMC qualities.

In Randstad south-ring, transient measurements were performed at three locations: both transition points (OSP14 and OSP32) and 380 kV substation BWK. The measuring system used is based on the aforementioned D/I principle [24, 106–108]. Apart from the easy installation and good EMC properties, challenges can arise during the post processing of the measurements. Since open air sensors are used, in addition to the individual phase aimed at, each sensor also receives parasitic contributions from the other two phases and possibly also from parallel circuits, thus the measuring signal of each phase is coupled to the other phases and measurement decoupling is required.

5.1.1 Measurement principle

The D/I measuring system consists of three capacitive pick-up electrodes, one for each phase, that are used to measure the phase to ground voltage due to the electric field from the overhead lines. The electric field lines from the HV phase conductors induce a current through the capacitive sensor. The configuration of a measurement system for a single phase open air capacitive sensor is shown in Fig. 5.1. A metallic plate (sensor) senses capacitively the electric field from the overhead lines ($C_{1,dif}$) and the value of this capacitance depends on sensor size, distance and possibly on conducting objects in the neighbourhood. As not all layout details of the installation are known, its value can only be roughly estimated beforehand. A measurement cable is connected to the assembly which is characteristically terminated at the far end, R_{dif} . Resistor R_a is a safety precaution to limit the sensor voltage to low values in case the measurement cable termination is not connected yet. Capacitor C_{1E} represents the capacitance between the sensor and ground.

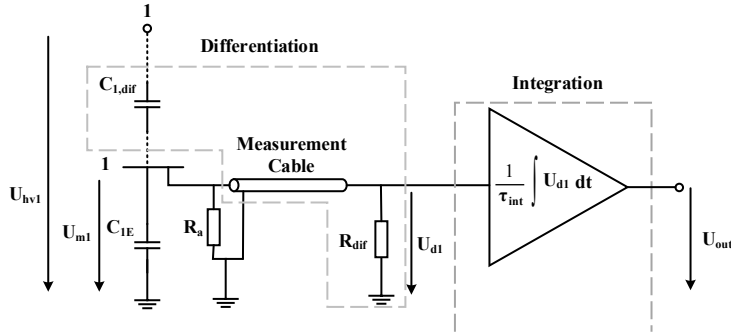


Figure 5.1: Single-phase sensor and D/I measuring set-up.

If R_{dif} equals the characteristic measuring cable impedance then, below the cut-off frequency determined by C_{1E} and R_{dif} , the voltage U_{d1} represents the time derivative of the phase voltage U_{hv1} :

$$C_{1,dif} \frac{dU_{hv1}(t)}{dt} = \frac{U_{d1}(t)}{R_{dif}} \quad (5.1)$$

Therefore, the phase voltage U_{hv1} derives from the integration of U_{d1} . Having an integrator as part of the measuring system, instead of performing digital integration after recording, prevents high induced voltages by very fast transients to damage the digitizer.

The phase voltage including the frequency content above the cut-off equals:

$$U_{hv1}(t) = \frac{C_{1E} + C_{1,dif}}{C_{1,dif}} \int dU_{d1}(t) + \frac{1}{C_{1,dif}R_{dif}} \int U_{d1}(t)dt \quad (5.2)$$

The equivalent capacitance between sensor 1 and ground, C_{1E} , can be obtained by on-site measurement [109]. Alternatively, the sensor can be designed such, that it has a predefined value (see Section 5.1.2).

The combination of the differentiating and integrating parts results in a flat total response with a low and a high cut-off frequency, as depicted in Fig. 5.2. The low cut-off frequency, $f_{c,int}$, depends on the integrator characteristics and the high cut-off, $f_{c,dif}$, depends on the summation of the HV capacitance and sensor capacitance to ground and the terminating resistance. Signal attenuation along the measurement cable and integrator characteristics may also affect the cut-off frequencies. High signal frequencies attenuate when propagating over a long measurement cable and operational amplifiers applied in the integrator have bandwidth limitations.

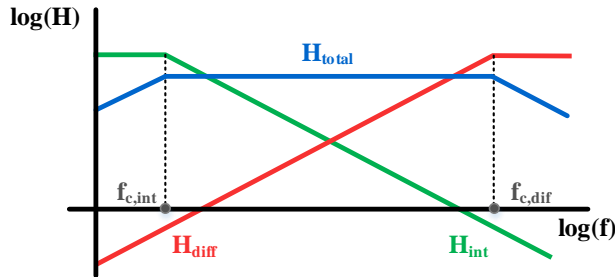


Figure 5.2: Transfer function of a D/I system.

EMC considerations

The benefits of the D/I system are mostly related to its excellent EMC properties. Switching transients at an OHL-UGC transition point are associated with large ground currents at the impedance transition from line to cable at each phase. These ground currents vanish when a symmetric three-phase voltage establishes and the phase currents add up to zero without significant current through the cable shields. However, shortly after transient events such symmetry in the phase voltages is not present.

The magnetic flux from ground currents can induce currents in cabling of secondary equipment. Since induction involves the time derivative of the magnetic flux, steep transients are especially harmful. This imposes a large

demand on the EMC design of measurement equipment and its connections, in particular when situated near transition points. EMC disturbance in signals may exhibit as a small distortion, can dominate the sensor signal and might even damage the equipment.

Disturbing voltages can be induced by magnetic fields from high currents nearby, which couple via the cable transfer impedance. In Fig. 5.3 a basic measurement scheme employing a divider consisting of a high voltage ($Z_{1,div}$) and low voltage ($Z_{2,div}$) arm demonstrates the problem.

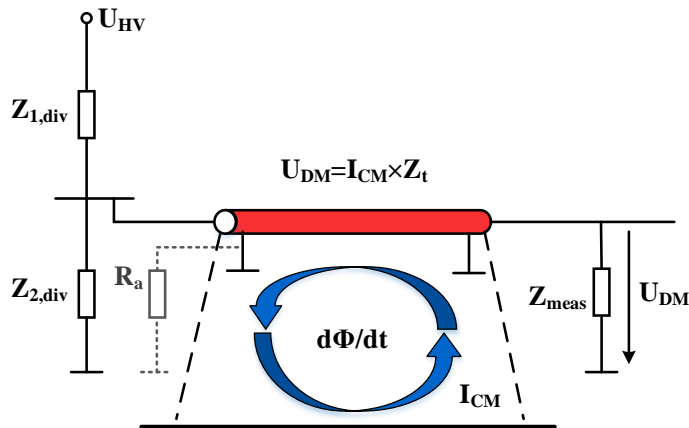


Figure 5.3: Interference by induced currents upon time-varying magnetic flux.

The arrows indicate the induced circulating current entering the measurement cable earth screen as a common mode current I_{CM} . Through the transfer impedance, Z_t , a differential mode voltage, U_{DM} , arises which divides over the impedances at both cable ends. For RC dividers Z_{meas} is relatively high compared to the impedance of $Z_{2,div}$ in order not to load the divider. As a result, most of the disturbing voltage will appear at the measurement side. On the other hand, for the D/I system the measurement impedance, Z_{meas} , is taken equal to the characteristic impedance of the measurement cable (50Ω) while at the divider side the safety resistance R_a in parallel to the impedance $Z_{2,div}$, below $f_{c,dif}$, is much larger. Thus, most of the disturbing voltage will arise at the sensor side, not disturbing the recordings at the measurement side. This significantly improves the immunity of the D/I system against interference by ground currents. In addition, the integration step reduces high-frequency interference which enters the circuit via the measurement cable.

Other precautions to minimize EMC concerns, implemented with the D/I measurement system, are listed below:

- Limit the possibility for ground currents to enter the measurement cables in the first place. This can be accomplished by minimizing the area between the sensor cables to prevent large coupling of magnetic flux from transient currents.
- Usage of high quality secondary cabling having a low transfer impedance. The cable transfer impedance characterizes the voltage arising at the measurement cable terminals upon a common mode current along the cable screen. This voltage will add to the sensor signal.
- Prevent common mode currents to enter the measurement equipment. This can be accomplished by using a common ground plate, or better an EMC cabinet, to which all screens of the sensor cables are connected and also the ground for the equipment power supply. This provides a natural path for common mode currents, preventing them to enter sensitive equipment and disturb its operation.

It should be noted that aforementioned points are essential for any measurement methodology, e.g. also those based on RC dividers, employed in an EMC harsh environment like the OHL-UGC transition point.

5.1.2 Measuring system set-up

Sensors were designed specifically for measurements at the Randstad south-ring connection. Each open-air sensor consists of two parallel square metallic plates with sides of 30 cm and 0.5 cm distance separated with Teflon insulation. The top plate senses the electric field while the bottom plate is earthed. The size of the sensor is chosen to obtain about 1 pF coupling capacitance. An RG218 cable is connected to the assembly which is characteristically terminated with 50Ω at the far end. Safety resistor R_a is taken $68 \text{ k}\Omega$ limiting the power frequency sensor signal below 10 V if the terminated measuring cable is not yet connected (assuming $C_{1,dif} \approx 1 \text{ pF}$). Capacitor C_{1E} represents the capacitance between the sensor plates (about 300 pF) and is designed to limit frequency components above the aimed range entering the measurement system. Together with the cable termination, R_{dif} , it provides a high-frequency cut-off of about 10 MHz [106].

In order to restore the transferred signal waveform, integration is performed at the input of the measuring cabinet. The voltage at the integrator input represents the time derivative of the voltage detected by the sensor. The applied integrator has a passive and active part, which are tuned such that it provides an integrating response over a wide frequency range, between 10 Hz and 5 MHz. The integrator design, with integration time constant τ_i of $20 \mu\text{s}$, is described

in detail in [110]. The output signal of the integrator is recorded by a 12-bit digitizer at 5 Msample/s with its bandwidth settings chosen to cut off frequencies above 20 MHz. The sensor design as well as the integrator for the conducted measurements are demonstrated in Fig. 5.4.



Figure 5.4: (a) Capacitive sensor design stand-alone; (b) Integrator cabinet including the passive and active integrator parts connected to a 12 bit, 4-channel digitizer.

The full response of the D/I system is determined through calibration.

Integrator Calibration

By means of a Network Analyzer (NA), the employed integrators were tested. A capacitance of 100 pF was used to mimic the capacitive coupling from the overhead lines. This value is about hundred times larger than what is actually expected from coupling to the 380 kV lines. On the other hand the NA signal magnitude is a few hundred thousand times smaller. The signals from calibration therefore have typically an amplitude of few thousands time less (over 60 dB) than during the actual measurement.

The results for the three channels with the specific integrator used prior to the actual measurement (dashed line) and after performing the field measurement (continuous line) are shown in Fig. 5.5. The measurement cable lengths used for the calibrations were 5 m for all channels before the field measurements; actual lengths at the OSPs were used for the calibration after the field measurements. These lengths were 50 m, 35 m and 25 m for channel 1, 2 and 3, respectively. The oscillations in the phase angles reflect that the wavelength of the applied signal fits (multiple times) within the cable length: peaks arise at frequency differences of v/L , with L the cable length and v the signal velocity (200 m/ μ s). As demonstrated in Fig. 5.5 the transfer function of the D/I system has its -3 dB point at 7 MHz. For EHV dividers it is hardly possible to reach such bandwidth,

due to their size.

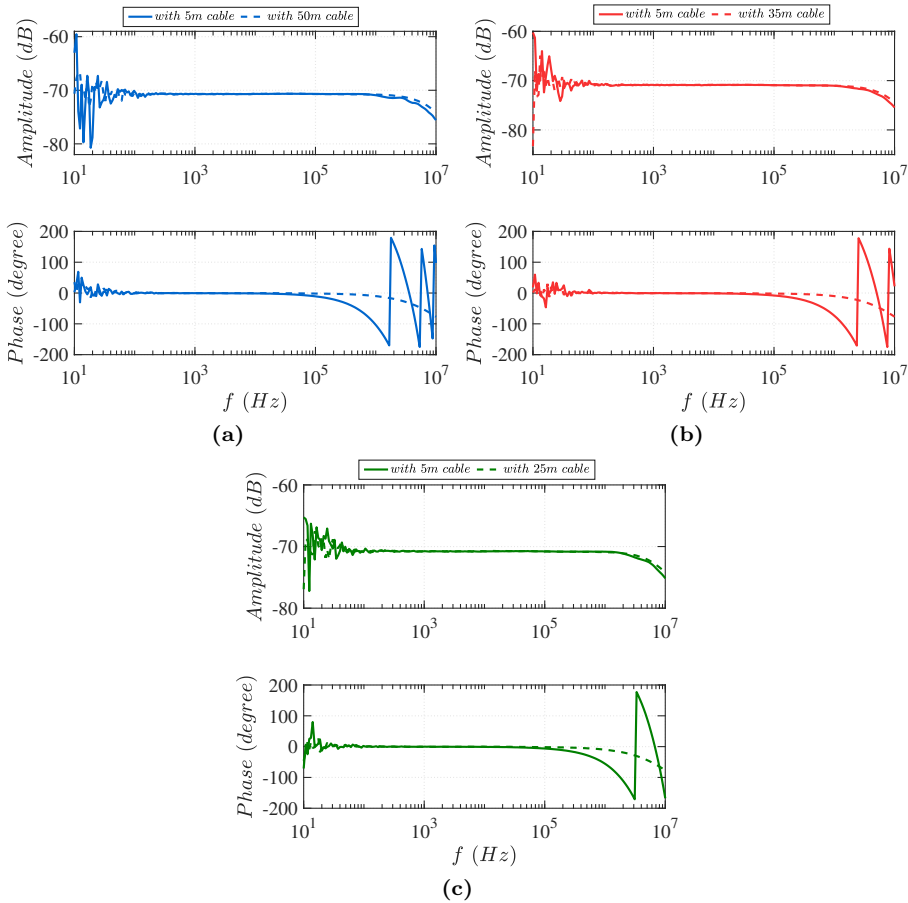


Figure 5.5: Calibration result of D - I measurement chain using 100 pF capacitance value inserted as differentiating capacitor for (a) channel 1, (b) channel 2 and (c) channel 3 of the integrator as a function of the frequency and measurement cable lengths.

At low frequencies the differentiated signal before integration is very low and impeded by noise. Therefore, calibration was repeated after increasing the 100 pF capacitance to 10 nF , resulting in 40 dB increase in signal. The curves in Fig. 5.6 represent the response from the three channels over the frequency range of 5 Hz to 10 kHz . There is a small resonance near 5 Hz , but at 10 Hz the deviation from a straight response is below 3 dB . Parallel RC dividers have an advantage here

as their response includes DC.

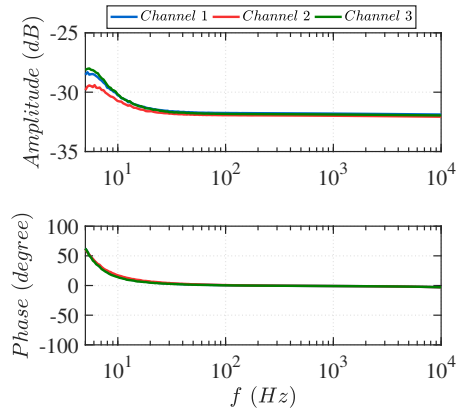


Figure 5.6: Calibration result of D - I measurement chain using 10 nF capacitance value inserted as differentiating capacitor and 10 m of measuring cable.

5.1.3 Measuring system placement

Measurements were performed at two distinct locations, the OHL-UGC transition points and substation BWK, for which the sensor placements differ significantly. The situation at a transition point and at substation BWK before the placement of the sensors is shown in Fig. 5.7.



Figure 5.7: (a) Representation of the transition point configuration; (b) configuration of one circuit at substation BWK.

For the case of the transition points each sensor is positioned in between the two cable terminations belonging to the same phase. In this location the distances

between the phases are relatively large (12 m) which implies small coupling of the sensors to the other phases. Moreover, this configuration further prohibits the cross-coupling since the terminations at both sides screen the electric fields from the other phases. The sensors were placed at the center of the two cable terminations and at the same height in order to achieve a symmetric configuration which is useful for the formulation of the decoupling matrix. The sensor placement of phase A is demonstrated in Fig. 5.8a and is exactly the same for the other two phases.

For substation BWK, the sensors were placed nearby the bushings on the SF₆ insulated GIS. The sensor placement of all three phases is shown in Fig. 5.8b-5.8d. The sensor positioning was such that significant cross-coupling could not be avoided. The two sensors placed at the sides profit from screening against cross-coupling from the metallic GIS structure, but the distance to it was rather large, reducing the screening effect. By mounting the side sensors directly against the metal structure of the GIS just beneath the bushings better screening would be obtained, but that would have required complete de-energization of the system just for the sensor installation.

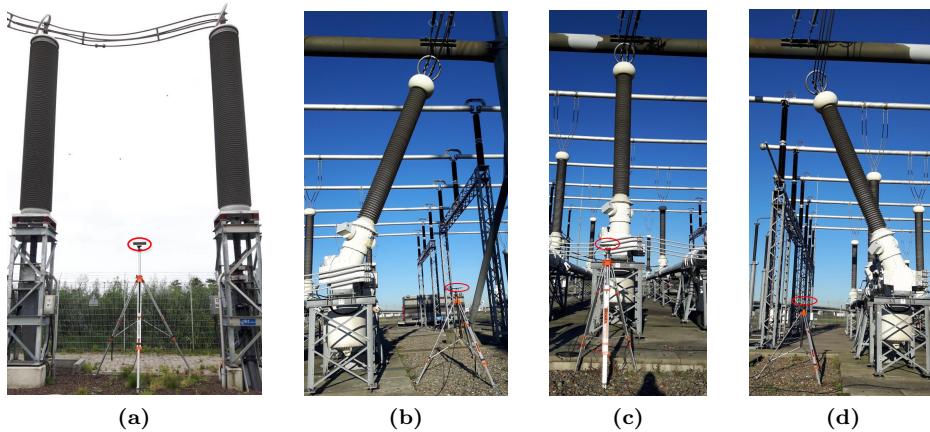


Figure 5.8: *Sensor placement at (a) phase A of transition point, (b) phase A, (c) phase B, (d) phase C of BWK.*

5.2 Measurement analysis

Despite the advantages of the D/I measuring system in respect with EMC, it faces the challenge of measurement decoupling. The open-air sensors couple to

all phase conductors (see Fig. 5.9) and voltage reconstruction to unravel this coupling is required.

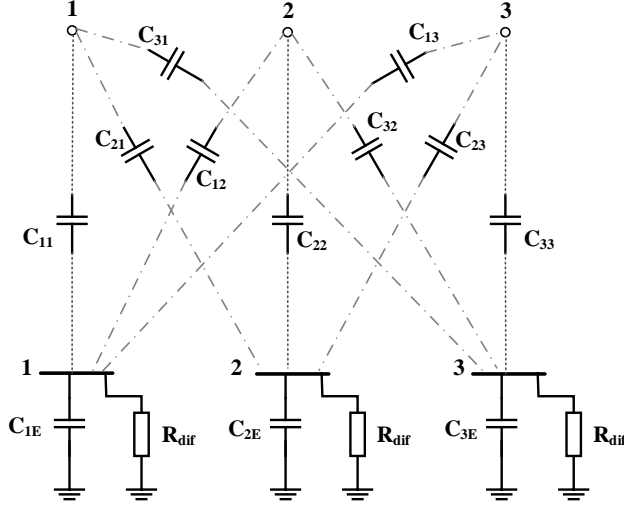


Figure 5.9: Capacitive coupling scheme of the three-phase HV conductors to the sensors.

5.2.1 Measurement decoupling

Since the D/I output voltages are a linear combination of the extra-high voltages a 3×3 coupling matrix can be defined:

$$\begin{bmatrix} U_{out,1} \\ U_{out,2} \\ U_{out,3} \end{bmatrix} = \begin{bmatrix} M_{11} & M_{12} & M_{13} \\ M_{21} & M_{22} & M_{23} \\ M_{31} & M_{32} & M_{33} \end{bmatrix} \cdot \begin{bmatrix} U_{hv,1} \\ U_{hv,2} \\ U_{hv,3} \end{bmatrix} \quad (5.3)$$

where $M_{ij} = \frac{R_{dif} C_{ij,dif}}{\tau_{int}}$, τ_{int} is the integrator time constant and $C_{ij,dif}$ is the capacitance between sensor i and phase j .

Determination of the matrix coefficients is based on comparing the recorded steady-state power cycle signals from the sensors reached after switching with the actual phase voltages. There are different aspects to consider for accomplishing this:

- **Availability phase voltage signals:** In case the actual phase voltages are available, e.g. through voltage transformers or dividers for power frequency

(and harmonics) monitoring, these recordings can be employed. If not, one can assume symmetric phase voltages with nominal amplitudes. Deviations from nominal voltage may introduce errors in the matrix components. However, when considering overvoltages in terms of per unit values this error tends to disappear as both overvoltage and power frequency voltage will have the same relative deviation.

- **Synchronisation of measurements:** The sensor recording is triggered upon the signal of a switching event and the starting time therefore is uncorrelated with the momentary phase voltage angles. Synchronisation can be achieved when this moment can be related to the actual phase angle of (one of) the phase voltages.

The placement of the sensors differ significantly between the location types and subsequently the same applies for the couplings to the phases [106]. The sensor capacitance matrix for both transition points and substation BWK was calculated from 3-D electrostatic field analysis (by means of Coulomb, [111]). The construction detail of the terminations was not available, but the analysis allowed to estimate the output signal amplitude for different sensor sizes and placements. The sensor dimensions were chosen to obtain approximately 1 V output magnitude from the complete D/I system, which is optimal for the available integrators (see Appendix C.1).

For the results presented here, the actual phase voltages were available from an RC divider situated at the WTR substation, but recordings were not synchronised with the measurements. The aforementioned approach cannot provide complete information on all nine matrix components in the coupling matrix in (5.3). By choosing symmetric sensor positions with respect to the phase conductors, the number of independent matrix components reduces. Assumptions and approximations have to be made which are location specific (differ between the OHL-cable transition points and the substation) and their consequences need to be evaluated in terms of uncertainty in the determination of the actual overvoltage. A detailed discussion on error propagation in the decoupling matrix for different situations is provided in [108] (see also Appendix C.2 and C.3).

Decoupling implementation

For the measurement expedition at the Randstad south-ring the voltage waveforms are acquired during ten power cycles, three power cycles prior to the switching event (pre-trigger) and seven power cycles after the event. The switching transient, for all the different measurements, damps out typically within the first two power cycles after the switching, so the last five cycles almost exclusively consist of the steady state voltage (post-trigger). These two voltage

signals, i.e. pre-trigger and post-trigger are the ones used to reconstruct the acquired voltage waveform of each phase with the other two phases as well as other circuits existing in the neighbourhood. The decoupling process used here is accomplished with the following steps:

Step 1 The pre-trigger voltage signal contains the coupling between the three sensors and neighbouring circuits, since no voltage is present in the other phases of the measured circuit. In order to remove this coupling, the pre-trigger signal of all three phases is fitted using least square curve fitting to a function with an offset:

$$v_{pre} = c_k \cdot \cos(\omega t + \phi_k) + b_k \quad (5.4)$$

and the optimal c_k , ϕ_k and b_k are determined. A small offset, b_k , originates from the active part of the integrator. Then the original data are corrected by subtracting the signal above, expanded for the whole acquisition time. In Fig. 5.10 an example of this procedure is illustrated for the same type of switching action captured at substation BWK (Fig. 5.10a and Fig. 5.10b) and at transition point OSP14 (Fig. 5.10c and Fig. 5.10d). For the transition points the sensor could be situated such that the relative pre-trigger contribution was more than a factor ten lower as compared to substation BWK.

Step 2 A base of EHV waveforms for the steady state needs to be defined. This can either be separate measurements captured by another device (e.g. voltage transformer, RC divider etc.) already installed at the measurement location or presumed symmetric three-phase voltages with nominal amplitude of the system at the specific moment of the measurement. This base voltage needs to be synchronized with the post-trigger measurement signal.

Step 3 The post-trigger measurement signal of all three phases as well as the base EHV waveforms are fitted using least square curve fitting to function (5.4) and the optimal c_k , ϕ_k and b_k are determined. Then the D/I measurement data are corrected by subtracting the calculated offset.

Step 4 The decoupling matrix M , defined in (5.3), is calculated using least square fitting for a system of three equations. More specifically, from the previous step six post-trigger sinusoidal voltage signals are calculated through fitting, i.e. three for the D/I measurements, $V_{out1,2,3}(t')$ and three for the base extra-high voltages $V_{hv1,2,3}(t)$, with $t' = t + t_0$ indicating the time correlation between sensor recordings and phase voltages. The D/I measurements are a linear combination of the base extra-high voltages with coefficients the elements of the decoupling matrix.

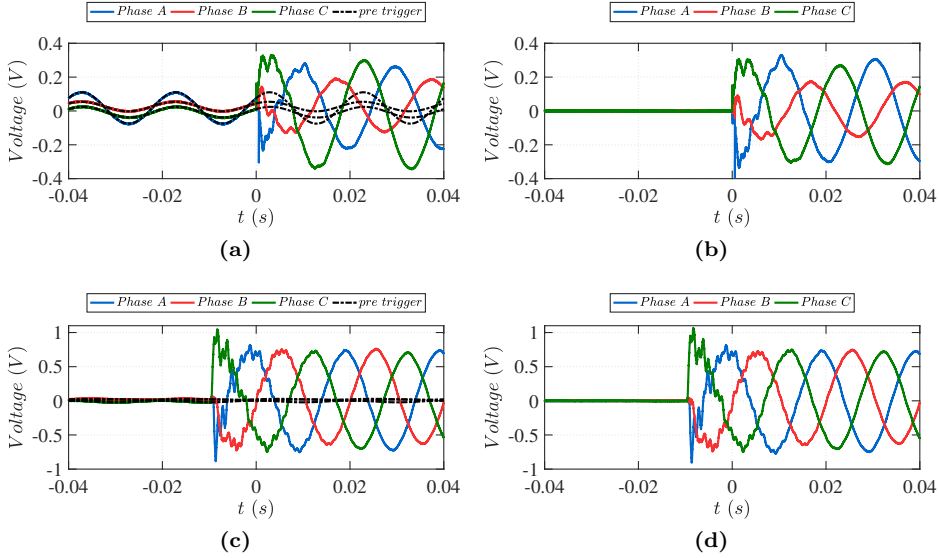


Figure 5.10: Time domain voltage waveform (a) before and (b) after pre trigger correction at substation BWK and (c) before and (d) after pre trigger correction at transition point OSP14.

$$\begin{cases} V_{out1}(t, \phi_0) - M_{11}V_{hv1}(t) - M_{12}V_{hv2}(t) - M_{13}V_{hv3}(t) = 0 \\ V_{out2}(t, \phi_0) - M_{21}V_{hv1}(t) - M_{22}V_{hv2}(t) - M_{23}V_{hv3}(t) = 0 \\ V_{out3}(t, \phi_0) - M_{31}V_{hv1}(t) - M_{32}V_{hv2}(t) - M_{33}V_{hv3}(t) = 0 \end{cases} \quad (5.5)$$

The voltages in (5.5) are sinusoidal waveforms of a single angular frequency ω . The phase angle ϕ_0 accounts for the time-base shift. When synchronising the measurement to the actual phase voltage, this value is a priori known; without synchronisation it becomes an additional fit parameter. Thus, a maximum of six parameters can be retrieved, leaving three (synchronised: M_{ij}) or four (unsynchronised: M_{ij}, ϕ_0) parameters undetermined. As an example [109], for a perfect symmetric sensor positioning with respect to the lines, the unknown elements can be reduced from nine to three (making 5.5 over-determined) taking into account the following assumptions (see Fig. 5.9):

- The capacitance values of lines to the nearest sensors are equal $M_{11} = M_{22} = M_{33}$.

- The configuration of the overhead lines/terminations and the sensors is symmetrical with respect to the central phase $M_{12} = M_{32}$ and $M_{21} = M_{23}$.
- The coupling of the outer phases to the sensors furthest away can be neglected for the case of the transition point while for the case of BWK substation is taken as a predefined percentage of the middle phase coupling.

Step 5 After calculating the matrix elements, using least square curve fitting, the decoupled voltage waveforms for the three phases are calculated with (5.3). Using the aforementioned assumptions each voltage waveform is decoupled and an example of the end result is plotted in Fig. 5.11. Subsequently, more freedom can be added into the system (5.5) by relaxing the assumptions and by defining realistic lower and upper bounds for the matrix elements.

Fig. 5.11 depicts the switching waveform before (left) and after (right) the decoupling. From top to bottom, the figures are zoomed a factor 10 each time. The top figures show the reconstruction of the symmetric power frequency phase voltages from the measured signals. The zoomed bottom figures show the traveling waves and their reflections at the transition points. Here, phase B is energized first and upon its reflection, phase A seems to be excited. Phase C is close to zero and connection is made at about $t=0.6$ ms.

As discussed in [106, 112] the aforementioned methods cannot provide complete information to determine all nine matrix elements in the coupling matrix from the three steady state equations. Though the number of independent matrix components can be reduced by choosing proper sensor positioning, even in a perfect symmetric sensor configuration the system is not fully determined [106]. Assumptions and approximations have to be made which are location specific (differ between the OHL-cable transition points and the substation) and their consequences need to be evaluated in terms of uncertainty in the determination of the actual overvoltage.

5.2.2 Measurement sensitivity

Simplifications may introduce inaccuracies that need to be further investigated to evaluate the effect of uncertainties in the decoupling matrix elements on the resulting transient voltage waveform. A Monte Carlo approach is utilized with three uncertainties for the direct coupling elements. Each direct coupling element follows a normal distribution with a chosen standard deviation (see Appendix C.2). The decoupling sensitivity process consists of the following steps:

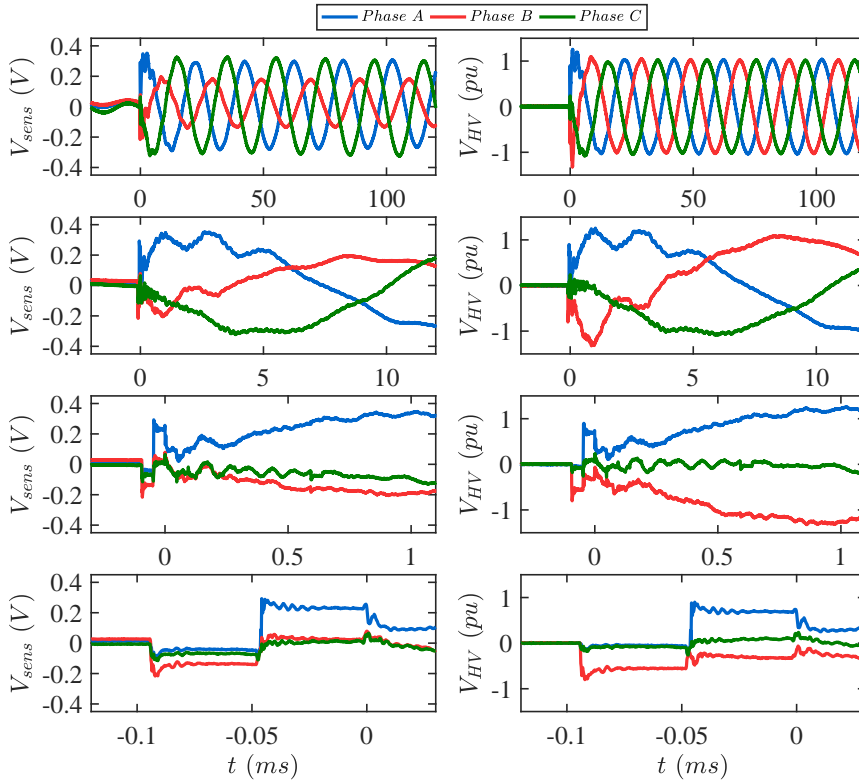


Figure 5.11: Time domain voltage waveform at substation BWK during switching before (left) and after (right) the decoupling process.

- A random value based on the normal distributions is chosen for each of the direct coupling elements.
- Having the aforementioned elements as knowns the remainder of the matrix elements are calculated using least square fitting.
- The magnitude of the decoupled steady state waveform produced is compared with the actual measured steady state waveform (from the RC divider) and if the deviation is higher than 3% (i.e. the amplitude of the decoupled waveform deviates from the measured one) the result is discarded.

The distributions of the maximum switching overvoltages (for 10000 runs) with the highest standard deviations for the three measuring locations (OSP32,

OSP14, BWK) are shown in Fig. 5.12. These distributions inform on the extent that uncertainties in the coupling matrix elements translates into deviations in predicted overvoltage values.

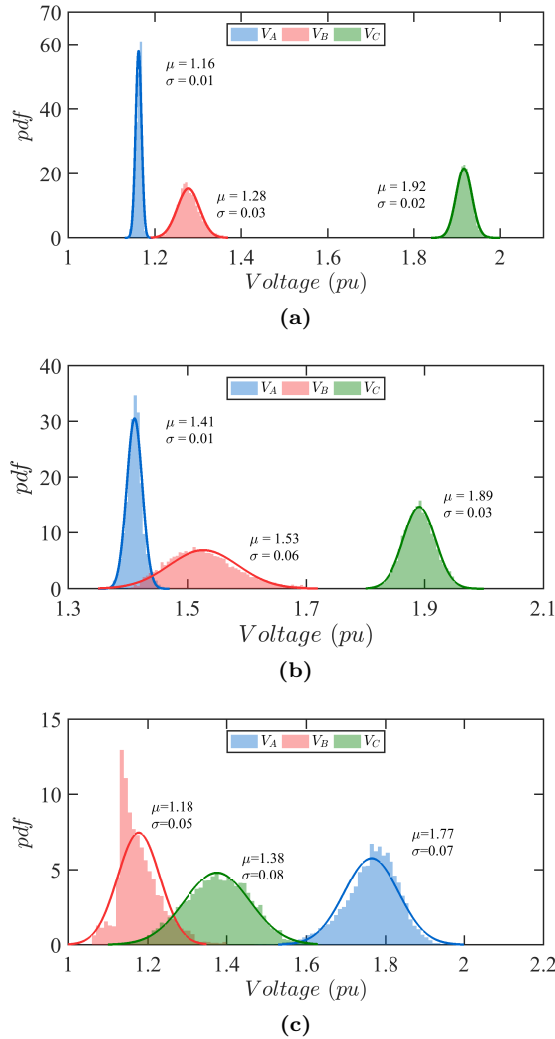


Figure 5.12: Histograms and fitted normal distributions of the maximum switching overvoltages at (a) OSP32, (b) OSP14 and (c) substation BWK.

In all cases the overvoltages seem to follow normal distributions with standard deviations that do not exceed 0.08 pu. The distribution widths for overvoltages

differ significantly between the phases and also depend on the switching event. In the case of the transition points the largest deviation is observed in the middle phase (B) where the uncertainty was taken more than six times larger compared with the uncertainties of the other two phases (see Appendix C.2). From the other two phases it is observed that the wider distributions correspond to maximum overvoltage occurring immediately after switching as the phase-voltages are strongly asymmetric. For the case of substation BWK the standard deviations of the overvoltages are significantly higher than the ones of the transition points since the chosen uncertainty limits were much wider. Also for BWK the standard deviation is higher when the overvoltage takes place at the first moments after energization.

Such behavior can be expected because for a maximum voltage occurring later on the power cycle, the three phase voltages (including the overvoltages) tend to add up to zero, and uncertainties in the decoupling matrix start cancelling each other in the reconstructed waveform, see (C.6) in Appendix C.2. This is studied in [108] where the error propagation is analyzed in more detail. It can be concluded that uncertainties in the decoupling matrix elements have a minor effect on the maximum switching overvoltages at the transition points and are also reasonably accurate at substation BWK (see Appendix C.3).

5.3 Simulation model validation

For the validation of the simulation model the entire Dutch 380 kV network has been modeled, as explained in Chapter 4. The loads (downstream network) were modeled as RL or RC parallel circuits directly connected on the secondary side of the transmission transformer. The values of the R, L and C were obtained from powerflow calculations on a specific network snapshot to capture the correct state of the system prior to the switching. Modeling the downstream network with more detail was avoided since for the specific case the simulation results with the simplified load model were already close to the measurements.

In order to validate the simulation model for use in transient simulations, its results were compared with measurements from switching actions at three locations (transition points OSP32, OSP14 and substation BWK). The model was validated for both low frequency resonances and high frequency (traveling wave) transients.

5.3.1 Low-frequency transients

For the low frequency transients, three types of switching actions were selected to be shown here in order to verify the model accuracy for distinct transient events. An overview of other switching actions performed during the measurement expedition is summarized in Appendix C.4.

- S1: the black circuit is energized from substation WTR while the white circuit is out of service.
- S2: the black circuit is energized from substation BWK while the white circuit is out of service.
- S3: the black circuit is energized from substation WTR while the white circuit is in service.

The maximum overvoltage deviation defined as:

$$\Delta V_{max} = \frac{V_{msr} - V_{sim}}{V_{msr}} \cdot 100\% \quad (5.6)$$

is shown in Table 5.1, for the aforementioned actions at all three locations. There is agreement for the maximum overvoltage between measurements and simulations with the largest deviation being around 16% while the majority stays below 5%, which is close to the achievable accuracy according to Fig. 5.12. The comparison of the transient voltage waveforms and the harmonic contents produced during switching are shown in Fig. 5.13 - Fig. 5.15.

Table 5.1: *Maximum overvoltage magnitude deviation between simulations and measurements.*

	OSP32 (%)			OSP14 (%)			BWK (%)		
	ΔV_A	ΔV_B	ΔV_C	ΔV_A	ΔV_B	ΔV_C	ΔV_A	ΔV_B	ΔV_C
S1	-3.0	0.6	5.9	-1.6	-2.4	3.6	-4.4	-7.4	13.6
S2	15.7	11.4	0.8	7.3	10.4	8.9	0.6	-0.9	3.6
S3	-8.0	4.6	5.8	1.6	8.6	2.1	1.5	4.9	-3.6

It is evident that different actions result in different waveforms and harmonic content. More specifically, when the white circuit is out of service and the black circuit is energized from WTR side (S1, result for OSP32 in Fig. 5.13) the dominant frequency is around 500 Hz together with a peak near 340 Hz, visible mainly in phase C. When the black circuit is energized from BWK side and again the white circuit is out of service (S2, result for OSP14 in Fig. 5.14) only a dominant frequency near 328 Hz is visible. Its oscillation is less damped

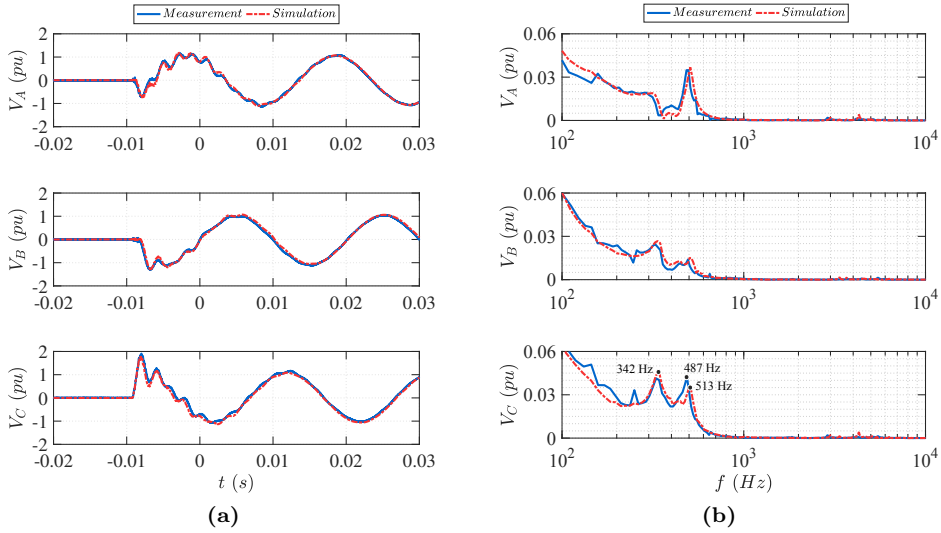


Figure 5.13: Voltage comparison between measurements and simulations at OSP32 for switching action $S1$ in (a) time and (b) frequency domain.

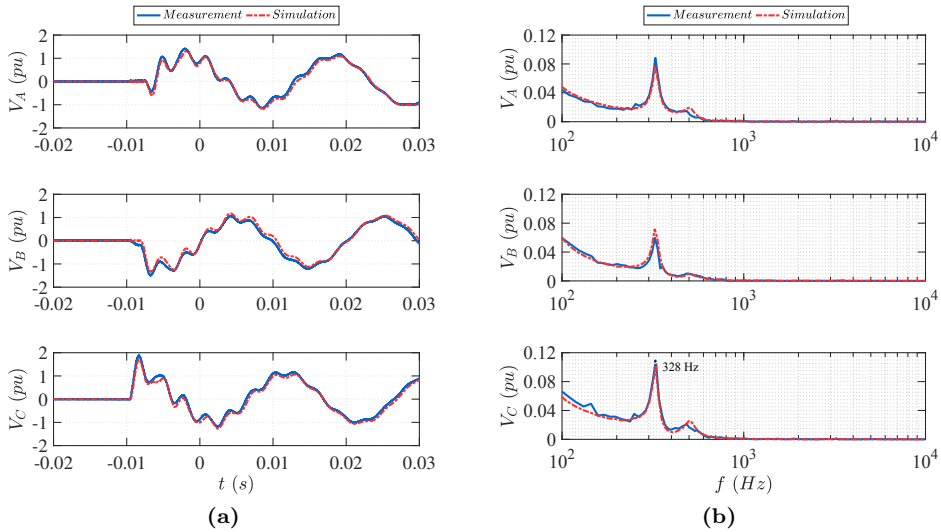


Figure 5.14: Voltage comparison between measurements and simulations at OSP14 for switching action $S2$ in (a) time and (b) frequency domain.

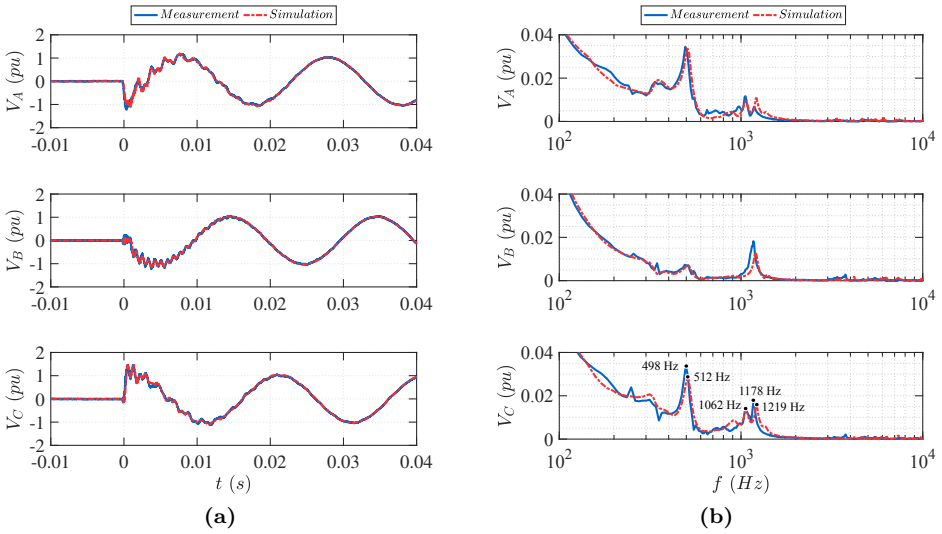


Figure 5.15: Voltage comparison between measurements and simulations at BWK for switching action S3 in (a) time and (b) frequency domain.

than the one in Fig. 5.13. Furthermore, when the energization of the black circuit occurs and the white circuit is in service (S3, result for BWK in Fig. 5.15) together with a frequency peak at 500 Hz there is a dominant higher frequency content at 1 kHz which matches the main series resonance of the white circuit, as illustrated in Fig. 5.16. The dominant frequencies produced at all three switching actions closely match the parallel resonance frequency peaks of the harmonic impedance during these actions (see Fig. 5.17). To what extent oscillations at these frequencies are excited in the measurements depends on the precise moments of switching.

Overall, the measured and simulated voltage waveforms are almost identical for all three types of switching actions and locations. Moreover, the dominant frequencies produced during energization show a close match with a slight shift to higher frequencies for the simulation model. It can safely be concluded that measurements confirm that no dangerous overvoltages are expected for both the transition points and the substation. Even at the worst case scenario, where the circuit is switched when one of the three phases is close to the maximum voltage (which is the case of phase C at S1, S2 and S3) the maximum overvoltage is well below the switching impulse withstand voltage limits. Moreover, no resonance is excited.

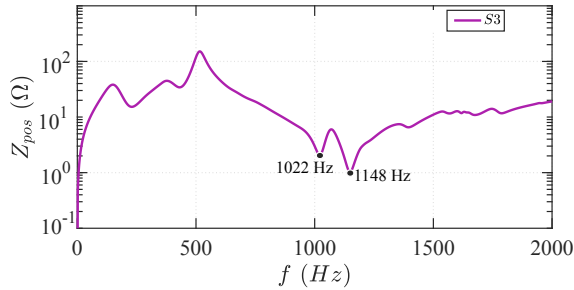


Figure 5.16: Positive sequence harmonic impedance during switching action $S3$ where the two series resonance frequencies are pointed out.

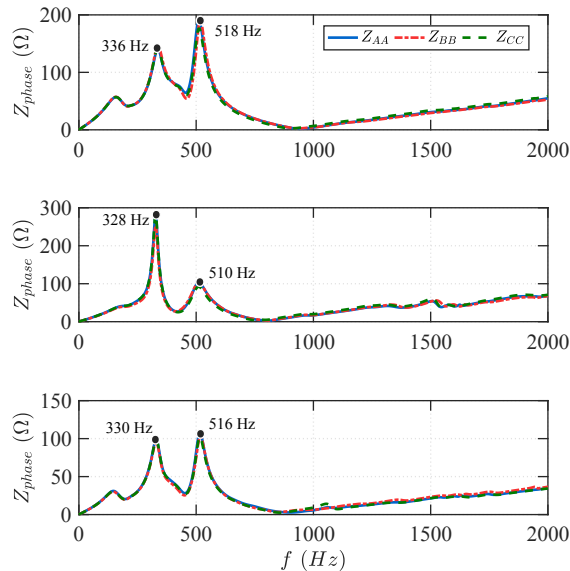


Figure 5.17: Harmonic self impedances for all three phases during switching action $S1$ (top), $S2$ (middle) and $S3$ (bottom) where the two parallel resonance frequencies are pointed out.

5.3.2 High-frequency transients

The simulation model was also verified for high frequency components in two of the transients captured at substation BWK. These two events were selected as they show interesting features at frequencies above 10 kHz for model evaluation. No remarkable features in the voltage waveforms above 10 kHz were observed at the transition points.

Case 1

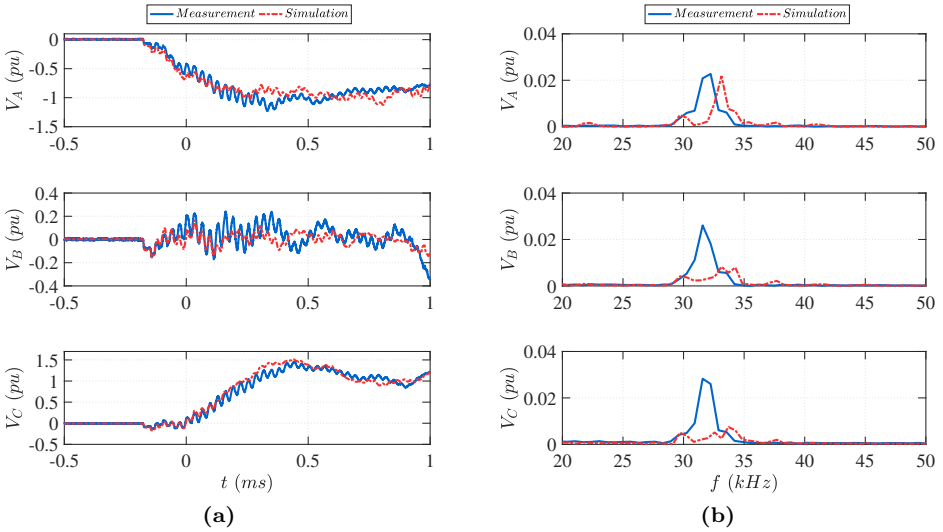


Figure 5.18: Voltage comparison between measurements and simulations at BWK for the initial high frequency resonance during switching action $S3$ in (a) time and (b) frequency domain.

Fig. 5.18a shows the voltage waveform at substation BWK for switching $S3$ where the traveling waves develop into a 32 kHz oscillation. This behavior can be understood as follows:

- When the circuit is energized, the series resonance frequencies of the parallel circuits (already in service) are observed in the harmonic content of the voltage of the circuit been energized [113]. As example, in Fig. 5.15 the voltage contains a dominant harmonic frequency at approximately 1 kHz which is the main series resonance frequency of the complete white OHL-UGC-OHL circuit (in service). This dominant frequency is not observed when the white circuit is out of service.
- By calculating the harmonic impedance (from the simulation model) it is observed that one series resonance of the 4.4 km OHL from WTR to OSP14 white circuit is around 34 kHz and with the white circuit in service this frequency is excited during energization.
- The OHL segment from OSP32 black circuit to BWK open end (6.8 km) has a parallel resonance at approximately 33 kHz, closely matching the series

resonance of the WTR-OSP14 white OHL segment. This suggests that the 34 kHz harmonic produced from the WTR-OSP14 white OHL segment is amplified at BWK open end. This amplification is visible in Fig. 5.19 whereas at the OSPs no amplification is present.

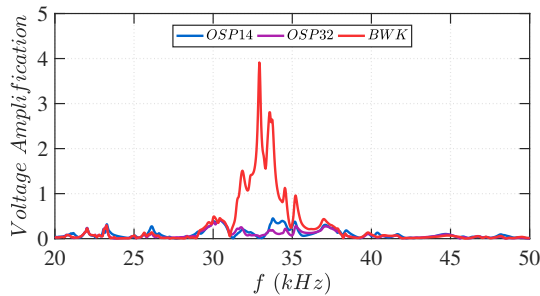


Figure 5.19: Simulated voltage amplification for the transition points and substation BWK during switching action S3.

Although this oscillation hardly contributes to the maximum overvoltage, it can cause EMC interference to equipment due to the high di/dt . The associated 32 kHz current component simulated for the closest transition point (OSP14) is typically 270 A. In [114] a similar type of energization resulted in high frequency voltage oscillations at the cable receiving end. This phenomenon caused the occurrence of flashovers from cable screens to grounded structures in a tunnel containing four EHV cable circuits from induced voltages.

The high frequency oscillation is also visible from the simulation, however, it is shifted to slightly higher value (34 kHz) and is of shorter duration (see Fig. 5.18b). As previously mentioned, the series resonance of the 4.4 km OHL part does not exactly match the parallel resonance of the 6.8 km OHL part and both do not match the 32 kHz in the measurements. However, slight changes at the configuration (even 200 m) significantly shift the resonances at such high frequencies. The exact length (routing) of the OHL can slightly differ from the one mentioned in the specification document. Furthermore, corners in the circuit, differences in the sag and the tower height along the way as well as the value of the earth resistivity can affect resonances at such high frequencies. To emulate this effect, in order to achieve a controlled perfect resonance match at 32 kHz, the lengths of the OHLs are adjusted to 4.68 km and 7.02 km and the simulation result is shown in Fig. 5.20. The oscillation is sustained longer and is similar to the measured event.

For achieving the resonance at 32 kHz both OHL lengths should be changed. Two additional cases are examined:

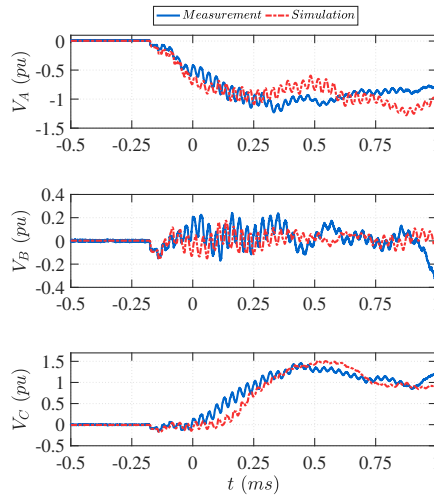


Figure 5.20: Time domain high frequency oscillation comparison between measurements and simulations at BWK for switching action S3 for adjusted 32 kHz oscillation.

- The first OHL part is kept at its base length of 4.4 km and the second OHL part is adjusted to 6.6 km to achieve a matching frequency of 34 kHz.
- The second OHL part is kept at its base length of 6.8 km and the first OHL part is adjusted to 4.535 km to achieve a matching frequency of 33 kHz.

The resulting waveforms of the aforementioned resonance shown in Fig. 5.21 are sensitive to absolute circuit length and not only to matching resonances from both OHL sections.

Case 2

Fig. 5.22 shows the the reflection pattern at BWK for energization of the black circuit from substation BWK while the white circuit is out of service (switching event S2).

The traveling times between BWK and OSP32 are clearly visible and similar for measurements and simulations. The voltage wave travels at the OHL part and reaches the cable (OSP32) after $22.5 \mu\text{s}$ causing a negative reflection which reaches again BWK at $45 \mu\text{s}$. Another reflection is observed at the cable receiving end (OSP14) which reaches BWK after around $169 \mu\text{s}$ for both measurement and simulation. The magnitude of the initial wave differs between simulation

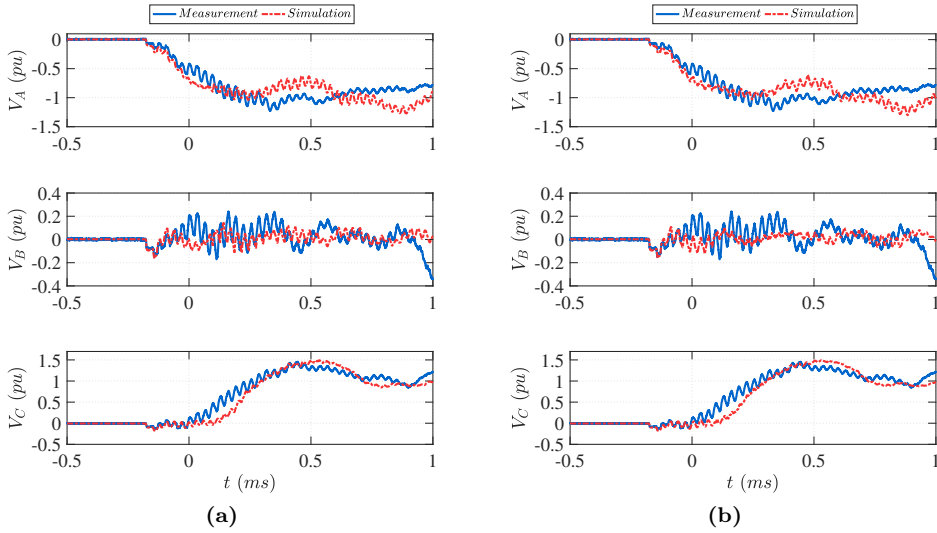


Figure 5.21: Time domain high frequency oscillation comparison between measurements and simulations at BWK for switching action $S3$ for adjusted (a) 34 kHz and (b) 33 kHz oscillation.

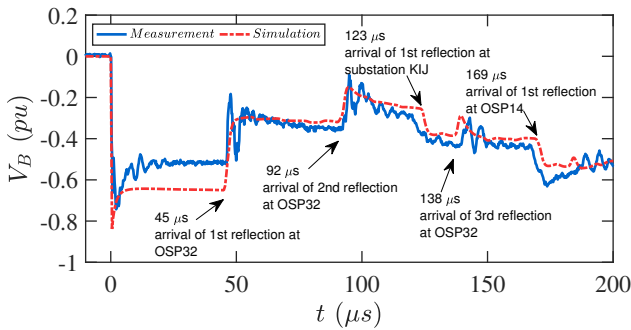


Figure 5.22: Time domain reflection pattern at BWK for energization of the black circuit from substation BWK while the white circuit is out of service.

and measurement. Uncertainties in the decoupling matrix components may contribute to the deviation, which are most paramount when the phase voltages are asymmetric (initially only one phase is excited). As employed in [24, 109] the stepwise response in the signals from all sensors (see Fig. 5.11, bottom left figure) informs on the relative coupling strengths of all sensors to the first excited phase. Including this information in the decoupling would in principle add to or even

complete (when also events with other phases being excited first are recorded) the information needed in constructing the coupling matrix (5.3).

5.4 Conclusion

The D/I method is not commonly applied as measurement technique in electrical energy networks [115]. However, from the presented statistical analysis it proves to be a competitive alternative compared with galvanically connected divider based measurements. In particular, when cross-coupling can be kept low, as in the case of transition points, accuracy is similar for both techniques. For a more complex substation configuration, overvoltages can still be reconstructed within 10% using the D/I method. Such accuracy still allows for comparison with simulation model predictions.

The overvoltage magnitudes from 18 switching events, summarized in Table C.1, can be statistically analyzed based on normal distributions and the distributions of the peak voltage deviations in all three locations are demonstrated in Fig. 5.23.

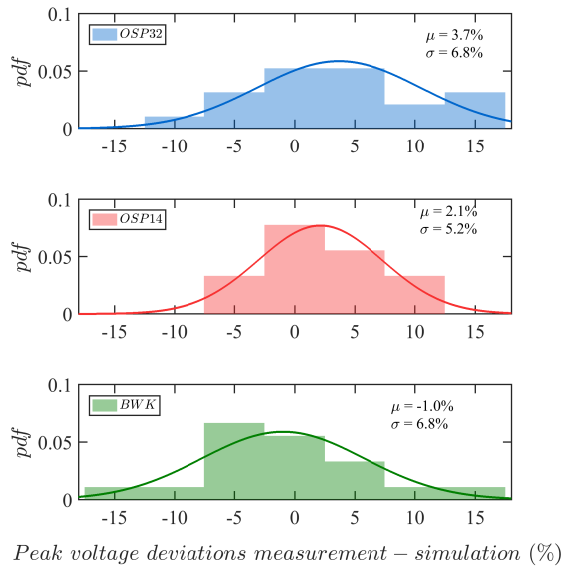


Figure 5.23: Distributions of the peak voltage deviations.

The overall standard deviation of 6.4% indicates that there are no fundamental

shortcomings in the applied modeling. For the substation, the deviation is in line with the expected accuracy from Fig. 5.12c and Fig. C.5b. Thus, it can be concluded that within the confidence margins measurements and simulations agree. On the other hand, for the transition points the estimated experimental margins are smaller, as indicated in Fig. 5.12a-5.12b and Fig. C.5a. Therefore, the deviation can be considered marginally significant.

From the spectral distributions in Fig. 5.13-5.15 it is observed that all resonances contributing to overvoltages are reproduced, but their simulated positions are sometimes slightly shifted, which may contribute to deviations. Possible causes could be the uncertainty in the parameters of components modeling as well as the simplified modeling of the downstream network which have an effect on the damping. Furthermore, the overvoltages occurring the first moments after the energization are very sensitive to the exact switching moment and the time difference between the three poles of the circuit breaker. In some cases there was a difficulty in deriving the switching timings of the three phases with high precision which can be a significant cause of overvoltage deviation.

6

Resonance and Slow-front Overvoltage Study

Insulation coordination studies are performed to appropriately select the dielectric strength of the equipment so that it can withstand the overvoltages occurring in the system. If the withstand capability is not guaranteed, these studies assist in selecting the necessary protective devices (and their optimal placement) in order to ensure that the equipment is safe [15]. For insulation coordination four type of overvoltages are examined: temporary overvoltages (TOV), slow front overvoltages (SFO), fast-front overvoltages (FFO) and very-fast-front overvoltages (VFFO) [23, 74]. This categorization is performed based on the main frequency oscillatory components and the duration of the disturbance. The main focus of this dissertation is the TOV and SFO with frequency content up to 10 kHz which can sustain for longer periods of time.

The shift towards more and longer UGC connections in the EHV grid has imposed the need to re-examine the network behavior under SFO (e.g. from energization, faults) and most importantly under possible resonance conditions (TOV). These kind of studies are critical, especially when UGCs are integrated in the transmission network due to their large capacitance and the need for shunt reactors for compensation, which potentially shift the natural frequencies of the network to significantly lower values [10].

For reliable operation of the transmission network and also future network planning, SFO and resonance phenomena need to be studied and thus simulated, using appropriate network models, for various network configuration and contingency scenarios. To this end statistical studies are conducted, especially when energization, re-strike and fault transients are concerned. Furthermore, the parameters that significantly affect the maximum overvoltage and the damping of the disturbance need to be identified so that suitable system operation actions are applied to avoid costly countermeasures if possible.

6.1 Series resonance study

Integration of long UGCs shifts the harmonic impedance of the network to lower frequencies and leads to temporary overvoltages (TOV) due to resonance through interaction with other network components [6]. In this section the series resonance involving leakage transformer inductance and HV cable capacitance is investigated. Although it is a low probability phenomenon, it has potentially a high risk and it is of importance to find the specific configurations that can excite such a resonance.

6.1.1 Introduction

The emphasis in this chapter is the low-frequency series resonance. In a transmission network the leakage inductance of a transformer can create a series resonant circuit with the capacitance of a downstream cable (see Fig. 6.1). When excited by a voltage disturbance of its natural frequency, it will draw a significant amount of current creating an overvoltage at the secondary side of the transformer [7, 10, 26]. A voltage disturbance can arise when energizing an EHV power cable and due to the high cable capacitance the harmonic content of the energization can shift down to frequencies of several hundreds hertz, causing a TOV due to the low damping at such frequencies.

The relevant quantities that need to be determined for such kind of studies are the natural frequency of the secondary circuit consisting of transformer, HV cable and load as well as the frequency of the voltage harmonic components during the energization of the EHV cable. The natural frequency of the secondary circuit can be determined using frequency scans or even by using approximate analytical expressions. However, the frequencies of the voltage harmonic components during EHV cable energization are more difficult to determine without using time domain simulations on a detailed network configuration, since there are many parameters that affect their values. In [113, 116, 117] the authors derive theoretical

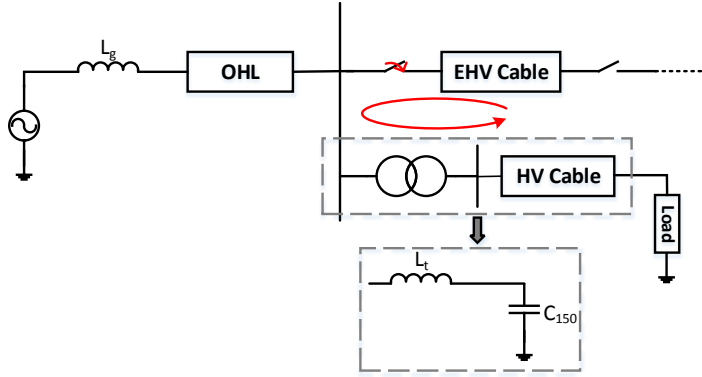


Figure 6.1: Series resonance configuration where the red arrow indicate the flow of the harmonic content from the EHV (400 kV) to the HV (150 kV) network upon cable energization.

formulas and calculation methods for the frequency component contained in the energization overvoltage of both cable and OHL responses. In those studies the effect of the source impedance and possible load connected at the receiving end of the EHV UGC/OHL were taken into account. However, the effect of the secondary circuit comprising the transformer and HV cable was not considered.

6.1.2 Derivation of analytical expressions

In order to estimate how each parameter affects the first series resonance as well as the harmonic content of the cable energization the simplified network of Fig. 6.1 is used. It contains an EHV/HV transformer with cable and load connected to the busbar with the OHL-UGC transition. For the OHL and cables the single Pi model is utilized, the transformer is modeled only by its leakage inductance and the load comprises of an RL circuit. In order to derive simple analytical expressions the mutual coupling between phases is not taken into account and each component is expressed using the ABCD matrix formalism. The configuration of Fig. 6.1 can be represented as shown in Fig. 6.2.

The harmonic content of the energization at the EHV side, i.e. 400 kV, is given by the expression:

$$\frac{V_{400}}{E} = \underbrace{[B_7^{-1}A_7 + C_3A_3^{-1} + D_8B_8^{-1}]^{-1} \cdot B_7^{-1}}_{G_1} \quad (6.1)$$

where index 7 refers to the combined ABCD matrix of L_g with OHL, and index

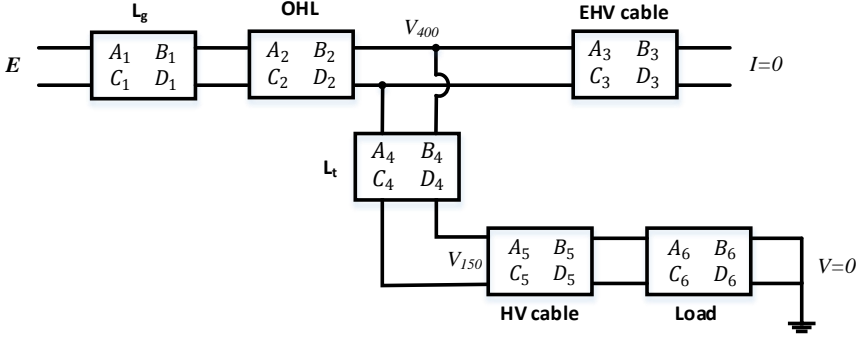


Figure 6.2: *ABCD matrix representation of the connection in Fig. 6.1.*

8 combines the matrices for transformer, HV cable and load.

For the 150 kV side, with index 9 referring to the combined HV cable and load, the harmonic content is given by:

$$\frac{V_{150}}{E} = A_4^{-1} \cdot [G_1 - B_4 D_9 B_8^{-1} G_1] \quad (6.2)$$

The expressions of the ABCD parameters for each component can be found in Appendix D.1.1. The resulting expressions of equations (6.1) and (6.2) are complex functions and in order to find the dominant frequencies of energization their absolute values are used and the frequencies of the local maxima are calculated. In order to calculate the harmonic impedance at the EHV side the source is short-circuited ($E=0$) and a current source (I_H) is assumed to be connected at the point of interest. From the nodal equation at this point the impedance is found as:

$$\frac{V_{400}}{I_H} = [B_7^{-1} A_7 + C_3 A_3^{-1} + D_8 B_8^{-1}]^{-1} \quad (6.3)$$

6.1.3 Sensitivity analysis

It is of importance to analyze the EHV-HV circuit interaction and to identify which are the parameters that affect the severity of the series resonance. To this end the circuit of Fig. 6.1 is utilized for a sensitivity analysis.

Effect of load model

Without connected load to the HV cable the natural frequency is:

$$f_n = \frac{1}{2\pi\sqrt{L_t C_{150}}} \quad (6.4)$$

where L_t is the leakage inductance of the transformer and C_{150} is the capacitance of the HV cable.

In order to introduce damping and to make the series resonance study more realistic a load is connected at the receiving end of the HV cable. The load will be based on the demand of active and reactive power. Two options, a parallel and a series connected R_{load} and L_{load} , as depicted in Fig. 6.3, are evaluated. The harmonic impedances of both options are:

$$Z_p = \frac{C_{150}L_tL_{load}R_{load}s^3 + L_tL_{load}s^2 + (L_t + L_{load})R_{load}s}{C_{150}L_{load}R_{load}s^2 + L_{load}s + R_{load}} \quad (6.5)$$

$$Z_s = \frac{C_{150}L_tL_{load}s^3 + C_{150}L_tR_{load}s^2 + (L_t + L_{load})s + R_{load}}{C_{150}L_{load}s^2 + C_{150}R_{load}s + 1} \quad (6.6)$$

The natural frequencies occur when the imaginary part with $s = j\omega$ is zero and are given by the roots of the equation:

$$\rho_4\omega^4 - \rho_2\omega^2 + \rho_0 = 0 \quad (6.7)$$

This equation results in two positive frequencies. The values of ρ_0 , ρ_2 and ρ_4 depend on the type of load model used.

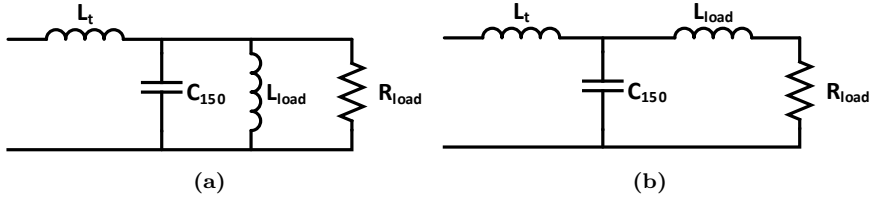


Figure 6.3: Series resonance circuit with (a) parallel load model and (b) series load model.

For the parallel load model (Fig. 6.3a) the coefficients are:

$$\begin{aligned} \rho_4 &= C_{150}^2 L_t L_{load}^2 R_{load}^2 \\ \rho_2 &= 2C_{150}L_tL_{load}R_{load}^2 + C_{150}L_{load}^2R_{load}^2 - L_tL_{load}^2 \\ \rho_0 &= (L_t + L_{load})R_{load}^2 \end{aligned}$$

For the series load (Fig. 6.3b) the coefficients are:

$$\begin{aligned}\rho_4 &= C_{150}^2 L_t L_{load}^2 \\ \rho_2 &= -C_{150}^2 L_t R_{load}^2 + 2C_{150} L_t L_{load} + C_{150} L_{load}^2 \\ \rho_0 &= -C_{150} R_{load}^2 + L_t + L_{load}\end{aligned}$$

The resistance and reactance values of these two load models are calculated as in [118]. However, the resonant behavior presents major differences between the load models for the same active and reactive power demand. For a base loading condition of 100 MW + j50 MVar and the same transformer leakage inductance the harmonic impedance comparison of the secondary circuit is depicted in Fig 6.4a. The network parameter values can be found in Appendix D.1.2. The series resonance occurs near 600 Hz corresponding to the higher frequency root in (6.7). For the parallel load option the series resonance is more damped, since the magnitude of the load impedance at the resonance frequency is much larger than in the series load case. In Fig. 6.4b the harmonic impedance comparison of the complete circuit of Fig. 6.1, measured at the EHV side for the two load models is illustrated where the damping is much higher in the parallel load case and the series resonance cannot be identified as in the series load case (zoomed-in part). Moreover, there is an obvious difference in the amplification ratio between EHV and HV (see Fig. 6.4c) whereas for the parallel load even at the series resonance frequency almost no amplification is present.

Thus, one must be cautious for the choice of load model when conducting a series resonance study. From the analysis it can be observed that the parallel load model provides excessive damping and it is almost impossible to identify series resonance cases even in a simple network. For the rest of the sensitivity analysis the series load model will be used.

Effect of 150 kV cable length

For conducting a series resonance study the steps that need to be followed are described in [7] and [10]. First, using time domain simulations the dominant harmonic components contained in the EHV cable energization are found as well as the voltage amplification ratio from EHV to HV. Next, for obtaining a series resonance, the natural frequency of the secondary circuit is adjusted (by changing the HV cable capacitance) in order to match the harmonic component of the energization. Then time domain simulations are again conducted to assess the severity of the resonance overvoltage. However, this method ignores that by changing the HV cable capacitance the harmonic content of the energization also changes. To demonstrate this effect using (6.1) and (6.2), the length of the HV cable is increased from 5 km to 50 km with a step of 1 km while the rest of the

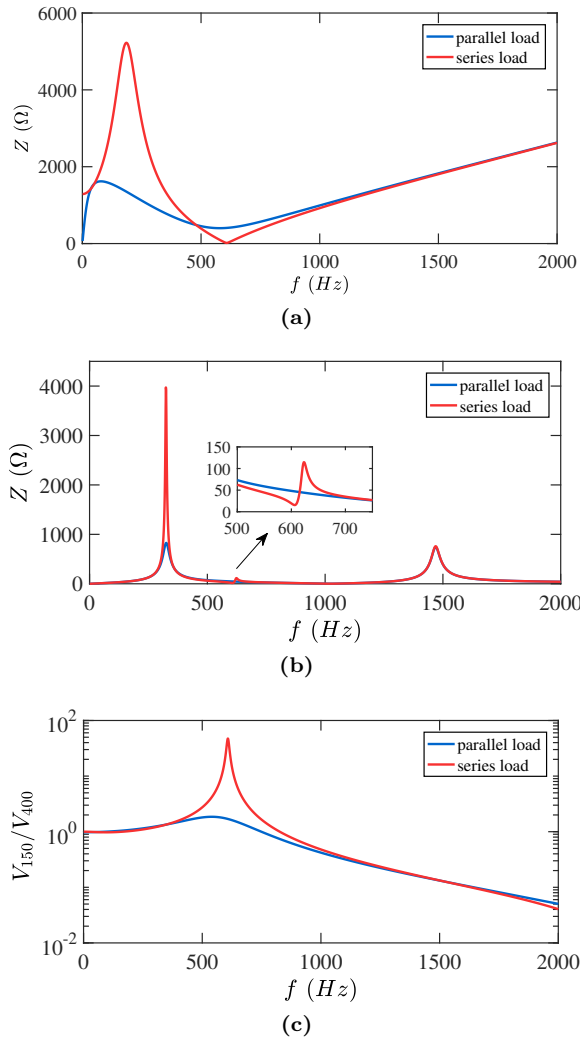


Figure 6.4: Comparison of (a) the harmonic impedance of the series resonant circuit, (b) the harmonic impedance of the full circuit and (c) the amplification ratio between EHV and HV for two load model types.

network parameters are constant. The base case of the network parameters can be found in Appendix D.1.2.

It can be seen from Fig. 6.5a that when the length of the 150 kV cable is 5 km the dominant energization frequency is 330 Hz while the series resonance frequency

is 866 Hz (the second energization frequency is almost the same as the series resonance but the amplitude is too low for significant impact). Following the method described above, the length of the 150 kV cable is adjusted in order for the series resonance frequency to become 330 Hz, which is accomplished for 32 km of cable. However, for 32 km of 150 kV cable the dominant energization frequencies have dropped to 278 Hz and 394 Hz. As can be seen in Fig. 6.5b the amplification ratio at these frequencies is a factor of 6, respectively 10, lower than at the actual series resonance frequency.

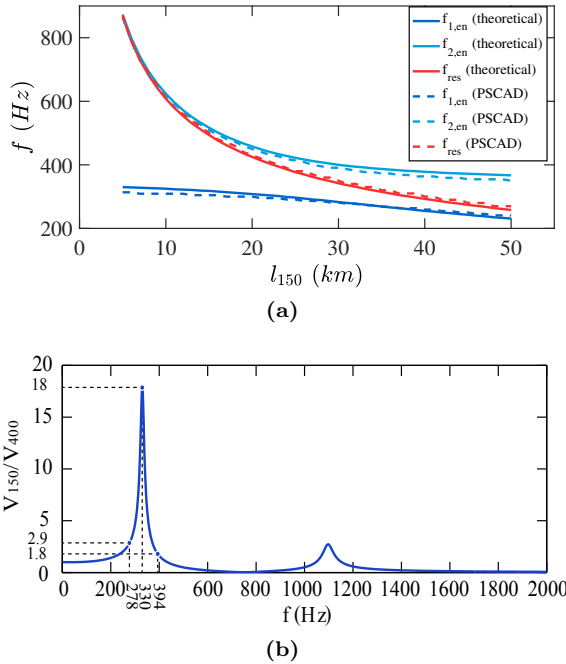


Figure 6.5: (a) Energization frequencies and series resonance as function of 150 kV cable length, where the continuous lines are obtained from the analytical expressions while the dashed lines are from PSCAD simulations and (b) amplification ratio for 32 km HV cable length and 0.217 H transformer inductance.

The frequencies obtained from the theoretical expressions are also compared with the ones calculated by time domain simulations where both cables and OHL were modeled using the Frequency-Dependent Phase model including cross-bondings for the 400 kV cable. Only minor deviations are observed between the two, confirming the validity of the approximate expressions. From the above analysis it can be concluded that the length of the 150 kV cable affects both the frequency of the series resonance and the harmonic content of the energization making it

more complex to intentionally enforce a series resonance.

6.1.4 Parametric Analysis

Even though the theoretical expressions provide a quick way to estimate the frequencies of the energization harmonic content as well as the amplification ratio between HV and EHV busbars, it is not clear how these values translate into time domain and more specifically into the maximum resonance overvoltage. In order to identify how each network parameter affects the maximum overvoltage a parametric analysis is conducted using the PSCAD/EMTDC software.

In Fig. 6.6 the variation of the maximum overvoltage at the 150 kV side is depicted for four different transformer inductances and three 400 kV cable lengths by taking multiples of the base case values. The length of the 150 kV cable is increased from 5 km to 80 km with a step of 1 km, which means that in total 912 simulation cases were run. It can be seen from Fig. 6.6 that for low transformer inductance no clear resonance peak over a certain range of 150 kV cable length is present. Moreover, for all four transformer inductance values, as the length of the 400 kV cable increases, the maximum resonant overvoltage decreases and its distribution widens. Furthermore, while in Fig. 6.6a the increase of transformer inductance causes an increase in the maximum overvoltage, for larger 400 kV cable lengths the highest simulated inductance value causes a decrease in the maximum overvoltage (see Fig. 6.6b and Fig. 6.6c).

The time domain waveforms of the voltages observed at the 150 kV busbar for the lowest and highest transformer inductances of Fig. 6.6a are shown in Fig. 6.7. It is clear that as the transformer inductance increases (and consequently the length of the 150 kV cable that gives rise to a resonance decreases) the series resonance becomes more severe. This can be attributed to the fact that when the transformer inductance is higher, smaller HV cable length is needed to achieve the series resonance and the energization dominant frequencies are closer to the series resonance frequency. This is illustrated in Fig. 6.8 for a transformer inductance of 0.868 H. For 11 km of HV cable (the length where the maximum overvoltage occur according to Fig. 6.6a) the dominant energization frequencies at 304 Hz and 359 Hz are closer to the series resonance frequency of 331 Hz compared to those shown in Fig. 6.5. Moreover, the amplification ratio for 11 km HV cable (see Fig. 6.8b) at these two frequencies is higher than the one in Fig. 6.5b. However, the increase in the transformer inductance results in a decrease of the amplification ratio peak at the resonant frequency. Thus there is a trade-off when increasing the transformer inductance between the distance of the dominant frequencies to the series resonance frequency and the decrease in the amplification ratio at the series resonance frequency.

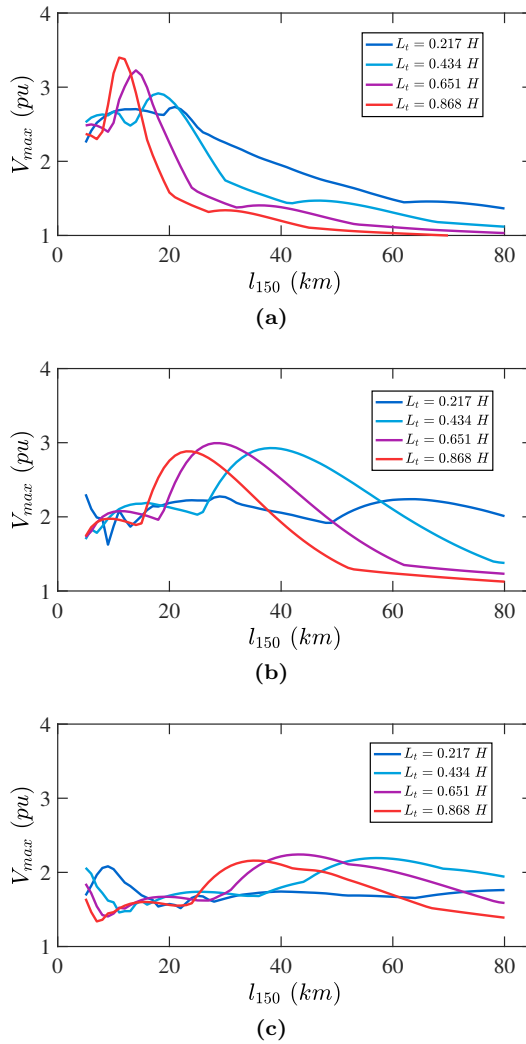


Figure 6.6: Maximum overvoltage variation at the 150 kV side for four different transformer inductances as function of the length of the 150 kV cable for (a) 28 km of 400 kV cable (b) 56 km of 400 kV cable and (c) 84 km of 400 kV cable.

6.1.5 Study on Dutch 380 kV grid

The harmonic impedance of the series resonant circuit (transformer-cable-load) was measured using a frequency scan and the series resonance frequency was

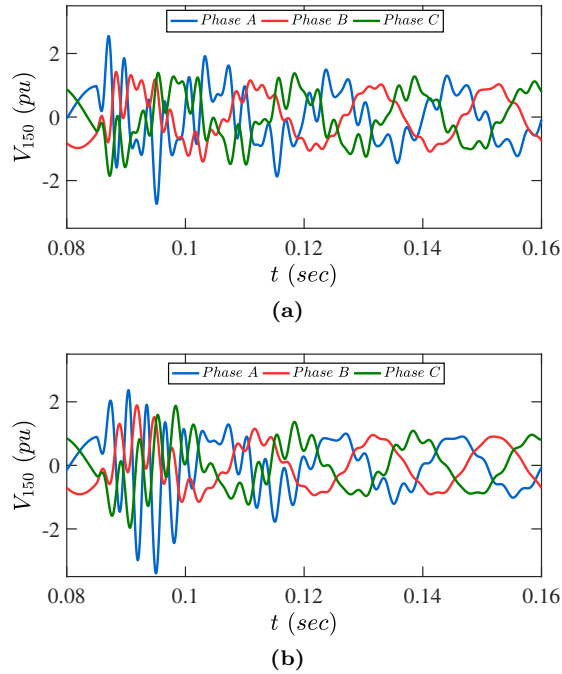


Figure 6.7: Voltage waveforms at the 150 kV side for 28 km of 400 kV cable and for transformer inductance (a) 0.217 H (b) 0.868 H.

found to be 468 Hz. The circuit is added to the BWK substation of the Randstad380 south-ring. For this series resonance study one of the possible worst case scenarios is examined, where one EHV circuit is energized (from Bleiswijk side) while the other circuit is out of service. Further, only one of the three transformers at this substation is in service and only one of the two 150 kV cables (of 17 km) is in operation. The modeling of the whole Dutch 380 kV network is as described in Chapter 4. In Fig. 6.9 there is a clear amplification of the energization harmonic content from EHV to HV at 410 Hz and 500 Hz since the dominant frequencies are relatively close to the series resonance. From the time domain waveforms in Fig. 6.10 it is observed that the maximum overvoltage of 1.4 pu at 400 kV becomes 1.8 pu at 150 kV, but it is still beneath the switching impulse withstand voltage and since the oscillations quickly damp the severity of the series resonance at this point under the specific conditions is low.

The case of a longer 150 kV cable (22 km) was examined in order for the series resonance to match the 410 Hz of the dominant energization frequency. Also in this case no severe series resonance was observed and the maximum overvoltage at 150 kV was even lower (1.7 pu). The harmonic content amplification and time

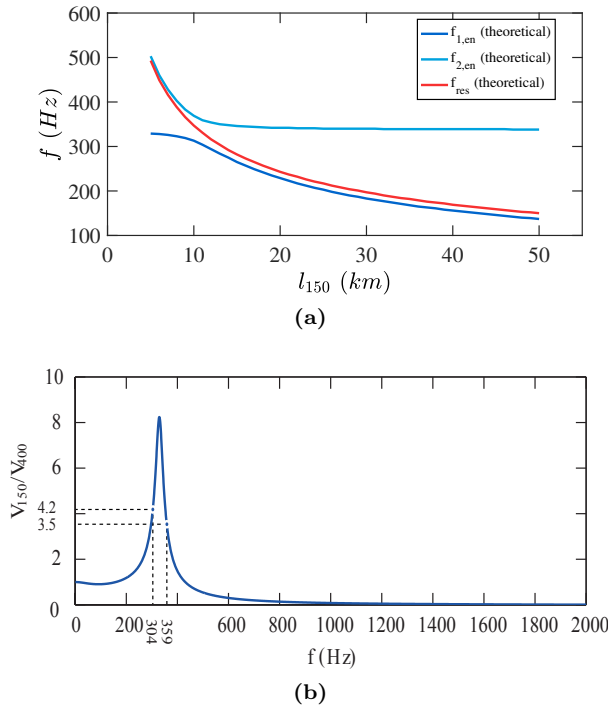


Figure 6.8: (a) Energization frequencies and series resonance as function of 150 kV cable length and (b) amplification ratio for 11 km cable length for 0.868 H transformer inductance.

domain waveforms are shown in Fig. 6.11 and Fig. 6.12. This can be attributed to the fact that the leakage inductance of the transmission transformer is low and the situation of Fig. 6.5a is observed where the energization frequencies shift significantly with the increase of the 150 kV cable length.

6.2 Slow-front Transients

According to IEC standards [94, 119] slow-front overvoltages have front durations from tens to some thousands of microseconds and tail durations in the same order of magnitude. They are oscillating by nature and can originate from line energization and de-energization, faults and fault-clearing, load rejections, switching of capacitive or inductive currents and distant lightning strokes to overhead lines. Because the resulting overvoltages depend on the momentary

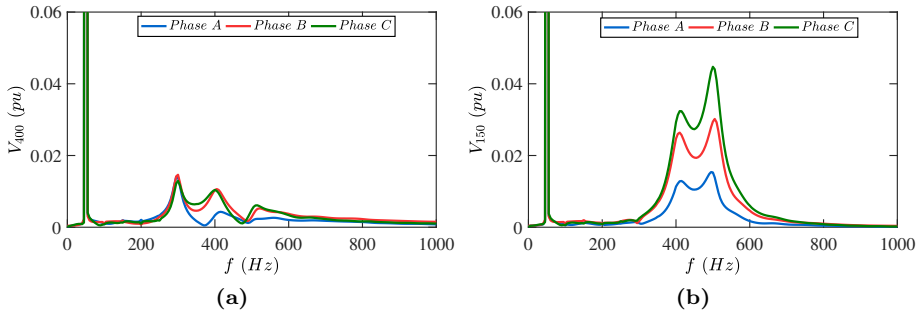


Figure 6.9: FFT transform on (a) 400 kV and (b) 150 kV voltage waveform upon energization with 17 km HV cable length.

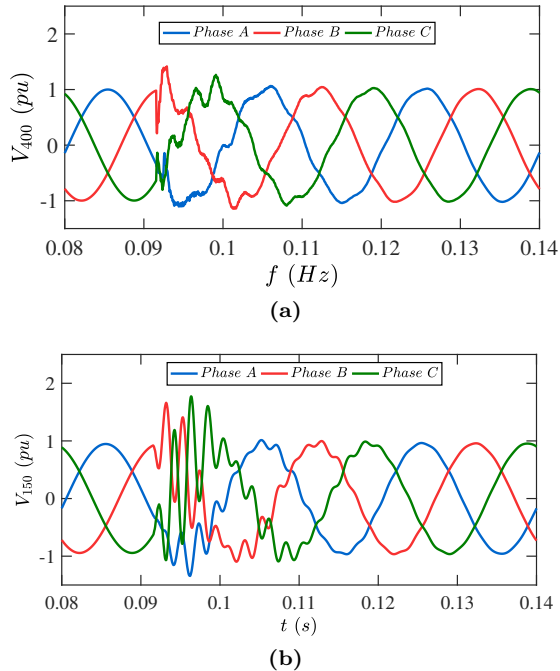


Figure 6.10: Voltage waveforms at (a) 400 kV and (b) 150 kV side of the transformer upon energization with 17 km HV cable length.

phase angles during the event, a statistical approach is utilized in insulation coordination studies. Statistical overvoltage studies for energization, re-strike, fault and fault-clearing are performed for the Dutch EHV grid and are presented

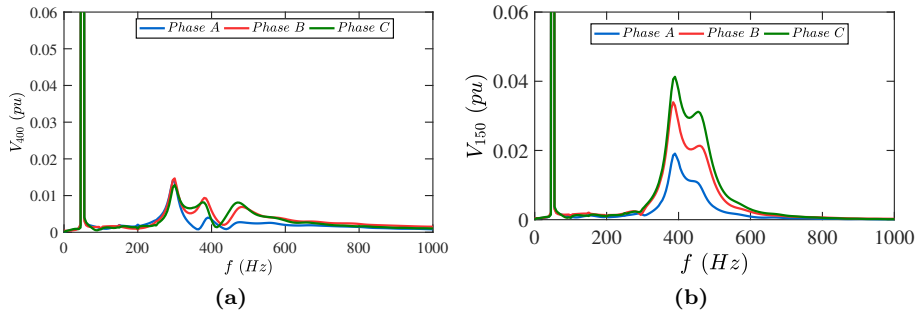


Figure 6.11: FFT transform on (a) 400 kV and (b) 150 kV voltage waveform upon energization with 22 km HV cable length.

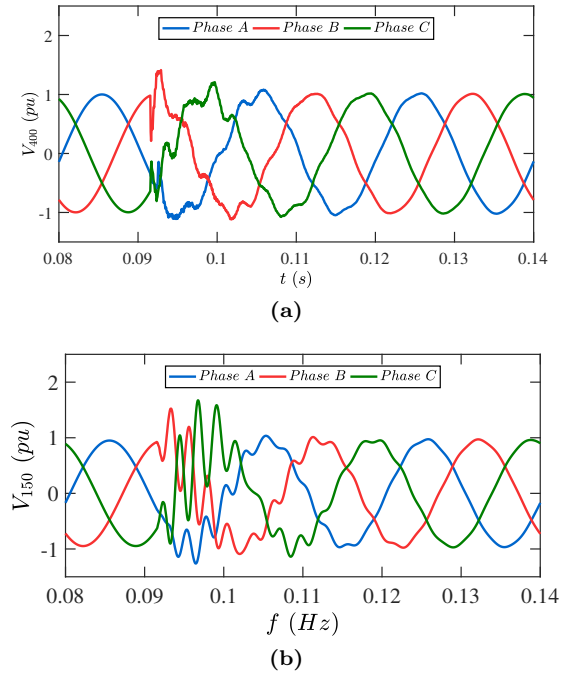


Figure 6.12: Voltage waveforms at (a) 400 kV and (b) 150 kV side of the transformer upon energization with 22 km HV cable length.

in the following sections.

6.2.1 Energization statistical overvoltage

For the evaluation of the energization overvoltages the statistical approach explained in Section 4.2.4 is adopted. The connection of interest is the Randstad south-ring (between substations WTR and BWK) with the mixed OHL-UGC connection. Energization overvoltages are statistical in nature since they highly depend on the point-on-wave of the circuit breaker pole closing as well as their spread among the three phases. Moreover, energization overvoltages are significantly affected by the exact configuration under study. To this end, six OHL-UGC configurations are examined for the south-ring connection differing in the position of the UGC in the connection.

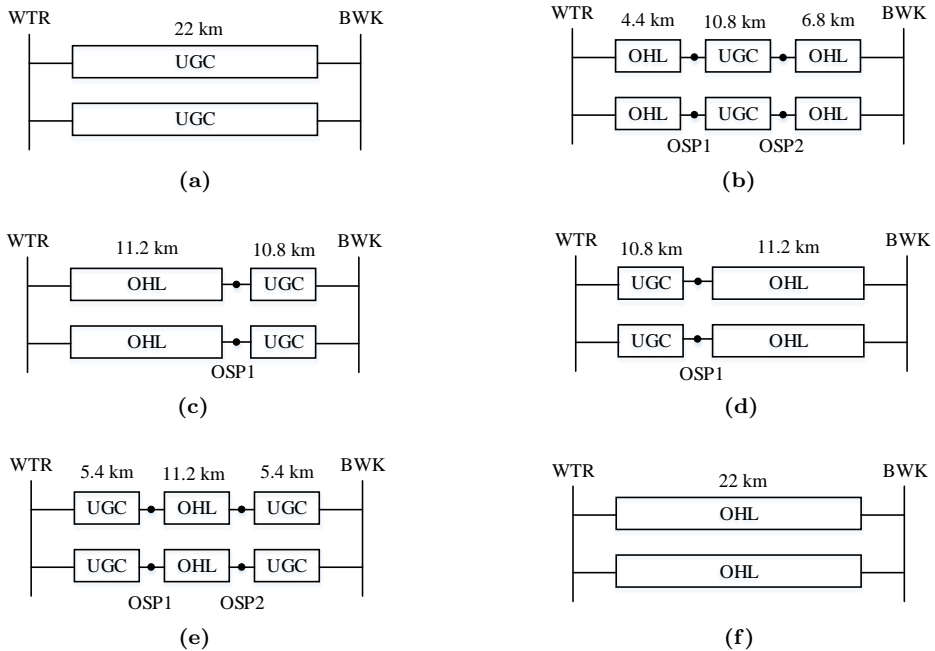


Figure 6.13: Six south-ring configurations for studying slow-front transients, with (a) only cable (C), (b) line-cable-line (L-C-L), (c) line-cable (L-C), (d) cable-line (C-L), (e) cable-line-cable (C-L-C) and (f) only line (L).

The configurations for the 22 km of the south-ring connection are (see Fig. 6.13):

- Case 1 (C): the complete connection of 22 km consists of UGC.
- Case 2 (L-C-L): the connection starts with 4.4 km OHL from WTR,

continues with 10.8 km of UGC and ends with 6.8 km of OHL to BWK (actual south-ring configuration).

- Case 3 (L-C): the connection starts with 11.2 km OHL from WTR and continues with 10.8 km of UGC to BWK.
- Case 4 (C-L): the connection starts with 10.8 km of UGC from WTR and continues with 11.2 km OHL to BWK.
- Case 5 (C-L-C): the connection starts with 5.4 km UGC from WTR, continues with 11.2 km of OHL and ends with 5.4 km of UGC to BWK.
- Case 6 (L): the complete connection of 22 km is OHL.

For the evaluation of the maximum energization overvoltage four switching scenarios are examined in order to study whether different actions result in different overvoltages:

- S1: energization of the top circuit from WTR side while the bottom circuit is out of service.
- S2: energization of the top circuit from WTR side while the bottom circuit is in service.
- S3: energization of the top circuit from BWK side while the bottom circuit is out of service.
- S4: energization of the top circuit from BWK side while the bottom circuit is in service.

The resulting maximum overvoltages obtained in 400 simulations, during the aforementioned switching scenarios, for each case are shown in Table 6.1 at four locations: substation WTR, substation BWK and the two transition points (transition point near WTR is referred to as OSP14 and near BWK as OSP32, in accordance with the naming in the southring). For cases 1 and 6, with single OHL and UGC, only values at the substations are given and for cases 3 and 4, consisting of UGC plus OHL, only one transition point is present. As demonstrated in Table 6.1, for nearly all cases and switching actions the highest maximum overvoltage is observed at the far open end of the energized connection while the lowest value occurs at the substation with the closing CB.

In general, when the south-ring connection is out of service substation BWK has a higher short circuit power than WTR. When one of the two circuits of the south-ring is in service the short-circuit strength of both substations slightly increases with BWK remaining the highest. When the connection is purely consisting of

Table 6.1: *Maximum energization overvoltages for the six configurations simulated for the four locations: S1,2 switching at WTR with second circuit out respectively in service; S3,4 switching at BWK with second circuit out and in service.*

		Case 1 (C)	Case 2 (L-C-L)	Case 3 (L-C)	Case 4 (C-L)	Case 5 (C-L-C)	Case 6 (L)
V_{WTR}	S1	1.62	1.83	1.74	1.69	1.71	1.78
	S2	1.38	1.49	1.74	1.43	1.51	1.73
	S3	1.82	1.92	1.87	1.92	1.97	2.18
	S4	2.00	1.75	2.99	1.76	1.77	2.16
V_{OSP14}	S1	-	1.75	1.85	-	1.82	-
	S2	-	1.68	1.85	-	1.99	-
	S3	-	1.89	1.80	-	1.96	-
	S4	-	1.67	1.95	-	1.65	-
V_{OSP32}	S1	-	1.79	-	1.75	1.91	-
	S2	-	1.76	-	1.86	1.57	-
	S3	-	1.82	-	1.86	1.66	-
	S4	-	1.56	-	1.67	1.90	-
V_{BWK}	S1	1.71	1.87	1.89	2.18	1.96	2.79
	S2	1.88	1.91	1.89	2.87	1.75	2.11
	S3	1.72	1.60	1.72	1.53	1.63	1.52
	S4	1.38	1.37	1.45	1.37	1.43	1.47

UGC (case 1) the lowest overvoltage at the open end (WTR for S3, S4 and BWK for S1, S2) is observed for S1 and the highest for S4. That is in accordance with the observations of [10, 105] where for cable connections the maximum overvoltage increases as the short circuit power increases. On the other hand, for a purely OHL connection (case 6) the lowest overvoltage at the open end is observed for S2 (V_{BWK} when energizing from WTR, having similar values as with S3 and S4 at WTR) and the highest for S1. This is also expected since for OHL connections the maximum overvoltage increases as the short circuit power decreases.

For the mixed OHL-UGC configurations it can be seen that overvoltages, almost reaching 3 pu, are observed at the far end for switching S2 and S4 (where the second circuit is in service) while the overvoltages on the switching end are lower compared with the other two switching scenarios. More specifically, for S2 and S4 the maximum overvoltages are observed for case 4 and case 3 respectively where for both cases the OHL part is at the far end of the connection.

The highest maximum overvoltage for each switching scenario is marked with red in Table 6.1 and it can be observed that they are within the standards for the

Switching Impulse Withstand Level (SIWL) ($1050 \text{ kV} \approx 3 \text{ pu}$) while the maximum overvoltages of S1, S2 and S4 are above the SIWL value with safe margin ($913 \text{ kV} \approx 2.66 \text{ pu}$) indicated by [120]. The corresponding voltage waveforms of the aforementioned worst cases are shown in Fig. 6.14. All voltage waveforms are characterized with frequency components in excess of 1 kHz, which are responsible for the highest overvoltage peaks although they are of short duration and vanish within typically a half power cycle.

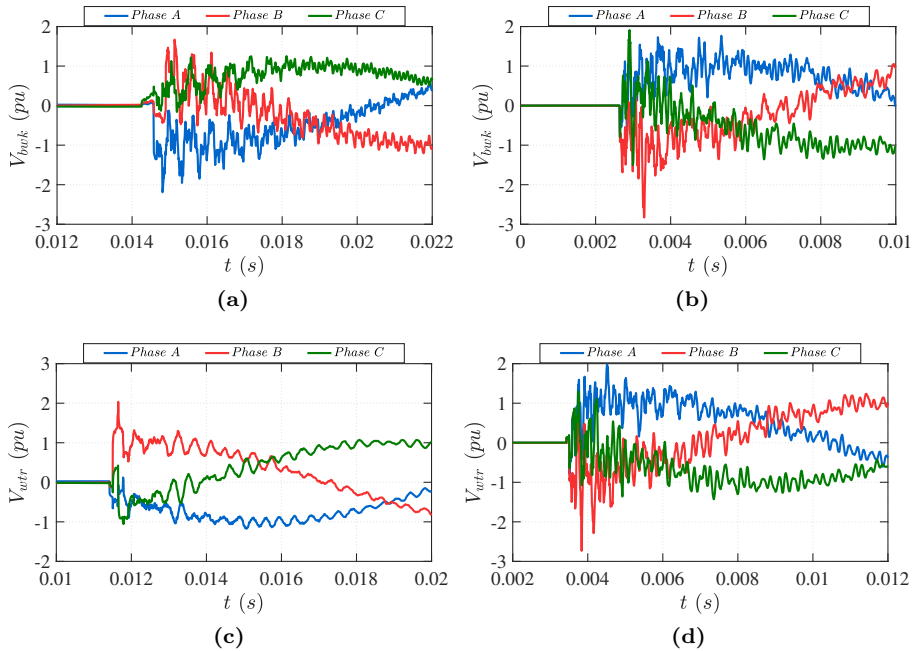


Figure 6.14: Voltage waveforms during energization for (a) switching scenario S1 and case 6, (b) switching scenario S2 and case 4, (c) switching scenario S3 and case 6 and (d) switching scenario S4 and case 3.

Another important aspect, besides the configuration of the cable connection of interest, is how the presence of more cable connections in the EHV network would affect the slow front overvoltages at a specific point in the network. In order to study this effect two new cable connections are placed in the model of the Dutch 380 kV grid (in addition to the south-ring) while the connection of interest for the maximum overvoltage study is the base mixed OHL-UGC south-ring connection (case 2). The two additional cables are configured as:

- Cable 1: addition of the north-ring cable configuration between substations

BWK and BVW (see Fig.1.3) which is in close proximity to the south-ring connection.

- Cable 2: addition of a mixed OHL-cable configuration (C-L-C-L-C-L) with three cable parts of 22 km, 18 km and 20 km respectively, between substations KIJ and DOD (see Fig. 4.2) which is more distant to the south-ring connection.

The resulting maximum overvoltages of the two additional cable scenarios compared with the base case are shown in Fig. 6.15 for the four switching actions S1-S4. It is observed that when the south-ring circuit is energized from WTR side (Fig. 6.15a and Fig. 6.15b) the addition of Cable 1 has hardly effect or even causes a small reduction in the maximum switching overvoltage. When switching the circuit from substation BWK (see Fig. 6.15c and Fig. 6.15d) which is the substation where Cable 1 is connected there is at most a slight increase in the maximum overvoltage when Cable 1 is added. In general, it can be concluded that the addition of a mixed OHL-cable configuration, with relatively small amount of cable, close to the connection of interest only slightly affects the maximum switching overvoltage. On the other hand, the addition of connection Cable 2, which consists of relatively long cable lengths, causes a significant increase in the energization overvoltages at all four locations for all switching scenarios. However, even in this case the switching overvoltages remain below the SIWL. Nevertheless, one should be careful when integrating new mixed OHL-UGC connections containing long UGCs since their addition can affect switching overvoltages even at remote connections.

In Appendix D.2.1 an overview of averages and standard deviations is provided related to the simulations for Table 6.1 and Fig. 6.15.

6.2.2 Re-strike statistical overvoltage

During line de-energization the contacts of the CB do not separate abruptly. In this time a re-strike or re-ignition can occur [74] if the voltage at the terminals of the CB exceeds its voltage withstand level. At that instant a breakdown of the CB dielectric takes place and the system is re-energized. If the CB re-closed within the first quarter of a cycle after opening, the phenomenon is called re-ignition. Re-strike is a one of the most severe transient phenomena which can result in severe overvoltages since the de-energized line still have charge and it is possible for the source and line voltage to have a voltage difference of 2 pu when interruption and re-strike occur at opposite voltage extremes. The resulting oscillation adds to a theoretical peak overvoltage of 3 pu when disregarding transmission line effects.

For the study of re-strike overvoltages the connection of interest is again the

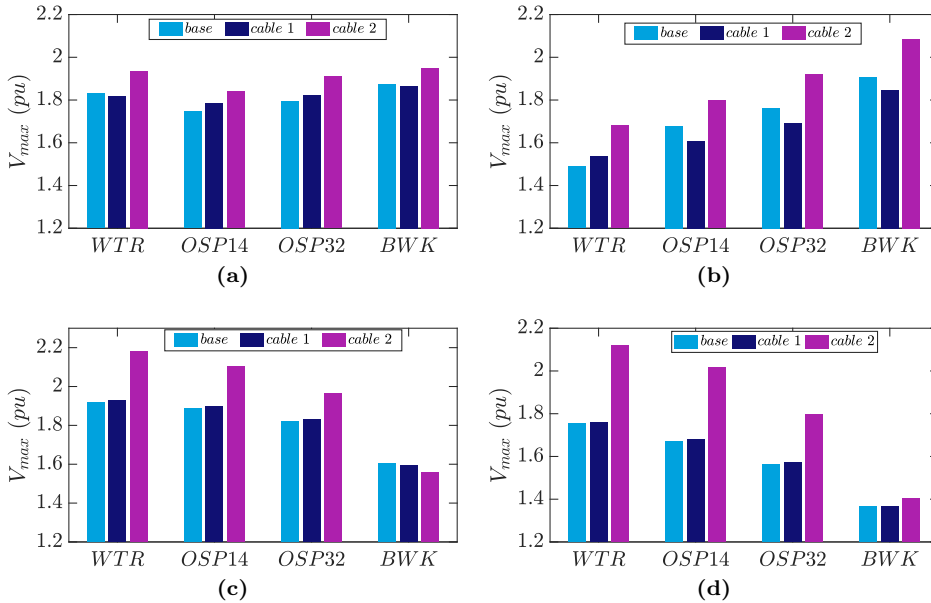


Figure 6.15: Maximum energization overvoltages for the two additional cable scenarios and at the four locations for switching action at WTR with second circuit (a) out of, (b) in service and at BWK with second circuit (c) out of and (d) in service.

Randstad south-ring. Re-strike overvoltages are also statistical in nature since they highly depend on the point-on-wave of the circuit breaker re-closing. As in the energization overvoltage study, the OHL-UGC configurations from Fig. 6.13 are examined for the south-ring connection and each of them are simulated for 400 switching timings.

For the evaluation of the maximum re-strike overvoltage four scenarios are investigated:

- R1: re-closing of the top circuit from WTR side while the bottom circuit is out of service.
- R2: re-closing of the top circuit from WTR side while the bottom circuit is in service.
- R3: re-closing of the top circuit from BWK side while the bottom circuit is out of service.

Table 6.2: Maximum re-strike overvoltages for the six configurations at the four locations: R1,2 for reclosing at WTR with second circuit out of respectively in service; R3,4 reclosing at BWK with second circuit out of respectively in service.

		Case 1 (C)	Case 2 (L-C-L)	Case 3 (L-C)	Case 4 (C-L)	Case 5 (C-L-C)	Case 6 (L)
V_{WTR} (pu)	R1	2.30	2.80	2.56	2.44	2.50	2.48
	R2	1.98	2.07	2.14	1.99	2.13	2.31
	R3	2.88	3.06	2.87	3.05	3.27	3.27
	R4	3.09	2.65	5.21	2.61	2.62	3.25
V_{OSP14} (pu)	R1	-	2.63	2.71	-	2.91	-
	R2	-	2.41	2.44	-	3.24	-
	R3	-	3.05	2.74	-	3.23	-
	R4	-	2.47	2.90	-	2.38	-
V_{OSP32} (pu)	R1	-	2.69	-	2.63	2.86	-
	R2	-	2.67	-	2.79	2.13	-
	R3	-	2.84	-	2.95	2.50	-
	R4	-	2.24	-	2.42	3.00	-
V_{BWK} (pu)	R1	2.51	2.76	2.82	3.30	2.91	4.12
	R2	2.70	2.92	2.50	5.40	2.46	3.14
	R3	2.57	2.35	2.49	2.18	2.37	2.01
	R4	1.90	1.81	2.05	1.82	1.91	1.89

- R4: re-closing of the top circuit from BWK side while the bottom circuit is in service.

The resulting maximum overvoltages at the four locations, for all six OHL-UGC configurations are shown in Table 6.2. It can be observed that for all cases and re-strike scenarios the highest maximum overvoltage takes place at the far open end of the re-closed connection while the lowest at the substation with the re-closing CB. The highest maximum overvoltage for each re-strike scenario is marked with red in Table 6.2. The highest values are observed when the second circuit is in service and the re-closing line far-end is OHL. Moreover, it is evident that the voltage surpasses the theoretical maximum value of 3 pu as observed also in [8]. Due to reflections and refractions in an OHL-UGC circuit with longer cable lengths and the inclusion of cross-bonding joints in the cable configuration the re-strike overvoltages can surpass this theoretical limit as explained in [8].

From the above observation, in the case of comparable lengths between OHL and UGC in a mixed configuration it is advised to energize the circuit from the substation with is connected to the OHL part in order to limit the maximum

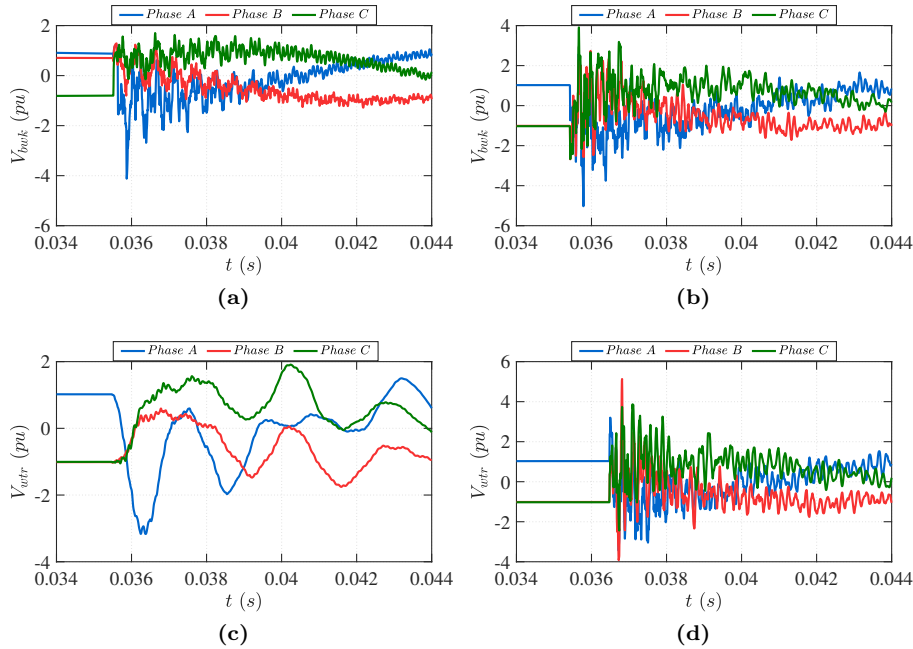


Figure 6.16: Voltage waveforms during re-strike for (a) scenario R1 and case 6, (b) scenario R2 and case 4, (c) switching scenario R3 and case 5 and (d) switching scenario R4 and case 3.

overvoltages. The corresponding voltage waveforms of the worst cases marked in red are shown in Fig. 6.16. All voltage waveforms except from R3 are characterized by high frequency components which are responsible for the highest overvoltage peaks although they are of short duration. These high frequency oscillations are suppressed when cable segments are present near both substations.

Also for re-strike transients the effect of including two additional cable connections (Cable 1 and Cable 2 in Section 6.2.1) is studied. The resulting overvoltage comparison is shown in Fig. 6.17. The trend of the maximum overvoltages during re-strike is similar to the one observed during energization.

Appendix D.2.2 provides an overview of the simulations for Table 6.2 and Fig 6.17 in terms of averages and standard deviations.

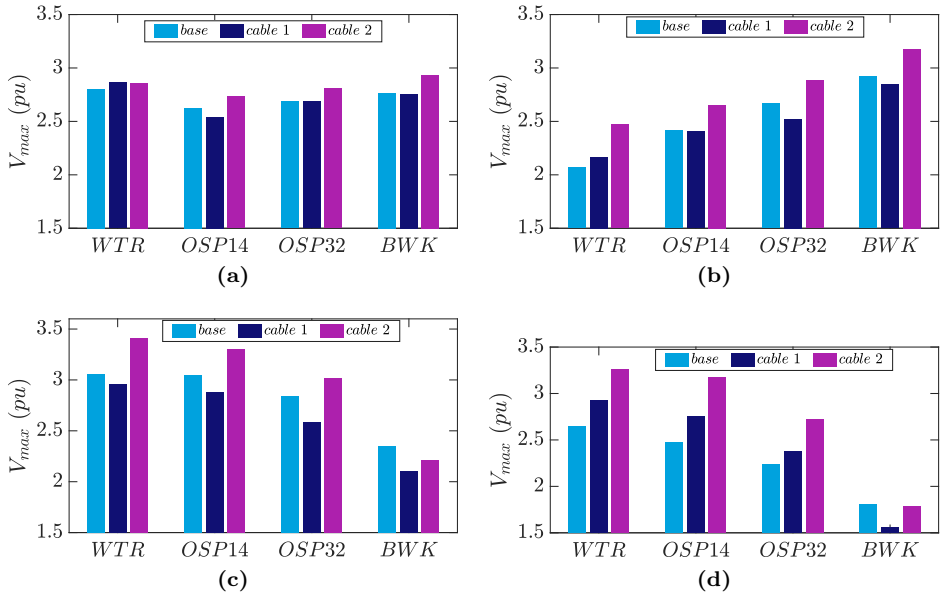


Figure 6.17: Maximum energization overvoltages for the two additional cable connections and at the four locations for re-strike scenarios: reclosure at WTR with second circuit (a) out of, (b) in service and at BWK with second circuit (c) out of and (d) in service.

6.2.3 Fault and fault-clearing statistical overvoltage

When a fault occurs in the network, high short-circuit currents trigger circuit breakers to open in order to disconnect the line with the fault. The sudden drop of the short-circuit current can cause overvoltages in nearby substations. For the fault and fault-clearing overvoltage analysis a statistical evaluation is applied since the fault location and the fault timing vary and cannot be controlled. Eight fault situations are examined for the Randstad south-ring and are listed below in case of a single-phase to ground fault (this is the most common type of fault):

- F1: fault on the top circuit at WTR while the bottom circuit is out of service.
- F2: fault on the top circuit at WTR while the bottom circuit is in service.
- F3: fault on the top circuit at BWK while the bottom circuit is out of service.

- F4: fault on the top circuit at BWK while the bottom circuit is in service.
- F5: fault on the top circuit at OSP14 while the bottom circuit is out of service.
- F6: fault on the top circuit at OSP14 while the bottom circuit is in service.
- F7: fault on the top circuit at OSP32 while the bottom circuit is out of service.
- F8: fault on the top circuit at OSP32 while the bottom circuit is in service.

Three configurations are examined for the south-ring connection: the base case, a pure OHL and a pure cable where for the latter two situations only fault types F1-F4 were applied since no transition points are present. Each of them are simulated for 20 switching timings uniformly distributed in one power cycle. The results of the maximum overvoltages during fault and fault-clearing for the three configurations and the first four fault scenarios at the two substations are depicted in Table 6.3.

Table 6.3: *Maximum overvoltages during fault and fault-clearing for the three configurations and the fault scenarios at WTR (F1 with one and F2 with two circuits in service) and BWK (F3 with one and F4 with two circuits in service) substations.*

		F1	F2	F3	F4
V_{WTR} (pu)	Base	1.34	1.46	1.19	1.26
	OHL	1.29	1.34	1.23	1.27
	Cable	1.45	1.56	1.49	1.51
V_{BWK} (pu)	Base	1.18	1.22	1.30	1.48
	OHL	1.19	1.22	1.40	1.41
	Cable	1.56	1.60	1.57	1.65

The level of maximum overvoltages during fault transients for the south-ring connection is significantly lower as compared with energization and re-strike transients and far-below the SIWL. In contrast with energization and re-strike transients, the maximum overvoltages for all four fault types are observed for the pure cable configuration.

Fault types F5-F8 are applicable only for the base (mixed OHL-UGC) configuration and the resulting maximum overvoltages along the connection (substation WTR, transition points OSP14 and OSP32 and substation BWK) are shown in Fig. 6.18. For F6-F8 the maximum overvoltage is depicted at the location of the fault while for F5 it is observed in the substation closest to the

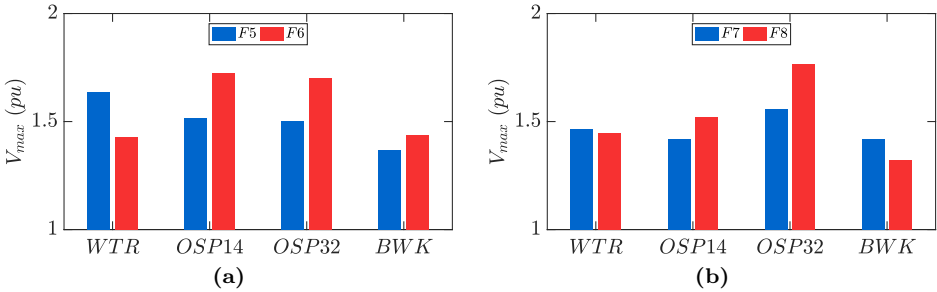


Figure 6.18: Maximum overvoltages along the connection for fault scenarios (a) F5 and F6 at OSP14 (with one respectively two circuits in service), (b) F7 and F8 at OSP32 (with one respectively two circuits in service).

fault. Furthermore, highest overvoltages are observed when the second circuit of the connection is in service (F6 and F8).

Also in the case of the fault and fault-clearing transients the effect of including two additional cable connections (Cable 1 and Cable 2) is studied and the resulting overvoltages are shown in Table 6.4. The highest overvoltages (indicated in red for each scenario) are observed when the fault takes place at the transition points (F5-F8). The overvoltages for these scenarios are explicitly depicted in Fig. 6.19. Similarly with the two previous slow-front transient studies, the addition of a mixed OHL-cable configuration, with relatively small amount of cable, close to the connection of interest only slightly affects the maximum overvoltage causing a slight shift to higher values. The addition of a long cable length causes a significant increase in the overvoltages at all four locations for all eight fault scenarios. However, the overvoltages remain well below the SIWL.

6.3 Conclusion

For the series resonance study the effect of the load and 150 kV cable length on the series resonance damping and frequencies was investigated and it can be concluded that the load model (series or parallel) has a dominant effect on the resonance damping whereas the variation in 150 kV cable length shifts the harmonic frequencies of energization. The parametric analysis also showed that the transformer inductance has a major effect on the severity of the series resonance. From the south-ring case study it can be concluded that under the specific conditions no severe series resonance case is caused by EHV cable energization, even when the 150 kV cable is adjusted to match the dominant

Table 6.4: *Maximum overvoltages for the eight fault scenarios and the two additional cable connections at the four locations of interest.*

		F1	F2	F3	F4	F5	F6	F7	F8
V_{WTR} (pu)	Base	1.34	1.46	1.19	1.26	1.64	1.43	1.47	1.45
	Cable 1	1.34	1.46	1.27	1.29	1.67	1.47	1.53	1.48
	Cable 2	1.49	1.66	1.43	1.45	1.81	1.62	1.67	1.64
V_{OSP14} (pu)	Base	1.25	1.31	1.29	1.29	1.52	1.72	1.42	1.52
	Cable 1	1.28	1.37	1.34	1.33	1.50	1.75	1.46	1.58
	Cable 2	1.39	1.53	1.51	1.48	1.62	1.90	1.59	1.77
V_{OSP32}	Base	1.32	1.33	1.26	1.29	1.50	1.70	1.56	1.77
	Cable 1	1.33	1.38	1.34	1.33	1.60	1.79	1.60	1.76
	Cable 2	1.45	1.54	1.52	1.50	1.75	1.96	1.72	1.99
V_{BWK} (pu)	Base	1.18	1.22	1.30	1.48	1.37	1.44	1.30	1.32
	Cable 1	1.15	1.20	1.39	1.46	1.34	1.38	1.24	1.27
	Cable 2	1.26	1.30	1.58	1.59	1.52	1.52	1.40	1.45

energization frequency. This can be mainly attributed to the low leakage inductance of the transformer.

For slow-front transients, the effect of cable integration on energization, re-strike and fault transients was examined. For energization transients, when the connection to be energized is purely consisting of cable the maximum overvoltage increases as the short circuit power increases. On the other hand, for a purely OHL connection the maximum overvoltage increases as the short circuit power decreases. Thus, when energizing a cable is safer to do so from the relatively weak side of the grid if no resonance is excited. For re-strike transients, which are most severe, the highest overvoltages are observed when, for a double circuit connection, the second circuit is in service and the re-closing line far-end is OHL. Thus, it can be concluded that in the case of comparable lengths between OHL and UGC in a mixed configuration it is advised to energize the circuit from the substation with is connected to the OHL part in order to limit the maximum overvoltages. The fault transients proved to be the least harmful with overvoltages remaining below 2 pu for all studied scenarios.

For the three examined types of slow-front transients (energization, re-strike and fault) the addition of a mixed OHL-UGC connection, which incorporates long cable lengths, causes a significant increase in the overvoltages for all studied scenarios with highest overvoltages observed during re-strike. Thus, the integration of new connections containing several tens of kilometers of UGCs should be carefully studied since their addition can affect overvoltages also at connections further away.

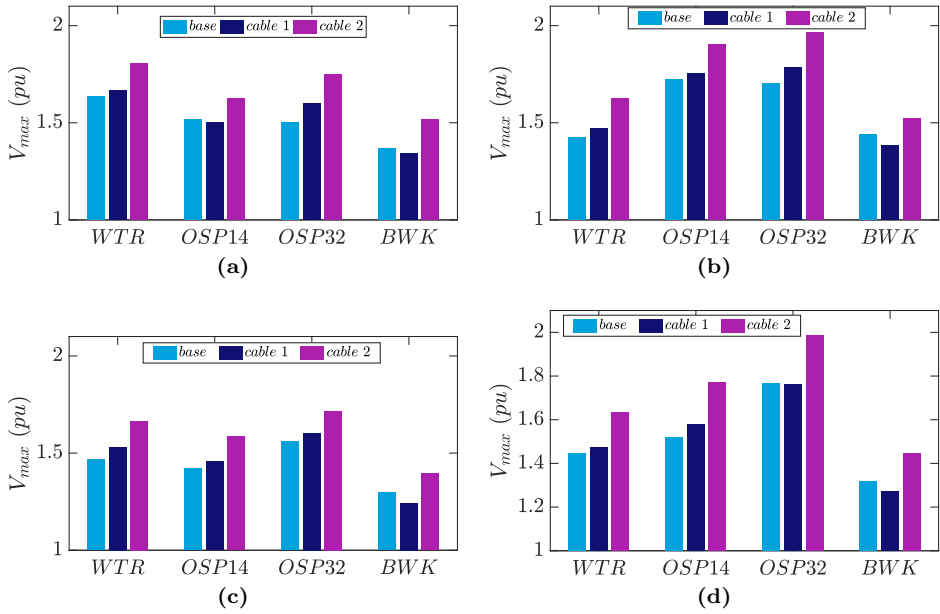


Figure 6.19: Maximum overvoltages for the two additional cable connections and at the four locations for fault at OSP14 (a) F5: one circuit, (b) F6: two circuits in service; at OSP32 (c) F7: one circuit and (d) F8: two circuits in operation.

7

Conclusions and Recommendations

7.1 Conclusions

EHV underground power cables integrated into the EHV transmission grid have impact on the transient and resonant grid behavior. This thesis evaluates appropriate simulation models for all network components and a more detailed transient model for the cable is presented. The simulation models are validated through on-line transient measurements from switching actions, using a rather unconventional measuring system, based on a Differentiating/Integrating principle. The validated simulation model is used to investigate the required modeling depth at both the same and across voltage levels as well as to evaluate the overvoltages during series resonance and slow-front studies when more cables are part of the EHV network.

Underground Power Cable Modeling

A sensitivity analysis was conducted for the cable design parameters as well as for the cable layout and bonding configurations. It is concluded that the conductor radius and insulation thickness have a significant effect in the harmonic impedance but the influence of the metal screen and outer sheath thickness are

minor. Furthermore, the bonding and trench type together with the number of simulated major sections should be accurately modeled since their effect in the harmonic impedance is critical even at frequencies down to 1 kHz.

For transient modeling of transmission lines a new model was developed based on the Finite-Difference Time Domain (FDTD) approach, which takes into account the frequency dependency of the series impedance, and implemented in PSCAD/EMTDC software. The motivation was to overcome stability problems, encountered when the Frequency-Dependent Phase Model (FDPM) was used for simulating connections with high level of design detail. From the comparison of the two models, it can be concluded that the FDTD model presents improved stability while the accuracy is comparable with the FDPM. However, the computational time needed for the FDTD model is significantly larger which limits its use to cases where FDPM instabilities cannot be circumvented by model simplifications without loss of accuracy. More specifically, the FDTD model could be used when short cable segments cannot be merged and incorporated as a larger segment or when a system contains a large amount of mutually coupled cables. Finally, the existence of an alternative accurate model (FDTD) is of great importance as it can be used as a benchmark to test simplified FDPM configurations, as in the case of the south-ring connection, to reassure that simplifications do not compromise results.

Network Modeling Detail

The necessary network modeling depth at the EHV level was investigated for two different study purposes: accurate representation of the maximum overvoltage during slow-front transients and accurate representation of the EHV network harmonic behavior. For the first study, two methods were utilized (namely "top-down" and "bottom-up") and both of them indicated that it is necessary to include in the model all the lines which are connected to substations, up to about 80 km distance in this study from the source of disturbance. Moreover, it was concluded that when a reference model, containing full detail of the EHV network, is not available ("bottom-up" approach), a reduced size reference network, up to a distance of at least 80 km, can be defined where all connections are represented by FD models. This can serve as a local reference to study further simplification and its effect on overvoltage prediction. From the accurate representation of the EHV network harmonic behavior, it was concluded that HVDC filters located nearby the connection of interest greatly affect the frequency and magnitude of the resonance peaks and should be accurately modeled, while HVDC converter stations having a large electrical distance from the point of interest can be modeled as a parallel PQ load based on the powerflow. Regarding the modeling depth for harmonic studies, the area that needs to be modeled in higher detail is

larger than needed for overvoltage study.

A downstream network affects the switching transient response of the EHV network mainly through the type of the 150 kV links. It has significant effect on the damping and the frequency of the energization as well as the maximum overvoltage. The end customer load model affects only the damping of the oscillations and together with the model detail of the 150 kV connections, they only slightly affect the maximum overvoltage. The effect of using simplified lumped models for the downstream model was investigated both in time and frequency domain. From the frequency domain results, it can be concluded that the use of simplified lumped models produce more damping at the low frequency resonance peaks but the predicted dominant frequency is close to the detailed model. From the time domain results, it can be concluded that both investigated simplifications present good agreement with the fully detailed model.

Simulation Model Validation with Measurements

The developed simulation models were validated with on-line measurements during switching actions. The custom-made measurement system used for this validation is based on the Differentiating/Integrating (D/I) principle. It displays improved EMC properties compared with conventional measurement techniques (e.g. RC dividers) but due to the use of open air sensors the measurements at each phase couple to the other phases as well. With appropriate sensor positioning, reliable decoupling of the measurements is achieved and from the statistical analysis of uncertainties in the measurements it can be concluded that uncertainties in the decoupling matrix elements have a minor effect on the maximum switching overvoltages both at the transition points and at substation BWK. Thus, the D/I measurement technique proves to be a competitive alternative compared with galvanically connected divider based voltage measurements at EHV transmission lines.

From the comparison between the simulation model of the Dutch EHV grid and the measurements, during switching operations the measured and simulated voltage waveforms are almost identical for all investigated types of switching actions and locations. Moreover, the dominant frequencies produced during energization show a close match with a slight shift to higher frequencies for the simulation model. The measurements confirm that no dangerous overvoltages are expected for both the transition points and the substation, in agreement with the simulations. Even at the worst case scenario, where the circuit is switched when one of the three phases is close to the peak voltage the maximum overvoltage is well below the switching impulse withstand voltage limits. Moreover, no resonance is excited.

Resonance and Slow-front Overvoltage Study

The validated simulation models were used for conducting resonance and slow-front transient overvoltage studies, where the Dutch 380 kV grid was used as a case study. For the series resonance study, it can be concluded that the load model and the length of the 150 kV cable have a significant effect on the resonance damping and the dominant energization frequencies. From the parametric analysis, it was observed that the transformer inductance has a major effect on the severity of the series resonance where for very low transformer inductances there is practically no dominant resonance overvoltage.

For energization transients, when the connection to be energized is purely consisting of cable the maximum overvoltage increases as the short circuit power increases while the opposite occurs for purely OHL connections. It can be advised to energize a cable connection from the weaker side of the grid if no resonance is excited. For both energization and re-strike transients, the highest overvoltages are observed when the energized or re-closed line far-end is OHL. Thus, it can be concluded that in the case of mixed OHL-UGC connection, its energization should be initiated from the substation where the OHL part is connected, in order to limit the maximum overvoltages. The fault and fault-clearing transients proved to be the least harmful with overvoltages remaining below 2 pu for all studied scenarios. Finally, for energization, re-strike and fault transients the addition of a mixed OHL-UGC connection, which consists of long cable lengths, causes a significant increase in the overvoltages for all studied scenarios. Thus, the integration of new connections containing several tens of kilometers of UGCs should be carefully studied since their addition can affect overvoltages even at connections further away.

7.2 Dissertation Contribution

The main contributions of this dissertation can be summarized as follows:

- A new transmission line mathematical model was developed based on the Finite Difference Time Domain (FDTD) approach which is mainly used in the field of electromagnetics. This model is able to simulate an arbitrary number of mutually coupled conductors (up to 24 in the current thesis) and it contains the full frequency-dependency of the series impedance. The FDTD model can successfully simulate a complicated cable configuration for which the Frequency-Dependent Phase Model (FDPM) encountered stability problems. The FDTD model was compared with the well established and highly accurate FDPM and it presented comparable

accuracy while having improved stability.

- The FDTD mathematical model was also interfaced with PSCAD/EMTDC software by means of a custom-made component with interfacing dialog box. This component can be incorporated into large networks consisting of various types of models and arbitrary number of conductors and length can be defined. The FDTD model, can also serve as a good alternative in cases where the FDPM encounters stability problems.
- Two approaches for defining the necessary modeling depth were developed and tested. For the modeling detail at the same voltage level, preliminary boundaries were derived. For the modeling detail across voltage levels, the downstream network parameters affecting the harmonic behavior and maximum overvoltages of the EHV grid were identified. Different types of simplified models for the downstream network based on lumped parameters were formed and their effect on the EHV system frequency and time domain response were identified.
- A measurement system, not commonly used for transient power system measurements, based on the Differentiating/Integrating principle, was tailored for application at the EHV network. The system response was proven to be accurate, with a constant transfer function for up to several MHz. This bandwidth is more than sufficient for slow-front and fast-front transient measurements. Moreover, taking advantage of a proper choice of sensor placement an efficient and accurate measurement decoupling scheme was defined.
- The D/I measurement system was tested for two different configurations, OHL-UGC transition points and GIS substation. It was proved to be a reliable, cheap and convenient way to measure both low and high frequency transients during switching actions with the complete EHV network in operation. Consequently, measurements of such system can be used for network simulation model validation.
- The impact of cable integration in an existing transmission network on series resonance, energizing, re-strike and fault transients was examined. The results can be used for establishing countermeasures to limit the maximum overvoltages by specific network operation sequences without the need of extra infrastructure.

7.3 Recommendations for future work

Some aspects of this thesis could be improved with future research. More specifically, regarding the Finite Difference Time Domain Model some ringing was

observed in the results mainly during fast voltage transitions. These oscillations are mostly caused due to the numerical integration technique used, which is the trapezoidal rule as well as the choice of central differences of first order. These numerical oscillations can be minimized or even eliminated when using a more elaborate integrating technique and central differences of higher order. Moreover, improvements can be made in the computational efficiency of the FDTD algorithm when implemented in PSCAD for a large system, e.g. by assigning a different time step for the FDTD component and the rest of the network.

The proposed D/I measuring system contains open air sensors and for the determination of the decoupling matrix between the sensors and the three phases the number of unknowns exceeds the number of equations and assumptions need to be made. However, by switching the three phases separately (e.g. through controlled switching) it is possible, using the three resulting distinct voltage jumps, to calculate all the unknowns uniquely. It would be interesting to compare the results between the decoupling procedure used in this thesis with the explicitly calculated decoupling components.

Finally, in this thesis the impact of passive network components and models was investigated for the resonant and transient grid behavior. However, it would be interesting to study the effect of active components, such as power electronic devices, during an electromagnetic transient event and their interaction with the rest of the network.



PSCAD Model Implementation

The Randstad south-ring connection consists of a cable part in between two OHL parts (see Fig 1.2). More specifically, the OHL from WTR substation to the cable transition point is 4.4 km and a double circuit at 150 kV level is also mounted at the same pylons. Then the line continues for 10.8 km as underground cable (two cables per phase resulting in 12 parallel cables). From the second transition point there is a 6.8 km OHL to substation BWK.

For the cable part, each cable comprises of 28 segments with length varying from 0.1 km up to 1 km, and different trench types. Five types of open trench and two types of horizontal directional drilling were used for the laying of the cable segments. The 28 cable segments are grouped into 12 minor sections and three successive minor sections form one major section of approximately 2.7 km length. Within one major section, the minor sections are connected via cross-bonding joints, while the major sections are connected via a grounded straight through joint. Two bare 300 mm² copper wires (compensating wires) are laid underground along the whole cable connection (0.3 m above the cables belonging to either circuit). The induced currents in this loop compensates the magnetic flux and helps to limit step voltages of human beings above the ground to a safe level [19].

The second OHL part comprises a double circuit at 380 kV level and two compensating wires (bundles each with two sub-conductors) to limit the ambient

electromagnetic field at 50 Hz [19]. Detailed information on UGC and OHL implementation in PSCAD is provided in A.1 and A.2. In A.3 details on the implementation of the FDTD method are provided.

A.1 Cable data

The physical single core cable used for the south-ring connection consists of seven distinct layers, as shown in Fig. A.1a. The core conductor is stranded, there are two semi-conducting layers (at the inside and outside of the insulation). There is a double layer earth screen consisting of a copper wire screen and a lead sheath surrounded by an insulating outer sheath. However, it is not possible to model all seven cable layers in commercial EMTP software and an equivalent four layer single core cable model need to be constructed (ssee Fig. A.1b).

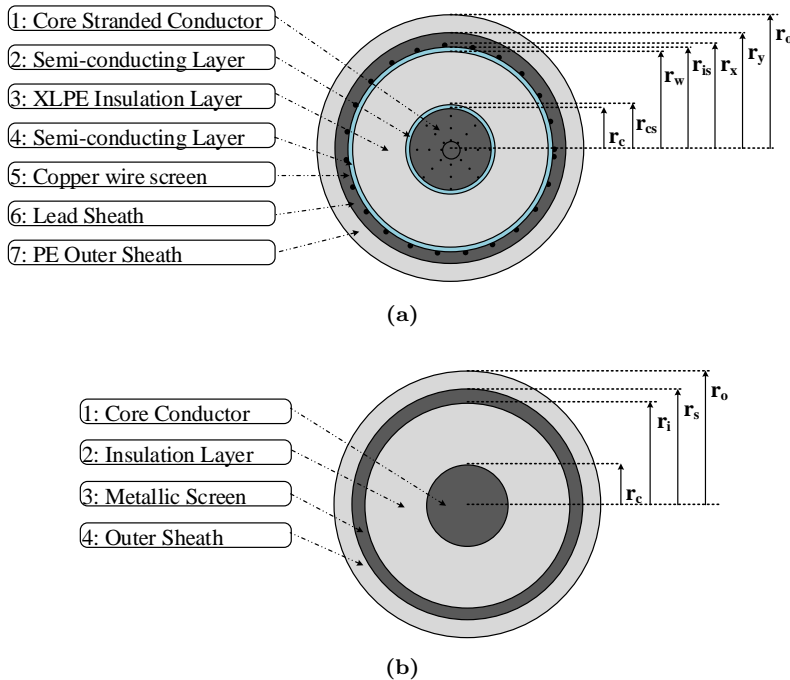


Figure A.1: Single core cable layers for (a) the physical and (b) the equivalent configuration used in EMTP modeling.

There are three main corrections that need to be made [19]:

1. Core Conductor

In EMTP software it is not possible to model stranded conductors and thus a solid copper conductor is used with corrected resistivity value in order to account for the empty spaces between the stranded/segmented wires of the conductor:

$$\rho_c = \rho_{cu} \frac{\pi r_c^2}{A} \quad (\text{A.1})$$

where ρ_{cu} is the resistivity of a solid copper conductor and A is the nominal area of the conductor.

2. Insulation layer

The semi-conductive layers are considered as part of the insulation. In order to calculate the outer radius of the insulation the copper wires in the screen are converted into a solid copper tube with the same DC resistance by adjusting its thickness. The outer radius of this equivalent layer is set to be equal to the inner radius of lead sheath r_x and its inner radius (i.e. the outer radius of the insulation) is calculated as:

$$r_i = \sqrt{r_x^2 - \frac{A_2}{\pi}} \quad (\text{A.2})$$

where A_2 is the nominal area of the copper wire screen.

Furthermore, in order for the equivalent insulation layer to have the same capacitance as the three combined layers the insulation permittivity needs to be corrected as in (A.3).

$$\varepsilon_i = \varepsilon_{xlpe} \cdot \frac{\ln(r_i/r_c)}{\ln(r_w/r_{cs})} \quad (\text{A.3})$$

Moreover, the copper wires of the screen are not straight along the cable but laid helical with N number of turns per meter. So a corrected equivalent permeability μ_I of the equivalent insulation layer is calculated as:

$$\mu_I = \mu_{xlpe} + \frac{\mu_{xlpe}}{\ln(r_i/r_c)} \cdot 2\pi^2 N^2 (r_i^2 - r_c^2) \quad (\text{A.4})$$

3. Metallic screen

The two layers of the metallic screen (copper and lead sheath) need to be converted into one equivalent solid tube. This can be achieved either by combining the layers with the same inner and outer radius and changing the resistivity of the layer to retain the DC resistance of the whole screen [74, 121] or by choosing for the equivalent layer the same resistivity as copper ($\rho_s = \rho_{cu}$) and correcting its outer radius [77]. For this model the

second option is chosen and the equivalent outer radius of the screen is calculated as:

$$r_s = \sqrt{\frac{\rho_s}{\rho_{Pb}}(r_y^2 - r_x^2) + r_x^2} \quad (\text{A.5})$$

where ρ_{Pb} is the resistivity of lead.

Since the outer radius of the metallic screen is changed and in order to keep the same outer radius of the cable the permittivity and permeability of the outer sheath need to be corrected as in (A.6) and (A.7) in order to retain the same admittance and impedance.

$$\varepsilon_o = \varepsilon_{pe} \cdot \frac{\ln(r_o/r_s)}{\ln(r_o/r_y)} \quad (\text{A.6})$$

$$\mu_o = \mu_{pe} \cdot \frac{\ln(r_o/r_y)}{\ln(r_o/r_s)} \quad (\text{A.7})$$

The values of the corrected parameters for the equivalent model are summarized in Table A.1.

Table A.1: *Corrected parameters for the equivalent four layer cable model.*

Radius		Resistivity		Permittivity		Permeability	
r_c (mm)	30.7	ρ_c (Ωm)	1.98×10^{-8}	$\varepsilon_{c,r}$	-	$\mu_{c,r}$	1
r_i (mm)	63.1	ρ_i (Ωm)	-	$\varepsilon_{i,r}$	2.79	$\mu_{i,r}$	1.17
r_s (mm)	63.7	ρ_s (Ωm)	1.68×10^{-8}	$\varepsilon_{s,r}$	-	$\mu_{c,r}$	1
r_o (mm)	71.5	ρ_i (Ωm)	-	$\varepsilon_{o,r}$	3.05	$\mu_{o,r}$	0.76

For the cable laying seven trench types were used; five open trench types, O1-O5 (see Fig. A.2a) with varying distances as shown in Table A.2 and two types of horizontal directional drilling, H1 and H2 (see Fig. A.2b and A.2c).

Table A.2: *Distance parameters for cable open trech type.*

	Δy (m)	Δx_1 (m)	Δx_2 (m)
O1	-0.90	0.60	8.45
O2	-1.15	0.60	8.45
O3	-0.90	0.75	8.45
O4	-1.15	0.75	6.95
O5	-0.90	0.75	6.95

Table A.3 shows the trench type and length for every cable segment.

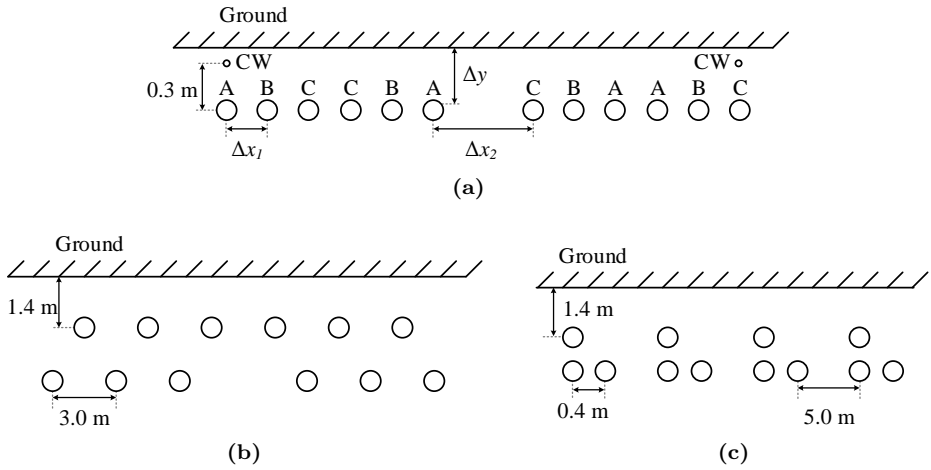


Figure A.2: Cable trench types with (a) open trench, (b) H1 and (c) H2 type of horizontal directional drilling where CW refers to compensation wires to lower the magnetic field strength above ground.

Table A.3: Cable segment trench type and length.

	Trench	Length (km)		Trench	Length (km)
MS01	O5	0.7	MS07	O4	0.6
	O3	0.2		H1	0.2
MS02	H1	0.4	MS08	O2	0.4
	O4	0.4		H1	0.5
MS03	O2	0.2	MS09	O1	1.0
	H1	0.5		O2	0.3
MS04	O1	0.3	MS10	H1	0.1
	H1	0.5		O4	0.5
MS05	O1	0.4	MS11	H1	0.5
	H1	0.3		O1	0.4
MS06	O1	0.3	MS12	O1	0.3
	O3	0.3		H1	0.2
MS06	H1	0.5		O3	0.1
	O4	0.4		H2	0.3

A.2 OHL data

The data for the overhead lines are given in Table A.4. The resistivities of both the 380 kV and 150 kV OHL are provided. The bundle conductors are replaced by single conductor with equivalent radius calculated according to:

$$r_{eq} = \sqrt[n]{nrR^{n-1}} \quad (\text{A.8})$$

where n is the number of sub-conductors in the bundle, r is the radius of each sub-conductor and R is the radius of the bundle. The relative permeability of every conductor is 1. The pylon configuration is demonstrated in Fig. A.3 both for the line between substation WTR and cable (OHL1) and transition point and substation BWK (OHL2).

Table A.4: Parameters of overhead line conductors. EW and CW are abbreviations for Earth Wires and Compensating Wires, respectively. The values for 380 kV level are equivalent to a bundle of 4 sub-conductors. The values for CW are equivalent to a bundle of 2 sub-conductors

	380 kV (m)	150 kV (m)	EW	CW
resistivity (Ωm)	2.05×10^{-6}	4.02×10^{-8}	4.78×10^{-8}	1.10×10^{-6}
radius (mm)	231	16.2	10.9	73.8

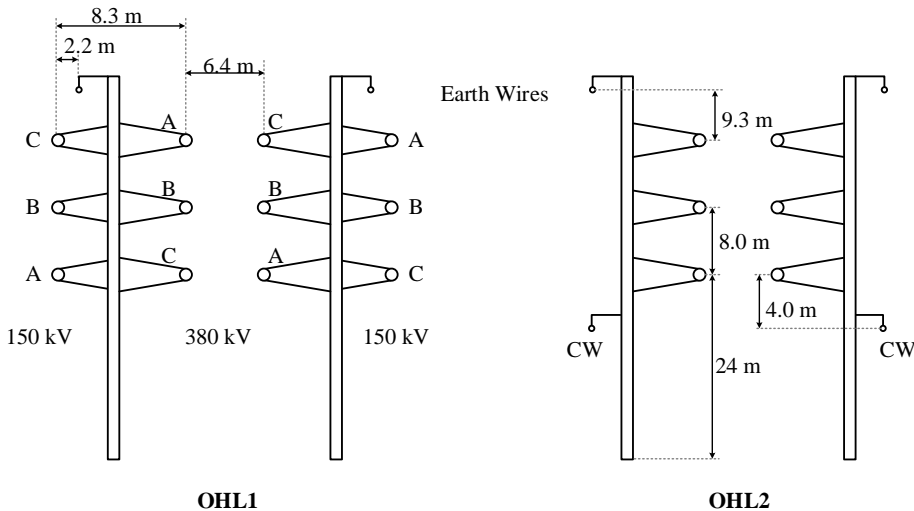


Figure A.3: Pylon configuration for OHL1 (left) and OHL2 (right) part.

A.3 Implementation in EMTP software

The equivalent circuit representation of (3.18) and (3.19) is demonstrated in Fig. A.4 and is the same as the one used in EMTP for modeling transmission lines, thus it can be incorporated into PSCAD/EMTDC software. The conductance matrix and history current sources were directly added at the EMTDC code of the custom component using the *EMTDC_ADDGM* and *CCBR* functions.

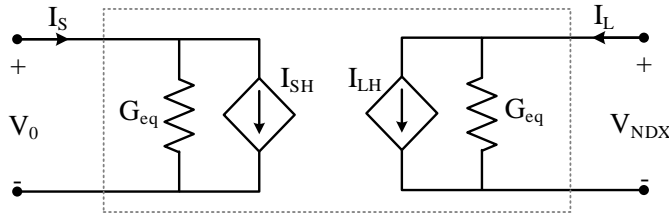


Figure A.4: *FDTD model equivalent circuit.*

The model implementation in PSCAD is performed in two steps:

- First an independent case file needs to be created where the definition of the cable characteristics (geometry, electrical properties etc.) is placed and the Line Constants (LC) routine is calculated. In this case instead of using the traditional FDPM vector fitting component (for fitting the characteristic impedance and propagation function) the Modified FDTD (MFDTD) vector fitting component is utilized (see Fig. A.5) where the fitting is performed in the series impedance.
- Then the custom FDTD component shown in Fig. A.6a should be placed in the case that needs to be studied and its input parameters need to be defined (see Fig. A.6b)

The input parameters to be defined by the user are:

1. The number of conductors of the OHL or cable (for the cable case the metallic sheath also counts as one conductor).
2. The name of the LC *.clo* file created during the first step.
3. An indication if the name of the LC file is an absolute or a relative path.
4. The length of the transmission line in km.

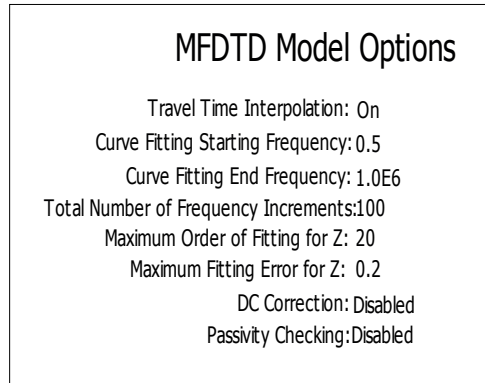
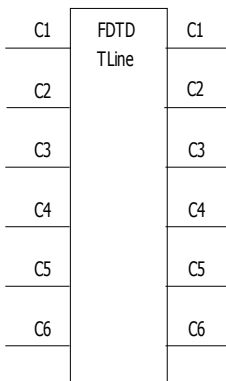
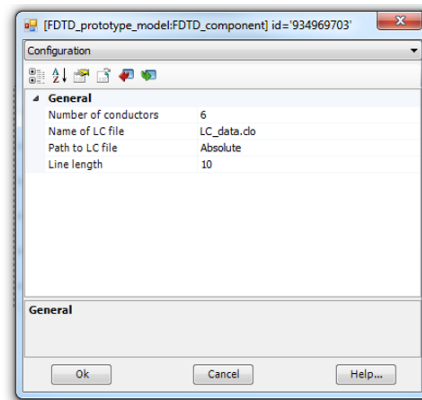


Figure A.5: *FDTD vector fitting component.*



(a)



(b)

Figure A.6: *FDTD model (a) pscad custom component and (b) input parameters.*

B

Downstream model

B.1 Statistical analysis

For the statistical energization study, presented in Section 4.2.4, four types of switching actions were performed:

- S1: Energization of the black circuit from WTR side while the white circuit is out of service.
- S2: Energization of the black circuit from WTR side while the white circuit is in service.
- S3: Energization of the black circuit from BWK side while the white circuit is out of service.
- S4: Energization of the black circuit from BWK side while the white circuit is in service.

For all switching actions the simulated overvoltages were measured in four locations: WTR, OSP14, OSP32 and BWK. The maximum overvoltage histograms at WTR, OSP14, OSP32 and BWK for S1-S4 are shown in Fig. B.1-Fig B.4 respectively. The fitted normal distribution mean and standard deviation values for the maximum switching overvoltages are presented in Table B.1.

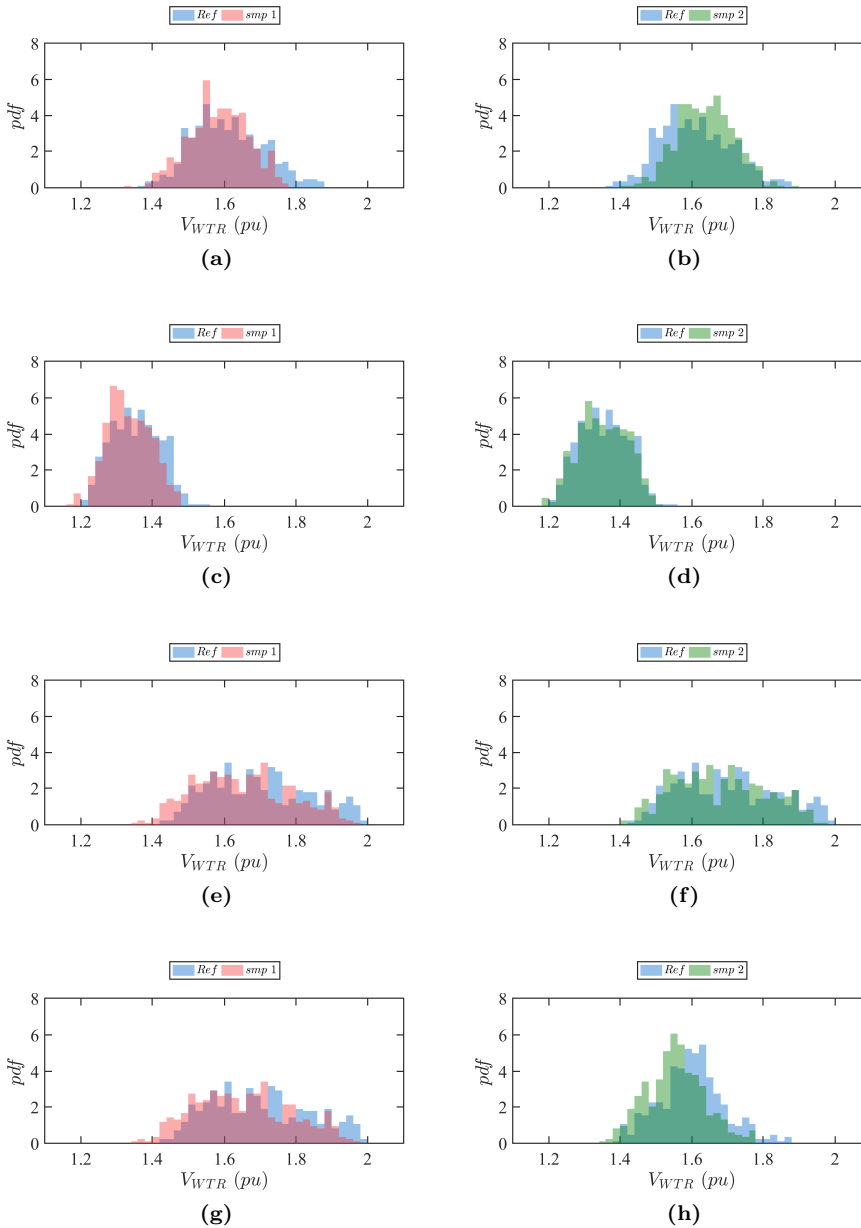


Figure B.1: Histogram plot comparison of the maximum switching overvoltage at substation WTR between the reference (a) smp 1 and (b) smp 2 model for S1, (c) smp 1 and (d) smp 2 model for S2, (e) smp 1 and (f) smp 2 model for S3 and (g) smp 1 and (h) smp 2 model for S4.

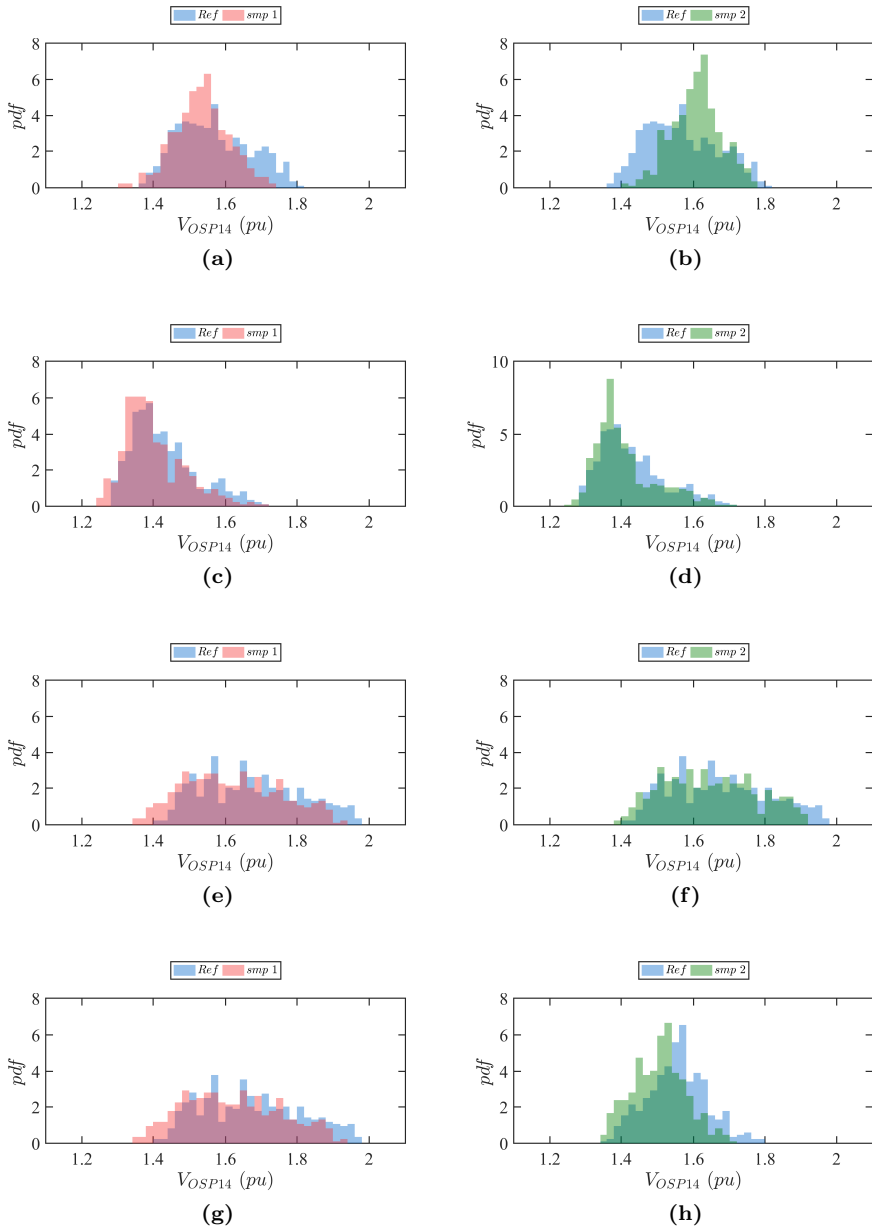


Figure B.2: Histogram plot comparison of the maximum switching overvoltage at OSP14 between the reference (a) smp 1 and (b) smp 2 model for S1, (c) smp 1 and (d) smp 2 model for S2, (e) smp 1 and (f) smp 2 model for S3 and (g) smp 1 and (h) smp 2 model for S4.

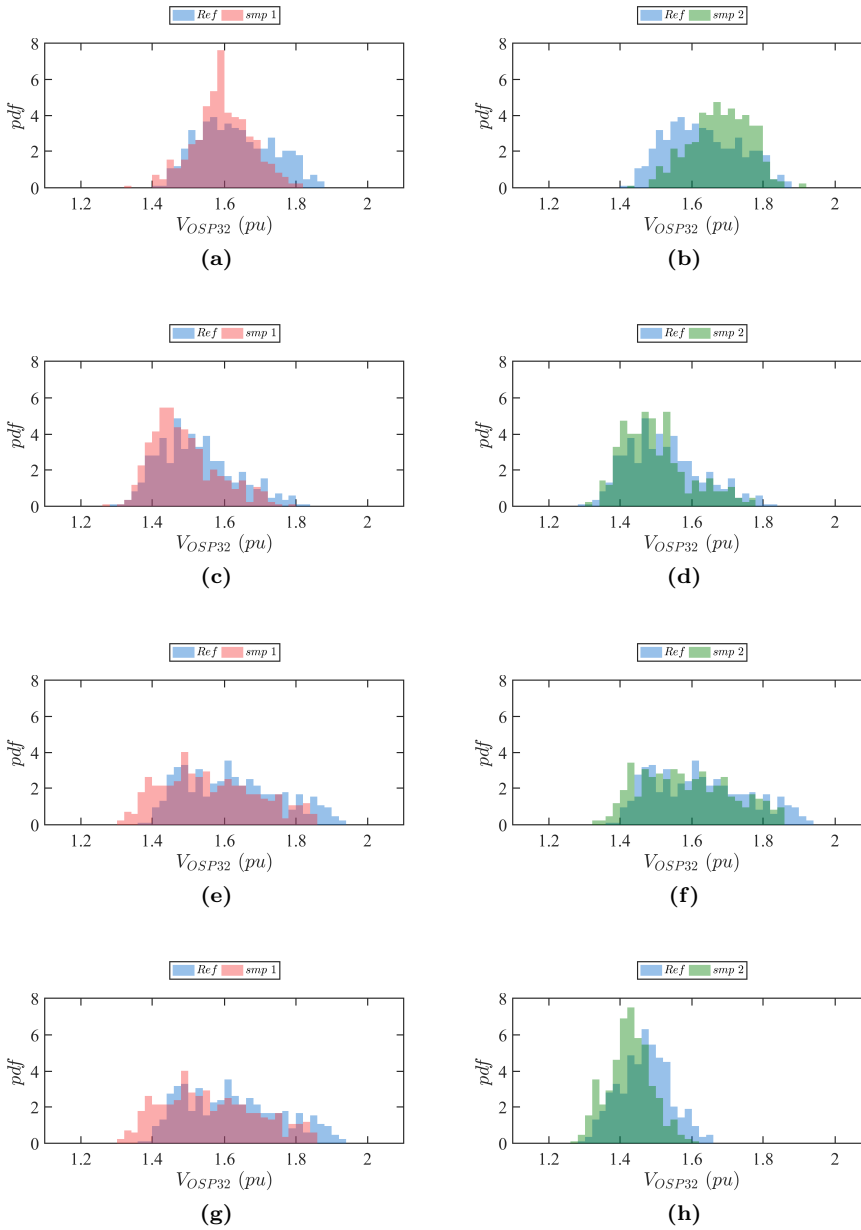


Figure B.3: Histogram plot comparison of the maximum switching overvoltage at OSP32 between the reference (a) smp 1 and (b) smp 2 model for $S1$, (c) smp 1 and (d) smp 2 model for $S2$, (e) smp 1 and (f) smp 2 model for $S3$ and (g) smp 1 and (h) smp 2 model for $S4$.

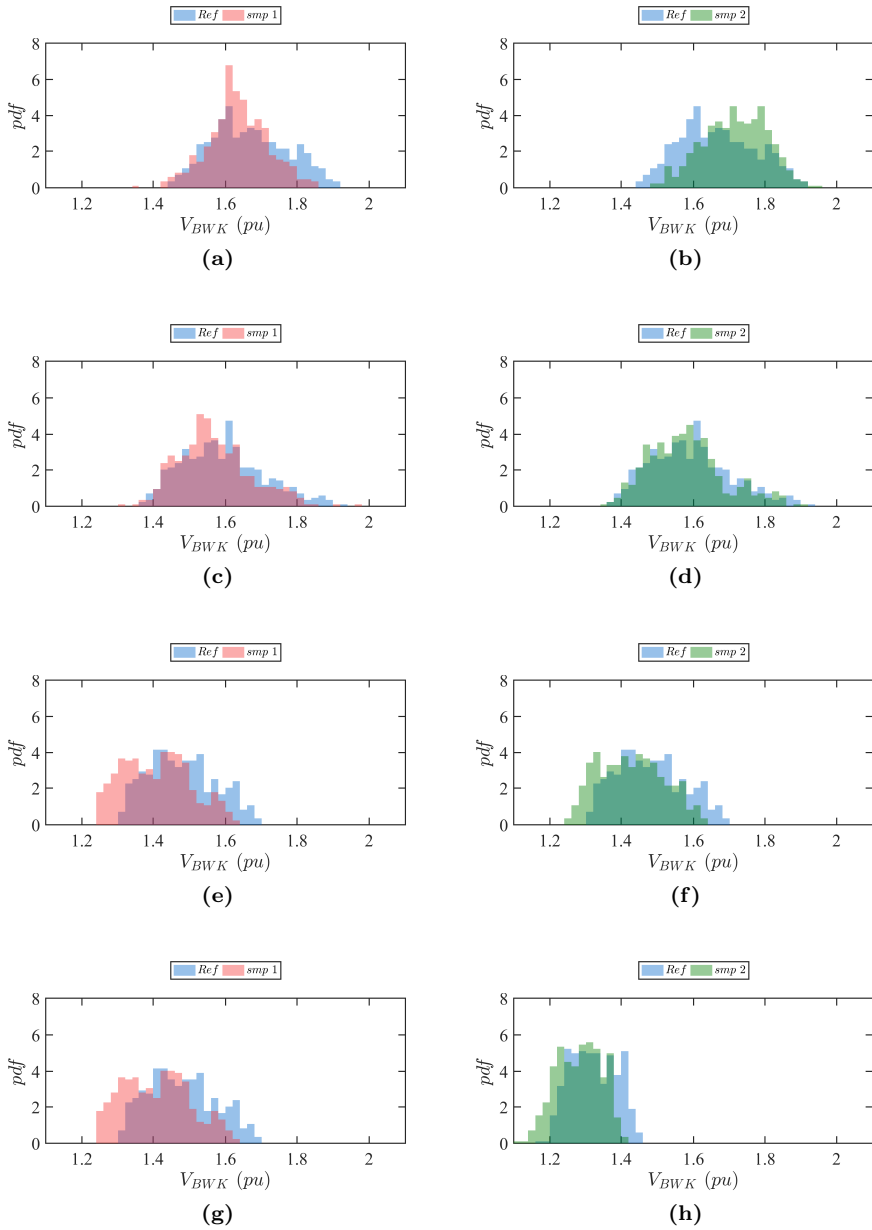


Figure B.4: Histogram plot comparison of the maximum switching overvoltage at substation BWK between the reference (a) smp 1 and (b) smp 2 model for S_1 , (c) smp 1 and (d) smp 2 model for S_2 , (e) smp 1 and (f) smp 2 model for S_3 and (g) smp 1 and (h) smp 2 model for S_4 .

Table B.1: *Fitted normal distribution mean and standard deviation values for the maximum switching overvoltage at WTR, OSP14, OSP32 and BWK for S1-S4.*

Switching actions	Location	$V_{max,Ref}$ (pu)	$V_{max,smp1}$ (pu)	$V_{max,smp2}$ (pu)
		$\mu \pm \sigma$	$\mu \pm \sigma$	$\mu \pm \sigma$
S1	WTR	1.61 ± 0.10	1.58 ± 0.08	1.64 ± 0.08
	OSP14	1.57 ± 0.10	1.53 ± 0.08	1.61 ± 0.07
	OSP32	1.63 ± 0.10	1.60 ± 0.08	1.68 ± 0.08
	BWK	1.67 ± 0.11	1.64 ± 0.08	1.72 ± 0.09
S2	WTR	1.36 ± 0.07	1.33 ± 0.06	1.35 ± 0.07
	OSP14	1.43 ± 0.09	1.40 ± 0.08	1.41 ± 0.09
	OSP32	1.52 ± 0.11	1.49 ± 0.09	1.50 ± 0.09
	BWK	1.59 ± 0.11	1.57 ± 0.10	1.58 ± 0.11
S3	WTR	1.70 ± 0.14	1.65 ± 0.13	1.68 ± 0.13
	OSP14	1.68 ± 0.14	1.62 ± 0.14	1.65 ± 0.13
	OSP32	1.62 ± 0.13	1.56 ± 0.13	1.59 ± 0.13
	BWK	1.48 ± 0.09	1.41 ± 0.09	1.43 ± 0.09
S4	WTR	1.60 ± 0.09	1.57 ± 0.09	1.56 ± 0.08
	OSP14	1.56 ± 0.08	1.52 ± 0.08	1.51 ± 0.07
	OSP32	1.47 ± 0.07	1.44 ± 0.07	1.43 ± 0.06
	BWK	1.32 ± 0.06	1.29 ± 0.06	1.28 ± 0.06

C

Measurement Decoupling

C.1 Electrostatic simulations

The geometry at both transition point and substation BWK were modeled in Coulomb electrostatic software in order to numerically obtain the coupling capacitance matrix and gain an indication for the expected magnitude of the output signal from the equipment.

The 3-D schematic of the transition point implemented in Coulomb is demonstrated in Fig. C.1. Three sensors are modeled on positions in between the two cable terminations belonging to each phase. Besides the connection from each phase to the two cable terminations, also the presence of RC divider and surge arrester with their connections to the lines are modeled. As the design details of these devices are not available, it is assumed that electric field lines can leave these devices halfway. This assumption provides the main uncertainty in calculating the coupling capacitances from electrostatic simulation. The supporting structures of these devices are modeled as cylinders at ground potential. The complete geometry is placed on a ground plane. The sensors are modeled as discs with a total area equal to the real square sensors. The ends of all modeled structures are rounded to prevent numerical issues related to sharp edges. The three sensors, three phases and ground structure result in a 7×7 capacitance matrix.

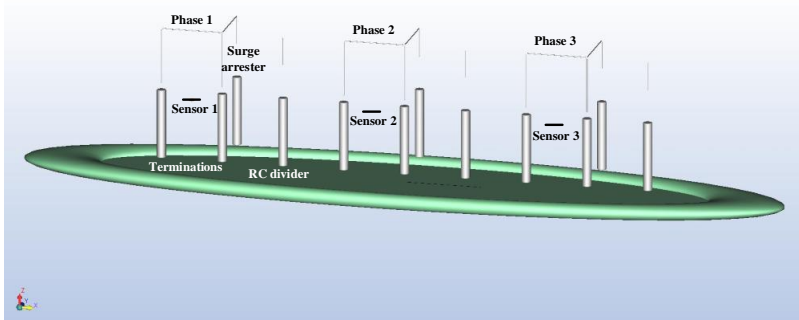


Figure C.1: Geometry of the transition point used for 3D electrostatic simulations.

The capacitance submatrix, containing the capacitances between sensors and phases only, can be extracted from the full matrix:

$$C_{osp} = \begin{bmatrix} 1.113 & 0.065 & 0.019 \\ 0.119 & 1.087 & 0.062 \\ 0.022 & 0.118 & 1.095 \end{bmatrix} \text{ pF} \quad (\text{C.1})$$

Even though the sensors were placed in such a way that a symmetric configuration is achieved it is obvious from (C.1) that the couplings of each phase to the nearest phase are not exactly equal. This can be attributed to the lines going to the RC dividers. As can be seen in Fig. C.1 the distance between sensor 1 and the RC divider of phase 2 is equal to the distance between sensor 2 and the RC divider of phase 3. The same applies for the distance between sensor 2 and the RC divider of phase 1 with sensor 3 and the RC divider of phase 2. The corresponding values of those pairs in the matrix therefore are close.

Taking into account only the direct coupling a first estimation of the output voltage amplitude is:

$$U_{out} = U_{hv} \cdot \frac{R_{dif} C_{ii}}{\tau_{int}} \approx 1 \text{ V} \quad (\text{C.2})$$

The couplings to the nearest phase reach a maximum of 10% of the direct coupling while the far end couplings do not exceed 2%. Using (C.1) as basis of the decoupling matrix, instead of the reconstructed based on measurements, resulted in typically 20% deviation in amplitude.

The 3-D simulation model of substation BWK in Coulomb is illustrated in Fig. C.2. Phase conductors are connected to a GIS system. Its geometry is modeled as cylinders on appropriate positions. Sensors 1 and 3 are placed beneath

the corresponding lines besides the GIS. Sensor 2 is positioned in front of the GIS below phase 2.

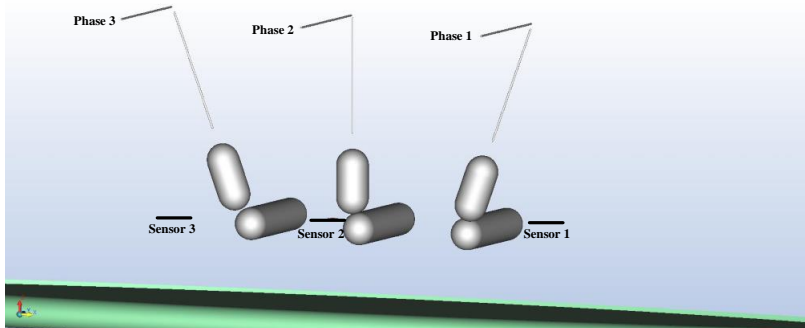


Figure C.2: *Geometry of substation BWK used for 3D electrostatic simulations.*

For the relevant couplings between sensors and phases the capacitance matrix is calculated as:

$$C_{bwk} = \begin{bmatrix} 0.287 & 0.070 & 0.028 \\ 0.105 & 0.252 & 0.105 \\ 0.028 & 0.070 & 0.287 \end{bmatrix} \text{ pF} \quad (\text{C.3})$$

The sensors near the side phases were put left and right of the bushings and the cross-couplings to the nearest phases are equal. For the middle phase the sensor was placed in front of the bushing and the coupling to the other phases is less screened than the coupling of the side sensors to the central phase. In addition, the equal coupling to the other phases add up to a signal with opposite phase angle, further reducing the measured signal from sensor 2 (see Fig. 5.10).

Taking into account only the direct coupling a first estimation of the output voltage amplitude is approximately 0.3 V and the relative couplings both to the nearest phase and the far end coupling are significantly larger than the ones calculated for the transition points. Analysis with a coupling matrix based on (C.3) resulted in an overestimate. Typically the reconstructed voltages from the measurements are 50-60% of the values obtained from (C.3). A possible reason is that grounded structures, supporting the GIS, were not modeled. These structures may draw field lines away from the sensors.

C.2 Uncertainty definition

When perfect symmetric phase voltages are assumed, they add up to zero. Considering a perfect symmetric open-air sensor to phase conductor coupling scheme:

- All direct couplings are equal: M_0
- All cross-couplings between sensor and a neighbor phase are equal: M_1
- Couplings of side sensors to phases furthest away are equal: M_2

Despite there are only three unknown components in M , a unique decoupling for perfect symmetric phase voltages is not possible. Considering the signals $U_{out,1} + U_{out,3}$, $U_{out,2}$ and $U_{out,1} - U_{out,3}$ and employing $U_{hv,1} + U_{hv,3} = -U_{hv,2}$:

$$\begin{bmatrix} U_{out,1} + U_{out,3} \\ U_{out,2} \\ U_{out,1} - U_{out,3} \end{bmatrix} = \begin{bmatrix} \alpha_2 - 2\alpha_1 & 0 \\ \alpha_1 & 0 \\ 0 & \alpha_2 \end{bmatrix} \cdot \begin{bmatrix} U_{hv,2} \\ U_{hv,1} - U_{hv,3} \end{bmatrix} \quad (C.4)$$

Due to phase voltage symmetry, only two parameter combinations can be extracted ($\alpha_1 = M_0 - M_1$ and $\alpha_2 = M_0 - M_2$). Thus, assumptions and approximations have to be made and their consequences need to be evaluated in terms of uncertainty analysis.

For the uncertainty analysis, it is assumed that a misjudgment is made in estimating the far end couplings, M_{13} and M_{31} in (5.3). When performing least square fitting, any deviation in the far end component implies that the other two components of the same row in the decoupling matrix need to be corrected with the same value in order to get the same fit result, since fitting is performed for the symmetric steady state phase voltages.

The decoupling matrix together with its errors is defined as:

$$\begin{bmatrix} U_{out,1} \\ U_{out,2} \\ U_{out,3} \end{bmatrix} = \begin{bmatrix} M_{11} + \Delta_1 & M_{12} + \Delta_1 & M_{13} + \Delta_1 \\ M_{21} + \Delta_2 & M_{22} + \Delta_2 & M_{23} + \Delta_2 \\ M_{31} + \Delta_3 & M_{32} + \Delta_3 & M_{33} + \Delta_3 \end{bmatrix} \cdot \begin{bmatrix} U_{hv,1} \\ U_{hv,2} \\ U_{hv,3} \end{bmatrix} \quad (C.5)$$

E.g. the first row can be rewritten as:

$$U_{out,1} = (M_{11}U_{hv,1} + M_{12}U_{hv,2} + M_{13}U_{hv,3}) + \Delta_1(U_{hv,1} + U_{hv,2} + U_{hv,3}) \quad (C.6)$$

The first term represents the correct signal, the second term is the consequence of misjudgment of the far coupling. A switching event leads to an asymmetric

transient excitation of the phases that develops into a symmetric three phase power frequency voltage. Already during this process the summation of the phase voltages starts to decrease (see Fig. C.3 for the summation of the three phase voltages of Fig. 5.11) and as a consequence the error in $U_{out,1}$ (second term) reduces.

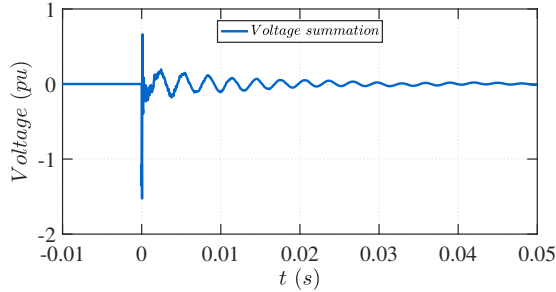


Figure C.3: *Summation of the three phase voltages after a switching action at substation BWK.*

Since the decoupling matrix has not only mathematical but also physical meaning, its elements cannot be negative. Thus, the maximum standard deviation σ of errors Δ_1 and Δ_3 that can be realistically chosen should be equal to M_{13} and M_{31} respectively. Based on the electrostatic simulation results (shown in C.1) we end up with $\sigma_1 = \sigma_3 = 1.5\%$ of M_{ii} for the transition points and $\sigma_1 = \sigma_3 = 10\%$ of M_{ii} for substation BWK. For the middle row an (overestimated) uncertainty is taken 50% of the average value of the neighbor couplings, $\Delta_2 = (M_{21} + M_{23})/4$ which results in a standard deviation of $\sigma_2 = 5\%$ of M_{ii} for the transition points and $\sigma_2 = 25\%$ of M_{ii} for substation BWK. These uncertainties are taken as the basis for the Monte Carlo analysis in Section 5.2.2.

C.3 Accuracy of D/I measurement system

An alternative procedure to determine measurement uncertainty is based on applying error propagation on the possible causes for errors. The calibration procedure to obtain the coupling matrix components results in the following sources of inaccuracy:

- Measurement accuracy: this is investigated by correlating obtained coupling matrices for different switching events recorded at one measurement site. As the sensor positions remain fixed, variations in the matrix components are related to stability of the D/I measurement system, to noise and to the fitting technique.

- The amplitudes of the phase voltages may differ from perfect symmetry. This will cause specific deviations in the matrix components, scaling with this deviation. This inaccuracy is strongly reduced when analyzing it as percentage of the power frequency amplitude, since the transient over-voltages will scale linearly with the actual phase voltages.
- As not all coupling matrix components can be reconstructed uniquely from the calibration method, assumptions need to be made. The propagation of the uncertainties introduced by these assumptions can be investigated by employing estimates (or even over-estimates) of their contributions.

C.3.1 Error propagation

The components in coupling matrix M_{ij} in (5.3) can be re-ordered such that it constitutes a linear set of nine parameters indicated as $x_{k=3(i-1)+j} = M_{ij}$. For these parameters the error matrix E_x needs to be determined, which contains all variances and covariances: $E_{x,kl} = \langle \Delta x_k \Delta x_l \rangle$. This matrix, based on estimated uncertainties in the coupling matrix components and their correlations, must be determined for the specific origin of uncertainty and for the specific structure of the adopted coupling matrix. The components of the inverted coupling matrix M^{-1} can be arranged in a linear set $y_{l=3(i-1)+j} = M_{ij}^{-1}$ as well, and its error matrix E_y can be evaluated according [122]:

$$E_y = O_1 E_x O_1^T \quad (\text{C.7})$$

with

$$O_{1,lk} = \frac{\partial y_l}{\partial x_k} \quad (\text{C.8})$$

The matrix O_1 represents a linearization of how component y_l of the inverted matrix depends on a variation in the value x_k of the original coupling matrix. Its calculation can conveniently be implemented by slightly varying numerically each coupling matrix component M_{ij} separately. Next, the phase voltage waveforms are reconstructed by matrix multiplication for each sample in the measurement recordings. The propagation of the error is described by means of matrix O_2 which provides information on how each of the three reconstructed phase voltages varies upon variation in each of the inverted matrix components. The reconstructed phase waveforms are evaluated with [122]:

$$E_U = O_2 E_y O_2^T \quad (\text{C.9})$$

with

$$O_{2,jl} = \frac{\partial U_j}{\partial y_l} \Rightarrow O_2 = \begin{bmatrix} u_1 & u_2 & u_3 & 0 & 0 & 0 & 0 & 0 & 0 \\ 0 & 0 & 0 & u_1 & u_2 & u_3 & 0 & 0 & 0 \\ 0 & 0 & 0 & 0 & 0 & 0 & u_1 & u_2 & u_3 \end{bmatrix} \quad (C.10)$$

This equation is evaluated for each measured data point. The square roots of the diagonal components in E_U provide the standard deviations for each phase (per sample point).

For the analysis, the element errors are similar to the ones defined in (C.5) with an additional uncertainty Δ_0 to account for the unsynchronized measurements:

$$\Delta = \begin{bmatrix} \Delta_1 & \Delta_1 & \Delta_1 \\ \Delta_2 - \frac{1}{2}\Delta_0 & \Delta_2 & \Delta_2 + \frac{1}{2}\Delta_0 \\ \Delta_3 & \Delta_3 & \Delta_3 \end{bmatrix} \quad (C.11)$$

With unsynchronized measurements the phase angle that relates measurements to actual phase voltages is extracted from solving system (5.3) with assumptions of symmetry. Uncertainty in this parameter can be implemented as a differential parameter Δ_0 in (C.11). A common value, Δ_{1-3} , will have no influence on the calculation of the phase angle with the assumption of perfectly symmetric three phases.

C.3.2 Reconstructed transient waveforms

The error matrix E_x is numerically evaluated for each origin of uncertainty, assuming the others are absent. From the deviations with the average values of all coupling matrix components E_x is constructed:

$$E_{x,kl} = \langle \Delta x_k \Delta x_l \rangle = \langle (x - \bar{x})_k (x - \bar{x})_l \rangle \quad (C.12)$$

Figures C.4 and C.5 contain results for switching the black circuit at WTR substation with the white circuit out of service.

Measurement error: For switching actions recorded at each measurement location C.12 can be evaluated. As the measurement of all switching actions took place during a half day, E_x gives an impression on its variability and the effect on decoupling results. Fig. C.4a shows the result for measurements at the substation. The margins, indicated with black lines, are deviations of maximum 2% based on the standard deviations obtained from the diagonal elements of E_U in (C.9). Similar values are obtained for the transition points.

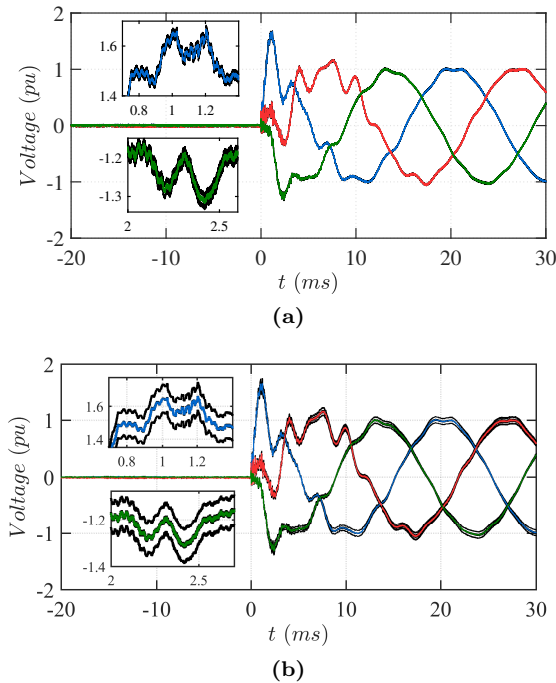


Figure C.4: Margins (black) due to (a) measurement inaccuracy and (b) non-symmetric phase voltages at BWK substation.

Non symmetric phase voltages: The effect of a 5% deviation in amplitudes is shown in Fig. C.4b for a recording at BWK. Basically, this deviation is reflected in the result with the dark lines, corresponding to one standard deviation, representing a systematic deviation over the full waveform. Normalizing on the power frequency part of the waveform provides the per unit over-voltage. The spread in this value, shown in the inset for U_1 , can just be observed as the dark curves near the original waveform. The assumption of symmetric three-phase voltages has negligible effect when considering over-voltages as a fraction of the power frequency amplitudes.

Model uncertainty: In order to evaluate the effect of model assumptions for the transition point and for the substation, matrix M is evaluated 1000 times taking normal distributions for each uncertainty parameter Δ_j . As shown in Fig. C.5a, the margin is within 2% for the transition point because the coupling matrix is close to diagonal. The situation is different for the BWK substation, Fig. C.5b, but the deviation just below 10%, is still acceptable.

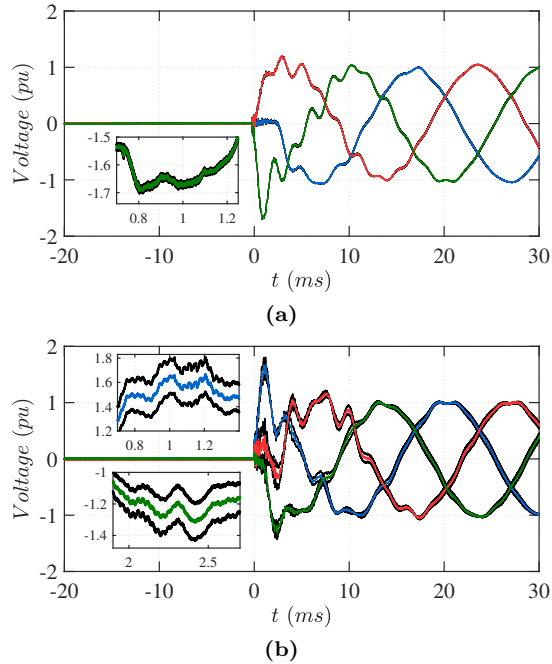


Figure C.5: *Effect of model uncertainties on over-voltages recorded at (a) transition point and (b) substation BWK.*

C.4 Energization measurements

For the low frequency transients all the types of switching actions performed during the measurement campaign at Randstad south-ring are summarized below.

- S1: the black circuit is energized from substation WTR while the white circuit is out of service.
- S2: the black circuit is energized from substation BWK while the white circuit is out of service.
- S3: the black circuit is energized from substation WTR while the white circuit is in service.
- S4: the black circuit is energized from substation BWK while the white circuit is in service.
- S5: the white circuit is energized from substation WTR while the white circuit is in service.

- S6: the white circuit is energized from substation BWK while the white circuit is in service.

The deviation of the maximum overvoltage for all six switching actions at the three measuring locations are shown in Table C.1.

Table C.1: *Maximum overvoltage magnitude deviation between simulations and measurements.*

	OSP32 (%)			OSP14 (%)			BWK (%)		
	ΔV_A	ΔV_B	ΔV_C	ΔV_A	ΔV_B	ΔV_C	ΔV_A	ΔV_B	ΔV_C
S1	-3.0	0.6	5.9	-1.6	-2.4	3.6	-4.4	-7.4	13.6
S2	15.7	11.4	0.8	7.3	10.4	8.9	0.6	-0.9	3.6
S3	-8.0	4.6	5.8	1.6	8.6	2.1	1.5	4.9	-3.6
S4	15.7	7.7	12.7	-4.9	2.3	2.8	8.2	3.9	-6.3
S5	3.6	-3.1	-2.4	-7.3	4.2	6.3	-4.5	-4.1	-15.5
S6	5.2	1.4	0.3	-6.4	2.2	0.9	-0.3	2.2	-8.7

The comparison between measurements and simulations at OSP32 for switching actions S2, S3, S4, S5 and S6 are shown in Fig. C.6 - Fig. C.10. Fig. C.11 - Fig. C.15 demonstrate the same comparison at OSP14 for switching actions S1, S3, S4, S5 and S6 while the results for substation BWK for switching actions S1, S2, S4, S5 and S6 are shown in Fig. C.16 - Fig.C.20.

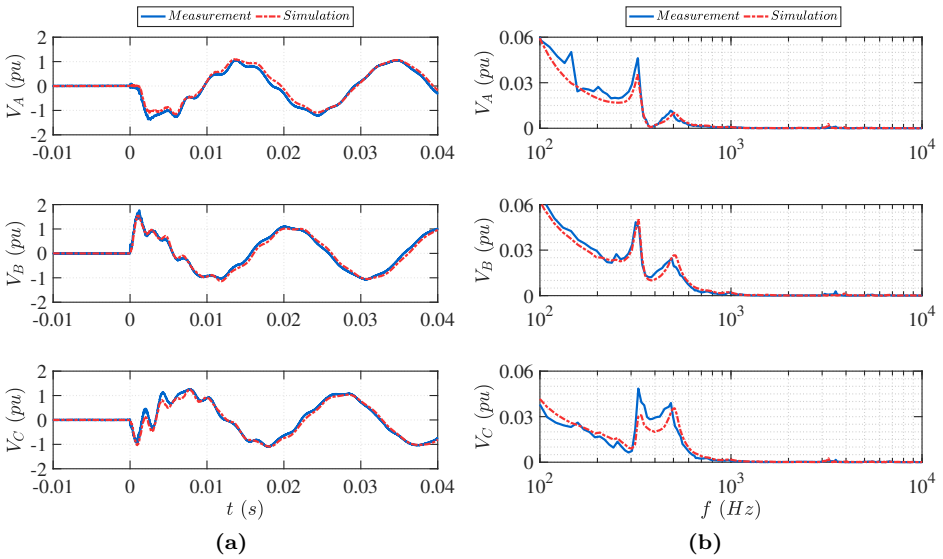


Figure C.6: Voltage waveform comparison at OSP32 for switching action S2 (a) in time and (b) frequency domain.

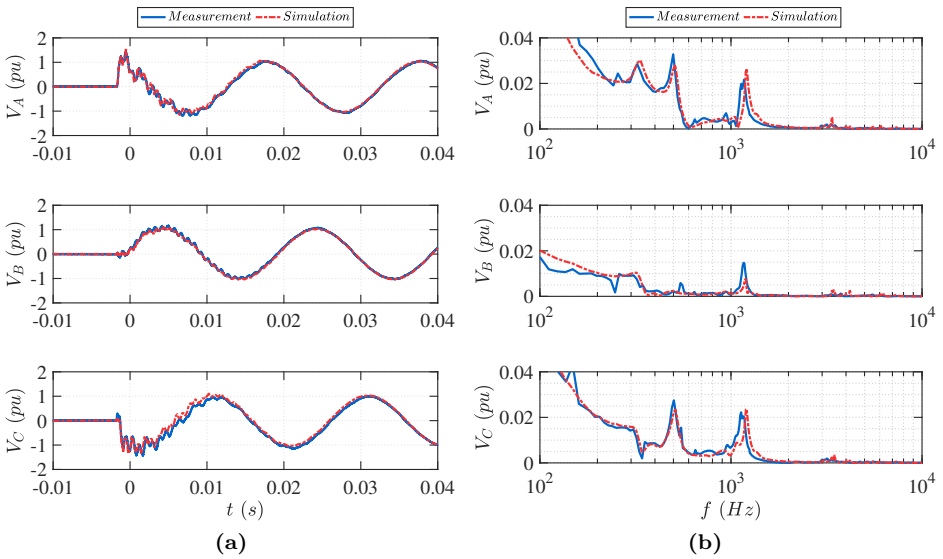


Figure C.7: Voltage waveform comparison at OSP32 for switching action S3 (a) in time and (b) frequency domain.

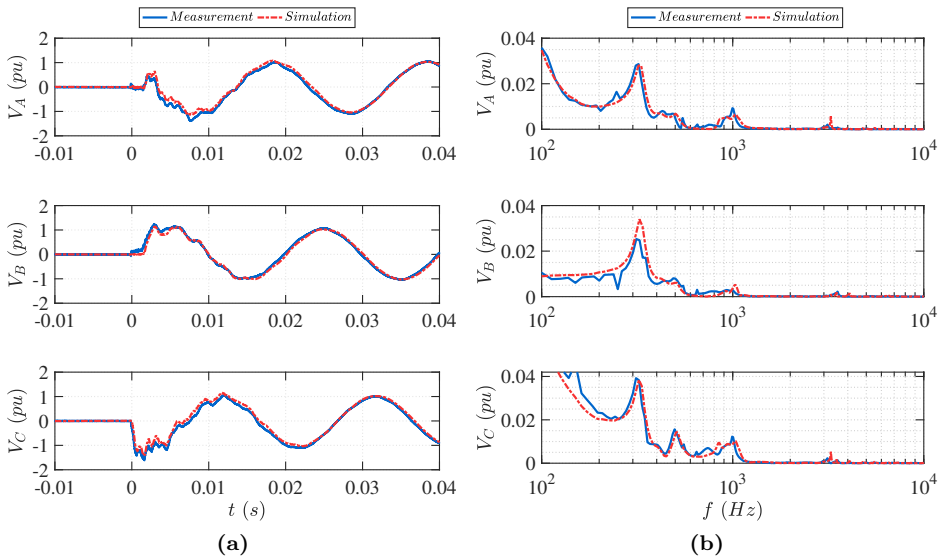


Figure C.8: Voltage waveform comparison at OSP32 for switching action S_4 (a) in time and (b) frequency domain.

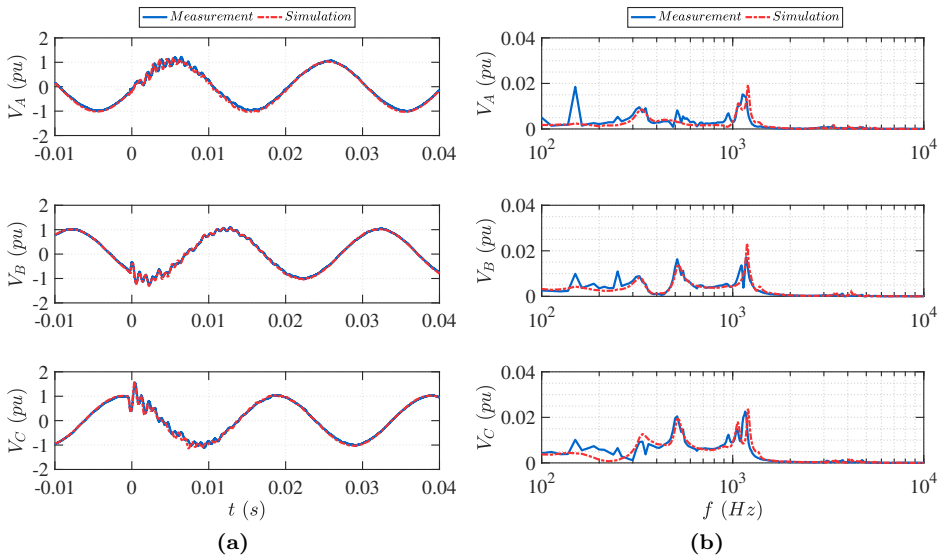


Figure C.9: Voltage waveform comparison at OSP32 for switching action S_5 (a) in time and (b) frequency domain.

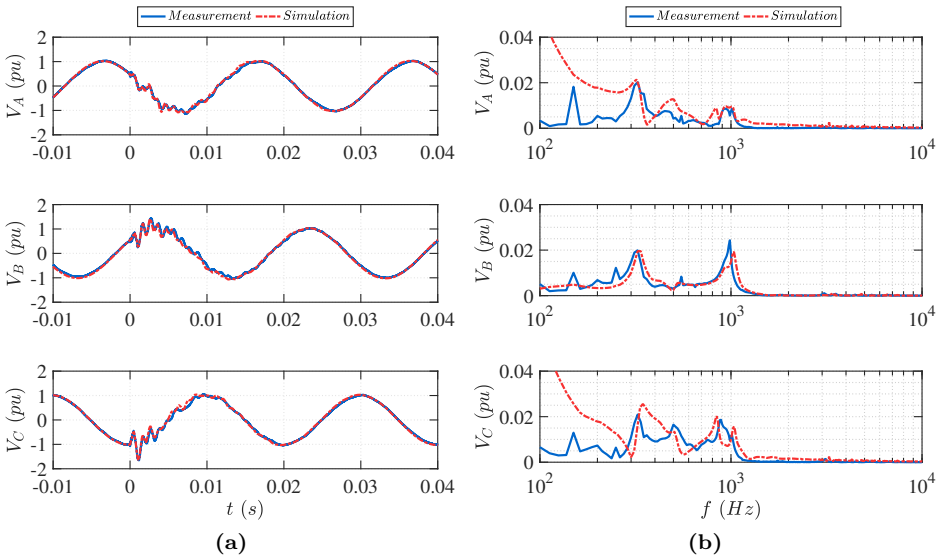


Figure C.10: Voltage waveform comparison at OSP32 for switching action S6 (a) in time and (b) frequency domain.

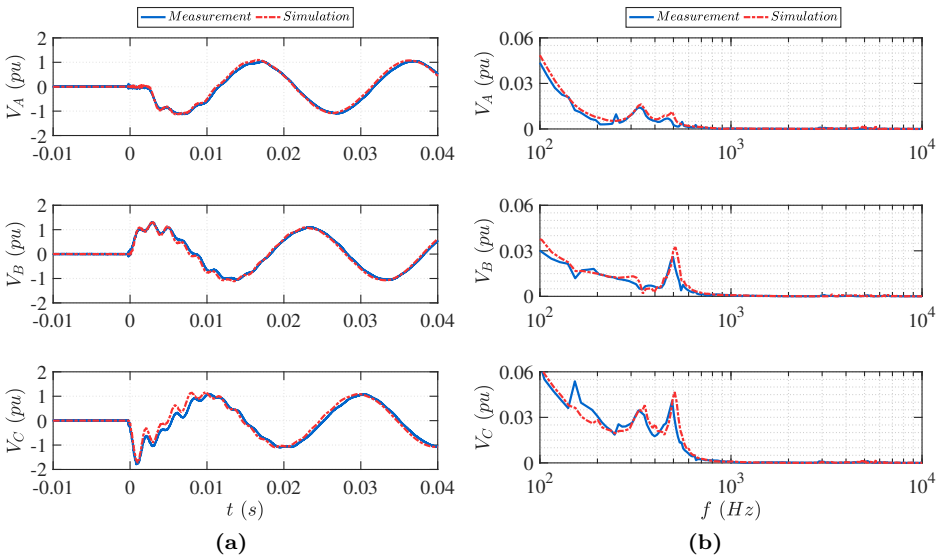


Figure C.11: Voltage waveform comparison at OSP14 for switching action S1 (a) in time and (b) frequency domain.

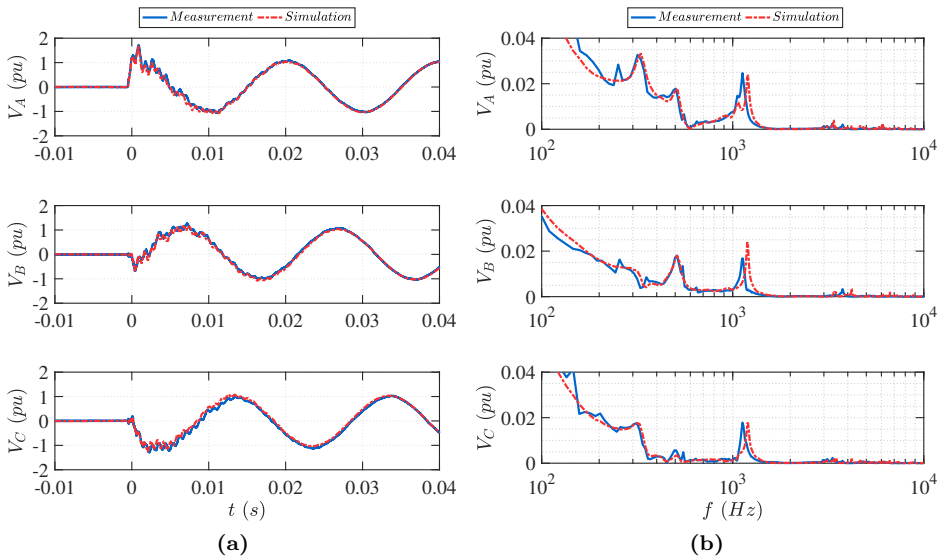


Figure C.12: Voltage waveform comparison at OSP14 for switching action S_3 (a) in time and (b) frequency domain.

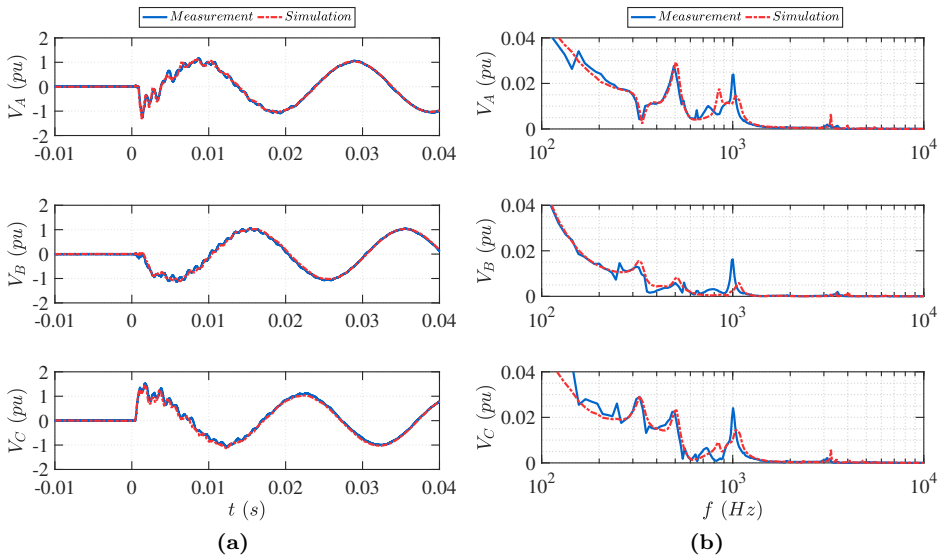


Figure C.13: Voltage waveform comparison at OSP14 for switching action S_4 (a) in time and (b) frequency domain.

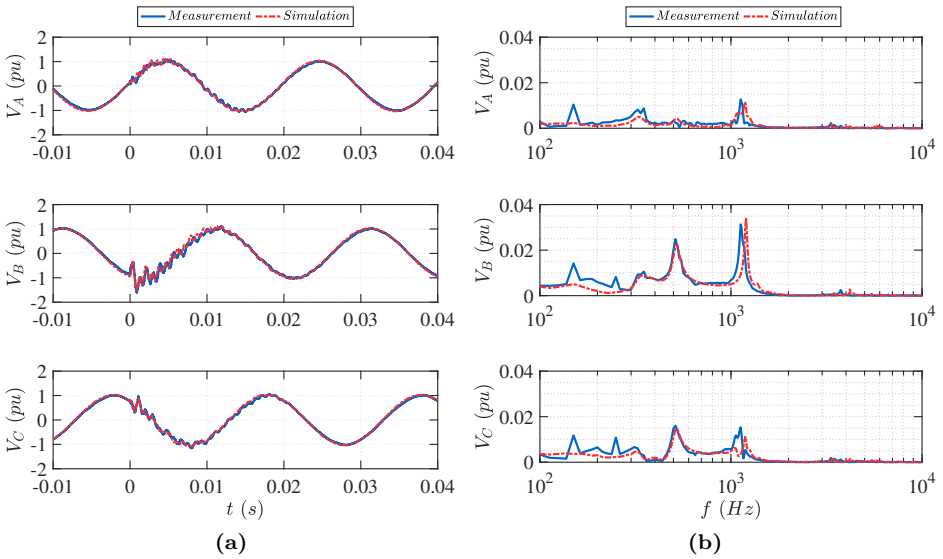


Figure C.14: Voltage waveform comparison at OSP14 for switching action S5 (a) in time and (b) frequency domain.

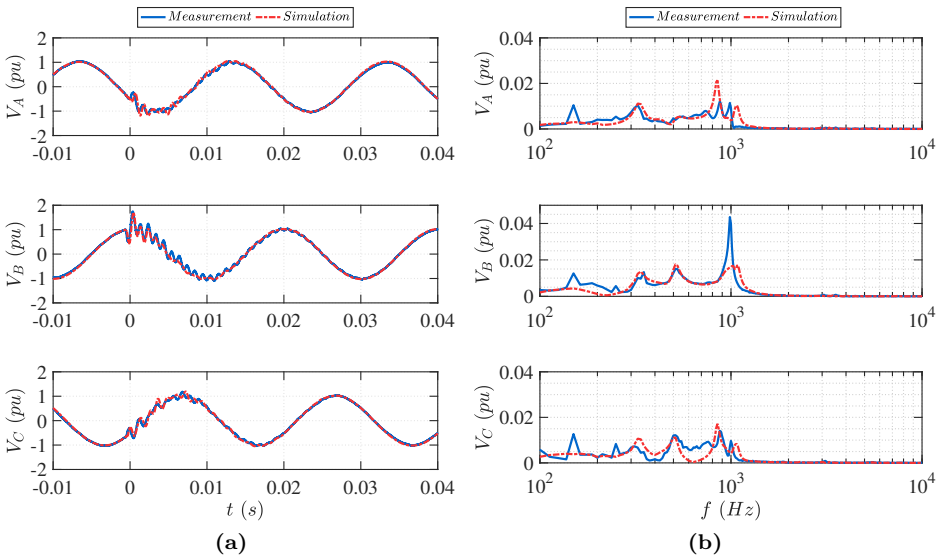


Figure C.15: Voltage waveform comparison at OSP14 for switching action S6 (a) in time and (b) frequency domain.

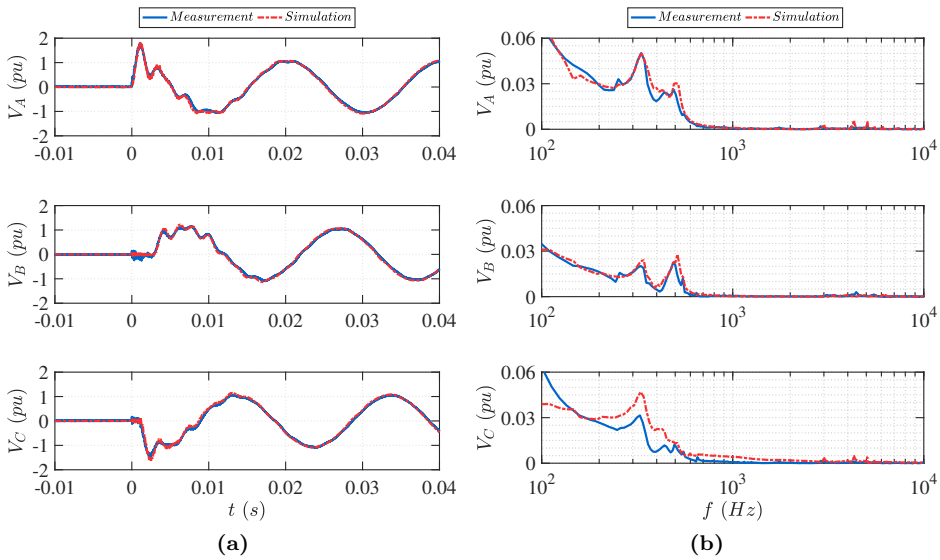


Figure C.16: Voltage waveform comparison at BWK for switching action $S1$ (a) in time and (b) frequency domain.

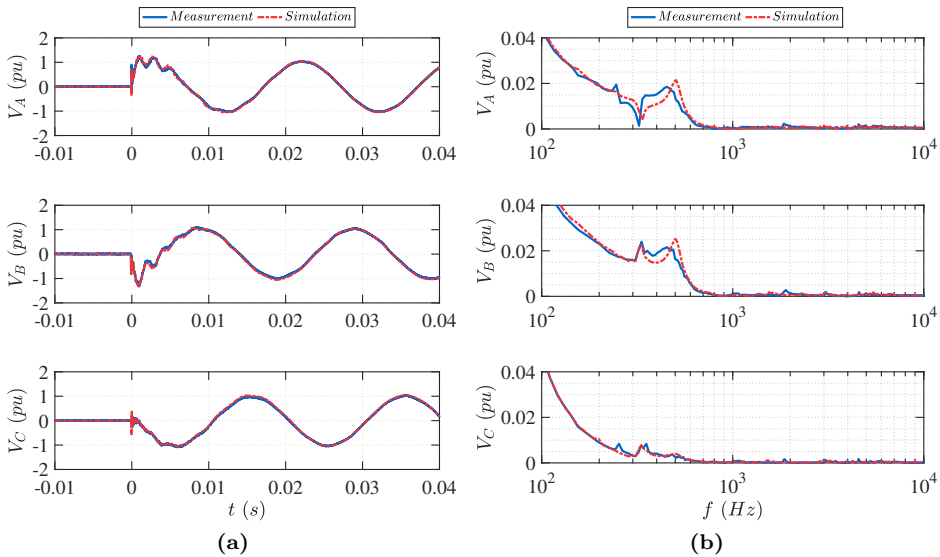


Figure C.17: Voltage waveform comparison at BWK for switching action $S2$ (a) in time and (b) frequency domain.

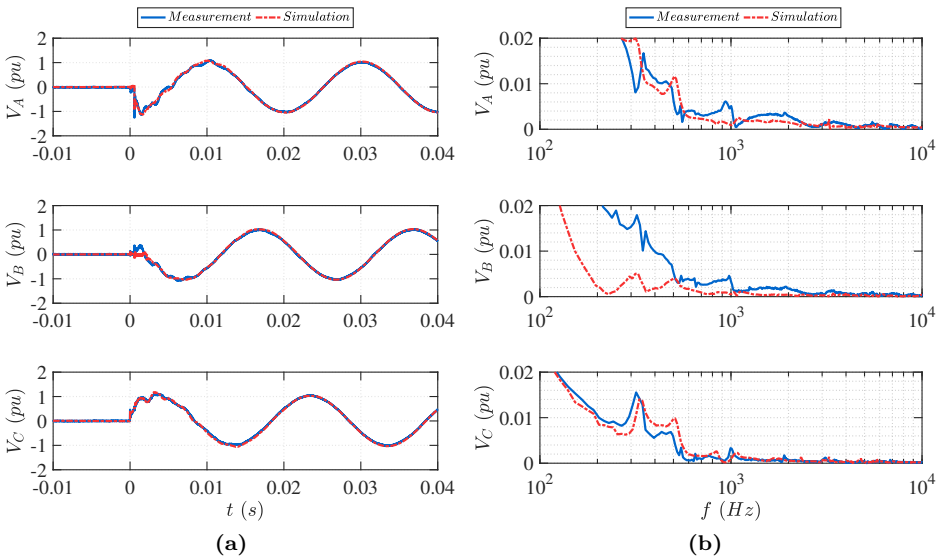


Figure C.18: Voltage waveform comparison at BWK for switching action S_4 (a) in time and (b) frequency domain.

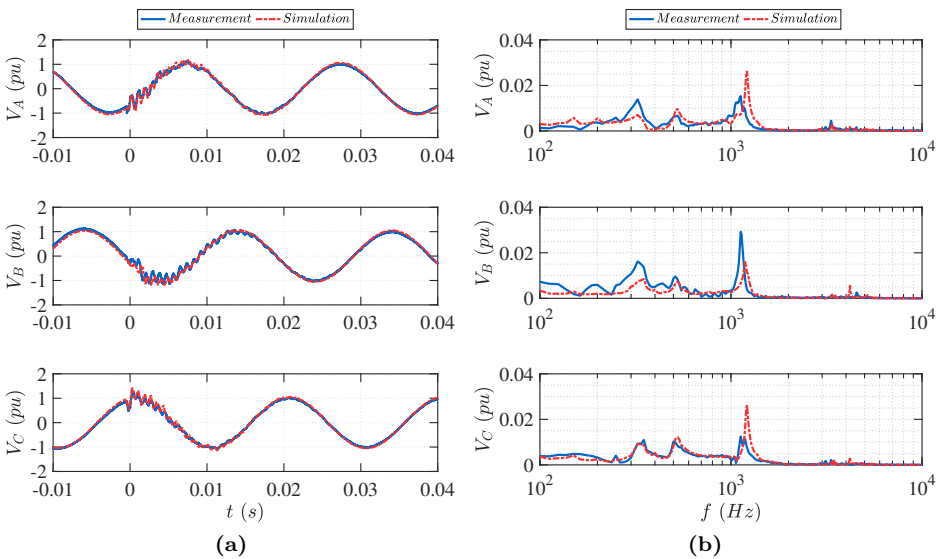


Figure C.19: Voltage waveform comparison at BWK for switching action S_5 (a) in time and (b) frequency domain.

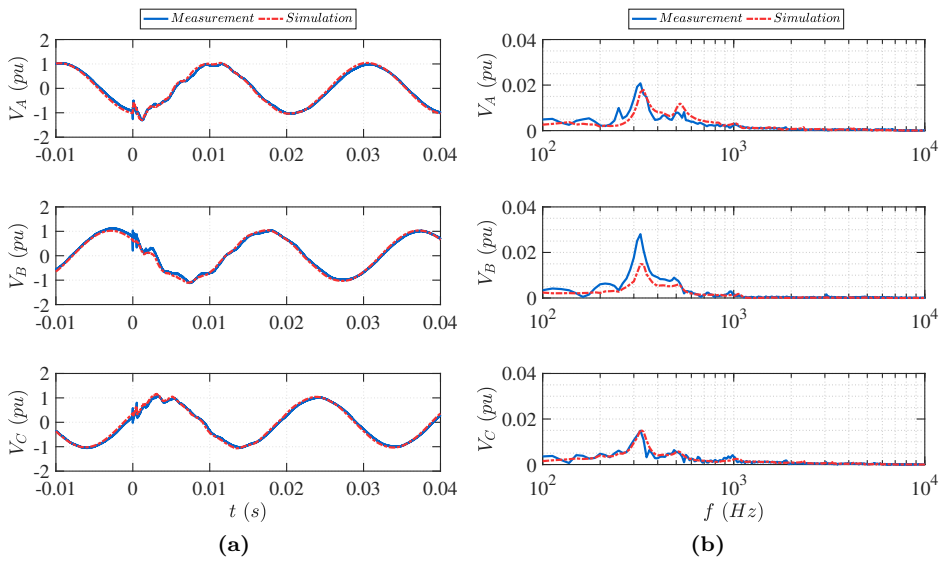


Figure C.20: Voltage waveform comparison at BWK for switching action $S6$ (a) in time and (b) frequency domain.

D

Transient studies

D.1 Series resonance

D.1.1 ABCD matrix components

The external network and transformer were modeled as a single inductance so:

$$\begin{bmatrix} A_{1,4} & B_{1,4} \\ C_{1,4} & D_{1,4} \end{bmatrix} = \begin{bmatrix} 1 & sL_{g,t} \\ 0 & 1 \end{bmatrix} \quad (\text{D.1})$$

For the OHL the Pi model was used with matrices of the form:

$$\begin{bmatrix} A_2 & B_2 \\ C_2 & D_2 \end{bmatrix} = \begin{bmatrix} 1 + ZY & Z \\ (2 + ZY)Y & 1 + ZY \end{bmatrix} \quad (\text{D.2})$$

where $Z = l \cdot (R + sL)$, $Y = l \cdot s\frac{C}{2}$ and l is the length of the line.

The same holds for both cable connections but in addition shunt reactors are connected at the sending and receiving end of the cable in order to achieve 100% compensation.

$$\begin{bmatrix} A_{3,5} & B_{3,5} \\ C_{3,5} & D_{3,5} \end{bmatrix} = \begin{bmatrix} 1 & 0 \\ \frac{1}{sL_c} & 1 \end{bmatrix} \cdot \begin{bmatrix} 1 + ZY & Z \\ (2 + ZY)Y & 1 + ZY \end{bmatrix} \cdot \begin{bmatrix} 1 & 0 \\ \frac{1}{sL_c} & 1 \end{bmatrix} \quad (\text{D.3})$$

where $L_c = \frac{2}{\omega^2 C}$ computed at the nominal frequency.

The load was modeled as a series impedance where the output voltage is zero (grounded):

$$\begin{bmatrix} A_6 & B_6 \\ C_6 & D_6 \end{bmatrix} = \begin{bmatrix} 1 & Z \\ 0 & 1 \end{bmatrix} \quad (\text{D.4})$$

where for the series load model $Z = R_l + sL_l$ while for the parallel load $Z = \frac{R_l \cdot sL_l}{R_l + sL_l}$.

Moreover, the following ABCD matrices are defined for the combination of several individual components:

$$\begin{bmatrix} A_7 & B_7 \\ C_7 & D_7 \end{bmatrix} = \begin{bmatrix} A_1 & B_1 \\ C_1 & D_1 \end{bmatrix} \cdot \begin{bmatrix} A_2 & B_2 \\ C_2 & D_2 \end{bmatrix} \quad (\text{D.5})$$

$$\begin{bmatrix} A_8 & B_8 \\ C_8 & D_8 \end{bmatrix} = \begin{bmatrix} A_4 & B_4 \\ C_4 & D_4 \end{bmatrix} \cdot \begin{bmatrix} A_5 & B_5 \\ C_5 & D_5 \end{bmatrix} \cdot \begin{bmatrix} A_6 & B_6 \\ C_6 & D_6 \end{bmatrix} \quad (\text{D.6})$$

$$\begin{bmatrix} A_9 & B_9 \\ C_9 & D_9 \end{bmatrix} = \begin{bmatrix} A_5 & B_5 \\ C_5 & D_5 \end{bmatrix} \cdot \begin{bmatrix} A_6 & B_6 \\ C_6 & D_6 \end{bmatrix} \quad (\text{D.7})$$

D.1.2 Network parameters

The low inductance of the external grid was chosen in order to represent a strong network as in the Netherlands. The UGC electrical characteristics are typical values for XLPE type cables with conductor cross-section of 2500 mm² for the EHV and 1600 mm² for the HV. The base case lengths are 20 km for the OHL, 28 km for the 400 kV cable and 20 km for the 150 kV cable. The transformer leakage inductance is a typical value for transmission transformers used in the Netherlands. For the loading condition a relatively low load of 100 MW + 50 MVar was chosen and the resistance and inductance value are calculated for the series connected load.

Table D.1: *Network parameters for base case scenario*

	R	L	C
External grid	-	0.02 H	-
OHL	0.0126 Ω /km	0.7585 mH/km	0.0152 μ F/km
400 kV Cable	0.0695 Ω /km	0.2883 mH/km	0.2147 μ F/km
Transformer	-	0.217 H	-
150 kV Cable	0.1112 Ω /km	0.3790 mH/km	0.2423 μ F/km
Load	180 Ω	0.2865 H	-

D.2 Statistics for slow front transients

In this section of the Appendix statistical information of the simulated maximum overvoltages during energization, re-strike and fault transients, for the 400 runs at each studied scenario, are presented.

D.2.1 Energization transient overvoltages

The mean overvoltage values during energization together with their standard deviations for the six different configurations at all four locations and for the four different switching scenarios are shown in Table D.2-D.5. Furthermore, the mean maximum overvoltage and standard deviation for the base case and for the addition of two new cable connections at all four locations during the four energization scenarios are depicted in Table D.6-D.9.

Table D.2: *Mean overvoltage value and standard deviation for the six different configurations at all four locations during energization action S1: energization at WTR with second circuit out of service.*

S1	WTR		OSP14		OSP32		BWK	
	μ (pu)	σ (pu)	μ (pu)	σ (pu)	μ (pu)	σ (pu)	μ (pu)	σ (pu)
case 1	1.45	0.06	-	-	-	-	1.53	0.07
case 2	1.59	0.06	1.37	0.09	1.47	0.10	1.54	0.11
case 3	1.55	0.08	1.57	0.09	-	-	1.64	0.09
case 4	1.53	0.07	-	-	1.58	0.08	1.79	0.10
case 5	1.52	0.07	1.60	0.08	1.64	0.10	1.66	0.10
case 6	1.53	0.09	-	-	-	-	2.19	0.22

Table D.3: Mean overvoltage value and standard deviation for the six different configurations at all four locations during energization action S2: energization at WTR with second circuit in service.

S2	WTR		OSP14		OSP32		BWK	
	μ (pu)	σ (pu)	μ (pu)	σ (pu)	μ (pu)	σ (pu)	μ (pu)	σ (pu)
case 1	1.24	0.05	-	-	-	-	1.57	0.11
case 2	1.33	0.06	1.37	0.09	1.47	0.10	1.54	0.11
case 3	1.38	0.06	1.49	0.07	-	-	1.55	0.07
case 4	1.27	0.06	-	-	1.62	0.09	2.14	0.21
case 5	1.36	0.07	1.66	0.11	1.36	0.07	1.46	0.07
case 6	1.49	0.08	-	-	-	-	1.74	0.13

Table D.4: Mean overvoltage value and standard deviation for the six different configurations at all four locations during energization action S3: : energization at BWK with second circuit out of service.

S3	WTR		OSP14		OSP32		BWK	
	μ (pu)	σ (pu)	μ (pu)	σ (pu)	μ (pu)	σ (pu)	μ (pu)	σ (pu)
case 1	1.57	0.11	-	-	-	-	1.47	0.09
case 2	1.64	0.12	1.60	0.12	1.54	0.12	1.40	0.08
case 3	1.57	0.12	1.49	0.11	-	-	1.45	0.10
case 4	1.63	0.11	-	-	1.59	0.11	1.36	0.07
case 5	1.60	0.14	1.59	0.14	1.50	0.08	1.47	0.08
case 6	1.73	0.11	-	-	-	-	1.35	0.07

Table D.5: Mean overvoltage value and standard deviation for the six different configurations at all four locations during energization action S4: energization at BWK with second circuit in service.

S4	WTR		OSP14		OSP32		BWK	
	μ (pu)	σ (pu)	μ (pu)	σ (pu)	μ (pu)	σ (pu)	μ (pu)	σ (pu)
case 1	1.66	0.12	-	-	-	-	1.24	0.05
case 2	1.54	0.08	1.49	0.08	1.41	0.07	1.25	0.06
case 3	2.12	0.22	1.64	0.10	-	-	1.25	0.07
case 4	1.58	0.08	-	-	1.51	0.07	1.26	0.06
case 5	1.52	0.09	1.28	0.06	1.47	0.08	1.64	0.10
case 6	1.82	0.11	-	-	-	-	1.31	0.07

Table D.6: Mean overvoltage value and standard deviation for the base case and for the addition of two new cable connections at all four locations during energization action S1: energization at WTR with second circuit out of service.

S1	WTR		OSP14		OSP32		BWK	
	μ (pu)	σ (pu)	μ (pu)	σ (pu)	μ (pu)	σ (pu)	μ (pu)	σ (pu)
base	1.58	0.08	1.55	0.08	1.61	0.09	1.65	0.09
cable 1	1.59	0.09	1.56	0.09	1.62	0.09	1.66	0.09
cable 2	1.66	0.10	1.63	0.09	1.69	0.10	1.73	0.10

Table D.7: Mean overvoltage value and standard deviation for the base case and for the addition of two new cable connections at all four locations during energization action S2: energization at WTR with second circuit in service.

S2	WTR		OSP14		OSP32		BWK	
	μ (pu)	σ (pu)	μ (pu)	σ (pu)	μ (pu)	σ (pu)	μ (pu)	σ (pu)
base	1.33	0.06	1.37	0.09	1.47	0.10	1.54	0.11
cable 1	1.37	0.07	1.41	0.07	1.47	0.07	1.57	0.09
cable 2	1.51	0.08	1.55	0.10	1.63	0.11	1.74	0.12

Table D.8: Mean overvoltage value and standard deviation for the base case and for the addition of two new cable connections at all four locations during energization action S3: energization at BWK with second circuit out of service.

S3	WTR		OSP14		OSP32		BWK	
	μ (pu)	σ (pu)	μ (pu)	σ (pu)	μ (pu)	σ (pu)	μ (pu)	σ (pu)
base	1.64	0.12	1.60	0.12	1.54	0.12	1.40	0.08
cable 1	1.64	0.13	1.60	0.13	1.55	0.13	1.40	0.09
cable 2	1.86	0.12	1.83	0.11	1.71	0.10	1.37	0.08

Table D.9: Mean overvoltage value and standard deviation for the base case and for the addition of two new cable connections at all four locations during energization action S4: energization at BWK with second circuit in service.

S4	WTR		OSP14		OSP32		BWK	
	μ (pu)	σ (pu)	μ (pu)	σ (pu)	μ (pu)	σ (pu)	μ (pu)	σ (pu)
base	1.54	0.08	1.49	0.08	1.40	0.07	1.25	0.06
cable 1	1.53	0.08	1.49	0.08	1.40	0.06	1.25	0.06
cable 2	1.83	0.11	1.77	0.11	1.62	0.09	1.29	0.04

D.2.2 Re-strike transients

The mean maximum overvoltage values during re-strike together with their standard deviations for the six different configurations at all four locations and for the four different re-closing scenarios are shown in Table D.10-D.13. Furthermore, the mean maximum overvoltage and standard deviation for the base case and for the addition of two new cable connections at all four locations during the four re-closing scenarios are depicted in Table D.14-D.17.

Table D.10: Mean overvoltage value and standard deviation for the six different configurations at all four locations during re-strike action R1: re-strike at WTR with second circuit out of service.

R1	WTR		OSP14		OSP32		BWK	
	μ (pu)	σ (pu)	μ (pu)	σ (pu)	μ (pu)	σ (pu)	μ (pu)	σ (pu)
case 1	1.72	0.36	-	-	-	-	1.82	0.42
case 2	1.87	0.44	1.85	0.42	1.93	0.47	1.98	0.49
case 3	1.87	0.40	1.92	0.44	-	-	2.00	0.48
case 4	1.80	0.42	-	-	1.88	0.45	2.20	0.59
case 5	1.77	0.40	1.87	0.45	2.01	0.51	2.05	0.52
case 6	1.71	0.32	-	-	-	-	2.54	0.79

Table D.11: Mean overvoltage value and standard deviation for the six different configurations at all four locations during re-strike action R2: re-strike at WTR with second circuit in service.

R2	WTR		OSP14		OSP32		BWK	
	μ (pu)	σ (pu)	μ (pu)	σ (pu)	μ (pu)	σ (pu)	μ (pu)	σ (pu)
case 1	1.40	0.18	-	-	-	-	1.89	0.41
case 2	1.47	0.2	1.60	0.28	1.77	0.35	1.87	0.40
case 3	1.53	0.28	1.74	0.35	-	-	1.81	0.39
case 4	1.45	0.22	-	-	1.97	0.45	2.95	0.82
case 5	1.53	0.27	2.02	0.50	1.54	0.30	1.70	0.36
case 6	1.69	0.27	-	-	-	-	2.01	0.50

Table D.12: Mean overvoltage value and standard deviation for the six different configurations at all four locations during re-strike action R3: re-strike at BWK with second circuit out of service.

R3	WTR		OSP14		OSP32		BWK	
	μ (pu)	σ (pu)	μ (pu)	σ (pu)	μ (pu)	σ (pu)	μ (pu)	σ (pu)
case 1	1.90	0.42	-	-	-	-	1.75	0.34
case 2	1.97	0.47	1.93	0.45	1.83	0.40	1.62	0.28
case 3	1.90	0.46	1.79	0.40	-	-	1.72	0.36
case 4	1.99	0.46	-	-	1.91	0.42	1.59	0.2
case 5	1.98	0.49	1.96	0.48	1.75	0.36	1.71	0.33
case 6	2.01	0.51	-	-	-	-	1.54	0.20

Table D.13: Mean overvoltage value and standard deviation for the six different configurations at all four locations during re-strike action R4: re-strike at BWK with second circuit in service.

R4	WTR		OSP14		OSP32		BWK	
	μ (pu)	σ (pu)	μ (pu)	σ (pu)	μ (pu)	σ (pu)	μ (pu)	σ (pu)
case 1	2.06	0.48	-	-	-	-	1.40	0.19
case 2	1.82	0.39	1.75	0.36	1.63	0.29	1.38	0.20
case 3	2.95	0.82	2.02	0.47	-	-	1.45	0.22
case 4	1.87	0.42	-	-	1.77	0.37	1.39	0.20
case 5	1.77	0.40	1.70	0.36	1.98	0.45	1.47	0.22
case 6	2.15	0.55	-	-	-	-	1.55	0.12

Table D.14: Mean overvoltage value and standard deviation for the base case and for the addition of two new cable connections at all four locations during re-strike action R1: re-strike at WTR with second circuit out of service.

R1	WTR		OSP14		OSP32		BWK	
	μ (pu)	σ (pu)	μ (pu)	σ (pu)	μ (pu)	σ (pu)	μ (pu)	σ (pu)
base	1.87	0.44	1.85	0.42	1.93	0.47	1.98	0.49
cable 1	1.90	0.46	1.86	0.44	1.93	0.47	1.99	0.50
cable 2	1.99	0.48	1.95	0.46	2.04	0.50	2.10	0.53

Table D.15: Mean overvoltage value and standard deviation for the base case and for the addition of two new cable connections at all four locations during re-strike action R2: re-strike at WTR with second circuit in service.

R2	WTR		OSP14		OSP32		BWK	
	μ (pu)	σ (pu)	μ (pu)	σ (pu)	μ (pu)	σ (pu)	μ (pu)	σ (pu)
base	1.47	0.26	1.60	0.28	1.77	0.35	1.87	0.40
cable 1	1.57	0.27	1.64	0.29	1.75	0.32	1.88	0.39
cable 2	1.75	0.34	1.83	0.34	1.97	0.37	2.11	0.45

Table D.16: Mean overvoltage value and standard deviation for the base case and for the addition of two new cable connections at all four locations during re-strike action R3: re-strike at BWK with second circuit out of service.

R3	WTR		OSP14		OSP32		BWK	
	μ (pu)	σ (pu)	μ (pu)	σ (pu)	μ (pu)	σ (pu)	μ (pu)	σ (pu)
base	1.97	0.47	1.93	0.45	1.83	0.40	1.62	0.28
cable 1	2.02	0.45	1.99	0.43	1.85	0.38	1.55	0.55
cable 2	2.31	0.52	2.27	0.50	2.08	0.42	1.64	0.25

Table D.17: Mean overvoltage value and standard deviation for the base case and for the addition of two new cable connections at all four locations during re-strike action R4: re-strike at BWK with second circuit in service.

R4	WTR		OSP14		OSP32		BWK	
	μ (pu)	σ (pu)	μ (pu)	σ (pu)	μ (pu)	σ (pu)	μ (pu)	σ (pu)
base	1.82	0.39	1.75	0.36	1.63	0.29	1.38	0.20
cable 1	2.01	0.46	1.93	0.42	1.74	0.32	1.29	0.11
cable 2	2.28	0.53	2.21	0.49	1.97	0.37	1.43	0.15

Bibliography

- [1] L.L. Grigsby, *The Electric Power Engineering Handbook*, 3rd ed. CRC Press LLC, May 2012.
- [2] B. Sørensen, *Renewable Energy: Physics, Engineering, Environmental Impacts, Economics and Planning*. Academic Press, Nov. 2010.
- [3] TenneT, “Derde structuurschema elektriciteitsvoorziening,” TenneT, ’s Gravenhage, Tech. Rep., 2009.
- [4] Joint Working Group 21/22.01, “Comparison of high voltage overhead lines and underground cables,” CIGRE, Tech. Rep., Dec. 1996.
- [5] Working Group B1.07, “Statistics of ac underground cables in power networks,” CIGRE, Tech. Rep., Dec. 2007.
- [6] Working Group B1.30, “Cable systems electrical characteristics,” CIGRE, Tech. Rep., Apr. 2013.
- [7] Working Group C4.502, “Power system technical performance issues related to the application of long HVAC cables,” CIGRE, Tech. Rep., Oct. 2013.
- [8] F.M.F. Da Silva, “Analysis and simulation of electromagnetic transients in HVAC cable transmission grids,” Ph.D. dissertation, Aalborg University, 2011.
- [9] U.S. Gudmundsdottir, “Modelling of long high voltage AC cables in the transmission system,” Ph.D. dissertation, Aalborg University, May 2010.
- [10] T. Ohno, “Dynamic study on the 400 kV 60 km Kyndbyværket Asnæsværket line,” Ph.D. dissertation, Aalborg University, 2012.
- [11] L. Powell, *Power System Load Flow Analysis*. McGraw Hill Professional, Nov. 2004.
- [12] W. Hofmann, J. Schlabbach, and W. Just, *Reactive Power Compensation: A Practical Guide*. John Wiley & Sons, Ltd., Dec. 2012.

-
- [13] A. Greenwood, *Electrical transients in power systems*. John Wiley & Sons, Ltd., 1991.
- [14] L. Van der Sluis, *Transients in Power Systems*. John Wiley & Sons, Ltd., 2001.
- [15] Joint Working Group 21/33, “Insulation co-ordination for HV AC underground cable system,” CIGRE, Tech. Rep., Jun. 2001.
- [16] M. Čepin, *Assessment of Power System Reliability: Methods and Applications*. Springer-Verlag London Limited, 2011.
- [17] TenneT, “Randstad380 south-ring project,” the Netherlands, <http://www.randstad380kv-zuidring.nl/>.
- [18] TenneT, “Randstad380 north-ring project,” the Netherlands, <http://www.randstad380kv-noordring.nl/>.
- [19] L. Wu, “Impact of EHV/HV underground power cables on resonant grid behavior,” Ph.D. dissertation, Eindhoven University of Technology, Oct. 2014.
- [20] G. Hoogendorp, “Steady state and transient behavior of underground cables in 380 kV transmission grids,” Ph.D. dissertation, Delft University of Technology, Oct. 2016.
- [21] B. Tuinema, “Reliability of transmission networks: Impact of EHV underground cables & interaction of offshore-onshore networks,” Ph.D. dissertation, Delft University of Technology, Nov. 2017.
- [22] *PSCAD User’s Guide*, v4.6 ed., Manitoba Hydro International Ltd., 2018.
- [23] H.M. Ryan, Ed., *High Voltage Engineering and Testing*, 2nd ed. Institution of Engineering and Technology, Dec. 2001.
- [24] E.J.M. Van Heesch, R. Caspers, P.F.M. Gulickx, G.A.P. Jacobs, W.F.J. Kersten, and P.C.T. Van der Laan, “Three phase voltage measurements with simple open air sensors,” in *7th International Symposium on High-Voltage Engineering*, Dresden, Germany, Aug. 1991.
- [25] K.S. Kunz and R.J. Luebbers, *Finite Difference Time Domain Method for Electromagnetics*. CRC Press LLC, 1993.
- [26] Tokyo Electric Power Company, “Joint feasibility study on the 400 kV cable line endrup-idomlund,” TEPCO, Tech. Rep., Apr. 2008.
- [27] C.R. Paul, *Analysis of Multiconductor Transmission Lines*, 2nd ed. John Wiley & Sons, Inc., 2008.

-
- [28] A. Ametani, T. Ohno, and N. Nagaoka, *Cable System Transients: Theory, Modeling and Simulation*. John Wiley & Sons Singapore Pte. Ltd., 2015.
- [29] H.M.J.S.P. De Silva, “Accuracy and stability improvements in electromagnetic simulations of power transmission lines and cables,” Ph.D. dissertation, University of Manitoba, 2008.
- [30] J.R. Carson, “Wave propagation in overhead wires with ground return,” *Bell System Technical Journal*, vol. 5, no. 4, pp. 539–554, 1926.
- [31] F. Pollaczek, “Sur le champ produit par un conducteur simple infiniment long parcouru par uncourant alternatif,” *Revue Gn. Elec*, vol. 29, pp. 851–867, 1931.
- [32] S.A. Schelkunoff, “The electromagnetic theory of coaxial transmission lines and cylindrical shields,” *Bell System Technical Journal*, vol. 13, no. 4, pp. 532–579, 1934.
- [33] L.M. Wedepohl and D.J. Wilcox, “Transient analysis of underground power-transmission systems. system-model and wave-propagation characteristics,” *Proceedings of the Institution of Electrical Engineers*, vol. 120, no. 2, pp. 253–260, 1973.
- [34] A. Ametani, “A general formulation of impedance and admittance of cables,” *IEEE Transactions on Power Apparatus and Systems*, vol. PAS-99, no. 3, pp. 902–910, 1980.
- [35] A. Deri, G. Tevan, A. Semlyen, and A. Castanheira, “The complex ground return plane a simplified model for homogeneous and multi-layer earth return,” *IEEE Transactions on Power Apparatus and Systems*, vol. PAS-100, no. 8, pp. 3686–3693, 1981.
- [36] W.D. Stevenson and J.J. Grainger, *Power System Analysis*. McGraw-Hill International Editions, 1994.
- [37] O. Saad, G. Gaba, and M. Giroux, “A closed-form approximation for ground return impedance of underground cables,” *IEEE Transactions on Power Delivery*, vol. 11, no. 3, pp. 1536–1545, 1996.
- [38] Manitoba HVDC Research Centre Inc., *Emtdc users guide*, Winnipeg, MB, Canada, 2010.
- [39] A. Ametani, Y. Miyamoto, and N. Nagaoka, “Semiconducting layer impedance and its effect on cable wave-propagation and transient characteristics,” *IEEE Transactions on Power Delivery*, vol. 19, no. 4, pp. 1523–1531, 2004.

- [40] G.K. Papagiannis, D.A. Tsiamitros, D.P. Labridis, and P.S. Dokopoulos, "Direct numerical evaluation of earth return path impedances of underground cables," *IEE Proceedings - Generation, Transmission and Distribution*, vol. 152, no. 3, pp. 321–327, 2005.
- [41] T.A. Papadopoulos, D.A. Tsiamitros, and G.K. Papagiannis, "Impedances and admittances of underground cables for the homogeneous earth case," *IEEE Transactions on Power Delivery*, vol. 25, no. 2, pp. 961–969, 2010.
- [42] T.A. Papadopoulos, A.I. Chrysochos, and G.K. Papagiannis, "Analytical study of the frequency-dependent earth conduction effects on underground power cables," *IET Generation, Transmission & Distribution*, vol. 7, no. 3, pp. 276–287, 2013.
- [43] H.W. Dommel, *Electromagnetic Transients Program Reference Manual (EMTP Theory Book)*, Prepared for Bonneville Power Administration, Dept. of Electrical Engineering, 1986.
- [44] A.B. Fernandes, W.L.A. Neves, E.G. Costa, and M.N. Cavalcanti, "Transmission line shunt conductance from measurements," *IEEE Transactions on Power Delivery*, vol. 19, no. 2, pp. 722–728, 2004.
- [45] T.C. Yu, "Influences of frequency-dependent shunt admittances on underground cable systems," *IEEE Transactions on Power Delivery*, vol. 23, no. 4, pp. 2385–2391, 2008.
- [46] H.W. Dommel, "Digital computer solution of electromagnetic transients in single-and multiphase networks," *IEEE Transactions on Power Apparatus and Systems*, vol. PAS-88, no. 4, pp. 388–399, 1969.
- [47] A.M. Gole, "Power systems transient simulation," 1998, course Notes, University of Manitoba.
- [48] N. Watson and J. Arrillaga, *Power Systems Electromagnetic Transients Simulation*. The Institute of Electrical Engineers, London, 2003.
- [49] B. Gustavsen, "Validation of frequency-dependent transmission line models," *IEEE Transactions on Power Delivery*, vol. 20, no. 2, pp. 925–933, 2005.
- [50] L.M. Wedepohl, "Application of matrix methods to the solution of travelling-wave phenomena in polyphase systems," *Proceedings of the Institution of Electrical Engineers*, vol. 110, no. 12, pp. 2200–2212, 1963.
- [51] L.M. Wedepohl and S.E.T. Mohamed, "Transient analysis of multiconductor transmission lines with special reference to nonlinear problems," *Proceedings of the Institution of Electrical Engineers*, vol. 117, no. 5, pp. 979–988, 1970.

- [52] L.M. Wedepohl and C.S. Indulkar, "Wave propagation in nonhomogeneous systems. properties of the chain matrix," *Proceedings of the Institution of Electrical Engineers*, vol. 121, no. 9, pp. 997–1000, 1974.
- [53] A. Semlyen and A. Dabuleanu, "Fast and accurate switching transient calculations on transmission lines with ground return using recursive convolutions," *IEEE Transactions on Power Apparatus and Systems*, vol. 94, no. 2, pp. 561–571, 1975.
- [54] E. Greenfield, "Transient behavior of short and long cables," *IEEE Transactions on Power Apparatus and Systems*, vol. PAS-103, no. 11, pp. 3193–3203, 1984.
- [55] B. Gustavsen, J. Sletbak, and T. Henriksen, "Simulation of transient sheath overvoltages in the presence of proximity effects," *IEEE Transactions on Power Delivery*, vol. 10, no. 2, pp. 1066–1075, 1995.
- [56] B. Gustavsen, J. Sletbak and T. Henriksen, "Calculation of electromagnetic transients in transmission cables and lines taking frequency dependent effects accurately into account," *IEEE Transactions on Power Delivery*, vol. 10, no. 2, pp. 1076–1084, 1995.
- [57] T. Noda, N. Nagaoka, and A. Ametani, "Phase domain modeling of frequency-dependent transmission lines by means of an ARMA model," *IEEE Transactions on Power Delivery*, vol. 11, no. 1, pp. 401–411, 1996.
- [58] P. Moreno and A. Ramirez, "Implementation of the numerical laplace transform: A review task force on frequency domain methods for EMT studies, working group on modeling and analysis of system transients using digital simulation, general systems subcommittee, IEEE power engineering society," *IEEE Transactions on Power Delivery*, vol. 23, no. 4, pp. 2599–2609, 2008.
- [59] U.S. Gudmundsdottir, B. Gustavsen, C.L. Bak, and W. Wiechowski, "Field test and simulation of a 400-kV cross-bonded cable system," *IEEE Transactions on Power Delivery*, vol. 26, no. 3, pp. 1403–1410, 2011.
- [60] A. Morched, B. Gustavsen, and M. Tartibi, "A universal model for accurate calculation of electromagnetic transients on overhead lines and underground cables," *IEEE Transactions on Power Delivery*, vol. 14, no. 3, pp. 1032–1038, 1999.
- [61] B. Gustavsen and A. Semlyen, "Simulation of transmission line transients using vector fitting and modal decomposition," *IEEE Transactions on Power Delivery*, vol. 13, no. 2, pp. 605–614, 1998.

- [62] B. Gustavsen and A. Semlyen, "Combined phase and modal domain calculation of transmission line transients based on vector fitting," *IEEE Transactions on Power Delivery*, vol. 13, no. 2, pp. 596–604, 1998.
- [63] B. Gustavsen and A. Semlyen, "Rational approximation of frequency domain responses by vector fitting," *IEEE Transactions on Power Delivery*, vol. 14, no. 3, pp. 1052–1061, 1999.
- [64] B. Gustavsen, "Improving the pole relocating properties of vector fitting," *IEEE Transactions on Power Delivery*, vol. 21, no. 3, pp. 1587–1592, 2006.
- [65] B. Gustavsen, "Optimal time delay extraction for transmission line modeling," *IEEE Transactions on Power Delivery*, vol. 32, no. 1, pp. 45–54, 2017.
- [66] L. Weinberg, *Network Analysis and Synthesis*. Mcgraw Hill Book Company, 1962.
- [67] M. Ronald, *Lumped and Distributed Passive networks, A generalized and Advanced Viewpoint*. Academic Press, 1969.
- [68] A. Chinaea and S. Grivet-Talocia, "A passivity enforcement scheme for delay-based transmission line macromodels," *IEEE Microwave and Wireless Components Letters*, vol. 17, no. 8, pp. 562–564, 2007.
- [69] H.M.J. De Silva, A.M. Gole, and L.M. Wedepohl, "Accurate electromagnetic transient simulations of HVDC cables and overhead transmission lines," in *International Conference on Power Systems Transients (IPST07)*, Lyon, Jun. 2007.
- [70] J. Marti, "Accurate modelling of frequency-dependent transmission lines in electromagnetic transient simulations," *IEEE Transactions on Power Apparatus and Systems*, vol. PAS-101, no. 1, pp. 147–157, 1982.
- [71] A. Ametani, "Wave propagation characteristics of cables," *IEEE Transactions on Power Apparatus and Systems*, vol. PAS-99, no. 2, pp. 499–505, mar 1980.
- [72] L. Wu, P.A.A.F. Wouters, and E.F. Steennis, "Frequency-domain transient analysis in double-circuit mixed HV overhead line-cable connection including cross-bonding," *International Transactions on Electrical Energy Systems*, vol. 26, no. 7, pp. 1408–1426, 2015.
- [73] F. Barakou, A. Vertkas, L. Wu, P.A.A.F. Wouters, and E.F. Steennis, "Transient modeling and sensitivity analysis of cable system parameters," in *51st International Universities Power Engineering Conference (UPEC)*, Coimbra, 2016.

-
- [74] F.M.F. Da Silva and C.L. Bak, *Electromagnetic Transients in Power Cables*. Springer London, 2013.
- [75] IEEE Modeling and Analysis of System Transients Working Group, “Modeling guidelines for switching transients,” IEEE, Tech. Rep., 1998.
- [76] Working Group 33.02, “Guidelines for representation of network elements when calculating transients,” CIGRE, Tech. Rep., 1990.
- [77] B.J.H. De Bruyn, L. Wu, P.A.A.F. Wouters, and E.F. Steennis, “Equivalent single-layer power cable sheath for transient modeling of double-layer sheaths,” in *IEEE Powertech Conference, Grenoble*, 2013.
- [78] Manitoba HVDC Research Centre Inc., “Applications of PSCAD/EMTDC,” 2008, winnipeg, Manitoba.
- [79] M.H.J. Bollen, S. Mousavi-Gargari, and S. Bahramirad, “Harmonic resonances due to transmission-system cables,” *Renewable Energy and Power Quality Journal*, pp. 712–716, 2014.
- [80] B. Gustavsen, “Panel session on data for modeling system transients insulated cables,” in *IEEE Power Engineering Society Winter Meeting*. IEEE, 2001.
- [81] B. Gustavsen, J.A. Martinez, and D. Durbak, “Parameter determination for modeling system transients—part II: Insulated cables,” *IEEE Transactions on Power Delivery*, vol. 20, no. 3, pp. 2045–2050, 2005.
- [82] H.M.J. De Silva, A.M. Gole, J.E. Nordstrom, and L.M. Wedepohl, “Robust passivity enforcement scheme for time-domain simulation of multi-conductor transmission lines and cables,” *IEEE Transactions on Power Delivery*, vol. 25, no. 2, pp. 930–938, 2010.
- [83] C. Chen, D. Saraswat, E. Gad, M. Nakhla, R. Achar, and M.C.E. Yagoub, “Passivity enforcement for method of characteristics-based multiconductor transmission line macromodels,” in *International Symposium on Signals, Systems and Electronics, Montreal*, 2007.
- [84] C. Chen, D. Saraswat, R. Achar, E. Gad, M.S. Nakhla, and M.C.E. Yagoub, “Passivity compensation algorithm for method-of-characteristics-based multiconductor transmission line interconnect macromodels,” *IEEE Transactions on Very Large Scale Integration (VLSI) Systems*, vol. 17, no. 8, pp. 1061–1072, 2009.
- [85] F. Barakou, H.M.J. De Silva, P.A.A.F. Wouters, and E.F. Steennis, “Evaluation of FDTD model for transient studies with complicated cable configurations,” in *Power Systems Computation Conference*, Dublin, Ireland, 2018.

-
- [86] B. Kordi, J. LoVetri, and G.E. Bridges, "Finite-difference analysis of dispersive transmission lines within a circuit simulator," *IEEE Transactions on Power Delivery*, vol. 21, no. 1, pp. 234–242, 2006.
- [87] K. Yee, "Numerical solution of initial boundary value problems involving maxwell's equations in isotropic media," *IEEE Transactions on Antennas and Propagation*, vol. 14, no. 3, pp. 302–307, 1966.
- [88] C. Chen, E. Gad, M. Nakhla, and R. Achar, "Passivity verification in delay-based macromodels of multiconductor electrical interconnects," *IEEE Transactions on Advanced Packaging*, vol. 30, no. 2, pp. 246–256, 2007.
- [89] M. Abdel-Rahman, "Frequency dependent hybrid equivalents of large networks," Ph.D. dissertation, University of Toronto, 2001.
- [90] F.M.F. Da Silva, C.L. Bak, and P. Holst, "Study of harmonics in cable-based transmission networks," in *Cigre*, Paris, 2012, pp. 1–14.
- [91] G. Alvarez-Cordero, A. Soler-Bachiller, A. Gomez-Exposito, J. Rosendo-Macias, and C. Gomez-Simon, "A methodology for harmonic impedance in large power systems. application to the lter of a VSC," in *Cigre*, Paris, France, 2012, pp. 1–8.
- [92] F.M.F. Da Silva, C.L. Bak, and P.B. Holst, "Estimation of the required modeling depth for the simulation of cable switching in a cable-based network," *IEEE Transactions on Power Delivery*, vol. 27, no. 4, pp. 1902–1908, 2012.
- [93] F. Barakou, A.R.A. Haverkamp, L. Wu, P.A.A.F. Wouters, and E.F. Steennis, "Investigation of necessary modeling detail of a large scale EHV transmission network for slow front transients," *Electric Power Systems Research*, vol. 147, pp. 192–200, 2017.
- [94] IEC TR 60071-4, "Computational guide to insulation co-ordination and modelling of electrical networks," IEC, Tech. Rep., 2004.
- [95] IEEE system transients working group, "Modeling guidelines for fast front transients," *IEEE Transactions on Power Delivery*, vol. 11, no. 1, pp. 493–506, 1996.
- [96] TenneT, "Kwaliteits /en capaciteitsdocument," TenneT TSO BV, Tech. Rep., 2017.
- [97] L. Wu, H. Fonk, P.A.A.F. Wouters, and E.F. Steennis, "Influence by parasitic capacitances on frequency response of a 380-150-50 kv transformer with shunt reactor," in *Proceedings of the 18th International Symposium on High Voltage Engineering (ISH 2013)*, Seoul, Korea, 2013.

- [98] DIgSILENT PowerFactory, *User Manual*, Online Edition, DIgSILENT GmbH, Gomaringen, Germany, 2017.
- [99] Working Group B4.47, “Special aspects of AC filter design for HVDC systems,” CIGRE, Tech. Rep., Oct. 2013.
- [100] A. Robert et al, “Guide for assessing the network harmonic impedance,” in *14th International Conference and Exhibition on Electricity Distribution (CIRED 1997 - Distributing Power for the Millennium)*, Birmingham, 1997.
- [101] F. Barakou, M.H.J. Bollen, S. Mousavi-Gargari, O. Lennerhag, P.A.A.F. Wouters, and E.F. Steennis, “Impact of load modeling on the harmonic impedance seen from the transmission network,” in *2016 17th International Conference on Harmonics and Quality of Power (ICHQP)*. IEEE, 2016.
- [102] J.H.R. Enslin, W.T.J. Hulshorst, A.M.S. Atmadji, P.J.M. Heskes, A. Kotsopoulos, J.F.G. Cobben, and P. Van der Sluijs, “Harmonic interaction between large numbers of photovoltaic inverters and the distribution network,” in *IEEE PowerTech Conference*, Bologna, 2003.
- [103] J.A. Martinez, R. Natarajan, and E. Camm, “Comparison of statistical switching results using gaussian, uniform and systematic switching approaches,” in *IEEE Power Engineering Society Summer Meeting*, Seattle, 2000.
- [104] M.Z. Daud, P. Ciufu, and S. Perera, “Statistical analysis of overvoltages due to the energisation of a 132 kV underground cable,” in *6th International Conference on Electrical Engineering/Electronics, Computer, Telecommunications and Information Technology*, Pattaya, 2009.
- [105] T. Ohno, C.L. Bak, A. Ametani, W. Wiechowski, and T.K. Sorensen, “Statistical distribution of energization overvoltages of EHV cables,” *IEEE Transactions on Power Delivery*, vol. 28, no. 3, pp. 1423–1432, 2013.
- [106] F. Barakou, D. Barakos, F.J.C.M. Beckers, J.J. Hoogerman, R.T.W.J. Van Hoppe, H.M. Van der Zanden, and P.A.A.F. Wouters, “Three-phase EHV measurements during switching transients with open air sensors,” in *20th ISH, Buenos Aires, Argentina*, 2017.
- [107] R.P.P. Smeets, W.A. Van der Linden, M. Achterkamp, G.C. Damstra, and E.M. De Meulemeester, “Disconnecter switching in GIS: three-phase testing and phenomena,” *IEEE Transactions on Power Delivery*, vol. 15, no. 1, pp. 122–127, 2000.

- [108] P.A.A.F. Wouters, F. Barakou, S. Mousavi-Gargari, J. Smit, and E.F. Steennis, "Accuracy of switching transients measurement with open-air capacitive sensors near OHLs," in *IEEE International Conference on High Voltage Engineering and Application (ICHVE 2018)*, Athens, 2018.
- [109] L. Wu, P.A.A.F. Wouters, E.J.M. Van Heesch, and E.F. Steennis, "On-site voltage measurement with capacitive sensors on high voltage systems," in *IEEE PowerTech Conference*. Trondheim: IEEE, 2011.
- [110] A.P.J. Van Deursen, H.W.M. Smulders, and R.A.A. De Graaff, "Differentiating/integrating measurement setup applied to railway environment," *IEEE Transactions on Instrumentation and Measurement*, vol. 55, no. 1, pp. 316–326, 2006.
- [111] IES, *Electro/Coulomb Version 9.3.*, Enginia Research Inc., 2015.
- [112] F. Barakou, P.A.A.F. Wouters, S. Mousavi-Gargari, J. Smit, and E.F. Steennis, "Merits and challenges of a differentiating-integrating measurement methodology with air capacitors for high-frequency transients," in *Cigre Sessions*, Paris, France, 2018.
- [113] A.I. Chrysochos, G.K. Papagiannis, and T.A. Papadopoulos, "Rigorous calculation method for resonance frequencies in transmission line responses," *IET Generation, Transmission & Distribution*, vol. 9, no. 8, pp. 767–778, 2015.
- [114] P.J. Schutte, W.C. Van der Merwe, and J.M. Van Coller, "Induced voltage behaviour analysis of an un-grounded outer layer semi-conductive coating of a 400 kV power cable system," in *20th ISH, Buenos Aires, Argentina*, 2017.
- [115] K.L. Chen, Y. Guo, and X. Ma, "Contactless voltage sensor for overhead transmission lines," *IET Generation, Transmission & Distribution*, vol. 12, no. 4, pp. 957–966, 2018.
- [116] T. Ohno, C.L. Bak, A. Akihiro, W. Wiechowski, and T.K. Sorensen, "Derivation of theoretical formulas of the frequency component contained in the overvoltage related to long EHV cables," *IEEE Transactions on Power Delivery*, vol. 27, no. 2, pp. 866–876, 2012.
- [117] Ch.G. Kaloudas, T.A. Papadopoulos, and G.K. Papagiannis, "Spectrum analysis of transient responses of overhead transmission lines," in *45th International Universities Power Engineering Conference (UPEC)*, Cardiff, 2010.

-
- [118] R. Burch, G. Chang, C. Hatziaioniu, M. Grady, Y. Liu, M. Marz, T. Ortmeyer, S. Ranade, P. Ribeiro, and W. Xu, "Impact of aggregate linear load modeling on harmonic analysis: a comparison of common practice and analytical models," *IEEE Transactions on Power Delivery*, vol. 18, no. 2, pp. 625–630, 2003.
- [119] IEC TR 60071-2, "Application guidelines," IEC, Tech. Rep., 2018.
- [120] IEC TR 60071-1, "Definitions, principles and rules," IEC, Tech. Rep., 2006.
- [121] C.F. Jensen, F.M.F. Da Silva, C.L. Bak, and W. Wiechowski, "Switching studies for the horns rev 2 wind farm main cable," in *International Power Systems Transient (IPST) Conference*, 2011.
- [122] J. Kuperus, "Meten in de fysika IIb," 1976, course material in Dutch, Utrecht University.

List of Publications

Journal papers

2018

Barakou, F., Wouters, P.A.A.F., Mousavi-Gargari, S., De Jong, J.P.W., and Steennis, E.F. (2018). Online Transient Measurements of EHV Cable System and Model Validation. *IEEE Transactions on Power Delivery*, Early Access, DOI:10.1109/TPWRD.2018.2876163.

2017

Barakou, F., Haverkamp, A.R.A., Wu, L., Wouters, P.A.A.F., and Steennis, E.F. (2017). Investigation of necessary modeling detail of a large scale EHV transmission network for slow front transients. *Electric Power Systems Research*, 147(June 2017), 192-200.

Conference papers

2018

Barakou, F., De Silva, H.M.J, Wouters, P.A.A.F., and Steennis, E.F. (2018). Evaluation of FDTD Model for Transient Studies with Complicated Cable Configurations. In *Power Systems Computation Conference*, Dublin, Ireland.

Barakou, F., Wouters, P.A.A.F., Mousavi Gargari, S., Smit, J., and Steennis, E.F. (2018). Merits and Challenges of a Differentiating-Integrating Measurement

Methodology with Air Capacitors for High-Frequency Transients. In *CIGRE, C4-203*, Paris, France

Barakou, F., Jensen, C.F., Lietz, G., and Val Escudero, M. (2018). Impact of uncertainties in HVAC cable modelling on transmission system harmonic behaviour. In *CIGRE, C4-304*, Paris, France

Wouters, P.A.A.F., Barakou, F., Mousavi Gargari, S., Smit, J., and Steennis, E.F. (2018). Accuracy of Switching Transients Measurement with Open-air Capacitive Sensors near OHLs. In *IEEE International Conference on High Voltage Engineering and Application (ICHVE 2018)*, Athens, Greece.

2017

Barakou, F., Bollen, M.H.J., Mousavi Gargari, S., Wouters, P.A.A.F., and Steennis, E.F. (2017). Downstream network modeling for switching transients in EHV networks containing cables. In *2017 IEEE Power and Energy Society PowerTech*, Manchester, United Kingdom.

Barakou, F., Pitsaris, A., Wouters, P.A.A.F., and Steennis, E.F. (2017). Study of series resonance overvoltage at LV side of transmission transformer during EHV cable energization. In *International Conference on Power Systems Transients*, Seoul, Republic of Korea.

Barakou, F., Barakos, D., Beckers, F.J.C.M., and Wouters, P.A.A.F. (2017). Three-phase EHV measurements during switching transients with open air sensors. In *20th International Symposium on High Voltage Engineering*, Buenos Aires, Argentina.

2016

Barakou, F., Vertkas, A., Wu, L., Wouters, P.A.A.F., and Steennis, E.F. (2016). Transient modeling and sensitivity analysis of cable system parameters. In *51th International Universities Power Engineering Conference*, Coimbra, Portugal.

Barakou, F., Bollen, M.H.J., Mousavi Gargari, S., Lennerhag, Oscar, Wouters, P.A.A.F., and Steennis, E.F. (2016). Impact of load modeling on the harmonic impedance seen from the transmission network. In *17th International Conference on Harmonics and Quality of Power (ICHQP)*, Belo Horizonte, Minas Gerais, Brazil.

Barakou, F., Wu, L., Wouters, P.A.A.F., and Steennis, E.F. (2016). Investigation of the necessary modeling depth in transmission systems with mixed OHL-Cable configuration. In *10th International Conference on Compatibility, Power Electronics and Power Engineering*, Bydgoszcz, Poland.

Khalilnezhad, H., Barakou, F., Kandalepa, N., Wu, J., Wu, L., Popov, M., Steennis, E.F., Wouters, P.A.A.F., Mousavi Gargari, S., Bos, J.A., de Jong, J.P.W., Jansen, C.P.J., Smit, J., and Kuik, R. (2016). Shunt compensation sizing, reliability analysis, and condition monitoring measurements and simulations for an EHV mixed OHL-Cable connection. In *CIGRE, C4-304*, Paris, France.

2015

Barakou, F., Koukoura, D., Dimeas, A., and Hatziargyriou, N. (2015). Fractal geometry for distribution grid topologies. In *2015 IEEE Power and Energy Society PowerTech*, Eindhoven, Netherlands.

Acknowledgements

Four years have past (so fast...) and the moment came to finalize this big chapter of my life. This journey had a lot of ups and downs and I would not have successfully completed it if I did not have the support of a number of people. Thus, I write this note to say a big THANK YOU to these people.

First of all, I would like to thank my promotor prof. Fred Steennis who accepted me as a PhD candidate and gave me the opportunity to explore the academic world. Fred thank you very much for your guidance throughout these four years and for standing up for me during a very crucial point of the project. If it was not for that action, I do not know if I could reach my final goals.

I am extremely grateful to my daily supervisor prof. Peter Wouters. Peter, I do not know if I can thank you enough for everything you did (both professionally and personally). If it was not for you, I am sure this work would not be complete. Whenever I was stuck, you always knew what to say to help me overcome any obstacle. Whenever I sent you an email (or burst in your office) with a question or a paper, you always made it your priority to respond and I am extremely grateful for that. You always supported my decisions and were reminding me to enjoy life (it took me some time but at the end I did it).

Shima, my lovely mentor from TenneT TSO B.V., thank you for all the discussions, some of them related to cables but most of them not. You believed in me (much more than I believed in myself) from the very beginning and fought for me until the end of this journey. You gave me the biggest confidence boost and at the end you convinced me to believe in my potential. A million thanks!

I would also like to thank prof. dr. ir T. Koonen, prof. dr. ir J.J. Smit, prof. dr. ir P.C.J.M. van der Wielen, prof. N. Hatziargyriou, prof. dr. ir M.H.J. Bollen for their roles as committee members in my Ph.D. defense. A more special thanks go to the last two; prof. Hatziargyriou for guiding me during my master thesis back in Greece, for seeding the idea of pursuing a PhD in my head and for proposing TU Eindhoven for this purpose; prof. Math Bollen for the numerous scientific discussions and brilliant ideas, some of them also incorporated in this book.

With this chance, I want to again express my thankfulness to TenneT TSO B.V. and especially to Nela Nevadovic, Jan de Jong, Frans van Erp and Jacco Smit who directly supported me.

During the third year of my PhD, I spent five months at the Manitoba HVDC Research Centre in Winnipeg, Canada as a guest researcher, and it turned out to be the best decision I made during my PhD. I would like to thank all the people at the Centre for their hospitality and support. More specifically, my highest gratitude goes to Dharshana Muthumuni who accepted my request to visit the Centre and did everything in his hand to make me feel like home. I consider him to be not only a supervisor but also a friend. I would especially like to thank Jeewantha de Silva for his help and guidance to implement a new cable model, which greatly contributed to the scientific impact of this thesis. To mention a few other names: Juan Carlos, my awesome roommate! Thank you for all the great times we had in your lovely house but most importantly for all the climbing trips in the middle of nowhere. My sweetest Randu, what can I say about you... There are no words to describe your kindness and positive energy. You will always have a place in my heart. The same goes for Triin and the sisterhood is completed! To my other awesome colleagues there: Laura, Kim, Jay, Ali, Malsha, Amal, George, John, Kristen and Rohitha thank you for all the great moments we had. You all made this visit a truly unforgettable experience.

I would like to thank all the EES colleagues for all the discussions during lunch and coffee breaks and for creating such a wonderful environment for working and studying. To mention some names, I want to thank Jerom (you were the first who approached me and made me feel welcome, thank you for all the personal and hilarious discussions, I really missed them in the last two years), Lei, Yan, Michiel, Gu, Mana, Stan and Yin. I also want to thank my students and friends Alex, Andreas and Dimitris for their great work.

To my greek TenneT group, Andrea and Nikki, thank you both for all the Tuesday lunch breaks where I enjoyed and could not stop laughing with all of our debates (and Andreas' trolling of course). I was looking forward to them and I KNOW you were too.

I would like to thank all my friends, new and old, in Eindhoven and back in Greece. Also, thanks to my greater family, uncles, aunts and cousins; Danai, Nefeli, Athina, Fotis and Fanoula. Finally, a big thanks goes to two very special people in my life; Katerina and Nikolas, you are always there for me no matter what. Without all of you I would not enjoy this journey as much.

Last but certainly not least, I want to thank my parents and brother. Thank you for all you have done for me and for believing in me. Your support is endless and I could not ask for more.

Μπαμπάκα μου αυτό το βιβλίο το αφιερώνω ειδικά σε σένα γιατί ξέρω πόσο πολύ περήφανος είσαι γι αυτό. Έβγαλες δύο ηλεκτρολογάρες!

Μαμάκα μου η ανιδιοτελής σου αγάπη, η φροντίδα και η στήριξη σου με έφτασαν εδώ που είμαι σήμερα.

Αδερφούλη μου, 28 χρόνια συνέχεια και παντού μαζί, δεν άντεχες να με αποχωριστείς (μέχρι τώρα). Ήσουν και είσαι το στήριγμα μου και ο τελευταίος χρόνος που μέναμε παρεούλα ήταν ο καλύτερος.

Σας αγαπώ πολύ όλους!

Curriculum Vitae

Fani Barakou was born on 2nd of February, 1990, in Athens, Greece. She received her diploma degree of electrical and computer engineering from National Technical University of Athens (NTUA), Greece, in 2013 with a specialization on electrical power systems. In the same year she joined the Smart grids Research Unit of the Electrical and Computer Engineering School (NTUA) where she worked as a researcher. In November 2014, she joined the Electrical Energy Systems group at Eindhoven University of Technology, as a Ph.D. candidate under the supervision of prof.dr.ir. E.F. Steennis and dr. P.A.A.F. Wouters. Her research topic is "Investigation of the Impact of EHV Underground Power Cables on the Resonant and Transient Grid Behavior". She is also participating in CIGRE related activities, being a member of active Working Groups.